



Provided by the author(s) and University of Galway in accordance with publisher policies. Please cite the published version when available.

Title	Upper ocean responses to solar heating and rain
Author(s)	ten Doeschate, Anneke M. M.
Publication Date	2018-07-20
Publisher	NUI Galway
Item record	http://hdl.handle.net/10379/7425

Downloaded 2024-04-24T09:46:11Z

Some rights reserved. For more information, please see the item record link above.



Upper Ocean Responses to Solar Heating and Rain

A DISSERTATION SUBMITTED IN ACCORDANCE WITH THE
REQUIREMENTS FOR THE DEGREE OF DOCTOR OF PHILOSOPHY IN
THE COLLEGE OF SCIENCE

by

Anneke M. M. ten Doeschate



School of Physics
National University of Ireland, Galway

Supervisor: Dr. Brian Ward

6 June 2018

Initial submission: 16 February 2018

Contents

Abstract	iii
Acknowledgements	vii
List of Figures	xiii
List of Tables	xix
1 Introduction	1
2 Background	5
2.1 Air-Sea Fluxes of Energy	5
2.1.1 Momentum Fluxes	5
2.1.2 Heat Fluxes	6
2.1.3 Ocean Salinity and Moisture fluxes	9
2.1.4 Buoyancy Flux	12
2.2 The COARE Bulk-Flux Algorithm	13
2.2.1 Theoretical Setup	14
2.2.2 Cool-Skin and Warm-Layer Correction	15
2.2.3 Implementation	16
2.3 Diurnal Warming	17
2.3.1 Models of Diurnal Warming	19
2.4 Turbulent Mixing in the OSBL	22
2.4.1 Defenition of Turbulence	22
2.4.2 Turbulence Theory	22
2.4.3 Ocean Turbulence in Practice	25
2.4.4 Spectral Analysis	28
3 Measurements and Methods	33
3.1 Introduction	33
3.2 ASIP	34
3.3 Scalar Fine Structure: Temperature and Salinity	35
3.3.1 Sensor Response	36
3.3.2 Sensor Calibration	40
3.3.3 Surface Detection	40
3.4 Position and Motion	42
3.5 Upper Ocean Turbulence Measurements	43
3.5.1 The Airfoil Shear Probe	43
3.5.2 Computation of ϵ from Shear: Spectral Analysis	44

3.5.3	Application of Universal Models to Derive ϵ	46
3.5.4	Evaluation of Methods to Compute ϵ	49
3.6	Using the Scalar Variance Spectrum	54
3.6.1	Case Study: the Signature of Rain in the Microstructure	55
4	Diurnal Warming of the Ocean Surface Boundary Layer	59
4.1	Introduction	59
4.2	Oceanographic Campaigns and Instrumentation	60
4.3	Observations	64
4.3.1	Oceanographic and Atmospheric Conditions	64
4.3.2	Observed Near-Surface Warming	71
4.3.3	Remnant Warm Layers and Irregular Warming	74
4.4	Warm Layer Depth Definition	79
4.5	Turbulent Mixing	84
4.6	Diurnal Warming Simulation with COARE	87
4.6.1	Set-up of the COARE 3.0 Algorithm	87
4.6.2	Model Results: North Atlantic	87
4.6.3	Model results: Mediterranean	91
4.7	Sensitivity Tests to the COARE Algorithm	94
4.7.1	Alternative Solar Absorption Parameterisations	95
4.7.2	Warm-Layer Simulation	100
4.8	Discussion and Conclusions	110
5	Upper Ocean Response to Rainfall	115
5.1	Introduction and Motivation	115
5.2	Oceanographic Campaign and Instrumentation	116
5.2.1	Microstructure Measurements	116
5.2.2	Meteorology and Air-Sea Fluxes	117
5.2.3	Wave Observations	118
5.3	Air-Sea Fluxes during Rain	118
5.4	Results	122
5.4.1	Overview of Oceanographic Conditions	122
5.4.2	Salinity, Temperature and Density Anomalies	123
5.4.3	Air-Sea Fluxes	125
5.4.4	Turbulence during Rain	128
5.5	Modelling Rain Induced Salinity Anomalies	130
5.5.1	Numerical Models	130
5.5.2	Satellite Validation	133
5.6	Discussion and Conclusion	135
6	Conclusions and Future Work	139
	Bibliography	144

Abstract

This thesis presents observations made in the ocean surface boundary layer (OSBL), with the Air-Sea Interaction Profiler (ASIP), in conjunction with measurements of meteorological variables. These are used to establish the relationship between atmospheric forcing, and the upper ocean response in terms of density stratification and turbulent mixing. Two regimes in the near-surface layer of the ocean are investigated: the diurnal cycle of heating as a result of solar irradiance, and the formation of sea surface salinity anomalies due to rain on the ocean. The ASIP measurements are used to analyse the upper ocean's response to both phenomena, from the perspective of changes in the vertical distribution of the physical variables temperature (T), salinity (S) and turbulent dissipation rate (ϵ). It is found that the evolution of a warm layer induced by daytime heating is strongly dependent on the balance between the turbulent mixing and buoyancy. Although these two forces collaborate during nighttime, under calm atmospheric conditions it is observed that a warm layer can persist over-night, which contributes to the gradual restratification of the OSBL in spring.

Diurnal warming is a regularly occurring phenomena that needs to be accounted for in coupled models of the ocean-atmosphere system and weather forecasting. The simulation of warm layer properties by the commonly used bulk-flux algorithm COARE 3.0 is compared to the observations of diurnal warm-layers from three oceanographic campaigns during which the ASIP was deployed. In this comparison it is found that the COARE model predicts the phase and amplitude of the diurnal sea surface temperature signal well. However, the deepening rate of the warm layer in the afternoon and evening is underestimated, due to the under-representation of convective mixing. A sensitivity study to the effect of varying the parameterisation of the solar radiation absorption in COARE is performed. The simulated sea surface temperature varies by several tenths of a degree between the different formulations tested, and the predicted warm layer depth by several meters.

Four periods of rainfall of varying intensity were encountered during a campaign in a mid-latitude region of the Northern Atlantic. Whether a stable layer of reduced salinity forms at the ocean surface as a result of rain, is observed to be highly dependent on the atmospheric forcing conditions associated with the rain event. Only one of the rain events observed resulted in the formation of a fresh water lens. Direct observation of ϵ shows that the shallow rain-induced stratification impacts the turbulence over the depth of the mixed layer. Within the fresh layer ϵ was somewhat enhanced, whilst in the remnant mixed layer below it it was rapidly reduced by two orders of magnitude. Relationships between rain rate and surface salinity anomaly based on numerical models and satellite validation studies are verified for the four rain events encountered. It is found that there is

a more significant causal relation between the total rain amount and the salinity anomaly at the surface than between the peak rain rate and the salinity response. Suggestions from literature that rain enhances the turbulent mixing at the surface are thought to explain the observed enhancement in the variance of the vertical salinity gradient derived from the microstructure C/T-sensors.

Declaration

The work of this thesis is based on research carried out in the Air-Sea Lab, School of Physics, NUI Galway.

No part of this thesis has been submitted elsewhere for any other degree or qualification. This thesis reports my own work, unless referenced otherwise.

Copyright © 2018 by Anneke ten Doeschate.

The copyright of this thesis belongs to the author. No quotations from it should be published without the author's prior written consent, and information derived from it should be acknowledged.

Dedication

To my parents Harrie and Caroline, and to my sister Mariel.

Bedankt lieverds voor jullie onvoorwaardelijke steun door alle jaren heen.

Acknowledgements

I would like to express my gratitude towards my PhD supervisor Dr. Brian Ward, for his inspiration and the lasting support towards the completion of this work. Thank you for giving me the freedom to pursue some of my stubborn ideas, and for providing opportunities and the best possible facilities to pursue this research project. Working together during several larger and smaller field campaigns gave me the chance to learn a lot, and to develop a positive working relationship.

I also would like to acknowledge the scientific teams and crew of the B/O Sarmiento de Gamboa, R/V Håkon Mossby and R/V Johan Hjørt, for their professional support during the oceanographic expeditions. To go to sea with loads of expensive equipment has been an adventure made into a good experience thanks to the skilled people involved.

I am grateful to have met various people whose experience and knowledge have contributed to mine. Welcome advice on ASIP data processing from Dr. Rolf Lueck has encouraged me to pursue the review of the ASIP-code. Opportunities provided by Dr. Kai Christensen from the Norwegian Met Office have given me a different perspective on ocean turbulence, and will hopefully soon lead to further collaboration.

The title of this work has evolved from ‘All I’ve learned’, via ‘Under the Weather’ to the actual title in the course of the last year and a half, which have been most crucial to my development as a post-graduate student, want-to-be-oceanographer. Five years of postgraduate research didn’t pass without any hardship, but definitely also brought loads of good experiences, which will hopefully constitute the lasting memories. Many of these involve fellow postgrad students and post-docs at the AirSea Lab, Leonie, Sebastian, Graig, Brian S., João, Niall, Valentina, Ciaran, Kieran, Danielle, Adrian and Ciara. Thank you for your companionship and advice through the years, in the lab and over coffee in the office, as well as for the good times enjoyed together — from stormy Arctic seas to smuggler’s beaches in Hawaii. My family has always been a great support.

I would like to thank my mother Caroline, for the inspiration she gave to the decision to move to Ireland. My father Harrie needs to be thanked for the lasting support he has given, albeit his rather rash decision. I am very grateful for the mental care received from my inspiring sister Mariel and my dear cousin Susanne; you have been, and I hope you will remain, a listening ear and the sweetest encouragers imaginable.

Pursuing a scientific career abroad puts a risk to keeping in touch with friends back home. I would like to thank my old friends, Milou, Mechteld, Els, Marianne, Carlijn,

Acknowledgements

Martine, Inge, Anna and Petra, who albeit my regular absence from birthdays or weekends-away, never seized to express their interest in my whereabouts. I cannot promise I will return to settle in the Nijmegen-area soon, but will try to make up for lost time in other ways.

I am grateful to all people that I've met in Galway, who have contributed to my integration in this worldly small town on the western verge of Europe; my fellow committee members and all the 'regulars' in the Mountaineering club, as well as the various people involved in equestrian sports in the region. A special thanks to Mark O'Callaghan, for his lasting interest and our friendship. Thanks also to Mary O'Shea for her knowledgeable views on making this work that bit more readable, and the many homemade treats delivered to the office in the final months of this work.

A last special note goes to my four-legged friend, dear Nino, without whom I doubt if I would have persevered, and for who this work eventually had to be completed.

Funding for this research was provided by the Office of Naval Research through Grant N62909-12-1-7064 and N62909-14-1-N296. Travel support was kindly provided by the COST Action ES1001, the Marine Institute, and the NUIG Ryan Institute.

List of Symbols

Symbol	Unit	Description
α	K^{-1}	thermal expansion coefficient
α	-	non-dimensional wavenumber in Batchelor/Kraichnan spectrum
β	kg g^{-1}	saline contraction coefficient
γ	s^{-1}	most negative strain rate in turbulent flow
δ	m	cool skin depth
ΔS_{max}	g kg^{-1}	maximum salinity anomaly
ϵ	$\text{m}^2 \text{s}^{-3}$	dissipation rate of turbulent kinetic energy
ζ	-	stability parameter
η	-	exponent in temperature profile <i>Zeng and Beljaars (2005)</i>
θ	-	generic symbol for scalar
θ	$^\circ$	solar zenith angle
κ	-	von Kármán constant
κ_S	$\text{m}^2 \text{s}^{-1}$	molecular diffusivity of salinity
κ_T	$\text{m}^2 \text{s}^{-1}$	molecular diffusivity of heat
λ	-	cool skin coefficient
μ	-	exponent in temperature profile <i>Gentemann et al. (2009)</i>
μ	$\text{kg m}^{-1} \text{s}^{-1}$	dynamic viscosity
ν	$\text{m}^2 \text{s}^{-1}$	kinematic viscosity
ρ	kg m^{-3}	density
ρ_a	kg m^{-3}	air density
ρ_r	kg m^{-3}	rain water density
ρ_w	kg m^{-3}	seawater density
σ	kg m^{-3}	potential density
σ	-	potential density divided by its value at a reference depth
τ	N m^{-2}	surface stress (general)
τ_{dp}	s	time constant in double-pole filter
τ_{sp}	s	time constant in single-pole filter
τ_w	N m^{-2}	wind induced surface stress
τ_r	N m^{-2}	rain induced surface stress

List of Symbols

ϕ	$\text{m}^2 \text{s}^{-2} \text{ cpm}^{-1}$	spectrum of turbulent velocity variance
χ_C	$\text{mS}^2 \text{ cm}^{-2} \text{ s}^{-1}$	dissipation of conductivity variance
χ_T	$\text{K}^2 \text{ s}^{-1}$	dissipation of temperature variance
χ_S	$\text{g}^2 \text{ kg}^{-2} \text{ s}^{-1}$	dissipation of salinity variance
ψ_{Cz}	$\text{mS}^2 \text{ cm}^{-2} \text{ rad}^{-1} \text{ m}^{-1}$ or cpm^{-1}	conductivity gradient spectrum
ψ_N	$\text{s}^{-2} \text{ rad}^{-1} \text{ m}^{-1}$ or cpm^{-1}	Nasmyth universal spectrum of shear
ψ_n	$\text{s}^{-2} \text{ rad}^{-1} \text{ m}^{-1}$ or cpm^{-1}	noise spectrum
ψ_{Sz}	$\text{g}^2 \text{ kg}^{-2} \text{ m}^{-2} \text{ rad}^{-1} \text{ m}^{-1}$ cpm^{-1}	or salinity gradient spectrum
ψ_{sh}	$\text{s}^{-2} \text{ rad}^{-1} \text{ m}^{-1}$ or cpm^{-1}	spectrum of shear
ψ_{Tz}	$\text{K}^2 \text{ rad}^{-1} \text{ m}^{-1}$ or cpm^{-1}	temperature gradient spectrum
ψ_{th}	$\text{s}^{-2} \text{ rad}^{-1} \text{ m}^{-1}$ or cpm^{-1}	theoretical spectrum
<hr/>		
A	-	universal constant for the inertial subrange of scalar gradient spectra
a	%	(sea-surface) albedo
a	$\text{psu mm}^{-1} \text{ h}^{-1}$	factor in peak salinity anomaly relationship
B_0	$\text{m}^2 \text{ s}^{-3}$	surface buoyancy flux
B_T	$\text{m}^2 \text{ s}^{-3}$	thermal component of surface buoyancy flux due
B_S	$\text{m}^2 \text{ s}^{-3}$	haline component of surface buoyancy flux
b	-	exponent in peak salinity anomaly relationship
C	mS cm^{-1}	water conductivity
c	$\text{psu mm}^{-1} \text{ h}^{-1}$	factor in relating R to ΔS_{max}
c_{pa}	$\text{J kg}^{-1} \text{ K}^{-1}$	specific heat of air at sea level pressure
c_{pw}	$\text{J kg}^{-1} \text{ K}^{-1}$	specific heat of water at constant pressure
c_T	$\text{mS cm}^{-1} \text{ K}^{-1}$	linearisation coefficient for T to C
c_S	$\text{mS cm}^{-1} \text{ g}^{-1} \text{ kg}^{-1}$	linearisation coefficient for S to C
D_w	m	warm layer depth
d	-	number of degrees of freedom
E_{ij}	s^{-1}	mean flow strain rate tensor
E_k	W m^{-2}	kinetic energy flux of rain
E_p	V	shear probe voltage
e_{ij}	s^{-1}	fluctuating strain rate tensor
f	s^{-1}	frequency
f_{Ny}	s^{-1}	Nyquist frequency
f_S	s^{-1}	sample frequency

f_x	-	fraction of absorbed shortwave radiative flux
G_N	$\text{s}^{-2} \text{rad}^{-1} \text{m}^{-1}$	analytical function for the Nasmyth universal shear spectrum
G_{PK}	$\text{s}^{-2} \text{rad}^{-1} \text{m}^{-1}$	analytical function for the Panchev-Kesich universal shear spectrum
g	m s^{-1}	acceleration due to gravity
H	-	response function
H_{sig}	m	significant wave height
I_d	W m^{-2}	spectrally integrated downward flux of solar irradiance
I_Q	J m^{-2}	time integral of net surface heat flux
I_τ	N s m^{-2}	time integral of surface momentum flux
K_S	$\text{m}^2 \text{s}^{-1}$	turbulent diffusivity of salinity
K_T	$\text{m}^2 \text{s}^{-1}$	turbulent diffusivity of heat
K_ν	$\text{m}^2 \text{s}^{-1}$	turbulent diffusivity of momentum; eddy viscosity
K_ρ	$\text{m}^2 \text{s}^{-1}$	turbulent diffusivity of density
k	rad m^{-2} or cpm^{-1}	wave number
k_*	rad m^{-2} or cpm^{-1}	transitional wave number between inertial and viscous-convective sub-range
k_b	rad m^{-2} or cpm^{-1}	Batchelor wave number
k_c	rad m^{-2} or cpm^{-1}	half-power wavenumber
k_{Ny}	rad m^{-2} or cpm^{-1}	wavenumber associated to Nyquist frequency f_{Ny}
k_s	rad m^{-2} or cpm^{-1}	Kolmogorov wave number
L	m	Monin-Obukhov length
L_e	J kg^{-1}	Latent heat of evaporation
Lh	-	log-likelihood
M	%	Mass fraction of dissolved ions in seawater
m	-	proportionality factor relating R_{tot} to R_{max}
N	s^{-1}	buoyancy frequency
p	N m^{-2}	pressure
R	mm h^{-1}	rain rate
R_{max}	mm h^{-1}	peak rain rate
R_{tot}	mm	total rain accumulation
Re_b	-	buoyancy Reynolds number
Re_r	-	roughness Reynolds number
Ri_b	-	bulk Richardson number
Ri_g	-	gradient Richardson number
RH	%	relative humidity

List of Symbols

r	mm	raindrop radius
r_c	mm	critical raindrop radius for penetrating the ocean surface
S	g kg^{-1} or psu	salinity
S_e	$\text{V m}^{-2} \text{s}^{-2}$	sensitivity of shear probe
S_{norm}	-	salinity divided by its value at a reference depth
S_z	g kg^{-1}	salinity at depth z below the surface
T	$^{\circ}\text{C}$	temperature
T_*	$^{\circ}\text{C}$	MOST temperature scaling parameter
T_{0-}	$^{\circ}\text{C}$	sea water temperature of at sub-skin level
T_a	$^{\circ}\text{C}$	air temperature
T_{int}	$^{\circ}\text{C}$	sea water temperature of the interface
T_{skin}	$^{\circ}\text{C}$	sea water temperature of the skin-layer
T_z	$^{\circ}\text{C}$	sea water temperature at depth z
Q_L	W m^{-2}	latent heat flux
Q_{LW}	W m^{-2}	longwave radiative flux
Q_{net}	W m^{-2}	net heat flux
Q_S	W m^{-2}	sensible heat flux
Q_{SW}	W m^{-2}	shortwave radiative flux
q	g kg^{-1}	water vapour mixing ratio
q_*	g kg^{-1}	MOST scaling parameter for water vapour mixing ratio
q_s	g kg^{-1}	water vapour mixing ratio of the sea surface interface
U	m s^{-1}	wind speed
U_{10}	m s^{-1}	wind speed at 10 m above (sea) surface level
u	m s^{-1}	first horizontal velocity component
u_*	m s^{-1}	friction velocity (air-side)
u_{*k}	m s^{-1}	friction velocity induced by vertical rain-drop impact (water-side)
u_{*r}	m s^{-1}	friction velocity induced by horizontal rain stress (water-side)
u_{*w}	m s^{-1}	friction velocity (water-side)
u_g	m s^{-1}	gustiness velocity)
v	m s^{-1}	second horizontal velocity component
W	m s^{-1}	travel velocity of shear probe
w_t	m s^{-1}	terminal velocity of raindrops
Z, z	m	depth

$Z_{\Delta S}$	m	(rain-induced) halocline depth
z_0	m	atmospheric roughness height
z_{0T}	m	atmospheric roughness height for temperature
z_{0q}	m	atmospheric roughness height for humidity

List of Figures

2.1	Schematic image showing various mechanisms of mixing in the OSBL. Reprinted from <i>Moum and Smyth (2001)</i> , with permission from Elsevier.	7
2.2	The spectrum of solar irradiance at sea level and 4 depths below the surface.	8
2.3	Schematic temperature profile in the upper 10 m of the ocean during night vs. day when diurnal warming is present, indicating the different definitions of sea surface temperature SST given in <i>Donlon et al. (2002)</i>	10
2.4	a. Marshall-Palmer distribution of raindrops with a drop-size radius r , for six commonly occurring rainfall rates R . b. The fraction of submerging rain drops for different rain rates R following (<i>Schlüssel et al., 1997</i>), when the critical dropsize radius $r_c = 0.4$ mm.	12
2.5	Schematic representation of the evolution of a diurnal warm mixed layer and its thermocline, based on <i>Soloviev and Lukas (2014)</i> . . .	18
2.6	Temperature profiles modelled with four different bulk-mixed layer models. From left to right PWP (<i>Price et al., 1986</i>), COARE 3.0 (<i>Fairall et al., 1996b</i>), (<i>Zeng and Beljaars, 2005</i>) and POSH (<i>Gentemann et al., 2009</i>).	21
2.7	One-dimensional universal spectra of velocity shear for different TKE dissipation rates ϵ	30
2.8	One-dimensional universal temperature gradient spectra for varying TKE dissipation rate ϵ and temperature variance dissipation rate χ_T	32
2.9	Varying q for $\epsilon = 1 * 10^{-7} \text{W kg}^{-1}$ and $\chi_T = 1.5 * 10^{-8} \text{K}^2 \text{s}^{-1}$, for both the Batchelor (solid line) and Kraichnan (dashed) model.	32
3.1	World map showing the location of past ASIP deployments, the year and the research vessel.	35
3.2	Three micro-structure sensor probes on ASIP, from left to right an FP07 thermistor, an SBE7 micro-conductivity sensor and an SPM38 shear probe.	36
3.3	a. Illustration of a temperature (T) and conductivity profile (C) when a warm-layer is present below the surface. b. High-pass filtered signal for the same profiles as in a.	37
3.4	Illustration of typical wavenumber spectra of vertical temperature gradient ψ_{Tz} and conductivity gradient ψ_{Cz}	38
3.5	Response functions for the FP07 thermistor probes by various authors. All except for <i>Bogucki et al. (2012)</i> are double pole responses.	39

3.6	Determination of the time response of the FP07 thermistor.	40
3.7	‘Slow’ C/T-sensors on ASIP: left the NBOSI sensor which consists of an internal field four-electrode conductivity cell and an integral, stable thermistor; right the mini-CTD 48M-probe by Sea&Sun Technology, equipped with a platinum temperature resistor, a 7-ring electrode conductivity sensor, and a Keller pressure sensor.	41
3.8	The surface detection procedure for the ASIP.	42
3.9	Schematic image of the functioning of an airfoil shear probe.	43
3.10	Flowchart describing the computation of the shear spectra, using the spectrum from the analog accelerometers to correct for instrument motions.	44
3.11	Result of the coherent noise removal technique.	45
3.12	Modelled non-dimensional Nasmyth spectrum in logarithmic (left) and linear coordinates (right), following equation (2.55), as well as the modelled integral of the non-dimensional spectrum. Coloured circles on the curves indicate where the shear variance reaches 10, 50, 80, 90 and 95% of the total.	47
3.13	Flowchart describing the computation of TKE dissipation rate ϵ , from the spectrum of measured shear ψ_{sh} , for method 1: a simple iterative fit to the Nasmyth spectrum ψ_N	50
3.14	Flowchart describing the computation of TKE dissipation rate ϵ from the spectrum of measured shear ψ_{sh} , for method 2: a fit to the Nasmyth spectrum ψ_N based on algorithms from the ODAS Matlab Library.	51
3.15	Flowchart describing the computation of TKE dissipation rate ϵ , from the spectrum of measured shear ψ_{sh} , for method 3: evaluating a universal model based on the Maximum Likelihood Estimator (MLE).	52
3.16	Comparison of 3 methods to derive ϵ from the spectral analysis using fits to universal models	53
3.17	Record of the upper 15 s of selected profiles of horizontal velocity shear $\partial u/\partial z$ and vertical conductivity gradient $\partial C/\partial z$ for selected profiles before (05:08 and 10:22) and during a short rain event of $R_{max} = 72 \text{ mm h}^{-1}$ (reds) and a longer event of $R_{max} = 45 \text{ mm h}^{-1}$ (blues).	56
3.18	Vertical conductivity and temperature gradient spectra computed over the upper 1.5 seconds of ASIP profiles during the major and minor rain events.	57
3.19	a. Rain rate R and b. Conductivity variance dissipation rate χ_C during the second half of an ASIP deployment during the Knorr-11 campaign in the North Atlantic.	57
4.1	Location of the SPURS area in the North Atlantic, and the deployment locations of the ASIP during the STRASSE and the MIDAS campaign on satellite images of chlorophyll and SST	61
4.2	Instrumentation used in SPURS-1 campaigns.	62

4.3	a. Location of the deployment of SkinDeEP during the NORBAL-5 campaign in the Mediterranean sea in April 2003, overlaid with a chlorophyll satellite image. b The SkinDeEP profiler.	63
4.4	Yearlong record of the central WHOI mooring in the SPURS area (24.5°N, 38°E).	65
4.5	Oceanographic and meteorological conditions during the STRASSE cruise, August/September 2012.	66
4.6	Oceanographic and meteorological conditions during the MIDAS-cruise, March/April 2013.	67
4.7	Potential density σ in the upper 200 m. as observed from daily (nighttime) CTD-casts during a. the STRASSE campaign and b. the MIDAS campaign.	69
4.8	Oceanographic an meteorological conditions during the NORBAL-5 cruise, April 2003.	70
4.9	Time series of buoyancy flux, wind stress, and ASIP observations during STRASSE of SST and ϵ at selected depths.	72
4.10	Time series of buoyancy flux, wind stress, and ASIP observations during MIDAS of SST and ϵ at selected depths.	73
4.11	T_{0-} normalised to its value at $t = t_0$, the time when the surface buoyancy flux becomes positive in the morning, as observed by the ASIP on 6 and 8 days during the two SPURS campaigns respectively.	74
4.12	Sequence of individual temperature profiles from ASIP on selected days during the STRASSE campaign when a DWL was observed. White dot indicates the depth of the warm layer D_{w0} in each profile. To illustrate the change, the first profile in each series is re-plotted in grey next to each consecutive profile.	76
4.13	Sequence of individual temperature profiles from ASIP on selected times and days of the MIDAS campaign when a DWL was observed. A remnant diurnal thermocline is present overnight after both 26/3 and 28/3. White dot indicates the depth of the warm layer D_{w0} in each profile. To illustrate the change, the first profile in each series is re-plotted in grey next to each consecutive profile.	77
4.14	Sequence of individual temperature profiles from ASIP on two consecutive days of the MIDAS campaign between which a remnant diurnal thermocline was observed. White dot indicates the depth of the warm layer D_{w0} in each profile. To illustrate the change, the first profile in each series is re-plotted in grey next to each consecutive profile.	78
4.15	Close-up on the upper 10 m of profiles with staircase features.	78
4.16	Observed temperature during the 2nd and 3rd deployments of the MIDAS campaign (a) and the 6th deployment of ASIP during STRASSE (b), with a selection of all tested criteria for D_w	80
4.17	Comparison of visually determined warm layer depth D_{w0} [m] versus various systematical methods for 225 profiles from the STRASSE campaign.	82

4.18	Comparison of visually determined warm layer depth D_{w0} [m] versus various systematical methods for 231 profiles from the MIDAS campaign.	83
4.19	Daily minimum depth of the layer of active mixing versus the peak diurnal amplitude in T_{0-} for both SPURS cruises.	84
4.20	The parameter h/L for the NORBAL-5, STRASSE, and MIDAS campaign.	85
4.21	Temperature difference over the upper 5 m (a, c) as well as warm layer depth D_w (b, d) simulated by the COARE model for the STRASSE and MIDAS datasets.	88
4.22	Comparison of simulated temperature directly below the surface (T_{0-}) versus the observed where available from the ASIP profiles (grey line) for both North Atlantic research cruises.	90
4.23	a.+b. Cool-skin and warm-layer correction following the COARE algorithm for the two North-Atlantic datasets. c. Cool-skin correction ΔT_c versus wind speed U_{10} following the COARE model runs for the STRASSE (blue circles) and MIDAS (green triangles). d. Idem for the ocean leaving heat flux Q_{out} and U_{10}	91
4.24	Output of COARE for 3 different combinations of input air temperature T_a and T.	92
4.25	Temperature difference over the upper 5 m (a) as well as warm-layer depth D_w (b) simulated by the COARE model for the NORBAL-5 dataset.	94
4.26	Irradiance absorption curves following 4.2.	96
4.27	Modelled irradiance curves following parameterisations of the oceanic watertypes of the optical classification by <i>Jerlov (1976)</i> , as described <i>Paulson and Simpson (1981)</i> (a), as well as for chlorophyll-dependent parameterisations by <i>Morel and Antoine (1994)</i> (dashed lines), <i>Ohlmann and Siegel (2000)</i> (solid lines) and <i>Ohlmann (2003)</i> (dash-dotted lines) for three different <i>Chl</i> -concentrations (b).	98
4.28	Mean evolution of the sea surface albedo a during the day at the three study sites, following the parameterisation in <i>Ohlmann and Siegel (2000)</i>	99
4.29	The fraction of absorbed radiation f_x as a function of depth below the surface, following the different parameterizations tested in section 4.7.2. Acronyms are explained in section 4.7.1.	100
4.30	Scatter plots the change in warm layer correction ΔT_{0-5m} for different shortwave absorption parameterisations.	104
4.31	Output of the COARE algorithm for different shortwave absorption parameterisations, STRASSE	105
4.32	Output of the COARE algorithm for different shortwave absorption parameterisations, MIDAS	106
4.33	Output of the COARE algorithm for different shortwave absorption parameterisations, NORBAL-5	107

4.34	Modelled ΔT_{0-5m} versus observed from ASIP / SkinDeEP profiles, for 12 different shortwave absorption parameterisations for low turbidity/[<i>Chl</i>] water (left) and higher turbidity/[<i>Chl</i>] water (right).	108
4.35	Modelled T_{0-} / T_{1m} versus observed from ASIP / SkinDeEP profiles, for 12 different shortwave absorption parameterisations for low turbidity/[<i>Chl</i>] water (left column) and higher turbidity/[<i>Chl</i>] water (right column).	109
4.36	Diurnal amplitude in T_{0-} from ASIP measurements during the MIDAS campaign, and following the COARE 3.0 and POSH algorithms. Purple dots indicate the diurnal amplitude following the parameterisation of <i>Webster et al.</i> (1996). Δ is the mean bias between the modelled and observed peak ΔT .	112
5.1	a. Map of the ship track of the Knorr-11 cruise, with circles indicating the approximate locations of ASIP deployments. Observations from deployment 1 are used in this chapter. b. The exact location of the ASIP profiles, with colors indicating the sections of both the ASIP and the ship track corresponding to the rainy periods.	117
5.2	Power law fit (red) to the exact solution (blue) of E_k in <i>Schlüssel et al.</i> (1997) and <i>Soloviev and Lukas</i> (2014)	121
5.3	Overview of the observations made during the first deployment of the ASIP in the Knorr-11 campaign.	123
5.4	Near-surface profiles of salinity (S), temperature (T) and potential density (σ) normalised to their value at 8 m, during each of the four rain events. Dashed line: profile corresponding to the occurrence of the maximum salinity difference between the surface and a reference depth for the specific rain event. Solid line: consecutive profile.	124
5.5	T-S curves of the upper 25 m, during each of the four rain events. In each panel a profile before (gray), at the peak of the rain rate (black) and after the rain (green) is plotted. The T-S relationship is evaluated at each 20 cm interval. To enhance detail the salinity scale is varied between the plots, and the temperature scale on the vertical axis in panel I differs from the other three.	125
5.6	Air-sea fluxes during the rain events.	126
5.7	a. Time-series of B_0 , friction velocities u_{*w} and $(u_{*w} + u_{*r})$. b. The ratio $ h/L $. c. Salinity at selected depths below the surface. d. ϵ at selected depths below the surface.	128
5.8	a. Observed ΔS_{max} versus peak rain rate R_{max} compared to result of models by <i>Drushka et al.</i> (2016) and <i>Bellenger et al.</i> (2017) (B'17). b. ΔS_{max} versus the total amount of rainfall R_{tot}	131
5.9	Illustration of the effect of applying a moving average to the time series of rain rate R .	132
5.10	Skin and sub-skin salinity S (top) and temperature T (bottom) output from the prognostic scheme in <i>Bellenger et al.</i> (2017). Thin grey line is the subskin value from the ASIP for comparison.	134

5.11 Comparison of the observed 60 min averaged rain rate R_{60} versus maximum salinity difference observed in the Knorr-11 campaign to linear relationships derived from satellite-data, as described in <i>Boutin</i> (2016).	135
--	-----

List of Tables

2.1	Sea salt composition for reference salinity in Standard Seawater, as determined by <i>Millero et al.</i> (2008). M is the mass fraction.	10
4.1	RMS-error between the systematically determined warm layer depth and the visually determined depth D_{w0} in n temperature profiles from the two SPURS datasets ($n_S = 225$, $n_M = 231$).	81
4.2	Red light fraction and attenuation lengths for the oceanic water types of the optical classification by <i>Jerlov</i> (1976), from <i>Paulson and Simpson</i> (1977).	96
4.3	Coefficients for the polynomial function to compute v_i or L_i in equation (4.6) and (4.7) of the chlorophyll concentration $[Chl]$ (<i>Morel and Antoine</i> , 1994).	96
4.4	Exponential coefficients for the nine wavelength solar absorption model from <i>Paulson and Simpson</i> (1981). In the last two columns the alternative values of $1/L_1$ for the different Jerlov water types are listed, following <i>Soloviev and Schlüssel</i> (1996).	97
4.5	Coefficients determined in the linear regression in <i>Ohlmann and Siegel</i> (2000), used to compute A_i and K_i in equation (4.10) for clear sky conditions.	99
4.6	Mean Absolute error $ \mu $ and Root Mean Square Error (RMSe) between the observed near-surface temperature difference ΔT_{0-5m} (ΔT_{1-5m} for NORBAL-5) and the output of the COARE 3.0 algorithm for the varied shortwave absorption parameterisations.	102
4.7	Mean Absolute error $ \mu $ and Root Mean Square Error (RMSe) between the observed subsurface temperature T_{0-} and the output of the COARE 3.0 algorithm for the varied shortwave absorption parameterisations. For the NORBAL-5 campaign the temperature at 1 m depth is compared.	103
5.1	Characteristics of the four observed rain events: peak rain rate R_{max} , cumulative rain R_{tot} , duration, mean and maximum 10-m windspeed U_{10} during the rain event.	118

*“ The Road goes ever on and on
Down from the door where it began.
And I must follow, if I can,
Pursuing it with eager feet,
Until it joins some other way
Where many paths and errands meet.
And whither then? I cannot say”.*

After J. R. R. Tolkien (1954)

1 Introduction

Seas and oceans cover 90% of the Earth's surface. As a result the coupled ocean-atmosphere system is of major importance in regulating the planet's climate. The dynamics of both the ocean and atmospheric boundary layer act to restore the fluid's thermodynamic equilibrium, which is continuously disturbed as a result of differences in solar radiation, the main energy source.

Lateral differences in temperature and heat content of the air cause wind to transfer momentum to the ocean surface. This drives surface currents, the shear instabilities of which are a main source of turbulent kinetic energy to the upper ocean. Waves formed as a result of wind forcing add to this stirring, and consequently change the properties of the ocean surface.

The tens of meters of the water column below the ocean surface are therefore generally well mixed. This mixed layer, together with the stratified region immediately below it, is sometimes called the 'ocean surface boundary layer' (OSBL), analogous to the atmospheric boundary layer which is the lower part of the atmosphere adjacent to it (*Thorpe, 2007*). The depth extent of this mixed layer varies slowly in temporal terms, driven by seasonal differences in the meteorological forcing in mid- and high latitudes.

Within the OSBL, the near-surface layer is defined to be the layer directly adjacent to the ocean surface, the properties of which vary on a daily basis as the result of local air-sea fluxes (*Soloviev and Lukas, 2014*). In return this layer directly feeds back to the atmosphere. It has a variable depth extent and depends on the process under consideration; air-sea exchange of moisture and gases (e.g. CO_2) occurs within the upper millimetre range, wave effects and diurnal warming on the scale of metres, whilst turbulent mixing processes can cause variability down to the depth of the seasonal mixed layer. Due to the many non-linear processes that act on sub-diurnal to inter-annual timescales, and at millimetre to planetary spatial scales, the near-surface layer of the ocean is a complex physical system. It is strongly coupled with the lower atmosphere above it and directly influences the climate which humans inhabit. Only through studying the coupled system can one advance the understanding of the individual components. Models for ocean and weather prediction, as well as climate studies, require both adequate boundary condition measurements and parameterisation of sub-grid processes. The dynamic character of the air-sea interface and the presence of sublayers means that these boundary conditions are most suitably described by fluxes of momentum, heat and moisture.

This thesis focusses on the vertical distribution of near-surface properties during two near-surface layer regimes of the ocean:

- **Diurnal Warming:**

Differential heating and cooling controls the buoyancy of the near-surface layer. Especially under calm conditions (low wind speeds, no waves breaking), the absorption of solar radiation drives the formation of a warm, stratified layer confined to the upper metres. Potential energy is transferred to kinetic energy by sea surface cooling once the forcing conditions change during nighttime. Nighttime convection will erode vertical temperature gradients buildup during the day. It is one of the largest sources of turbulent mixing, and usually affects the full depth of the OSBL. Especially in low latitudes this pattern of diurnal warming is prevalent. Daytime changes in forcing conditions, like increases in the windspeed and cloud formation, modify the thermal restratification process. There is a major interest in the diurnal cycle of the ocean surface with respect to its influence on exchange processes between the ocean and the atmosphere, and its relation to weather and climate (*Kawai and Wada, 2007*). Especially in tropical regions there is a strong feedback between diurnal warming and the occurrence of deep atmospheric convection. A bi-diurnal periodicity in high convective cloud formation and strong diurnal warming was observed by (*Chen and Houze*). On a warming Earth the frequency of occurrence of near-surface thermal stratification in mid and high-latitudes can be expected to increase, as well as the amplitude of the diurnal sea surface temperature variability. On the other hand the intensification of atmospheric convection, and associated cloud systems, downdrafts and storms, may oppose the occurrence of near-surface stratification. Model results indicate that diurnal warming affects the atmospheric circulation (*Clayson and Chen, 2002*), and both global and regional increases in sea surface temperatures (SST) can provide energy to intensify weather phenomena. Changing patterns in near-surface stratification have direct consequences for primary production, which has a dependency on both the SST and the vertical mixing of nutrients to the surface (*Hahn-Woernle et al., 2014*).
- **Near-surface freshening due to rain:**

Apart from temperature, the salinity of the ocean water controls its buoyancy. The salinity of the near-surface layer is the result of the regional freshwater balance (evaporation - precipitation), and ocean circulation and mixing processes. The highest sea surface salinity (SSS) is found in subtropical oceans, as a result of net-evaporation and balanced by a high SST. On sub-diurnal time scales precipitation causes SSS anomalies, through the formation of a 'lens' of water of reduced salinity at the surface. Rain-induced stratification of the near-surface layer is typically observed in regions of intense rainfall (e.g. the tropics). Although often a very local phenomenon, persistent freshwater lenses can have similar effects to the air-sea exchange as a diurnal warm layer, and have therefore become a research focus of recent years.

Diurnal warming and rainfall can lead to the formation of a shallow stratification in the near-surface layer. How and how much this changes the fluxes of heat and momentum, has rarely been determined from in-situ observations. It has been proven that both effects could be sufficiently important to require their inclusion in numerical weather prediction models. This requires parameterisation of both

phenomena, as well as their effect on air-sea fluxes of heat and momentum. Rapid developments in remote sensing techniques have taken place through which the state of the ocean and atmosphere can be assessed with global coverage. Remote sensing of the oceans from space provides information about the ocean surface, or at most the upper millimetres, in terms of temperature, salinity, sea surface roughness (waves) and currents, as well as sediment and biochemical products in the water. Together with in-situ observations from mooring arrays, buoys, ships of opportunity and research campaigns this data is assembled into global products for use in weather prediction and climate models.

However, the assimilation of data from these various sources, which are all measured at different time and spatial scales, into one product, requires thorough knowledge of processes in the OSBL. Also, variability in sea surface properties which occur on time scales smaller than the measurement frequency in a certain location (e.g. within the period of the repeated crossing of a polar-orbiting satellite), leads to biases in the interpretation of marine observations. Where satellites measure horizontal variations in near-surface properties, profiles through the deeper layers of the ocean up to the surface contribute to our understanding of vertical processes and their temporal variability. CTD casts taken during oceanographic research campaigns only provide sporadic information. This is one of the motivations behind the global Argo-program, which has seen the launch of 3800 autonomous CTD profiling floats over the last 18 years (www.argo.ucsd.edu). Measurements from Argo are also widely used for the validation of satellite observations of sea surface temperature (SST) and salinity (SSS) (*Riser et al.*, 2008). Nevertheless, most of these now routine oceanographic measurements do not provide the level of vertical precision necessary to observe diurnal variability in heating or water cycle processes in the upper 10 m of the ocean.

It is unknown to what extent haline and thermal stratification in the near-surface layer both suppress and are at the same time being gradually broken down by turbulence. While the depth of the layer of near-uniform density, the mixed layer depth (MLD), represents the time-integrated response to mixing events, the depth of active mixing depends on the instantaneous balance between stabilising buoyancy forces and destabilising turbulent mixing. The depth of this ‘mixing layer’ (XLD), as well as the turbulence intensity, is usually highly intermittent, and often embedded within the MLD (*Brainerd and Gregg*, 1995; *Thomson and Fine*, 2003; *Sutherland et al.*, 2014a). Turbulence is conventionally quantified through the dissipation rate of TKE (ϵ), though often this quantity is not directly measured but estimated from scaling theories, using wind speed, or a combination of wind, buoyancy and wave information (*Lombardo and Gregg*, 1989; *Terray et al.*, 1996; *Esters et al.*).

Over a shallow layer of $O(1 \text{ mm})$ directly below the ocean surface momentum exchange with the atmosphere is controlled by viscosity. Within this layer the even thinner diffusive microlayers for heat and salt are contained. The dominance of molecular diffusion results in a nearly permanent temperature and salinity inversion over these layers (*Saunders*, 1967; *Veron et al.*, 2011). The convective instability of

the cool and haline ocean ‘skin’ layer drives surface renewal. However, the infrared and a significant fraction of the microwave part of the solar spectrum, comprising of 5 – 10% of the total incoming solar radiation, is absorbed over the depth of the thermal microlayer (*Paulson and Simpson, 1981*). Strong daytime heating, as well as surface freshening due to rain, impact the cool skin and associated air-sea flux mechanisms. On the other hand, rain drops that ‘break’ the surface layer are thought to temporarily enhance exchange of heat and gases also (*Houk and Green, 1976; Schlüssel et al., 1997*).

New observations are presented of salinity and temperature in the upper tens of meters of the open ocean, along with measurements of the active turbulence in this layer. Observations of variability in the vertical distribution of these variables as a result of diurnal warming and precipitation, are compared to commonly used 1D models. The ocean surface is highly dynamic; to even define the air-sea interface, and more so to accurately measure the temperature, salinity and turbulent properties of the surface and near-surface layer below it, present a major technological challenge. It requires an interest in and input from both the ocean physics and oceanographic technology to make progress in this field.

Central to this manuscript are observations made with the Air Sea Interaction Profiler (ASIP) (*Ward et al., 2014; ten Doeschate et al., 2017*), an autonomous, upwardly rising profiler, specifically designed to study the fine- and microstructure variability of the near-surface layer. The ASIP can be considered a unique piece of technology.

The outline of this thesis is as follows: This introduction is followed by a literature review chapter, presenting concepts and definitions. Chapter 3 forms an elaborate description of the measurement techniques of the ASIP. Chapter 4 presents observations of diurnal warming from three research campaigns in two different oceanic regions, and a comparison with the diurnal warming simulation of the commonly used air-sea flux model COARE 3.0. In chapter 5 observations of rain-induced surface stratification are presented. The relationship between rain rate and surface salinity anomaly is verified and compared to recent model results. In the final chapter the thesis is summarised and conclusions as well as suggestions for further work are listed.

2 Background

This chapter presents a general background on topics covered in the thesis. It gives an overview of the theory and presents terms and concepts of air-sea fluxes, diurnal warming and salinity variability in the upper ocean, as well as a theoretical background on turbulence in the upper ocean.

2.1 Air-Sea Fluxes of Energy

The OSBL is constantly exchanging energy, in the form of heat and momentum, with the atmosphere above it through the ocean surface. These fluxes are governed by turbulent motions, except for at the air-water interface, where over a layer of sub-millimetre scale the transport mechanism is governed by molecular diffusion. Understanding of the complex processes involved in air-sea exchange directly feeds into the quality of weather prediction and climate models (*Liss and Duce, 2010*).

2.1.1 Momentum Fluxes

Radiative forcing causes local to regional differences in the density of both the air of the lower atmosphere and the surface of the ocean, at sub-diurnal time scales. The atmosphere responds by means of winds, in an attempt to restore equilibrium. From atmospheric boundary layer studies it is known that the wind profile above a certain height of the ocean approximates a logarithmic curve (*Monin and Obukhov, 1954; Drennan et al., 1999*):

$$u(z) = \frac{u_*}{\kappa} \left(\ln \frac{z}{z_0} - \psi_u(\zeta) \right), \quad (2.1)$$

for $z \geq z_0$, the roughness height. The wind speed is approximately constant between the ocean surface and the level of the roughness height and equals the friction velocity u_* . The von Kármán constant $\kappa \approx 0.4$ is a dimensionless constant required in the law of the wall formulation of (2.1). Under neutral stability, the stability function $\psi_u(\zeta) = 0$, but when buoyancy controls the atmospheric stability, the wind profile deviates from the logarithmic. The friction velocity is related to the stress that the wind exerts on the ocean surface:

$$\tau = \rho_a u' w' = \rho_a u_*^2, \quad (2.2)$$

where ρ_a is the air density, and u' and w' are the turbulent velocity fluctuations about the mean horizontal and vertical wind components. The stress is a measure

of the atmospheric momentum transfer, which drives ocean surface currents. The roughness height z_0 is dependent on the sea state. Under influence of winds $> 3 \text{ ms}^{-1}$, the roughness of the sea surface increases due to the growth of surface gravity waves generated by the wind stress (*Edson et al.*, 2013). This affects the wind velocity profile over the ocean and increases u_* .

Surface forcing of the ocean causes imbalances, which are counteracted by various vertical and horizontal mixing mechanisms in the OSBL. Stress exerted on the ocean surface will cause a vertical velocity shear in the upper meters of the OSBL, decreasing with depth following a logarithmic profile as well. The accumulation of momentum also causes a shear at the bottom of the mixed layer, which can lead to Kelvin-Helmholtz instabilities and entrainment of deeper water (*Moum and Smyth*, 2001). Similar to the atmospheric boundary layer, it is assumed that over a shallow layer directly below the ocean surface the current velocity is equal to the water-side u_* :

$$u_{*w} = \sqrt{\frac{\tau_w}{\rho_w}}, \quad (2.3)$$

where subscript w indicates the water-side equivalent of the variables presented in eq. 2.2. Assuming continuity at the interface, $\tau_a = \tau_w$ so u_{*w} is a factor $\sqrt{\rho_a/\rho_w}$ smaller than u_* . The depth of the constant stress layer in the ocean deepens as a result of wave-breaking under high winds, which is a source of strong turbulent mixing (*Thorpe*, 2005). Langmuir circulations are a third mechanism of wind-induced motion in the OSBL (*Gargett*, 1989; *Sutherland et al.*, 2014b). These develop in a positive feedback mechanism between the wave-induced Stokes drift velocity and the surface current shear, forming counterrotating vortices aligned in the direction of the mean wind. Figure 2.1 schematically illustrates the sources of mixing in the OSBL listed here, with exception of convective mixing which will be discussed in section 2.1.4.

2.1.2 Heat Fluxes

The specific heat capacity of water is four times larger than air, whilst seawater also has a density 800 times larger than air. This means that the ocean can absorb large amounts of heat and transport them or slowly release heat back into the atmosphere. The heat content of the OSBL varies on a seasonal scale. Nevertheless, the temperature near the ocean surface can vary a few degrees per day, reflecting the differences between day and night. Heat is exchanged between the ocean and atmosphere via the fluxes of sensible heat Q_S , the direct heating of the air, and latent heat Q_L , the heat lost by evaporation.

$$Q_S = \rho_a c_{pa} \overline{w'T'} \quad (2.4)$$

$$Q_L = \rho_a L_e \overline{w'q'} \quad (2.5)$$

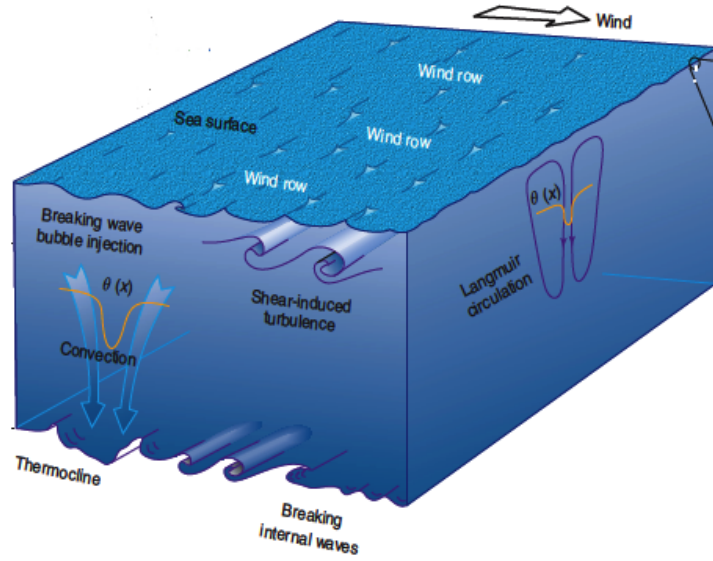


Figure 2.1: Schematic image showing various mechanisms of mixing in the OSBL. Reprinted from *Moum and Smyth* (2001), with permission from Elsevier.

w' , T' and q' are the turbulent fluctuations of vertical (wind)-velocity, temperature and water vapour mixing ratio in the atmosphere, c_{pa} is the heat capacity of air ($\text{J kg}^{-1} \text{m}^{-3}$), and L_e the latent heat of evaporation (J kg^{-1}). The turbulent fluctuations are very difficult to measure, therefore Q_S and Q_L are derived from the difference in temperature and humidity between the ocean and atmosphere (e.g. *Large and Pond* (1981)). The ocean is a near black body, and emits longwave radiation, whilst also receiving a substantial amount of it re-emitted from the atmosphere and by clouds. The upward (ocean-emitted) longwave radiative flux is computed as:

$$Q_{LW\uparrow} = e\sigma T^4, \quad (2.6)$$

where σ is the Stefan Boltzmann constant, $5.67 \times 10^{-8} \text{ W m}^{-2} \text{ K}^{-1}$, and $e \sim 0.985$ is a correction factor for the ocean's departure from blackbody radiation (*Gill*, 1982). The sensible heat flux is typically a fraction of the latent heat flux over the ocean. In mid-latitude oceans the net longwave heat flux is of the same order of magnitude as the latent heat flux (*Dickey and Simpson*, 1983).

The largest source of heat to the ocean is from direct solar radiation, Q_{SW} , where *SW* stands for shortwave; the part of the solar spectrum that reaches the bottom of the atmosphere ranges from 250-2500 nm, however most energy is contained at shorter wavelengths. A small fraction of solar radiation is reflected by the sea surface; this is the sea surface albedo a . The remainder of the radiant energy enters the water, where some of it is used for photosynthesis, however the majority is converted to heat on absorption by the water (*Jerlov*, 1976). In contrast to the other heat fluxes, radiative heating is considered a volume flux instead of a surface

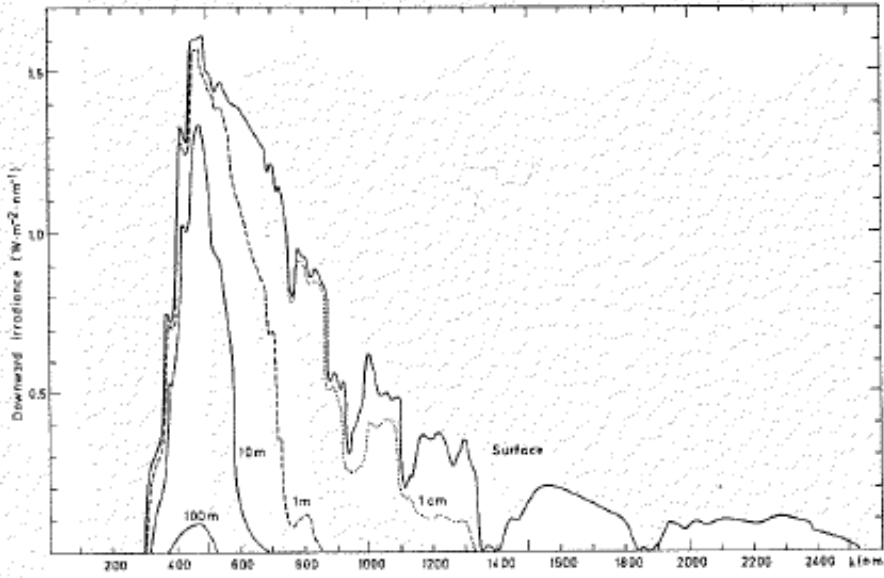


Figure 2.2: The spectrum of solar irradiance at sea level and 4 depths below the surface. Reprinted from *Jerlov* (1976) with permission from Elsevier

flux (*Soloviev and Lukas, 2014*), since different wavelengths of the total spectrum of solar radiation get absorbed at different depths in the water. In total about half of the solar radiation reaching the bottom of the atmosphere is absorbed in the upper 10 m of the ocean (*Paulson and Simpson, 1977*). Irradiance of wavelengths beyond 1300 nm (infrared) are attenuated at the very surface, whilst shorter, visible wavelengths (400-700 nm) get absorbed at deeper levels (*Paulson and Simpson, 1977; Morel and Antoine, 1994; Sweeney et al., 2005*), as illustrated in fig. 2.2. The absorption of solar radiation is further influenced by inherent optical properties of the water, caused by dissolved and particulate matter e.g. chlorophyll-pigment from primary producers, sediments and coloured dissolved organic matter (CDOM) (*Morel, 1998*). The solar angle, atmospheric aerosol and cloud cover change the distribution of the incoming light, whilst the sea state affects the sea surface albedo (*Morel and Antoine, 1994; Ohlmann et al., 2000*).

To compute the heat budget of a near-surface layer of depth D , the net surface heat flux follows from:

$$Q_{net} = Q_{in} - Q_{out} = (1 - a)Q_{SW}(D) - (Q_S + Q_L + Q_{LWnet}). \quad (2.7)$$

Here $Q_{LWnet} = Q_{LW\downarrow} - Q_{LW\uparrow}$.

Sea Surface Temperature

The magnitude of Q_S , Q_L and Q_{LW} is a function of sea surface temperature (SST). However, in observational oceanographic data the depth at which this is reported varies widely due to the large array of sensors: the temperature measured in the water intake of ships of opportunity is located at a depth roughly between 1 and 8 m. The ever growing array of autonomous Argo floats in the ocean are

a great asset for global coverage of seawater properties. However the uppermost measurement in standard Argo profile is located at a depth of 4 – 10 m, to avoid fouling of the sensors and air-bubbles in the pumped CTD system when the float is at the surface (*Roemmich et al.*, 2009). Satellite mounted sensors that measure in the infrared, like the AVHRR (Advanced Very High Resolution Radiometer) and the SEVIRI (Spinning Enhanced Visible and InfraRed Imager) sample the upper 10 – 20 μm , whilst satellite mounted microwave radiometers, like the AMSR-E (Advanced Microwave Scanning Radiometer on the Earth Observing System), measure down to a depth of 1 mm (*Donlon et al.*, 2002). This ambiguity in the use of SST, which complicates the composition of global maps and is the largest cause of bias in satellite measurement validation, was pointed out by *Donlon* (2005). They recommend that a clear distinction be made between the interfacial sea surface temperature, T_{int} , which is equal to the temperature at the top of the ocean skin layer, and the temperature at other depths. T_{skin} is the mean temperature over the skin layer, the layer of $O(1\text{ mm})$ thickness in which molecular processes dominates the air-sea exchange. Since the net heat flux over the skin layer is nearly always negative, there is a permanent temperature gradient of several tenths of a degree, also known as the cool-skin (*Paulson and Simpson*, 1981; *Schluessel et al.*, 1990; *Wick et al.*, 2005).

Directly below the skin layer the subskin temperature (T_{0-}) represents the surface mixed layer temperature during nighttime, possibly differing from the daytime value if a warm-layer develops (see fig.2.3). Finally, the common SST measured at some deeper level below the ocean surface is named T_z . If this depth z corresponds to a level where diurnal variation in the seawater temperature (sec. 2.3) is negligible, one also speaks of the foundation temperature. In the remainder of the thesis T_z will be used when the depth z is known and relevant to the analysis. When speaking about the sea surface temperature in a generic sense the acronym SST will be used. Similarly SSS stands for sea surface salinity in generic terms, versus salinity at a specific depth S_z .

2.1.3 Ocean Salinity and Moisture fluxes

The term ‘salinity’ is used for the total mass concentration of salt in seawater, and is a thermodynamic state variable of the ocean. Water in the seas and oceans contains salt minerals as a result of evaporative processes that have carried freshwater from the basins for billions of years, leaving dissolved components behind. The composition ratio of the different components is more or less invariant between oceans. Table 2.1 gives a complete overview of the main components and their mass percentage in Standard Seawater¹. Salinity is traditionally expressed in practical salinity units, psu. For more consistency in the representation of thermodynamic properties of seawater, *Millero et al.* (2008) recommend the use of absolute salinity S_A , in units of g kg^{-1} , which is the salinity used in this thesis unless indicated

¹Standard Seawater is seawater of a reference composition, defined by *Millero et al.* (2008). From this is derived the Reference Salinity S_R ; the best estimate of absolute salinity S_A of Standard Seawater (*IOC et al.*, 2010).

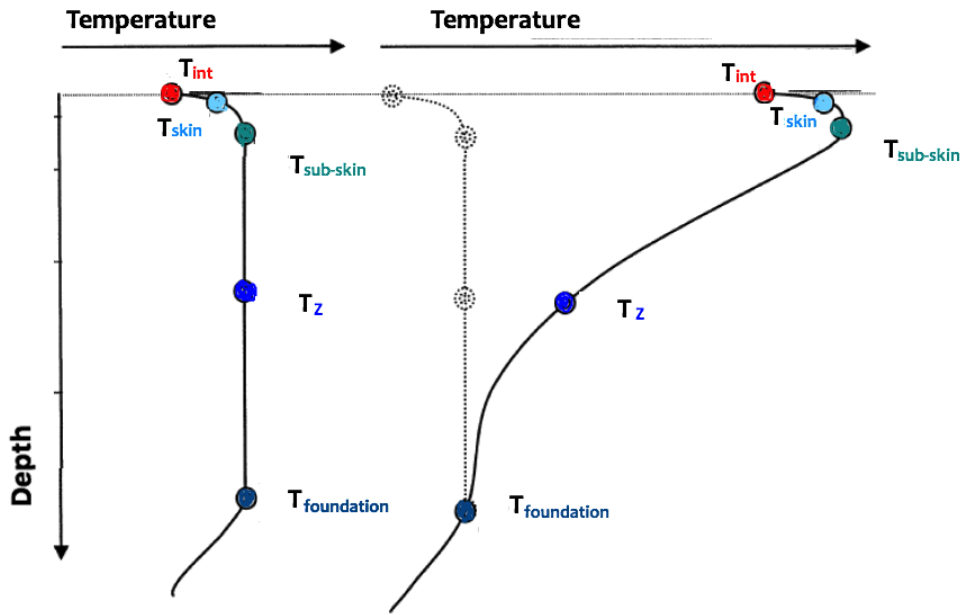


Figure 2.3: Schematic temperature profile in the upper 10 m of the ocean during night vs. day when diurnal warming is present, indicating the different definitions of sea surface temperature SST given in *Donlon et al. (2002)*.

otherwise.

Solute	M (%)	Solute	M (%)
Na^+	30.660	HCO_3^-	0.298
Mg^+	3.651	Br^-	0.1913
Ca^{2+}	1.172	CO_3^{2-}	0.0408
K^+	1.135	$B(OH)_4^-$	0.0226
Sr^{2+}	0.0226	F^-	0.00369
Cl^-	55.034	OH^-	0.00038
SO_4^{2-}	7.713		

Table 2.1: Sea salt composition for reference salinity in Standard Seawater, as determined by *Millero et al. (2008)*. M is the mass fraction.

q The salinity of the near-surface layer is the net result of the moisture fluxes between the ocean and atmosphere: evaporation and precipitation. The world's seas and oceans together play a major role in the global hydrological cycle with 86% of the global evaporation, and 78% of global precipitation occurring over the oceans. The North Atlantic and Indian Ocean carry large amounts of water to the continents, from which they receive most in return, whilst water in the Pacific is mainly recirculated over different parts of the ocean (*Bengtsson, 2010*). In-situ observation of moisture fluxes is limited; however, changes in sea-surface salinity can serve as a measure of changes in the water cycle (*Schmitt, 1995*). This has motivated an intensification of research into the patterns of near-surface salinity and variability therein in the past ten years (*Lindstrom et al., 2015*). Since the

launch of the Aquarius (operational from 2011 to 2015) and SMOS (Soil Moisture Ocean Salinity, operational since 2010) satellites, the salinity of the top centimeter of the ocean is monitored from space using L-band radiometry (*Lagerloef, 2012; Mecklenburg et al., 2012*).

Evaporation is the surface flux of water vapour. It is rarely ever directly measured over water surfaces, but instead computed when the local latent heat flux is known (*Schlüssel, 1996*):

$$E = \rho_a \overline{w'q'} = \frac{Q_L}{\rho_a * Le}. \quad (2.8)$$

Evaporation is positively correlated to windspeed, and requires a positive sea-air temperature difference (ΔT_{s-a}), whilst the humidity of the air is relatively low. Regions of high evaporation rate are typically found in the subtropical oceans. Strong warming in these regions forces the salinity to increase as a result of evaporation and is often density-compensated by a high SST, such that these regions have a high SSS (*Gordon et al., 2015*).

Precipitation, here limited to rainfall, is both a surface and a volume flux of freshwater to the ocean surface boundary layer, since raindrops of a certain critical radius (r_c) large enough to penetrate the surface, will reach to a depth of up to a hundred times that radius (*Manton, 1973; Schlüssel et al., 1997*). Rain causes a reduction in SSS, and sometimes a shallow halocline is formed, which will gradually evolve into a shallow mixed layer (*Price, 1979; Riser et al., 2015*). The strength and lifetime of rain-induced salinity anomalies (also referred to as freshwater lenses), depends on the vertical and horizontal turbulent mixing processes present in the near-surface layer, the air-sea heat fluxes, and the size of the rain event (*Katsaros and Buettner, 1969; Soloviev et al., 2015; Drushka et al., 2016*). At the same time, a freshwater lens influences the near-surface turbulence (*Soloviev et al., 1999*). Shallow stratification isolates the water below from direct contact with the atmosphere, thereby limiting air-sea exchange to the shallow layer. Turbulence below the rain-induced stratification has been observed to rapidly decay with the onset of heavy rainfall, as the vertical flux of surface-generated turbulence is inhibited (*Smyth et al., 1997*). The stratification could thus focus the momentum flux from wind, waves and rain into the shallow layer of reduced salinity, causing a surface jet (*Price et al., 1986*), and making this layer respond more rapidly to atmospheric forcing. *Bao et al. (2003)* showed an increase in surface currents of up to 0.4 m s^{-1} in a modelled freshwater anomaly. Such an acceleration of horizontal currents was also observed by *Wijesekera et al. (1999)* to occur within a large fresh water lens in the eastern tropical Pacific.

Katsaros and Buettner (1969) observed that rainfall of larger drop size efficiently mixes the surface, whilst small drops cause a larger surface salinity change. The distribution of raindrop size in a precipitation event is thought to be dependent on rain rate, such that during heavier rainfall events the fraction of raindrops of a drop radius $r \leq r_c$ is higher than for rainfall of a lower intensity. One commonly

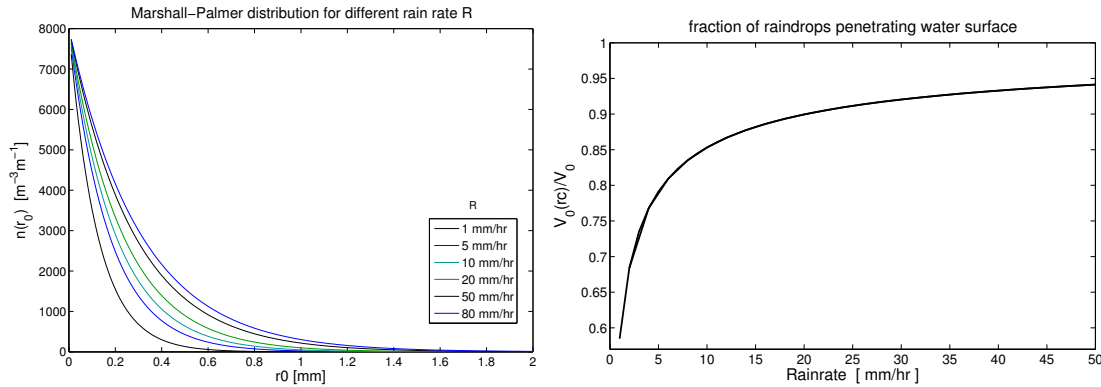


Figure 2.4: **a.** Marshall-Palmer distribution of raindrops with a drop-size radius r , for six commonly occurring rainfall rates R . **b.** The fraction of submerging rain drops for different rain rates R following (Schlüssel *et al.*, 1997), when the critical dropsize radius $r_c = 0.4$ mm.

used distribution to represent 'natural rainfall' is the Marshall-Palmer distribution (Marshall and Palmer, 1948), illustrated in fig. 2.4. A shift to more intense rainfall will be associated with a larger amount of deep penetrating raindrops, and can be expected to enhance surface mixing. In lab experiments artificial rain of a natural drop size distribution has been observed to enhance turbulence in the upper 10 cm and increase the air-sea gas transfer velocity (Ho *et al.*, 2004; Zappa *et al.*, 2009; Turk *et al.*, 2010; Harrison *et al.*, 2012). However, because in these experiments the raindrop distribution was invariable, a significant increase of turbulence for increased rain rates was not observed. On the other hand, it is a sailor's wisdom that rainfall has a calming effect on the sea (Cavaleri *et al.*, 2015), dampening gravity waves and reducing wave breaking. However the physical mechanism behind this is poorly understood and experiments in wave tanks have not been conclusive in relating wave attenuation to rain rate (Tsimplis, 1992; Schlüssel *et al.*, 1997; Peirson *et al.*, 2013).

2.1.4 Buoyancy Flux

Temperature and salinity together control the seawater density

$$\rho_w = \rho_0(1 + \beta\delta S - \alpha\delta T), \quad (2.9)$$

where α and β are the thermal expansion and saline contraction coefficient respectively and ρ_0 is the reference water density of the mixed layer. When the density of the surface water is reduced (due to warming and/or freshening), its buoyancy is increased. Conversely, cooling and evaporation reduces the buoyancy of a layer of water. This causes vertical instability of the water column, and drives convective mixing in the OSBL. Spatial and temporal differences in solar heating, evaporation and rainfall are the main causes of convective mixing, which is the most important vertical mixing mechanism of the OSBL (Brainerd and Gregg, 1993; Moum and Smyth, 2001).

The buoyancy change of a unit volume of water can be represented by the surface buoyancy flux B_0 :

$$B_0 = -\frac{g}{\rho_0}Q_\rho, \quad (2.10)$$

where g is the gravitational acceleration, ρ_0 a reference seawater density and the density flux Q_ρ , computed following *Schmitt et al.* (1989):

$$Q_\rho = \rho_w(\alpha F_T + \beta F_S), \quad (2.11)$$

$$F_T = \frac{-Q_{net}}{\rho_w c_{pw}}, \quad (2.12)$$

and

$$F_S = \frac{(E - P) \cdot S}{(1 - S)}. \quad (2.13)$$

The heat-flux term αF_T represents the change of density due to temperature changes from the net heat flux Q_{net} (2.7). F_S represents the change of density due to salinity changes from evaporation (2.8) and precipitation. This formulation implies that a negative density flux (reduction of ρ_w due to warming/freshwater dilution) corresponds to $B_0 > 0$, increasing the buoyancy of the surface mixed layer, whilst $B_0 < 0$ is indicative of convective overturning (*Weller et al.*, 2002).

2.2 The COARE Bulk-Flux Algorithm

To directly measure turbulent fluxes of heat and moisture at sea requires specialised instrumentation, and correction of wind-speed measurements for air-flow distortion, as well as platform motion (*Landwehr et al.*, 2015). Instead, more readily measured mean variables on both sides of the air-sea interface are used to derive the fluxes with a bulk-flux algorithm. A bulk-flux algorithm uses $\Delta Y_{sea-air}$, in combination with some form of (atmospheric) stability function, where Y can be either temperature T , humidity q or wind speed U (U_{sea} corresponds to the surface current velocity). The Coupled Ocean-Atmosphere Response Experiment (COARE) in 1992 was an observational and modelling project aimed at improving the understanding of the climatological coupling between ocean and atmosphere. The study was focussed on the Western Pacific warm-pool, as this tropical open ocean region is characterised by the highest sea surface temperatures and strong atmospheric convective circulation, playing a major role in the global climate (*Webster and Lukas*, 1992). A bulk flux algorithm was developed and published as COARE 2.5b in 1996 (*Fairall et al.*, 1996a). This model has become the most commonly used algorithm in the air-sea flux community. To make the model applicable to regions

outside the Tropics, a dependence on the ambient conditions was added to some parameterisations, which after verification led to COARE version 3.0 (*Fairall et al.*, 2003). A gas flux parameterisation for carbon dioxide, ozone and di-methyl sulfide based on the COARE model was presented by *Fairall et al.* (2011).

2.2.1 Theoretical Setup

Instead of (2.4), (2.5) and (2.2), the fluxes are represented by the product of the wind speed with the air-sea difference of its bulk value ΔY , times a transfer coefficient:

$$\overline{w'y'} = C_y \overline{U} \Delta Y = c_y^{1/2} c_d^{1/2} \overline{U} \Delta Y. \quad (2.14)$$

The total transfer coefficient C_y is the product of c_d , the wind drag coefficient, and c_y , the bulk transfer coefficient for the variable y , \overline{U} is the mean windspeed at an arbitrary reference height.

When the atmosphere is neutral, the mean atmospheric profile is assumed to be logarithmic from the roughness height z_{0y} upward, z_{0y} being the height where the value of y is considered equal to the value at the surface. The neutral bulk coefficients are related to z_0 through:

$$c_{yn}^{1/2} = \frac{\kappa}{\ln(z/z_{0y})}. \quad (2.15)$$

When the atmospheric stability is different, Monin-Obukhov Stability Theory (MOST) is used to correct the transfer coefficients. MOST uses an empirical function $\psi_x(\zeta)$ to describe the mean atmospheric profile of y as a function of stability parameter ζ .

$$c_y^{1/2} = c_{yn}^{1/2} / \left[1 - \frac{c_{yn}^{1/2}}{\kappa} \psi(\zeta) \right], \quad (2.16)$$

where $\kappa = 0.4$ is the von Kármán constant. Instead of using the kinematic fluxes, $\overline{w'y'}$, MOST defines scaling parameters T_* , q_* and u_* . This u_* is also known as the ‘friction velocity’:

$$\begin{aligned} u_*^2 &= -\overline{w'u'} = c_d \overline{U} (u_s - u), \\ T_* &= -\overline{w'T'}/u_* = -c_T^{1/2} (T_s - T_a), \\ q_* &= -\overline{w'q'}/u_* = -c_q^{1/2} (q_s - q), \end{aligned} \quad (2.17)$$

where c_T , c_q and c_d are the transfer coefficients for heat, moisture and stress respectively, T_s is the sea surface interfacial temperature, u_s the surface current and q_s the interfacial value of the water vapour mixing ratio, computed from the saturation mixing ratio at $T_a = T_s$ (*Fairall et al.*, 1996a). The terms T_a , q and u are the air temperature, water vapour mixing ratio and wind speed measured at reference height z_r .

The mean horizontal wind speed includes a ‘gustiness’-term, representing boundary layer scale eddies: $\bar{U} = \sqrt{(u^2 + v^2 + u_g^2)}$.

$$u_g = \beta W_* = \beta \left(\frac{g \overline{w'\theta'_v} z_i}{T} \right)^{1/3}, \quad (2.18)$$

with z_i the depth of the convective boundary layer, W_* the boundary layer convective scaling velocity and $w'\theta'_v$ the virtual heat flux.

In COARE the velocity roughness length z_0 in equation (2.15) is computed by combining two parameterizations, for rough flow by *Charnock* (1955) and for smooth flow by *Smith* (1988):

$$z_0 = \frac{\alpha u_*^2}{g} + \frac{0.11\nu}{u_*}. \quad (2.19)$$

The Charnock parameter α is a constant (0.011) in COARE version 2.5, however in version 3.0 it is set to increase linearly from 0.011 to 0.018 for wind speeds of 10-18 m s^{-1} and above (*Fairall et al.*, 2003). The scalar roughness lengths z_{0T} and z_{0q} are related through the roughness Reynolds number $Re_r = u_* z_0 / \nu$ following *Liu et al.* (1979).

2.2.2 Cool-Skin and Warm-Layer Correction

In the ideal situation the interfacial or the skin sea surface temperature, T_{int} or T_{skin} , is used as an input to COARE. However, as these are not routinely measured in-situ the value has to be estimated from the more commonly available ‘bulk’-SST at a certain depth below the surface. To derive T_{int} from T_z , two processes are taken into account by COARE:

- In the thin layer (10 μm – 1 mm) below the interface molecular diffusion is the dominant transfer mechanism. As the outgoing heat and freshwater flux over this layer is usually larger than the absorbed solar radiative flux, the skin layer is typically cooler than the water directly below it. The bulk-sea surface temperature is corrected for this ‘cool-skin effect’, which is typically ranges from 0.1-0.5 K *Fairall et al.* (1996b). Over the cool-skin of thickness δ the total temperature difference is

$$\Delta T_c \propto Q_{net} \delta / k, \quad (2.20)$$

and

$$\delta = \lambda \frac{\nu}{u_{*w}}. \quad (2.21)$$

Numerous studies to determine the cool-skin scaling coefficient λ have been performed (*Ward and Donelan*, 2006). In the COARE algorithm the coefficient is dependent on the relative contributions of shear and convection to the cool-skin

properties:

$$\lambda = 6 \left[1 + \left(\frac{Q_{net} 2^4 g \alpha \rho c_p \nu^3}{u_{*w}^4 k^2} \right)^{3/4} \right]^{-1/3}, \quad (2.22)$$

where the net heat flux Q_{net} over the cool-skin layer δ is generally out of the ocean, as only 5% of the solar radiation is absorbed in the top 1 mm (*Saunders, 1967*).

- The absorption of solar radiation in the upper metres of the ocean causes a diurnal cycle of temperature measurable in the upper layer of O(20 m). Especially on clear days and low wind conditions a strong stratification can form in the top few metres of the water with a temperature gradient of several degrees, causing an input of T_z to significantly underestimate T_{int} . COARE uses a simplified form of the mixed layer model by *Price et al. (1986)* to compute the warm-layer depth and temperature correction from the balance between the integral of the surface heat flux and wind stress, see sec. 2.3.1.

2.2.3 Implementation

COARE requires an input consisting of time series of the following atmospheric and oceanic variables: wind speed u , current speed in the wind direction u_s , air temperature T_a , relative humidity RH , measurement height of wind speed, air temperature and humidity z_u , z_t and z_q , downward shortwave radiation Q_{SW} , downward longwave radiation $Q_{LW\downarrow}$, rain rate R , atmospheric pressure P , T_z , and S_z . The atmospheric water vapour mixing ratio is computed from RH and T_a , the saturated mixing ratio from T_z .

After loading the data and defining some constants, first the input T_z is corrected for the presence of a warm-layer. Then the main bulk flux algorithm is applied, which iteratively computes the drag coefficients, the scaling parameters and the cool-skin correction in the following steps:

1. First guess of gustiness velocity u_g and cool skin correction. From this a first estimate of the 10-meter windspeed u_{10} and u_* is derived, and consequently the roughness height z_0 assuming a Charnock parameter for low wind speeds ($\alpha = 0.011$). and the drag coefficients assuming neutral atmospheric stability.
2. The initial stability parameter ζ is guessed using the bulk Richardson number, here computed as $Ri_b = \frac{gz_r}{T_a} \frac{\Delta T}{U^2}$, where $\Delta T = T_s - T_a$.
3. The initial ζ and cool skin correction are used to update the first guess of the scaling parameters u_* , T_* and q_* .
4. The Charnock parameter is changed if $u_{10} > 10 \text{ m s}^{-1}$.

5. Bulk loop of three iterations:
 - computation of z_0 , Re_r and z_{0T} and z_{0q} .
 - computation of u_* , T_* and q_* using updated stability parameter ζ .
 - computation of u_g and correction of total mean wind speed \bar{U} and u_{10} .
 - computation of heat fluxes Q_S , Q_L and net Q_{LW} and Q_{SW} absorption in the skin layer.
 - computation of cool skin correction from the balance between net heat fluxes and u_* using eq. 2.22, 2.21 and 2.20).
6. Final heat flux and wind stress computations as well as computation of rain-induced sensible heat and momentum flux².
7. Final computation of drag coefficients at the measurement height as well as 10m-neutral drag coefficients.

2.3 Diurnal Warming

Solar radiation is progressively absorbed over depth, heating up the surface layer of the ocean during daytime. As a result a warm, stratified surface layer can form in the ocean surface boundary layer, especially under relatively calm and clear-sky conditions (*Stommel et al.*, 1969; *Fairall et al.*, 1996b; *Soloviev and Lukas*, 1997; *Kawai and Wada*, 2007). Wind shear and waves cause mixing of the near-surface layer and will vertically re-distribute the heat accumulated, such that a diurnal warm-layer (DWL) typically consists of a relatively shallow mixed layer, above a sharp thermocline. The remnant mixed layer below this diurnal thermocline is largely isolated from atmospheric exchange, and the turbulence in it is often strongly reduced (*Brainerd and Gregg*, 1993; *Caldwell et al.*, 1997). The available surface momentum flux will be focussed into the DWL (*Sutherland et al.*, 2016). The resulting turbulent mixing will contribute to homogenising the warm-layer and the gradual deepening of the thermocline during the day. Once the surface heat flux turns negative, the sea surface will start to lose heat to the atmosphere, and additional convective mixing will provide energy to further entrain water from below the diurnal thermocline, and eventually merge the diurnal warm-layer with the seasonal mixed layer (*Brainerd and Gregg*, 1993; *Price et al.*, 1986; *Prytherch et al.*, 2013; *Soloviev and Lukas*, 2014). A schematic representation of these phases in the formation and evolution of a typical DWL is drawn up in fig. 2.5. The phenomena is most prevalent in tropical and subtropical ocean regions, but can also be significant in mid-latitude seas and oceans during calm conditions in spring and summer (*Brainerd and Gregg*, 1993; *Kawai and Wada*, 2007; *Weller et al.*, 2014). Diurnal warming typically results in a variability in T_{int} of 0.1-0.5 °C, however cases of a diurnal amplitude in SST of several degrees have also been observed (e.g. *Fairall et al.* (1996b); *Soloviev and Lukas* (1997); *Ward* (2006)).

A complete understanding about the occurrence and properties of diurnal warm-layers is necessary to relate the various measurements of T_z to the T_{int} required

²The rain-induced fluxes are presented in more detail in equations 5.1 and 5.2

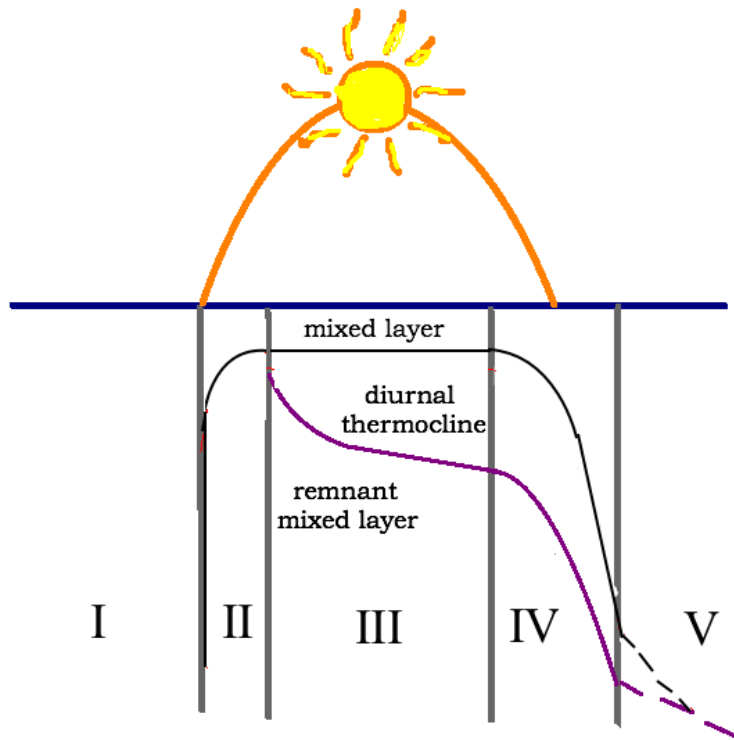


Figure 2.5: Schematic representation of the evolution of a diurnal warm mixed layer and its thermocline under low-wind speed conditions in five phases, based on *Soloviev and Lukas (2014)*; phase I is the well mixed nighttime OSBL, II the early morning when heat flux turns positive into the ocean and the diurnal warm-layer is formed and maintained during phase III, daytime warming. The temperature gradient over the diurnal thermocline gradually increases. In phase IV the positive buoyancy flux reduces such that momentum fluxes rapidly deepen the DWL, until towards the evening during phase V, convective mixing due to the negative surface buoyancy flux erode the diurnal thermocline.

for satellite validation, flux computations, and for boundary conditions to large scale weather and climate models (*Donlon, 2003*). Remote sensing has the major advantage of providing global coverage, and diurnal warming can be retrieved from comparison of day and nighttime passings at the same location, or from geostationary satellites (*Gentemann et al., 2008*). The global mean diurnal warming amplitude is 0.25-0.5 °C under low to moderate wind speed conditions ($U < 7 \text{ m s}^{-1}$) (*Merchant et al., 2014*). Heat budget calculations that do not include this diurnal variability, can significantly underestimate the fluxes at regional scale (*Clayson and Bogdanoff, 2013*). In the regions of the Earth with the highest seawater temperature, the western regions of the tropical oceans, high SST's drive both high-impact regional weather patterns (hurricanes) and interact with both intraseasonal and interannual climate phenomena like the Madden-Julian oscillation and ENSO cycles (*Cronin and Kessler, 2002; Bernie et al., 2005*).

2.3.1 Models of Diurnal Warming

Three types of models of diurnal warming can be discerned:

- Empirical parameterisations, which predict the amplitude of the diurnal SST-cycle from an input of daily-averaged meteorological conditions. This type of model is most often used in ocean models that do not have a fine enough vertical resolution to be more specific (*Karagali et al.*, 2017). It is typically developed using statistical analysis over long time series of T_z at a fixed location, but can therefore be subject to regional bias. An example is the parameterisation by *Webster et al.* (1996) developed from observations and simulations with a geophysical mixed layer model for the TOGA-COARE region (tropical Western Pacific), which predicts the amplitude of T_{skin} as a function of daily mean wind speed, precipitation and peak insolation:

$$\Delta T_{skin} = a(Q_{SWmax}) + b \ln P + c \ln \bar{U} + d Q_{SWmax} \ln \bar{U} + e \bar{U} + f. \quad (2.23)$$

Two sets of coefficients a, b, c, d, e, and f represent conditions of $\bar{U} \leq 2 \text{ m s}^{-1}$ and $\bar{U} > 2 \text{ m s}^{-1}$. *Gentemann et al.* (2003) derived an empirical model of the diurnal warming amplitude from several years of global satellite-derived SST. To include sub-diurnal variability of weather conditions on the phase of the diurnal warming, a parameterisation requiring average $Q_S W$ and U for four periods of a day was suggested by *Stuart-Menteth et al.* (2005) .

- Bulk algorithms compute the evolution of a simplified temperature profile in the surface mixed layer as a result of the surface heat-and momentum fluxes integrated over this layer. The DWL in the one-dimensional model by *Price et al.* (1986), is described as a shallow warm mixed layer above a thermocline. Solar heating and momentum from the wind accumulate in the DWL, which causes a shear and a temperature gradient over the thermocline, the deepening of which is determined by three stability criteria: Convective stability, a bulk Richardson number describing mixed layer stability, and a gradient Richardson number criterion for the shear flow stability:

$$\partial \rho_w / \partial z \geq 0, \quad (2.24)$$

$$Ri_b = \frac{g \Delta \rho_w H}{\rho_0 (\Delta V)^2} \geq 0.65, \quad (2.25)$$

$$Ri_g = \frac{g \partial \rho / \partial z}{\rho_0 (\partial V / \partial z)^2} \geq 0.25 \quad (2.26)$$

The Δ -terms in the above equations describes the difference between the mixed layer and the layer below it for any variable, and ρ_0 the mean (background) value of the water density. In the model scheme at each time step heat and momentum is accumulated in the surface mixed layer of depth H . When the total accumulated momentum in the layer becomes too large, and/or the vertical shear of the horizontal current vector V is too large, the layer deepens until Ri and Ri_g again satisfy their respective criteria.

As mentioned in sec. 2.2.2, the interfacial sea surface temperature required for

the flux computations in the COARE-bulk flux algorithm is determined from T_z using a warm-layer model, as well as a correction for the cool-skin. The diurnal warming component is a simplified version of the PWP model. During daytime surface heat-and momentum fluxes accumulate over a layer of depth D_w , where the algorithm assumes a linear gradient in temperature between the surface and D_w . No heat or momentum is exchanged with the layer below, and D_w can reach a maximum depth of 19 m. The warm-layer depth is determined by the temporal integral of the surface heat-and momentum fluxes, assuming that Ri_b over the layer is equal to the critical value $Ri_{b\,crit} = 0.65$:

$$D_w = \sqrt{\frac{2Ri_{b\,crit}c_{pw}}{\alpha g \rho_w} \frac{I_\tau}{\sqrt{I_Q}}}, \quad (2.27)$$

where I_τ represents the time integral of the momentum flux $I_\tau = \int \rho_w u_{*w}^2 dt$, with u_{*w} the friction velocity in the water, and I_Q the time integral of the net surface heat flux $I_Q = \int Q_{net} dt$ (Fairall *et al.*, 1996b; Gentemann *et al.*, 2009). The temperature difference of the DWL then is:

$$\Delta T_w = \frac{2I_Q}{\rho_w c_{pw} D_w} \equiv \sqrt{\frac{2\alpha g}{Ri_{b\,crit} \rho_w} \frac{I_Q^{1.5}}{I_\tau c_{pw}^{1.5}}}. \quad (2.28)$$

The net surface heat flux Q_{net} is computed from (2.7) for $D = D_w$. To represent the absorption of solar irradiance, the COARE algorithm computes the fraction (f_x) of the radiative flux absorbed at depth D_w :

$$Q_{SW}(z) = f_x * (1 - a) Q_{SW0}, \quad (2.29)$$

with a the ocean surface albedo and Q_{SW0} the downwelling solar radiative flux measured at a level above the ocean surface. The absorbed fraction is approximated with a three-component exponential decay function, representative of spectral absorption over three wavelength bands (this is further elaborated on in sec. 4.7).

During nighttime the COARE model does not define a warm-layer, but sets $z = 19$ m and $f_x = 0.5$. As soon as after sunrise $Q_{in} > Q_{out}$ heat starts to accumulate in a layer of depth D_w . At each time-step Δt equation (2.27), (2.28) and f_x are solved in 5 iterations³.

The main differences between the warm-layer representation in COARE compared to PWP and various other bulk mixed layer algorithms, concerns the mixed layer stability description and the shape of the temperature profile, as illustrated in fig. 2.6.

To apply a warm-layer correction in weather forecasting and data assimilation, a prognostic scheme was developed by Zeng and Beljaars (2005) and applied to the ECMWF model. It uses a similar description of the heat accumulation

³In chapter 4 the diurnal warming simulation in COARE 3.0, is evaluated by means of a comparison to in-situ observations from vertical profilers

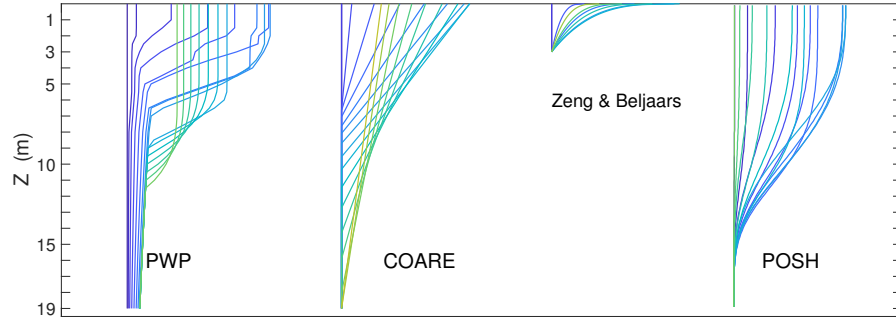


Figure 2.6: Temperature profiles modelled with four different bulk-mixed layer models. From left to right PWP (*Price et al.*, 1986), COARE 3.0 (*Fairall et al.*, 1996b), (*Zeng and Beljaars*, 2005) and POSH (*Gentemann et al.*, 2009).

as COARE, instead determining the depth of the warm-layer from a stability function based on similarity theory (*Large et al.*, 1994). Another main difference is that the warm-layer depth is fixed at 3 m and that the warm-layer profile has an exponential shape:

$$T(z) = T_{-\delta} - \left(\frac{z + \delta}{-D_w + \delta} \right)^\eta * \Delta T_w, \quad (2.30)$$

where ΔT_w is the difference over the warm-layer confined between the warm-layer depth and the cool skin $-D < z < -\delta$, and the constant $\eta = 0.3$. The prognostic scheme in *Large and Caron* (2015), for use in a coupled general circulation model, uses a similar temperature profile (using $\eta = 0.2$), and it also has been modulated by *Bellenger et al.* (2017) to represent temperature and salinity anomalies as a result of rainfall, for which the exponent η has been made wind speed dependent. To improve the credibility of the vertical structure of the warm-layer in COARE, an alternative bulk-algorithm was designed by *Gentemann et al.* (2009). The temperature profile in the POSH model (Profiles of Ocean Surface Heating) is a windspeed dependent exponential curve:

$$\Delta T_w(z) = e^{-9.5 \left(\frac{z}{D_w} \right)^\mu}, \quad (2.31)$$

in which μ varies linearly from 2 to 9 for wind speed $1.5 < U < 7.5$. Where in COARE the warm-layer only accumulates heat and momentum until midnight, in POSH a fraction of this is lost at each time step, to represent losses by entrainment at the bottom of the mixed layer, conduction and dissipation.

- Diffusion models. This type of model represents the turbulent mixing of the near-surface layer, using parameterisations to solve the equations of turbulent flow. The more realistic representation of the physics comes at a cost of increased computational intensity. The model by *Kantha and Clayson* (1994) is specifically developed to model diurnal warming, thereby improving *Mellor and Yamada* (1982). The one-dimensional General Ocean Turbulence Model (GOTM) (*Burchard et al.*, 1999), uses a similarity scaling approach. It was evaluated by *Pimentel et al.* (2008) and *Karagali et al.* (2017) to be successful

in estimating the diurnal SST variability in comparison to observations at six different oceanographic locations.

2.4 Turbulent Mixing in the OSBL

2.4.1 Defenition of Turbulence

Turbulence is a phenomenon in fluid dynamics that occurs in a multitude of forms, both in natural as in engineered flows. There is no formal definition of the term but some characteristics of turbulence are (*Thorpe, 2007; Kundu and Cohen, 2008*):

- Turbulent flows appear to be random and chaotic.
- Turbulent flows have a high Reynolds number⁴.
- A turbulent flow has a rotational character and a highly fluctuating vorticity;
- Turbulent flows are non-linear, resulting in vortex stretching and transfer of energy through disturbances of ever smaller length scales until it dissipates kinetic energy through friction.
- Turbulent flows rapidly diffuse momentum and heat, due to macroscopic mixing of fluid properties.

Turbulence has a stirring effect on a fluid, dispersing particles which were originally close to each other. This stretches patches and layers in a fluid, increasing the spatial gradients to scales at which molecular diffusion becomes important. The net result is a more homogenised, well mixed fluid (*Thorpe, 2005*). Turbulence dissipates energy, as turbulent eddies transport energy from large down to ever smaller scales, until the eddy-size gets so small that viscous forces become important and energy is dissipated by viscous friction. The amount of energy that is dissipated is a measurable quantity, and often used to quantify the turbulence of a flow. Only a small fraction of the *TKE* is used to raise the potential energy of the fluid, the rest is dissipated (*Lueck et al., 2002*). The majority of the dynamical processes in the ocean involve turbulence. Ocean turbulence research has generally followed two paths: a theoretical approach, founded by mathematicians during the first half of the 20th century, as well as a more practical approach with the aim to quantify turbulence in-situ. In this section some theory will be presented, to provide a background to the measurement of turbulence presented in chap.3.

2.4.2 Turbulence Theory

Theories and models of ocean turbulence are built on fundamental concepts of fluid dynamics. This section and the following is largely inspired by textbooks by *Kundu and Cohen (2008)* and *Thorpe (2005)*.

⁴The Reynolds number Re is a dimensionless parameter representing the ratio of inertia over viscous forces; $Re = \frac{Ul}{\nu}$, where U is a characteristic velocity, l the characteristic length scale of the flow, and ν is the viscosity of the medium.

Any incompressible, Newtonian fluid can be described with the Navier-Stokes equations, in vector notation:

$$\rho \frac{D\vec{u}}{Dt} = -\nabla p + g(\rho - \rho_0)\delta_{i3} + \mu \nabla^2 \vec{u}, \quad (2.32)$$

$$\frac{\partial \vec{u}}{\partial \vec{x}} = 0, \quad (2.33)$$

$$\frac{\partial T}{\partial t} + \vec{u} \frac{\partial T}{\partial \vec{x}} = \kappa_T \frac{\partial^2 T}{\partial \vec{x} \partial \vec{x}}, \quad (2.34)$$

$$\frac{\partial S}{\partial t} + \vec{u} \frac{\partial S}{\partial \vec{x}} = \kappa_S \frac{\partial^2 S}{\partial \vec{x} \partial \vec{x}}, \quad (2.35)$$

Equation 2.32 describes the acceleration of a unit volume of fluid to be the result of the sum of all forces working on it. The flow is non-divergent (2.33), and forcing is due to pressure-gradients (∇p), gravity ρg and viscous stresses $\mu \nabla^2 \vec{u}$. Equations 2.34 and 2.35 describe the change of temperature and salinity of the fluid, with κ_T and κ_S the molecular diffusivity for heat and salt respectively (unit $\text{m}^2 \text{s}^{-1}$).

A turbulent flow at any instant will satisfy the Navier-Stokes equations. To fully predict the flow is practically impossible, since there are too many different spatial and temporal scales to resolve. In 1883 Osborne Reynolds suggested that variables in a turbulent flow are the sum of a mean and a fluctuation:

$$\tilde{a}_i = A_i + a_i, \quad \bar{a}_i = 0, \quad (2.36)$$

This ‘Reynolds decomposition’ is applied to both the velocity components and the scalar variables. A turbulent flow field creates turbulent fluctuations in the dynamically passive scalar field⁵.

Derivation of the Turbulent Kinetic Energy equation

The Reynolds decomposition is applied to all variables (u , p , ρ , T) in the Navier-Stokes momentum equation (2.32), and the mean of this equation is taken to result the mean momentum equation:

$$\frac{DU_i}{Dt} = \frac{1}{\rho_0} \frac{\partial \bar{\tau}_{ij}}{\partial x_j} - g(\bar{\rho} - \rho_0)\delta_{i3}. \quad (2.37)$$

⁵Here we change to the notation as in *Kundu and Cohen* (2008) on which this section is largely based; instantaneous quantities are denoted by a tilde ($\tilde{}$), the mean value by an uppercase letter and the turbulent fluctuations by a lowercase letter. For temperature, salinity and density the SI units are used, so instead for those variables we use an overbar for the mean and a prime for the turbulent fluctuation. Subscript i and j is the standard Einstein notation for the three components of direction

with

$$\bar{\tau}_{ij} = -P\delta_{ij} + \mu\left(\frac{\partial U_i}{\partial x_j} + \frac{\partial U_j}{\partial x_i}\right) - \rho_0\overline{u_i u_j}. \quad (2.38)$$

Equation 2.38 represents the dominant forces in the flow: the pressure, the viscous stresses and the third term, the Reynolds stress tensor. This last term is an additional stress on the mean flow exerted by the turbulence. It is of similar form as the viscous stress but usually much larger. The Reynolds stress is a 9 component (symmetric) tensor of the cross and autocorrelation of the turbulent velocities; the off-diagonal components are zero if the different components are not correlated, implying that the turbulence is completely isotropic. This will not be the case in a strongly sheared or stratified flow.

Multiplication of the mean momentum equation by U results in the kinetic energy balance of the mean flow:

$$\frac{D}{Dt} \left(\frac{1}{2} U_i^2 \right) = \frac{\partial}{\partial x_j} \left(-\frac{1}{\rho_0} P U_j + 2\nu U_i E_{ij} - \overline{u_i u_j} U_i \right) - 2\nu E_{ij} E_{ij} + \overline{u_i u_j} \frac{\partial U_i}{\partial x_j} - \frac{g}{\rho_0} \bar{\rho} U_3. \quad (2.39)$$

Here the mean strain rate is introduced, $E_{ij} = \frac{1}{2} \left(\frac{\partial U_i}{\partial x_j} + \frac{\partial U_j}{\partial x_i} \right)$.

The mean kinetic energy per unit mass changes due to advection by the pressure gradient, viscous stresses and Reynolds stresses (first three terms on the right hand side of (2.39)). The fourth term represents the loss of kinetic energy to viscous dissipation, the fifth to the turbulent flow field and the last term is the effect of gravity on the kinetic energy balance; kinetic energy is lost when the mean vertical motion is upward in exchange of a gain in potential energy.

Finally the turbulent kinetic energy balance is derived by subtracting the mean momentum equation (2.37) from the total momentum equation (2.32), and then multiplying the result by u_i . Taking the average gives:

$$\frac{D}{Dt} \left(\frac{1}{2} \overline{u_i^2} \right) = - \underbrace{\frac{\partial}{\partial x_j} \left(-\frac{1}{\rho_0} \overline{p u_j} + \frac{1}{2} \overline{u_i^2 u_j} - \nu/2 \frac{\partial \overline{u_i^2}}{\partial x_j} \right)}_a - \underbrace{\overline{u_i u_j} \frac{\partial U_i}{\partial x_j}}_b - \underbrace{\frac{g}{\rho_0} \overline{\rho' u_3}}_c - \underbrace{\nu \left(\frac{\partial \overline{u_i}}{\partial x_j} \right)^2}_d, \quad (2.40)$$

The total rate of change of turbulent kinetic energy (TKE) is due to:

- a) The local advection of TKE by the turbulence itself (the first two terms on the r.h.s.) and by viscous transport.
- b) Interaction of the Reynolds stresses with the shear of the mean flow.
- c) The vertical buoyancy flux; this is a source of energy in an unstable flow (density increasing upward), and a sink when the turbulence has to work against a stable density profile.
- d) Dissipation of energy by molecular friction. This term represents the dissipation of TKE, and will be denoted by the symbol ϵ in the rest of this manuscript.

Over a short period of time, in which the ocean can be approximated to be in a quasi-steady state, the shear production (b), buoyancy (c) and dissipation term (d) dominate the energy transfer, and are in approximate balance with each other (*Thorpe, 2005*). Instead of directly measuring the Reynolds stresses of all velocity components, often ϵ is used to quantify the turbulence intensity of oceanic flows.

Derivation of the Scalar Equation of a Turbulent Flow

The scalar field in a high Reynolds number flow is randomised by the fluctuating turbulent velocities, resulting in small scale variability of dynamically passive scalar variables like temperature and salinity. Analogous to the Navier-Stokes equations of motion and the derivation of the TKE equation, a mean equation for scalars and an equation for the scalar variance can be derived. For any scalar θ :

$$\frac{D\bar{\theta}}{Dt} = \frac{\partial}{\partial x_j} \left(\kappa_\theta \frac{\partial \bar{\theta}}{\partial x_j} - \overline{u_j \theta'} \right), \quad (2.41)$$

with κ_θ representing the molecular diffusivity of the scalar. The change of the mean scalar flux is the result of the molecular heat flux plus a turbulent flux. Like the Reynolds stress term in (2.37), the turbulent scalar flux ($-\overline{u_j \theta'}$) is directed down a mean background gradient.

Subtracting this mean scalar equation from the total Navier-Stokes equation (2.34), and multiplying it by θ' results in the evolution equation for scalar variance $\overline{\theta'^2}$ (*Lueck, 2016b*):

$$\frac{D}{Dt} \overline{\theta'^2} + \underbrace{2\overline{u_j \theta'} \frac{\partial \theta}{\partial x_j}}_e + \underbrace{\frac{\partial}{\partial x_j} \overline{u_j \theta' \theta'}}_f = \underbrace{\kappa_\theta \nabla^2 \overline{\theta'^2}}_g - \underbrace{2\kappa_\theta \overline{\left(\frac{\partial \theta'}{\partial x_j} \right)^2}}_h. \quad (2.42)$$

As opposed to the momentum equations, (2.41) and (2.42) are linear. Term e in (2.42) is the turbulent flux, which works against the background mean gradient to produce scalar variance. Term f is the turbulent transport of scalar variance. Molecular dissipation is the ultimate sink of scalar fluctuations, dominated by term h, as this is proportional to the square of the gradient of the fluctuations. This last term is also known as the dissipation of scalar variance, χ_θ , and is another parameter used to characterise turbulence (*Thorpe, 2005*).

Osborn and Cox (1972) derived that in a quasi-steady state the production term e and dissipation term h in eq. (2.42) are dominant.

2.4.3 Ocean Turbulence in Practice

Dissipation

The rate of viscous dissipation of TKE as formulated in (2.40) contains 9 terms. However, in the inertial subrange down to the dissipative scales, the turbulent velocity field is considered to be isotropic. This reduces the computation of ϵ to

only one of the 9 terms, for example

$$\epsilon = \frac{15/2}{\nu} \overline{\left(\frac{\partial u}{\partial z}\right)^2}, \quad (2.43)$$

with $\partial u/\partial z$ the vertical shear of horizontal velocity fluctuations. This is the velocity component of largest importance to research presented in this thesis, as it is the component measured by shear probes on a vertical profiler.

Similarly the rate of loss of variance of a scalar θ reduces to

$$\chi_\theta = 6\kappa_\theta \overline{\left(\frac{\partial \theta'}{\partial z}\right)^2}, \quad (2.44)$$

when assuming isotropic turbulence (*Oakey, 1982*).

Dissipation rate ϵ is proportional to the large scale turbulence (*Kundu and Cohen, 2008*), and therefore used to quantify turbulence in the ocean. It can range from $< 10^{-10} \text{ W kg}^{-1}$ in the abyssal ocean to 0.1 W kg^{-1} in a strong tidal current.

Length Scales

Large eddies are produced in a flow that is strained, due to converging and diverging streamlines, or in a current which has a spatial gradient in the direction normal to mean the flow direction (shear). The size L_0 of these eddies which extract kinetic energy from the mean flow field is comparable to the dimensions of the large scale flow, e.g. the depth of a tidal channel or the overturning scale in a stratified ocean. Smaller eddies are strained by the velocity field of larger eddies and consequently extract kinetic energy from them. This energy cascade continues without loss of energy until the very small scales $O(10^{-3} \text{ m})$ at which viscous forces become important in dissipating the kinetic energy.

Kolmogorov in 1941 suggested on dimensional grounds that this scale is dependent on the viscosity of the fluid and the actual dissipation rate ϵ , which leads to the definition of the Kolmogorov scale :

$$L_K = \left(\frac{\nu^3}{\epsilon}\right)^{1/4}. \quad (2.45)$$

Between eddies of sizes $L_O < L < L_K$ there is an energy redistribution, and velocity fluctuations will be increasingly isotropic. This range is also called the ‘inertial subrange’.

The kinematic viscosity ν and molecular diffusivities of heat and salt, κ_T and κ_S have the same function of dissipating variations across a gradient, however they are related to different processes. Instead of friction, heat is transferred by conduction and salinity through molecular diffusion, these three processes are increasingly slow, thus salinity gradients persist longer than temperature and velocity gradients: $\nu \sim 10^{-6} \text{ m}^2 \text{ s}^{-1}$, $\kappa_T \sim 1.5 \times 10^{-7} \text{ m}^2 \text{ s}^{-1}$ and $\kappa_S \sim 1.5 \times 10^{-9} \text{ m}^2 \text{ s}^{-1}$ (*Nash and Moum, 1999*). Dissipation of scalar fluctuations thus occurs at even smaller scales,

depending on the diffusivity of the specific scalar θ :

$$L_{B\theta} = \left(\frac{\kappa^2 \nu}{\epsilon} \right)^{1/4}. \quad (2.46)$$

This scale is known as the Batchelor scale (*Batchelor, 1952*).

In a stratified flow the scale of the largest turbulent eddies (L_0) is limited by the strength of the stratification, which is measured in terms of the squared Brunt Väisälä frequency N^2 :

$$N^2 = -\frac{g}{\rho_0} \frac{\partial \rho}{\partial z}. \quad (2.47)$$

The associated length scale is the Ozmidov scale:

$$L_O = \left(\frac{\epsilon}{N^3} \right)^{1/2}. \quad (2.48)$$

Eddy Diffusivity

The vertical turbulent fluxes of heat and salt in the ocean are respectively $\rho_w c_{pw} \overline{wT'}$ and $\rho_w c_{pw} \overline{wS'}$. To parameterise vertical fluxes both momentum, mass and heat in the ocean, the product of the mean vertical gradient and an ‘eddy coefficient’ can be used (*Osborn and Cox, 1972*):

$$\begin{aligned} \text{Eddy viscosity:} & \quad -\overline{uw} = K_\nu \frac{\partial U}{\partial z} \\ \text{Turbulent diffusivity of heat:} & \quad -\overline{wT'} = K_T \frac{\partial T}{\partial z} \\ \text{Turbulent diffusivity of salt:} & \quad -\overline{wS'} = K_S \frac{\partial S}{\partial z} \\ \text{Turbulent diffusivity of density:} & \quad -\overline{w\rho'} = K_\rho \frac{\partial \rho}{\partial z} \end{aligned} \quad (2.49)$$

When there is a balance between the production of scalar variance down the mean scalar gradient (term e in eq. (2.42)) and the dissipation, K_T and K_S can be computed from the ratio of the dissipation rate of scalar variance and the mean vertical gradient of the scalar, which can both be derived from measurements (*Osborn and Cox, 1972; Nash and Moum, 2002*):

$$K_T = 3 \kappa_T \frac{\overline{(\partial T'/\partial z)^2}}{(\partial T/\partial z)^2} = \frac{\chi_T}{2(\partial T/\partial z)^2}. \quad (2.50)$$

Isotropy

The presence of a strong thermal or haline gradient may impeach the isotropy of the turbulence. To evaluate the degree of isotropy in a layer the buoyancy Reynolds number can be computed:

$$Re_b = \frac{\epsilon}{\nu N^2}, \quad (2.51)$$

with the strength of the stratification is characterised by N , the buoyancy frequency.

2.4.4 Spectral Analysis

Computation of ϵ from shear spectra

Turbulence is a spatial phenomenon. The total variance of the cross-stream turbulent velocity fluctuations can be expressed as the integral over the one-dimensional wave number spectrum:

$$\overline{u^2} = \int_0^\infty \phi_{22}(k) dk. \quad (2.52)$$

$\phi_{22}(k)$ represents the energy density of the velocity component orthogonal to the direction of the wave number. Over the inertial subrange, where turbulence is generally homogeneous, ϕ is only dependent on wave number k , the rate of dissipation ϵ and viscosity ν (Kolmogorov, 1941). Dimensional analysis gives the 1D wave number spectrum over this range $\phi_{22} = C_k \epsilon^{2/3} k^{-5/3}$. The ‘Kolmogorov constant’ C_k is 1/5 for the spectrum of cross-stream fluctuations when k has units of cpm, 2/3 when k is in rad m^{-16} . For wave numbers approaching $1/L_K$, where dissipation due to viscous friction begins to affect the turbulence, the spectrum rolls-off rapidly.

The dissipation rate of TKE can be estimated from measurements of the shear spectrum $\psi_{sh}(k) = k^2 \phi_{22}(k)$:

$$\epsilon = \frac{15}{2} \nu \overline{\left(\frac{\partial u_i}{\partial x_j} \right)^2} = \frac{15}{2} \nu \int_0^\infty \psi_{sh}(k) dk \quad [m^2 s^{-3}]. \quad (2.53)$$

The velocity shear spectrum $\psi_{sh}(k)$ has a $k^{1/3}$ slope over the inertial subrange. For high dissipation rates a larger fraction of the spectral energy occurs at higher wave numbers, and the total energy density is larger too. The sensor type most commonly used for ocean turbulence observations, the airfoil shear probe, can only resolve fluctuations over a certain wave number band, due to spatial averaging of eddies at scales smaller than its wave number resolution (see sec. 3.5). To resolve all the variance of the shear, the probe’s resolution has to be higher or equal to

⁶Throughout this thesis k is the cyclic wave number with units cpm unless stated otherwise. Conversion between the two wave number notations $k_{cpm} = 1/2\pi k_{rad/m}$, whilst spectra $\phi(k_{cpm}) = 2\pi \phi(k_{rad/m})$ (e.g. McMillan et al. (2016)).

the Kolmogorov wave number, which especially for higher ϵ is seldom the case. To overcome the limited bandwidth over which the velocity gradient spectrum can be measured, a common technique to determine ϵ from $\psi_{sh}(k)$ is to fit a universal spectrum to the well-resolved part of the measured spectrum. These universal models are based on the hypothesis that the shape of the spectrum of an isotropic turbulent flow is universal, and that the amplitude solely depends on ϵ . The models describe the energy density over the inertial and viscous range of velocity fluctuations for isotropic turbulence as a function of the non-dimensional wave number $\tilde{k} = k/k_s$, where $k_s = 1/L_K = (\epsilon/\nu^3)^{1/4}$, the Kolmogorov wave number. A widely accepted model by Panchev-Kesich (1969), based on turbulence theory, is represented by the following analytical function (Sanchez *et al.*, 2011):

$$G_{PK}(\tilde{k}) = 0.9372\tilde{k}^{0.3748} \exp(-6.011\tilde{k}^{1.548}). \quad (2.54)$$

Here k in \tilde{k} , like k_s , is the angular wave number with units [rad m⁻¹]. The Panchev-Kesich theoretical universal spectrum has a similar shape to the even more widely used Nasmyth spectrum (Gregg, 1999). From a large set of measurements of the velocity spectrum over a range of dissipation rates, Nasmyth (1970) proposed an empirical universal model $G_N(\tilde{k})$, which was presented in Oakey (1982). Tabulated values of \tilde{k} and $G_N(\tilde{k})$ in this paper use the cyclic wave number [cpm] for k (not for k_s !). An analytical fit to the non-dimensional Nasmyth model, derived by Wolk *et al.* (2002); Lueck (2016a), also uses this form of \tilde{k} :

$$G_N(\tilde{k}) = \frac{8.05\tilde{k}^{1/3}}{1 + (20.6\tilde{k})^{3.715}}. \quad (2.55)$$

To convert the both non-dimensional universal spectra to $\psi_{sh}(k)$, $G(\tilde{k})$ is multiplied by $k_s^2(\epsilon\nu^2)^{1/4}$. Figure 2.7 illustrates the dimensional forms of both the Panchev-Kesich and Nasmyth spectrum for a range of dissipation rates.

Scalar Variance

The dissipation rate of scalar variance, χ_θ , can be computed through integration of the one-dimensional scalar gradient spectrum $\psi_{\theta z}$, assuming the turbulent flow field is homogeneous, isotropic and stationary:

$$\chi_\theta = 6\kappa_\theta \overline{\left(\frac{\partial\theta'}{\partial z}\right)^2} = 6\kappa_\theta \int_0^\infty \psi_{\theta z}(k) dk, \quad (2.56)$$

where k is the wave number. For wave numbers in the inertial subrange and beyond, ψ_θ is a function of wave number, ϵ and χ_θ . In analogy to Kolmogorov's theory of the inertial subrange of the turbulent velocity distribution, the scalar gradient spectrum in a turbulent flow field is proportional to $k^{1/3}$ for $k < k_s$, the inertial-convective subrange (Dillon and Caldwell, 1980):

$$\psi_{\theta z}(k) = A\chi_\theta\epsilon^{-1/3}k^{1/3}, \quad (2.57)$$

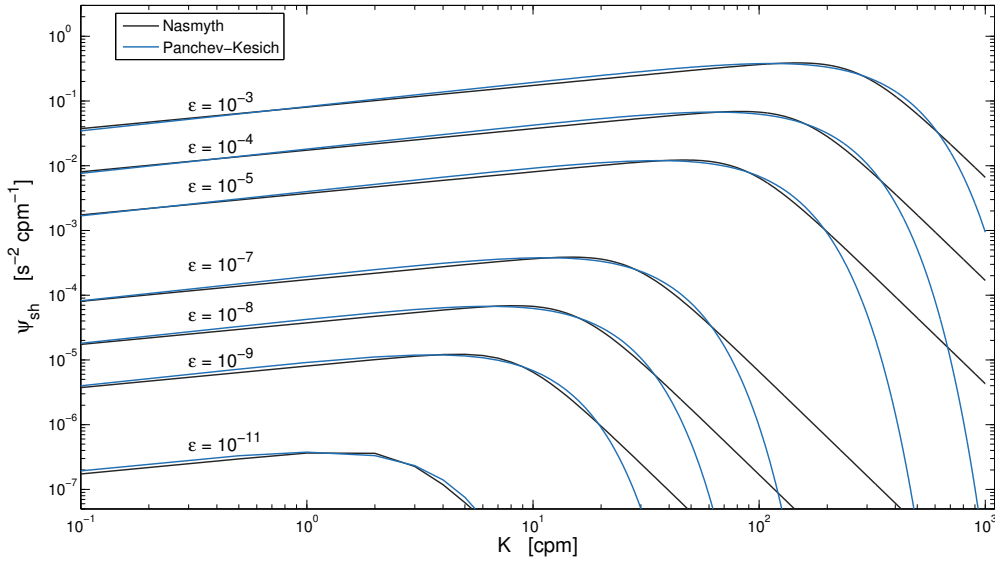


Figure 2.7: The 1-D universal spectra of velocity shear for different TKE dissipation rates ϵ . Black curves result the Nasmyth universal model, blue curves the Panchev-Kesich form.

When $\nu \gg \kappa_\theta$, as is the case for the molecular diffusivities of heat and salinity, *Batchelor et al.* (1959) hypothesised that $\psi_\theta(k)$ at wave numbers beyond the inertial subrange is first governed by convective straining and eventually by molecular diffusion. For these viscous-convective ($k_s < k \ll k_B$, where $k_B = 1/L_B$) and viscous-diffusive wave number ranges ($k \sim > 0.1k_B$), the Batchelor universal model can be written as (*Dillon and Caldwell*, 1980; *Nash and Moum*, 1999; *Ruddick et al.*, 2000):

$$\psi_{\theta z B}(k) = \left(\frac{q}{2}\right)^{1/2} \frac{\chi}{k_B \kappa_\theta} f(q, \hat{k}). \quad (2.58)$$

Here both k and k_B are in units rad m^{-1} , and $\hat{k} = k/k_B$. The non-dimensional parameter q is related to the most negative strain rate, $\gamma \sim \sqrt{\epsilon/\nu}$ and q is used to compute the non-dimensional wave number $\alpha = \sqrt{2q} \hat{k}$, such that

$$f(\alpha) = \alpha \left\{ e^{-\alpha^2/2} - \alpha \int_\alpha^\infty e^{-x^2/2} \right\}. \quad (2.59)$$

The wave number at which the transition from the inertial to the viscous-convective subrange occurs is approximated as

$$k_* = (A/q)^{3/2} (\nu/\kappa_\theta)^{-1/2} k_B. \quad (2.60)$$

Scalar variance is rapidly diffused at $k = k_B$, so for wave numbers on the order of k_B $\psi_{\theta z}$ rolls-off rapidly, whilst it is $\propto k^{-1}$ over the viscous-convective subrange. The spectral amplitude is inversely proportional to ϵ , as high levels of turbulence smear the scalar gradients out to higher wave number ($k_B \sim \epsilon^{1/4}$).

An alternative universal model for the one-dimensional scalar gradient spectrum, proposed by *Kraichnan* (1968), formulates $f(\alpha)$ as follows:

$$f(\alpha) = \alpha \exp(-\sqrt{3}\alpha). \quad (2.61)$$

Figure 2.8 shows both universal models for three different levels of ϵ , as well as for different values of q . Though the Batchelor model is often used, various authors argue that temperature gradient spectra in the upper ocean are better described by the Kraichnan universal model. Both *Sanchez et al.* (2011) and *Bogucki et al.* (2012) come to this conclusion after fitting different models to measured temperature gradient spectra from a lake and a tank experiment respectively.

As can be seen in fig. 2.8 the Kraichnan model describes a less steep roll-off for wave numbers in the viscous-diffusive subrange. For the same value of ϵ and q the peak in the Batchelor spectrum is located at a wave number k_c which is 6% higher than the Kraichnan model. Estimates of ϵ and the dissipation rate of scalar variance χ_θ , can be determined through fitting one of the universal models for scalar variance to a measured temperature or salinity gradient spectrum. The universal parameter q is a source of uncertainty in this procedure, since various values of q for both models can be found in literature, ranging from 2 to 12. For the Batchelor model a q_B ranging between 3 and 5 is dominantly used in literature (*Grant et al.*, 1968; *Oakey*, 1982; *Nash and Moum*, 1999; *Luketina and Imberger*, 2001), whilst for the Kraichnan model q_K ranges between 3.4 and 7.9 (*Smyth*, 1999; *Nash and Moum*, 2002; *Sanchez et al.*, 2011; *Bogucki et al.*, 2012). The effect of varying q is shown in fig. 2.9.

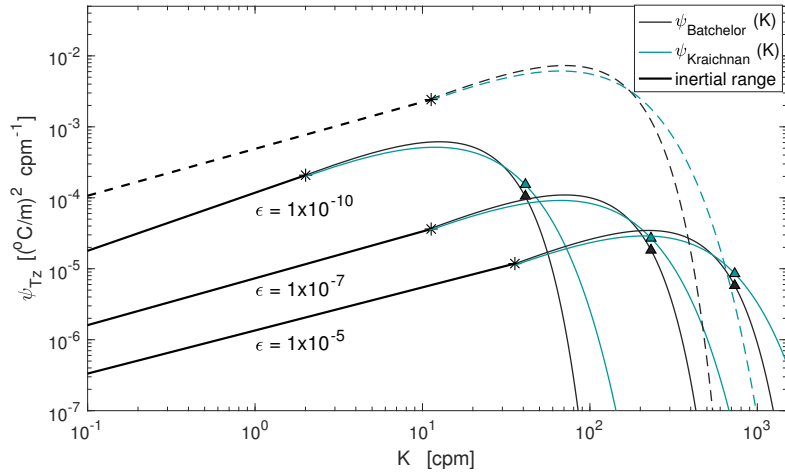


Figure 2.8: The 1D universal temperature gradient spectra for three different TKE dissipation rates ϵ , $\chi_T = 1.5 \times 10^{-8} \text{ K}^2 \text{ s}^{-1}$, and turbulent parameter $q = 2$. Black curves result the Batchelor (1952) universal model, blue-green curves the Kraichnan (1968) model. The dashed curves correspond to $\epsilon = 1 \times 10^{-7} \text{ W kg}^{-1}$ and $\chi_T = 1 \times 10^{-6} \text{ K}^2 \text{ s}^{-1}$. Triangles indicate the Batchelor wave number k_B and stars the transition wave number k_* .

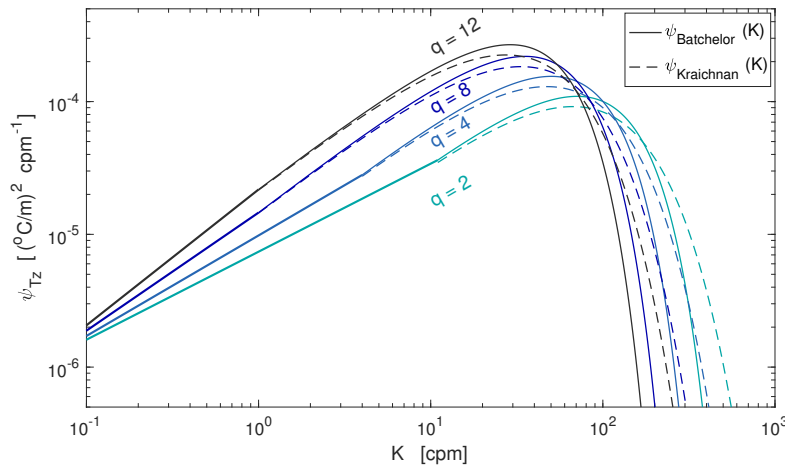


Figure 2.9: Varying q for $\epsilon = 1 \times 10^{-7} \text{ W kg}^{-1}$ and $\chi_T = 1.5 \times 10^{-8} \text{ K}^2 \text{ s}^{-1}$, for both the Batchelor (solid line) and Kraichnan (dashed) model.

3 Measurements and Methods

3.1 Introduction

The oceanographic observations presented in this thesis have predominantly been obtained with the Air-Sea Interaction Profiler (ASIP). During my postgraduate work I have spend a lot of time evaluating and improving the methods used in post-processing of the data obtained in several campaigns. Measurements from the following campaigns are used in this thesis:

1. Knorr-11 campaign: North Atlantic campaign in June/July 2011, targeting upper ocean measurements and air-sea gas exchange in a region of high biological activity (see also *Bell et al.*, 2013; *Sutherland et al.*, 2013; *Scanlon et al.*, 2016; *Scanlon and Ward*, 2016; *Bell et al.*, 2017). Part of this data set is used in chapter 5.
2. STRASSE campaign: month-long cruise in the subtropical North Atlantic, August/September 2012 aboard R/V *Thalassa* (France), for the European leg of the first cruise of the international SPURS-I project (Salinity Processes Upper Ocean Regional Study). This project was aimed at understanding the thermohaline structures in the salinity maximum region of the North Atlantic (see also *Reverdin et al.*, 2015; *Sutherland et al.*, 2016).
3. MIDAS campaign: second cruise of the European leg of SPURS-I. March/April 2013 aboard R/V *Sarmiento de Gamboa* (Spain). This cruise focussed on the centre of the North Atlantic Salinity Maximum (NASM) region (see also *Busecke et al.*, 2014; *Landwehr et al.*, 2015). Dataset from both SPURS-I cruises are used in chapter 4.
4. RETROSPECT-cruise: 1 week cruise in the fjord south of the Lofoten islands in northern Norway, aboard R/V *Johan Hjort*. This project is a collaboration with the Norwegian Met Institute and Institute of Marine Research, focussing on improving regional forecasting capabilities of areas important to Norway: fishing grounds. The ASIP was deployed to obtain observations of variability in vertical mixing within the fjord, and how this impacts the vertical distribution of cod-eggs in the water. Data from this campaign are used for evaluation of methods in this chapter.

This chapter gives an overview of the ASIP¹, and details of the data processing relevant to results presented in this thesis. For more details to the electronic and

¹There is some ambiguity in the use of articles when talking and writing about the Air-Sea-Interaction Profiler; during periods of lab-and field work it has been common to personify the instrument, as ‘ASIP’ is very much part of the team and often suspected to have a mind of its own. However, for grammatical correctness it should be written ‘the ASIP’; in this manuscript both ways are used, purposefully keeping the ambiguity alive.

mechanical design of the instrument reference is made to *Ward et al. (2014)*.

3.2 ASIP

The ASIP is a vertical, free-rising, microstructure profiler, designed to resolve microstructure variability of scalar variables as well as turbulence in the OSBL, linking the bulk of the mixed layer to the ocean surface. The profiler is about 2.8 m long and weighs ~ 90 kg in air (fig. 3.1). To produce a profile, it first descends by means of three thrusters to a programmed depth (maximum depth rating: 100 m). When the thrusters switch-off, the instrument rises under its own buoyancy at a constant rise velocity of $\sim 0.4 - 0.6 \text{ m s}^{-1}$. On its upward facing side the profiler is equipped with a suite of microstructure sensors (Rockland Scientific): 2x an FP07 thermistor, 1x a dual pin micro-conductivity sensor (SBE7) and 2 airfoil shear probes (SPM38). The scalar microstructure sensors require in-situ calibration, for which a slow-response CT-instrument with long term sensor stability is attached on the side of the profiler. To obtain accurate depth readings a fast responding pressure transducer (Keller) is used, and to track ASIP's orientation it is equipped with both accelerometers and a full motion package. A LI-COR PAR sensor (Photosynthetic Active Radiation) and an oxygen sensor (Aanderaa) are usually mounted also. The profiler's major asset is its autonomy, i.e. ASIP operates automatically, detached from the research vessel. This results in measurements of vertical profiles of upper ocean microstructure up to the very surface, without contamination from the ship's wake. The ASIP carries a battery package with a capacity to profile over a total of 6000 m per individual deployment, after which the profiler has to be brought back on board to recharge the batteries and download the gathered data, stored on the onboard computer. The ASIP is equipped with an antenna, which extends after each profile to get a GPS-fix and communicate this to the research vessel via the Iridium satellite communication system. Apart from the GPS coordinates, this Iridium message contains information on the battery status of the profiler. Simple mission-commands, e.g. to change the target depth or the number of profiles, or to pause or abort profiling, can be communicated from the ship to the ASIP.

The fragile sensors on the top of the profiler, are surrounded by a metal guard, without which deployment and recovery of the instrument directly from the ocean onto a research vessel remains somewhat risky. Albeit this it has been practice to deploy the ASIP from a small boat, some distance away from the ship (see fig. 3.1). This puts some limitation on the sea states in which the profiler can be deployed and recovered.



Figure 3.1: World map showing the location of past ASIP deployments, the year and the research vessel. Insert from left to right: ASIP on the deck of the R/V Thalassa, a close-up of the top section of the profiler with the sensors surrounded by the guard, and the deployment of ASIP from a small workboat in Plymouth Sound in May 2014. Figure taken from *ten Doeschate et al.* (2017)

3.3 Scalar Fine Structure: Temperature and Salinity

Temperature and salinity are the most commonly measured water properties in the ocean. ASIP is equipped with two microstructure temperature (μT) sensors. These are of the type FP07 (Thermometrics USA via Rockland Scientific Inc.), glass-coated thermistor beads of $\varnothing \approx 1.8$ mm (fig. 3.2a).

As opposed to temperature, the salinity of the water is not directly measured, but calculated from the measured conductivity, which is the result of both the temperature and the salinity of the seawater. Salinity is thus computed by comparing the measured C and T-signals to the known salinity of seawater at 15 °C and 35 psu, using standard formulas defined in *Unesco* (1981) and updated in *IOC et al.* (2010). For this method it is essential to use measurements of the same water volume, otherwise the computed salinity profile will contain erroneous spikes. Common CTD instruments are typically equipped with a thermistor in direct contact with the water and a conductivity cell through which water is either free-flowing or pumped. The two signals then need to be corrected for thermal inertia of the conductivity cell (*Lueck and J.J.Picklo*, 1990; *Mensah et al.*, 2009).

The shaft of one of the FP07 probes is tilted, such that the tip of the sensor



Figure 3.2: Three micro-structure sensor probes on ASIP, from left to right an FP07 thermistor, an SBE7 micro-conductivity sensor and an SPM38 shear probe.

is positioned very close to the tip of the SBE7 micro-conductivity (μC) sensor on ASIP. The SBE7 sensor consists of two electrodes at the tip of two needles, about 0.5 mm apart, to which a voltage difference is applied which drives a current through the water of an amplitude proportional to the conductivity (fig. 3.2b).

An example of a temperature and a conductivity profile from ASIP with a significant fine structure as a result of diurnal warming near the surface and deeper stratified layers is shown in fig. 3.3a. Removing the mean gradient from the T and C-profile via a high-pass filter reveals the microstructure within these stratified layers (fig. 3.3b).

These microstructure measurements can be used to determine the turbulent fluxes of heat and salt, applying the model of *Osborn and Cox* (1972)(2.50).

3.3.1 Sensor Response

In microstructure measurements it is common practice to sample the signal plus its scaled derivative (*Mudge and Lueck*, 1991). This technique of pre-emphasis conserves information at high frequencies, which typically contain less energy and thereby have a low signal-to-noise ratio. After analog-to-digital conversion, the so called enhanced version of the original signal is obtained by applying a simple low-pass filter. This technique is applied to the μC and μT signals.

It takes a finite amount of time for the FP07 thermistor probe to equilibrate with the environmental temperature, so the sensor has a frequency response, especially on a moving platform. The response of the sensor acts as a low-pass filter to the environmental signal, since more rapid fluctuations and fluctuations of a smaller size are not well resolved. This puts significant limitations on the fraction of the total temperature gradient spectrum ψ_{T_z} resolvable with the ASIP. Additionally this makes the thermistor ‘slow’ compared to the μC -sensor, which can cause erroneous spikes in the computed salinity due to a mismatch in C and T . To counteract this short-term mismatch (*Morison et al.*, 1994), the thermistor signal is first aligned to the conductivity signal. This is done in post-processing of the ASIP profiles, by

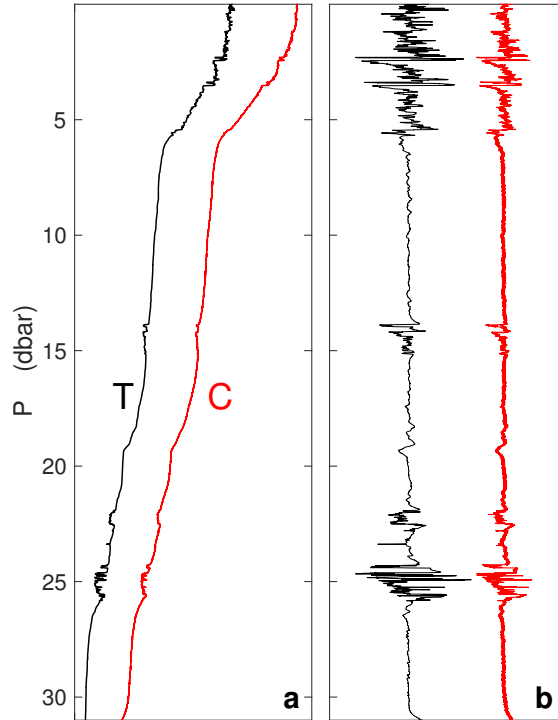


Figure 3.3: **a.** Illustration of a temperature (T) and conductivity profile (C) when a warm-layer is present below the surface. **b.** High-pass filtered signal for the same profiles as in **a.**

computing the cross-correlation between the μT and μC signals, to determine the lag in μT required to arrive at the best correlation.

The μC measurement by the SBE7 sensor represents the average over a specific volume between and around the two electrodes, thus some spatial averaging of fluctuations smaller than this volume occurs, also limiting the minimum size of well resolved fluctuations.

Knowledge of the response of each sensor is necessary to relate the measured signal to the true environmental signal, increase the resolution of the resolved variability, and further reduce salinity spiking. Figure 3.4 shows average spectra of the vertical gradient of temperature and conductivity, ψ_{Tz} and ψ_{Cz} , measured with ASIP. It clearly illustrates that ψ_{Tz} peaks at a wavenumber about 10 times lower than ψ_{Cz} , and contains a lot of electrical noise at higher frequency/wavenumber.

To recover lost variance, measured scalar gradient spectra can be adjusted using the amplitude-squared response function $|H(f)|^2$ (Emery and Thomson, 1998):

$$\psi_{\theta z \text{ true}}(f) = \frac{\psi_{\theta z \text{ measured}}(f)}{|H(f)|^2}, \quad (3.1)$$

where f is frequency. The manufacturer of the FP07-thermistor probe specifies a half-power frequency of 23 Hz (7 ms). However, the response characteristics can differ between individual probes (Gregg, 1999; Nash *et al.*, 1999), and different types of frequency response functions are found in literature (fig. 3.5). Gregg and

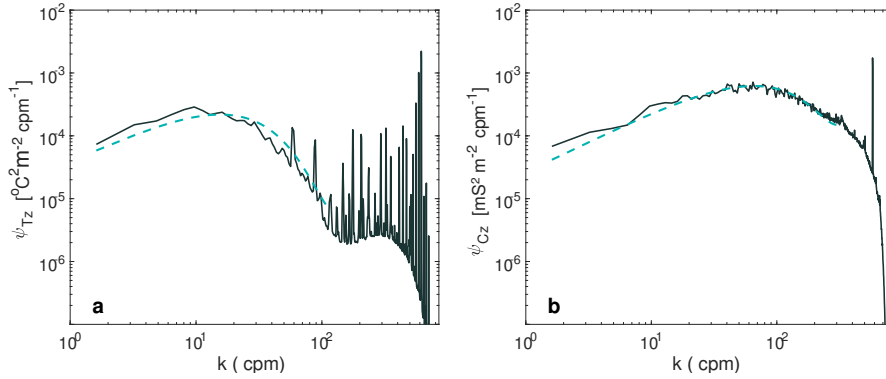


Figure 3.4: Typical wavenumber spectra of vertical temperature gradient ψ_{Tz} (a) and conductivity gradient ψ_{Cz} b, measured by the FP07 and SBE7 probe on ASIP. Ensemble mean spectrum computed from 464 individual spectra in approximately the upper 3-10 m., Knorr-11 campaign deployment 1. Dashed line shows a best-fit of the Kraichnan universal spectrum to the mean spectrum.

Meagher (1980) find the dynamic response of three glass rod thermistors mounted on a vertical profiler to be best described with a double pole filter:

$$|H_{dp}(f)|^2 = \frac{1}{[1 + (2\pi f\tau)^2]^2}. \quad (3.2)$$

Time constant $\tau \equiv 1/2\pi f_c$, the cut-off frequency, which for this filter corresponds to the 6 dB level. τ was found to vary from 8.4 to 11.3 ms and to be inversely proportional with the profiling speed W : $\tau = \tau_0 W^\gamma$. *Gregg and Meagher* (1980) finds $\gamma = -0.32$, whilst *Hill* (1987) finds $\gamma = -0.5$. More recently *Bogucki et al.* (2012) also find their FP07 probe to have a current-speed dependent response, with $\gamma = -0.3$, but their suggested response function has the shape of a single pole filter with $\tau_0 = 5.3$ ms:

$$|H_{sp}(f)|^2 = \frac{1}{1 + (2\pi f\tau)^2}, \quad (3.3)$$

The high frequency roll-off of this filter type is less steep, such that f_c corresponds to the half-power frequency or 3 dB level. A discussion in *Sommer et al.* (2013) again describes the response function of the FP07 by a double pole filter with a time response of 10 ms, but the dependence on W is removed. *Sommer et al.* (2013) also suggested that the SBE7 μC -sensor has a frequency response $\tau = 2$ ms when profiling speed $W > 0.2 \text{ m s}^{-1}$. This would imply that in the spectral domain frequencies below the half power frequency of 55 Hz are significantly reduced. Previously it was assumed that the μC -sensor only had a some spatial response, modelled by *Hill and Woods* (1988) as:

$$H(k) = \exp(-2\pi ka), \quad (3.4)$$

where a is half the distance between the two electrodes (~ 25 mm).

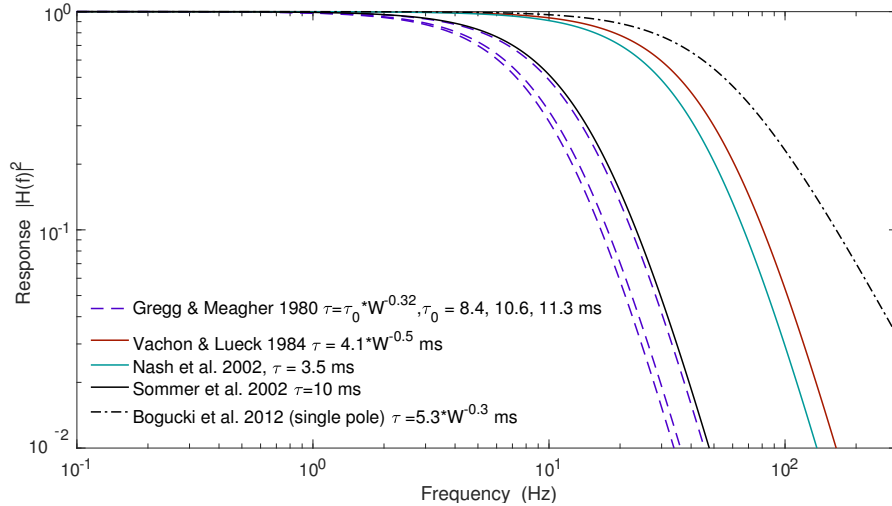


Figure 3.5: Response functions for the FP07 thermistor probes by various authors. All except for *Bogucki et al.* (2012) are double pole responses.

As shown in fig. 3.4, the average conductivity spectrum is a lot better resolved than the temperature spectrum. The half-power frequency in the plotted ensemble mean ψ_{Cz} is found at approximately 65 Hz, placing a question mark behind the time response discussed in *Sommer et al.* (2013). The spectral roll-off follows the shape of a theoretical spectrum (the Kraichnan universal spectrum model, see chapter 2) quite well.

Considering the range of response functions for FP07 probes, it would be necessary to determine the time response for each thermistor used on the ASIP. One method is to execute repeated measurement, at varying profiling speed, through a turbulent structure of which the properties are stationary for the period of the experiment. Such an experiment dedicated to determining sensor responses, has never been done with the ASIP. Alternatively, *Nash and Moum* (2002) suggest to compare ψ_{Tz} to ψ_{Cz} in sections of the profile where temperature dominates the conductivity-gradient. The power-response transfer function can be identified over a range of frequencies where the FP07 response is attenuated but the SBE7 is not: $H^2(f) = c_T^2 \psi_{Tz} / \psi_{Cz}$, with $c_T = 0.95 \text{ mS cm}^{-1} \text{ K}^{-1}$ the linearisation coefficient for temperature to conductivity. Figure 3.6 shows a trial of this method in wavenumber space for one of the FP07-probes on ASIP, using a warm layer observed in the Knorr-11 campaign. The above method is used over a narrow wavenumber range only, to avoid the noisy part of the FP07 spectrum. Both single and a double pole filter functions are computed for a cutoff frequency range $7 < f_c < 29 \text{ Hz}$. The filter with the lowest mean absolute bias to the sensor response is the double pole filter with $\tau_{dp} = 7.8 \text{ ms}$, which falls within the expected range of responses in fig. 3.5. For the other FP07 probe a $\tau_{dp} = 5.7 \text{ ms}$ and $\tau_{sp} = 6 \text{ ms}$ is found using the same method.

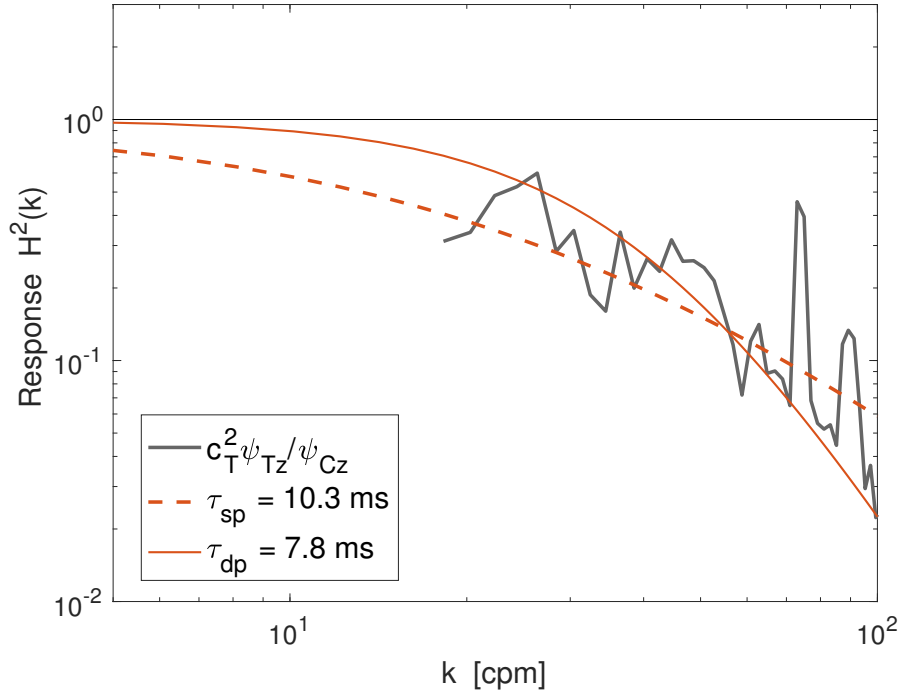


Figure 3.6: Determination of the time response of the FP07 thermistors on ASIP with the aid of the SBE7 conductivity sensor: fit to $b^2\psi_{Tz}/\psi_{Cz}$. For this an ensemble of spectra from a warm layer encountered in the third deployment of the Knorr-11 campaign is used. The optimal single pole and double pole filter to describe the response are shown.

3.3.2 Sensor Calibration

Microstructure sensors lack long-term stability; their output to a specific environmental signal changes over time. Therefore most microstructure profilers are equipped with a more stable, but slower, C/T sensor pack for local calibration. On ASIP this is a C/T-sensor by Neil Brown Ocean Sensors Inc. (NBOSI), and in later campaigns (from 2013 onwards) a mini-CTD probe by Sea&Sun Technology GmbH (fig. 3.7). Both these sensor packages sample C and T at a frequency of 10 Hz. The μC and μT time series are low-pass filtered and then fitted to the slower sensors. The coefficients obtained in this first order linear fit, are used to calibrate the original microstructure signals. This method works best when a profile includes some features with strong gradients.

3.3.3 Surface Detection

The micro-conductivity signal abruptly drops when the sensor passes through the air-sea interface. This property is used to determine the surface cut-off of the time series. The procedure described in *Ward et al.* (2014) is to determine the first minimum of the second derivative of the uncalibrated conductivity signal in the upper part of the profile (where pressure $P < 3$ dB). The final guess is the level



Figure 3.7: ‘Slow’ C/T-sensors on ASIP: left the NBOSI sensor which consists of an internal field four-electrode conductivity cell and an integral, stable thermistor; right the mini-CTD 48M-probe by Sea&Sun Technology, equipped with a platinum temperature resistor, a 7-ring electrode conductivity sensor, and a Keller pressure sensor.

below this point where the conductivity signal is constant, i.e. within $1/4$ of a standard deviation from the mean of the 2 - 0.5s before the level of the first guess. However, an alternative way is proposed here and has been executed on the datasets from 2013 onwards. The process of deconvolution of the pre-emphasised signal of conductivity, involves the application of a low-pass 1st order Butterworth filter (*Mudge and Lueck, 1991*). A side-effect of this, is the smoothing of the ‘spike’ corresponding to the abrupt change in conductivity at the surface. To avoid this, the surface is determined in the pre-emphasised signal using the same procedure, as illustrated in fig. 3.8. The uncertainty in the surface level corresponds to the spatial response of the μC -sensor of $O(10^{-2} \text{ m})$. Although small, this implies that variability over the ocean skin layer is not measured with the current suite of sensors on ASIP.

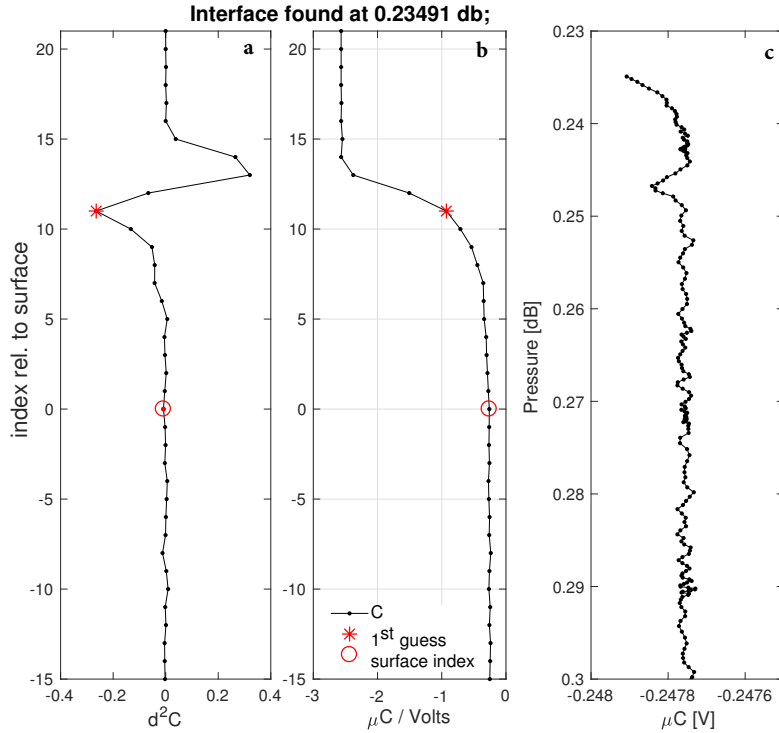


Figure 3.8: Surface detection procedure: **a.** the 2nd derivative of the uncalibrated pre-emphasised conductivity signal and **b.** the pre-emphasised conductivity signal, with the minimum in **a** (red asterisk) and the chosen surface level (red dot). **c** the resulting upper 7 cm of the deconvoluted uncalibrated conductivity.

3.4 Position and Motion

The depth of the ASIP in the water column is accurately measured by a Keller pressure sensor embedded in the sensor end cap. A second pressure sensor on the lower end of the profiler is present for redundancy. The rise velocity of the instrument is computed using the first difference to the low-pass filtered pressure record.

The profiler is further equipped both with a solid state accelerometer and a 3D motion package, which records acceleration and angular rate. Currently this information is only used to compute the tilt-angle of the profiler. In the presence of waves this can be larger than 3° in the upper half metre. This could lead to a misrepresentation of the measured turbulent dissipation rate over this depth, as the assumption of a constant rise velocity, required for both Taylor's hypothesis and the shear probe's signal conversion, would be violated.

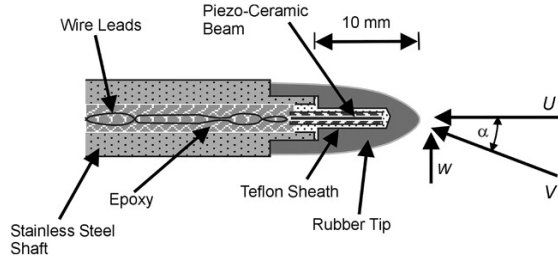


Figure 3.9: Schematic image of the functioning of an airfoil shear probe, from *Macoun and Lueck* (2004) ©American Meteorological Society. Used with permission.

3.5 Upper Ocean Turbulence Measurements

3.5.1 The Airfoil Shear Probe

The airfoil shear probes on ASIP measure the velocity microstructure of two orthogonal components of the horizontal velocity. The dissipation rate of turbulent kinetic energy ϵ is computed from these measurements. Assuming stationary conditions and homogeneous turbulence, ϵ is equal to the production rate of TKE, and thus a measure for the turbulence of a flow (*Thorpe*, 2005). The shear probe consists of a bi-morph piezo-ceramic beam, which generates an electrical charge if bent due to cross-axial forces. This charge is proportional to the product of cross-stream fluctuations and the travel velocity of the probe ($u \times W$). Electronics transfer the charge to a capacitor which produces a voltage. The first shear probe successfully deployed in the ocean was developed by *Osborn* (1974). Since then several variations of probes with different dimensions have been developed (*Moum et al.*, 1995; *Lueck et al.*, 2002). The commercially available shear probes used on ASIP (Rockland Scientific Inc.) have a beam length of 8.5 mm (from tip to fulcrum), 1.6 mm and 0.5 mm thick. The beam is anchored in a stainless steel shaft with a waterproof axisymmetric silicone rubber tip (fig. 3.2c and 3.9).

The profiling velocity (or ambient current velocity for a probe mounted on a fixed structure in a current) W should be about 3 times larger than the cross stream fluctuations to ensure the angle of attack be not too large. The probe voltage E_p is then proportional to both W and the cross-stream velocity u :

$$E_p = S_e W u, \quad (3.5)$$

with S_e the sensitivity of the individual probe determined by the manufacturer's calibration.

Spatial scales are most often used in turbulence terminology (see section 2.4). However measurements from a shear probe on a single moving profiler like ASIP, provide a time series of the fluctuating velocity. In converting this time series to a vertical profile the Taylor Frozen Field hypothesis is assumed:

$$\frac{\partial u}{\partial z} = \frac{1}{W} \frac{\partial u}{\partial t} = \frac{1}{S_e W^2} \frac{dE_p}{dt}. \quad (3.6)$$

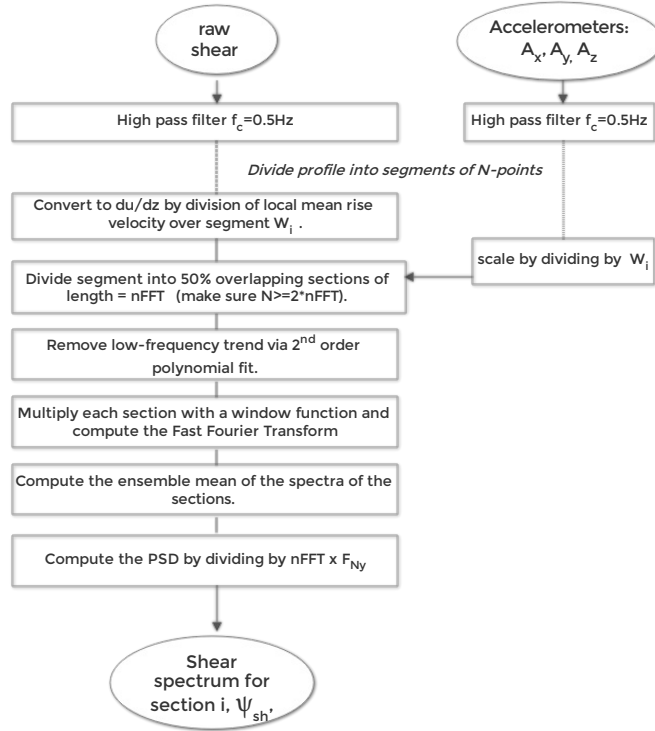


Figure 3.10: Flowchart describing the computation of the shear spectra, using the spectrum from the analog accelerometers to correct for instrument motions.

This assumption is valid when the statistical properties of the turbulent field are invariant during the sample time, and requires W to be fairly constant. The turbulent dissipation rate ϵ is then computed following (2.43), assuming the field is isotropic. In isotropic conditions $\partial u/\partial z$ and $\partial v/\partial z$ are statistically independent, so by measuring both components, as done on ASIP, the statistical confidence of the observation is increased.

3.5.2 Computation of ϵ from Shear: Spectral Analysis

Instead of directly computing the turbulent kinetic energy dissipation rate, ϵ , from the instantaneous shear signal, it is commonly derived from the integral of the wavenumber spectrum of the velocity shear (2.53). This allows for better decontamination of the signal for noise that is not related to ocean turbulence.

The lower frequency limit due to the shear probe's dimension is about 0.1 Hz (Lueck, 2016a). The finite size of the shear probe also causes spatial averaging of high frequency fluctuations. To correct for the loss of variance at high frequencies, a single-pole response function is applied to the wavenumber spectrum, following

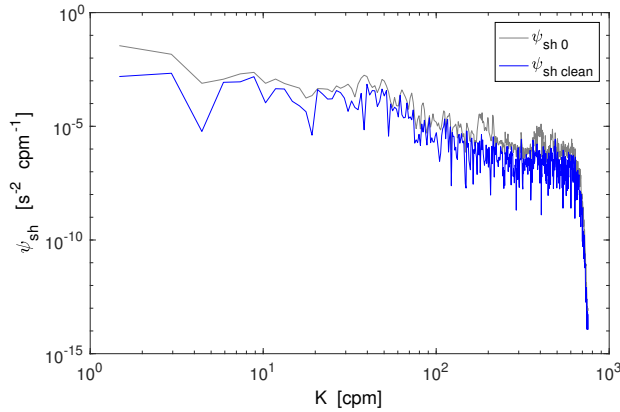


Figure 3.11: Result of the coherent noise removal technique.

Oakey (1982):

$$H(k) = \frac{1}{1 + (k/k_c)^2} \quad (3.7)$$

The half-power wavenumber k_c , is estimated to be $48 \pm 10\%$ cpm (*Wolk et al.*, 2002; *Macoun and Lueck*, 2004).

Figure 3.10 shows the procedure used to compute spectra from the shear, as well as the accelerometers and the microstructure scalar sensors on ASIP. An FFT is performed on i overlapping segments of the measured signal. Each segment contains N data points, where N is at least 2 times the FFT-length ($nFFT$). The FFT gives a spectral estimate for the wavenumbers $k = 0 : k_{Ny}/nFFT : k_{Ny}$, where k_{Ny} is the wavenumber associated with the Nyquist frequency, half the sampling rate f_S . ASIP's sampling rate is set to 1000 Hz so $F_{Ny} = 500$ Hz. To convert frequency to cyclic wavenumber k with units cpm, required for the spatial series, both the input time series of shear as well as f_S are divided by the mean rise velocity over a segment W_i . The function `csd_ogas.m` from the ODAS MatLab library (Rockland Scientific Inc.) is used to compute the power spectra as follows:

Each segment is divided into 50% overlapping sections of length $nFFT$, which are first multiplied by a window function (normalised cosine window), then the power spectrum is computed. Optionally a polynomial can be fitted to the time series before executing the FFT, in order to remove low frequency trends. This is specifically useful for the first segments below the ocean surface, where wave induced velocity can enter the spectrum.

The choice of $nFFT$ is a compromise between spectral resolution and spatial resolution of the resulting profile of ϵ . An $nFFT$ of 512 or 1024 is most often used for ASIP, with a segment length of $3 \times nFFT$, such that a dissipation rate estimate is computed for approximately each 750-1500 ms of data; each 0.5-0.75 m at a mean profiling velocity of 0.5 m s^{-1} . However, at typical background ϵ levels below the mixing layer in the upper ocean, of $10^{-10} - 10^{-9} \text{ W kg}^{-1}$, the peak in ψ_{sh} is found between 4 and 6 cpm, so even an $nFFT$ of 1024 will only result in 2-5 spectrum values before this peak (the inertial subrange). For statistical significance

a minimum of three overlapping spectra per segment is required, over which an ensemble average is used for the dissipation rate estimate (*Sanchez et al.*, 2011). A well resolved shear spectrum shows the inertial subrange, where $\epsilon \propto k^{1/3}$, a spectral peak, and a roll-off to a spectral minimum at least two orders of magnitude lower than the peak. At higher wavenumbers the spectrum can be enhanced again due to instrument vibrations and electrical noise. To estimate ϵ , it is imperative to integrate the inertial-and viscous parts of the shear spectrum, without including this noise. When these ranges are not well resolved, either ϵ is too low, such that the signal-to-noise ratio falls below 10, or ϵ is larger than $2 * 10^{-5} \text{ W kg}^{-1}$, such that part of the viscous range lies above the high wavenumber limits of the shear probe ($k > 150 \text{ cpm}$), universal shear spectra are used to improve the estimate of ϵ . As presented in chapter 2.4.4, two universal spectral models commonly used by oceanographers are the Panchev-Kesich model and the Nasmyth spectrum.

Noise and Motion correction

The wavenumber band over which to integrate the shear spectrum has to be selected well, to avoid over-estimation of ϵ by including spectral noise. Vibration of the sensor platform will raise the energy in the spectrum. Coherent noise cancellation techniques are used to correct the spectrum of velocity fluctuations for instrument vibration through comparison with the spectrum of a profiler's integrated accelerometer (*Soloviev et al.*, 1999; *Levine and Lueck*, 1999; *Goodman et al.*, 2006), as illustrated in fig. 3.11. ASIP is equipped with both an analog accelerometer, and a separate digital motion package.

3.5.3 Application of Universal Models to Derive ϵ

Universal spectra can be used in several ways to estimate ϵ from measured shear through spectral analysis. A universal shape can be fitted to the well-resolved part of the spectrum, and consequently used to extrapolate this down the inertial subrange to a minimum wavenumber of $k \sim 0.1 \text{ Hz}$, as well as up to the Kolmogorov wavenumber. Alternatively, when using the Nasmyth spectrum, the integral model in *Lueck* (2016a) can be used to compute the missing variance of the measured spectrum.

Figure 3.12 shows the non-dimensional Nasmyth spectrum from the tabulated values in *Oakey* (1982) and the mathematical fit by *Wolk et al.* (2002); *Lueck* (2016a), eq. 2.55, both on a logarithmic and linear axes. Points on the modelled curves indicate where certain fractions of total shear variance reside in the spectrum. It shows that less than 50% of the variance resides below the peak of the spectrum (the exact peak corresponds to about 33% of the variance), and not much more than 10% of the total variance is covered by the inertial subrange. Ideally the shear spectrum is well resolved without significant noise contamination up to the wavenumber corresponding to the 95% variance level.

In the past, two different methods were used to fit a universal form to the shear spectra obtained from the airfoil shear probes on ASIP, and to compute the dissipa-

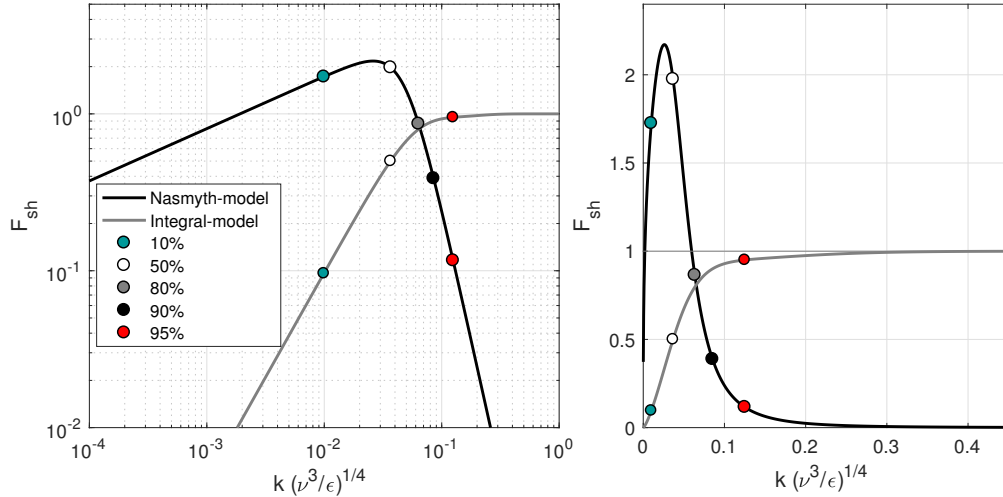


Figure 3.12: Modelled non-dimensional Nasmyth spectrum in logarithmic (left) and linear coordinates (right), following equation (2.55), as well as the modelled integral of the non-dimensional spectrum. Coloured circles on the curves indicate where the shear variance reaches 10, 50, 80, 90 and 95% of the total.

tion rate: an iterative method and an algorithm which uses a maximum likelihood estimator. These methods are here evaluated, as well as the method used in the ODAS data-processing software provided by Rockland Scientific Inc., the leading supplier of shear probes and ocean turbulence instruments. In the remainder of this section these three methods are first briefly described and illustrated schematically in fig. 3.13, 3.14 and 3.15, followed by a comparison of their performance.

1. Simple iterative fit to the Nasmyth spectrum

The measured shear velocity spectra $\psi_{sh}(k)$ are integrated over the bandwidth $k_{min} = 2$ to $k = 6$ cpm for a first guess of ϵ and the Kolmogorov wavenumber k_s (eq. 2.43 and 2.45). Then the upper integration limit is iteratively increased in steps of 2 to 5 cpm, and at each iteration ϵ and k_s are recalculated. The iteration ends when k_s and the upper integration limit have convoluted to less than 2 cpm of each other. A Nasmyth universal spectrum for the iteratively determined ϵ is computed via equation (2.55). This $\psi_N(k)$ is then used to extrapolate the measured spectrum beyond the integration limits, such that the total ϵ is computed as:

$$\epsilon = \frac{15}{2}\nu \left[\int_0^{k_{min}} \psi_N(k)dk + \int_{k_{min}}^{k_{max}} \psi_{sh}(k)dk + \int_{k_{max}}^{\infty} \psi_N(k)dk \right]. \quad (3.8)$$

2. Fit to the Nasmyth spectrum from the ODAS Matlab Library

A different method is adapted from the current analysis code provided by Rockland Scientific Inc. (ODAS MatLab Library v.4.02). An initial guess of ϵ is made by integrating the measured spectrum from 0 to 10 cpm. The total dissipation rate is expressed as a function of this ϵ_{10} , by a simple mathematical

model (Lueck, 2016a):

$$\frac{\epsilon}{\epsilon_{10}} = \sqrt{1 + 1.0774 \times 10^{-9} \epsilon_{10}}. \quad (3.9)$$

Based on this first guess of ϵ a Nasmyth spectrum is computed, which is compared to the measured spectrum over the wavenumber band of the inertial subrange, approximately corresponding to the non-dimensional wavenumber $\tilde{k} = 0.02$. The fitted spectrum ψ_N is compared to the measured ψ_{sh} over the inertial subrange, and the first guess of ϵ is scaled by the fit error (see fig. 3.14). This is done 5 times, removing values with a fit-error > 0.5 after the third iteration.

When the first guess of ϵ was larger than $1.5 \times 10^{-5} \text{ W kg}^{-1}$ the algorithm ends here. Otherwise the spectrum is expected to be resolved beyond the spectral peak, and the next step is to determine the wavenumber of the spectral minimum after the peak, k_{dip} , which serves as the upper limit of integration. For wavenumbers beyond k_{dip} high frequency noise dominates the spectrum. Knowledge about the fraction of total variance resolved (see fig. 3.12), is used to compute k_{95} , the wavenumber for which 95% of the total variance would be resolved at the second guess of ϵ . A higher order (4-8) polynomial is fitted to ψ_{sh} over k_{obs} up to k_{95} , the minimum of this polynomial corresponds to k_{dip} . Then a third guess of ϵ is computed through trapezoidal integration of the measured spectrum up to the lower one of k_{dip} and k_{95} . The percentage of variance resolved is computed and used to upscale ϵ_3 in an iterative way, until convolution. Finally, the missing variance between 0 and the first non-zero wavenumber resolved (k_1), due to the use of the trapezoidal method for integration (Lueck, 2016a), is computed as $1/4k_1\psi_N(k_1)$ and added to ϵ_3 .

3. Maximum Likelihood fit to the shear spectrum

This method, outlined in fig. 3.15 determines ϵ directly from a theoretical spectrum fitted to the spectrum of the shear observations. Inspired by Ruddick *et al.* (2000), who used it for temperature gradient spectra, Sanchez *et al.* (2011) extended the method to shear spectra. Both the Nasmyth and Panchev-Kesich spectrum can be used as a theoretical spectrum $\psi_{th}(k)$. The $\psi_{th}(k)$ associated to a range of Kolmogorov wavenumbers k_s is computed using equation (2.54) or (2.55). The logarithm of the likelihood of $\psi_{th}(k)$ for each k_s is computed, assuming a chi-squared probability distribution with n degrees of freedom (χ_n^2 -pdf):

$$Lh = \sum_{i=1}^N \ln \left(\frac{n}{\psi_{th}(k) + \psi_n(k)} * \chi_n^2 \left[\frac{n\psi_{sh}(k)}{\psi_{th}(k) + \psi_n(k)} \right] \right), \quad (3.10)$$

where N is the size of ψ_{sh} , and ψ_n is the noise spectrum, which is formulated based on the spectral level in non-turbulent parts of the ASIP profile and the shear probe response function (3.7). To avoid fitting ψ_{th} to noise, ψ_n is

added to ψ_{th} prior to applying the MLE algorithm, such that the different fits of ψ_{th} only differ for the bandwidth over which they exceed the noise level. The maximum value of Lh corresponds to the best fitting model spectrum ψ_{th} . The number of degrees of freedom d depends on the FFT length and the window function used to compute ψ_{sh} .

3.5.4 Evaluation of Methods to Compute ϵ

To evaluate the three approaches to fit a universal spectral model to the measured shear spectra from ASIP, a re-analysis of (parts of) several datasets has been performed. For a total of 152 profiles and both individual shear probes ϵ has been recomputed. A comparison of the value of ϵ computed from the different methods is shown in fig. 3.16.

The ODAS method results in lower ϵ than the original simple iterative fit (Method 1), except over the lower part of the profile (fig. 3.16 a). In this plot ϵ estimates from both shear probes are used. Method 1 assumes that the shear spectrum is well resolved, such that the variance near k_s adds little to the total integral. When noise enters the spectrum far before k_s , this may get included and lead to an overestimation of ϵ . The ODAS method (Method 2) does not make use of k_s in determining the upper integration limit. Instead the shape of ψ_{sh} is used to determine the upper integration limit from a local minimum in the spectrum, and smart use is then made from knowledge of the percentage of variance resolved at this wavenumber limit. Visual inspection of the measured shear spectra and the Nasmyth spectra fitted to it in this method suggests that Method 2 gives the better fit and more reliable estimate of ϵ .

Comparison between the ODAS method and the Maximum Likelihood Estimator method (Method 3) is shown in fig.3.16 b. The MLE method often estimates ϵ to be several orders of magnitude larger than the ODAS method, for either universal spectrum used. In this method ϵ is computed directly from the theoretical spectrum (Nasmyth/Panchev-Kesich), using the value of k_s associated to the best fitting model level. The large deviation of ϵ can be explained from an unsuitable noise-model: a too-low noise-model results in the inclusion of noise to the part of the spectrum used for the fit, or (in case of scalar spectra) in noise over the part of the spectrum used to compute ϵ .

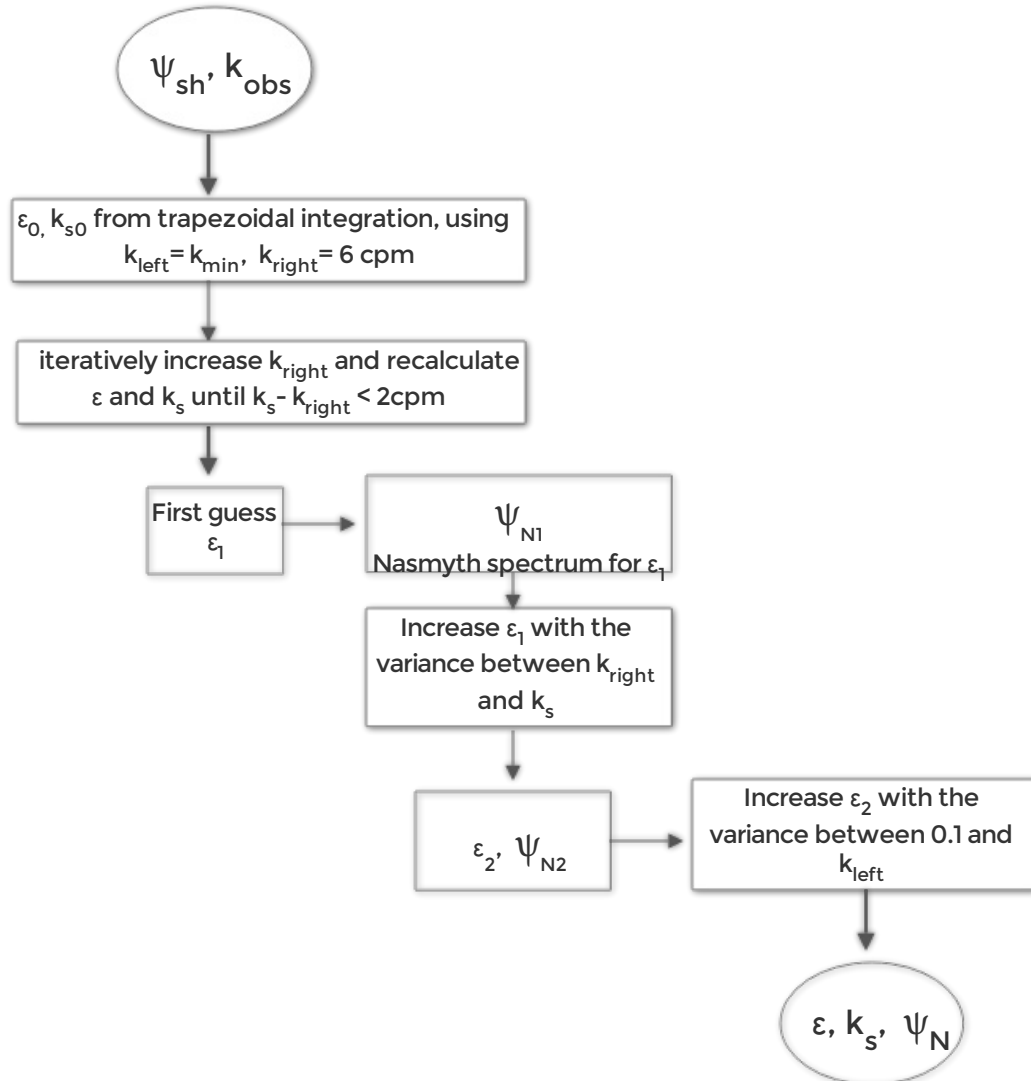


Figure 3.13: Flowchart describing the computation of TKE dissipation rate ϵ , from the spectrum of measured shear ψ_{sh} , for method 1: a simple iterative fit to the Nasmyth spectrum ψ_N .

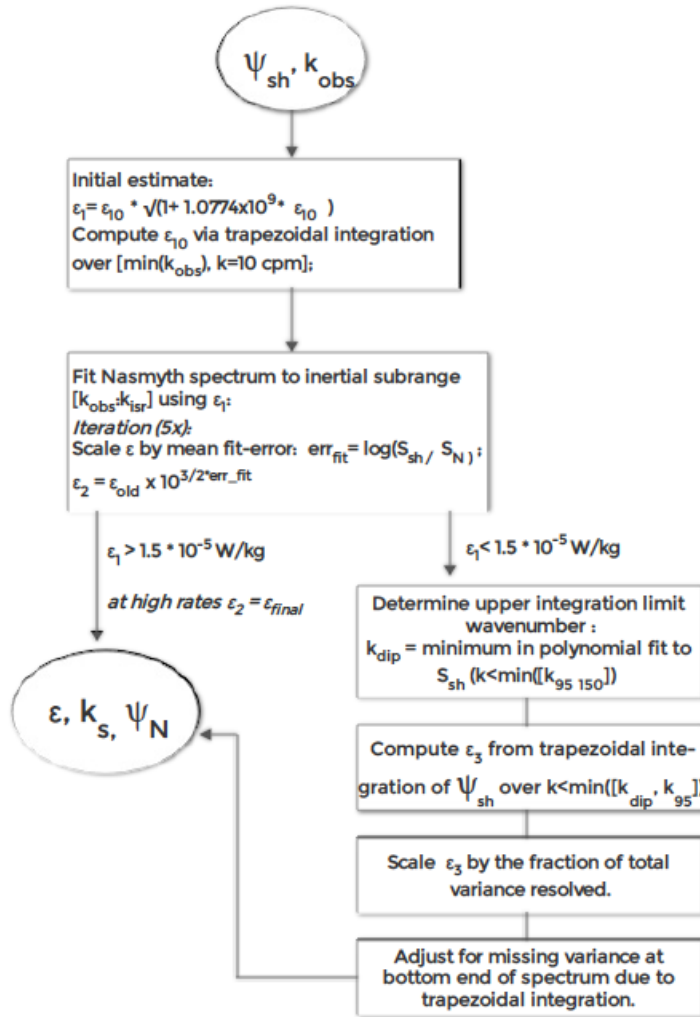


Figure 3.14: Flowchart describing the computation of TKE dissipation rate ϵ from the spectrum of measured shear ψ_{sh} , for method 2: a fit to the Nasmyth spectrum ψ_N based on algorithms from the ODAS Matlab Library.

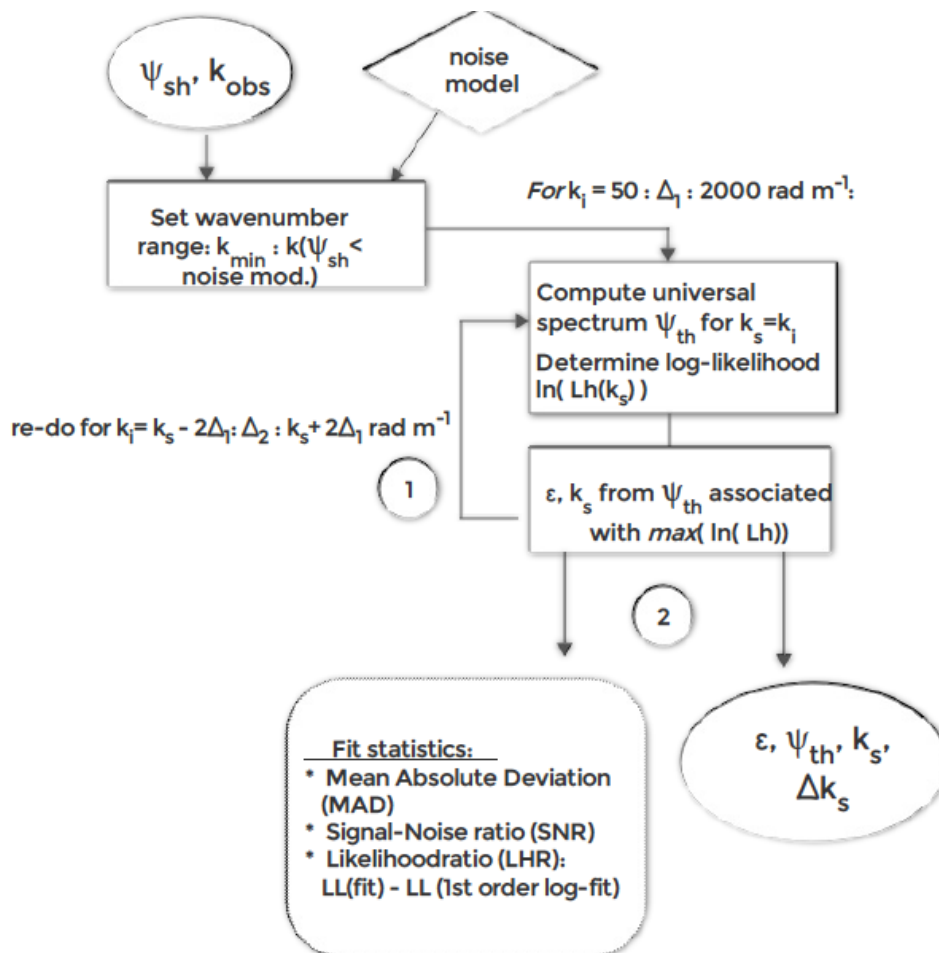


Figure 3.15: Flowchart describing the computation of TKE dissipation rate ϵ , from the spectrum of measured shear ψ_{sh} , for method 3: evaluating a universal model based on the Maximum Likelihood Estimator (MLE).

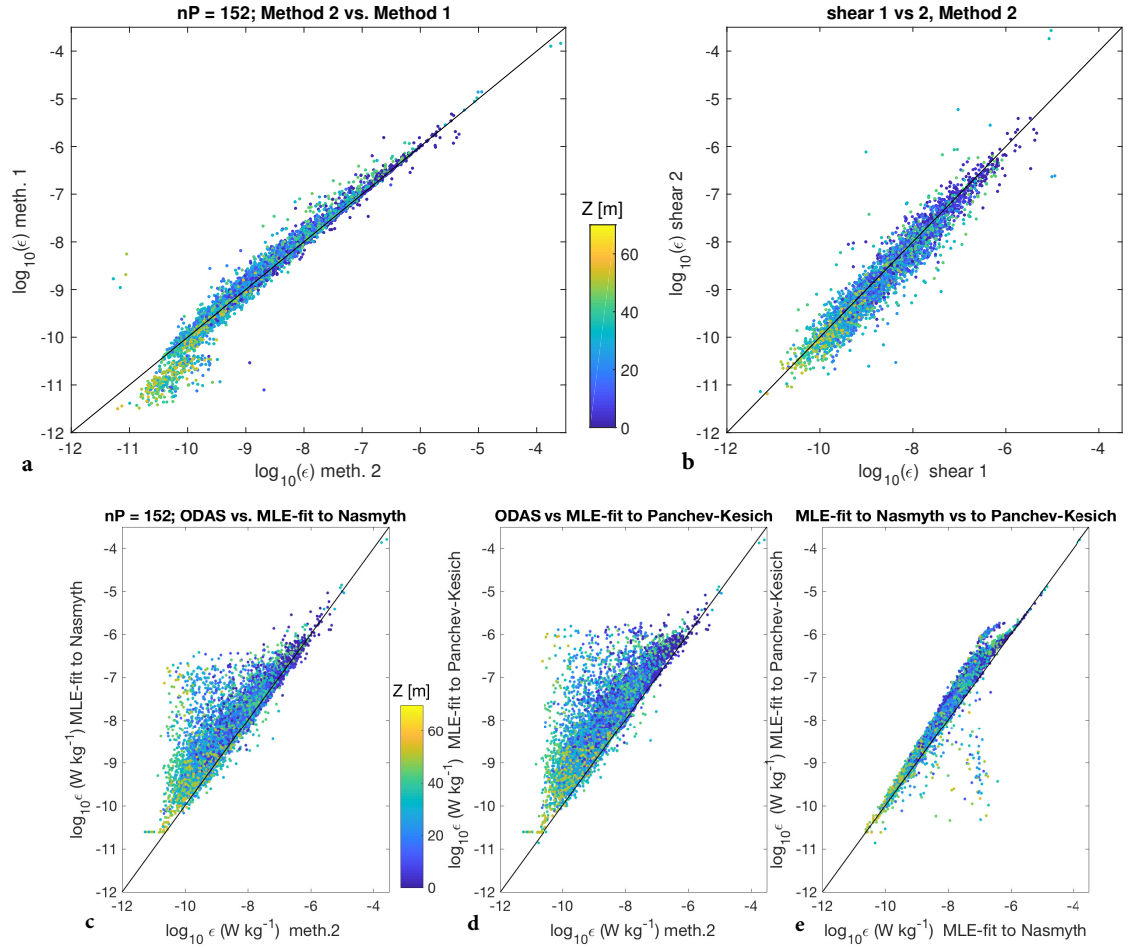


Figure 3.16: Comparison of 3 methods to derive ϵ from the spectral analysis using fits to universal models outlined in sec. 3.5.3. **a.** Method 2 versus Method 1. **b.** Verification of the uniformity in ϵ from simultaneous measurement of both shear probes, using Method 2. **c.** Method 2 versus Method 3 using an MLE-fit to the Nasmyth theoretical spectrum. **d.** Method 2 versus Method 3 using an MLE-fit to the Panchev-Kesich theoretical spectrum. **e.** Method 3 comparing ϵ from MLE-fits to the Nasmyth versus the Panchev-Kesich theoretical spectrum.

3.6 Using the Scalar Variance Spectrum

Signals measured with the microstructure temperature and conductivity sensors can be used to compute the dissipation rate of temperature and salinity variance, χ_T and χ_S , to allow for the determination of the vertical eddy diffusivity of heat and salt (2.4.3). Both scalar gradient spectra are a function of ϵ (2.57); in the absence of fluctuating velocity measurements, χ_T has been used to compute ϵ (Oakey, 1982; Luketina and Imberger, 2001; Perlin and Moum, 2012, e.g.).

For a fully resolved temperature gradient spectrum (ψ_{Tz}) χ_T can be computed with (2.56), assuming the turbulence field is isotropic. However, the frequency response of the FP07-thermistors limits resolving large parts of this spectrum. The conductivity gradient spectrum ψ_{Cz} is often better resolved, and Nash *et al.* (1999) suggest that when the salinity gradient is small, ψ_{Tz} can be inferred from it. Nash and Moum (2002) obtained sufficiently resolved spectra ψ_{Cz} and ψ_{Tz} with a fast μCT probe, when profiling at 0.25-0.35 m s^{-1} . The ASIP profiles have typically been made at 0.5-0.6 m s^{-1} , and ASIP is normally equipped with a slightly slower set of μT and μC sensors. Instead of using fully resolved spectra to estimate χ_T , the observed part of a spectrum has to be fitted to a universal spectral model.

Some authors use the inertial subrange only to estimate ϵ from ψ_{Tz} , under the assumption that $K_T = K_\rho$ and $K_\rho = \Gamma\epsilon/N^2$, where $\Gamma \approx 0.2$ is the mixing efficiency (Osborn, 1980). Using this assumption, (2.57), and (2.50)

$$\psi_{Tz} = \beta \left(\frac{2\Gamma(\overline{\partial T/\partial z})^2}{N^2\chi_T} \right)^{1/3} \chi_T^{2/3} k^{1/3}, \quad (3.11)$$

such that a best fit of the measured ψ_{Tz} to $k^{1/3}$ will determine χ_T (Moulin *et al.*, 2018).

When ψ_{Tz} and ψ_{Cz} are resolved beyond the inertial subrange, a universal form can be fitted via curve-fitting algorithms (Ruddick *et al.*, 2000; Luketina and Imberger, 2001; Sanchez *et al.*, 2011). This requires some part of the measured spectrum to be shaped like the Batchelor (or Kraichnan) spectrum. Following the MLE-method in Ruddick *et al.* (2000) and Sanchez *et al.* (2011), a Batchelor or Kraichnan spectrum can be fitted to the observed temperature and conductivity gradient spectra measured by ASIP. This requires the definition of a noise model, based on temperature and conductivity gradient spectra from a quiescent region. The algorithm is largely the same as that used for the shear spectrum as illustrated in fig. 3.15, except that in principle two parameters can be tuned to find the optimal fit of the universal spectral form: χ_θ and ϵ . An initial guess of χ_θ is computed from the integral of the observed $\psi_{\theta z}$ over the wavenumber range below the noise level. A universal model is then fitted following the MLE-method, which is used to compute the additional χ_θ at the unresolved wavenumbers. This process is repeated up to 10 iterations or until the MAD-fit statistic is sufficiently low. The best fit then yields the Batchelor wave number k_B , which through (2.46) can be used to calculate the turbulence dissipation rate ϵ (Oakey, 1982).

Another method proposed by Bogucki *et al.* (2012) relates the wavenumber at which the peak in the spectrum is found, k_c , to k_B for both the Batchelor and

Kraichnan model respectively:

$$L_B = 0.433/(2\pi\sqrt{q_B k_c}), \quad (3.12)$$

and

$$L_B = 1/(2\pi\sqrt{6q_K k_c}), \quad (3.13)$$

This empirical method has not yet been evaluated for the measured ASIP spectra.

3.6.1 Case Study: the Signature of Rain in the Microstructure

In cases where the salinity flux is important in controlling the buoyancy, for example when rainfall results in negative salinity anomalies at the surface, ψ_{Sz} becomes of interest. Investigation of ASIP profiles during rainfall² shows that rain causes high variance in the scalar microstructure. This is illustrated by profiles of the vertical conductivity gradient ($\partial C/\partial z$) in fig. 3.17. The lower panel shows ($\partial C/\partial z$) in the upper 15 s (~ 9 m), in one profile before the onset of rain, and in two/four consecutive profiles, during two rain events of peak rain rate 72 mm h^{-1} (red hues) and 45 mm h^{-1} (blue hues)³. The vertical conductivity gradient is greatly enhanced below the surface. There is some increase in the magnitude of the signal in the corresponding profiles of ($\partial u/\partial z$) as well. However, the spatial response of the micro-conductivity probe on the ASIP is higher than that of the shear probe, and whereas the pre-rain $\partial C/\partial z$ is very low, the pre-rain profiles of $\partial u/\partial z$ also show patches of elevated turbulence near the surface, so the rain-effect is less distinguishable. Conductivity is the result of temperature and salinity fluctuations, which are both expected to be significant during rain. To verify this, spectra of scalar variance are computed from the upper 1.5 s (≈ 80 cm) of data during rain- and non rain profiles, for both conductivity and temperature. There is a significant increase in the amplitude of ψ_C with increasing rain rate, see fig. 3.18a. The changes in ψ_{Tz} during rain in fig. 3.18b, are less significant than in ψ_{Cz} , especially at higher wavenumbers. A method to derive the salinity spectrum by *Nash and Moum* (1999, 2002), makes use of the assumption that the measured conductivity gradient is a linear combination of salinity and temperature fluctuations:

$$\psi_{Sz}(k) = \frac{1}{c_S^2}\psi_{Cz}(k) - \frac{2c_T}{c_S^2}\psi_{CzTz}(k) + \frac{c_T^2}{c_S^2}\psi_{Tz}(k). \quad (3.14)$$

c_T [$\text{S m}^{-1} \text{ }^\circ\text{C}^{-1}$] and c_S [$\text{S m}^{-1} \text{ psu}^{-1}$] are the linearisation coefficients. The shape of the co-spectrum ψ_{CzTz} is dependent on the $T - S$ relation. The lower response of the FP07 thermistors, as well as the electrical noise issues encountered with these sensors in this specific data set, make that ψ_{Tz} is a lot less resolved than

²This dataset, comprising of 58 profiles during the Knorr-11 campaign, is further presented in ch. 5.

³Rain event III and IV in ch. 5 respectively.

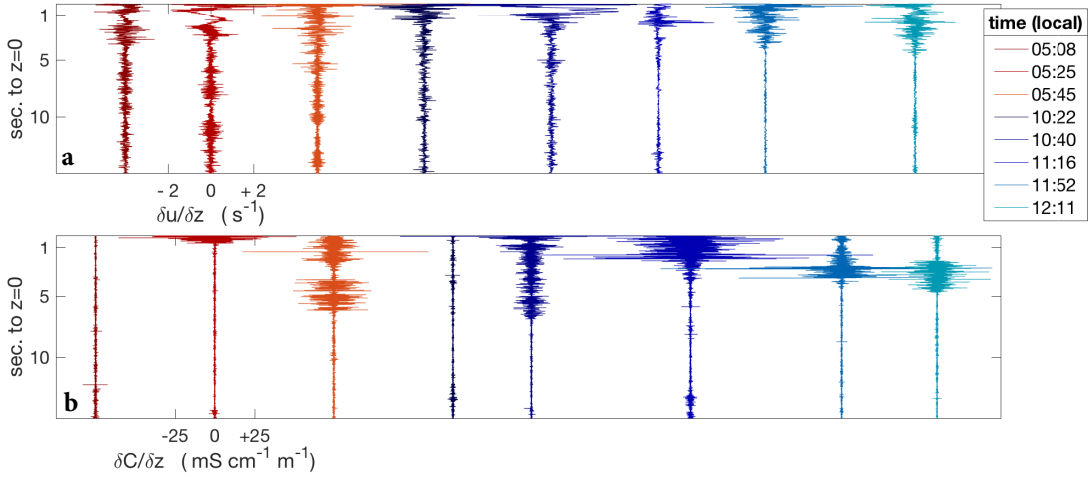


Figure 3.17: Record of the upper 15 s of selected profiles of horizontal velocity shear $\partial u / \partial z$ and vertical conductivity gradient $\partial C / \partial z$ for selected profiles before (05:08 and 10:22) and during a short rain event of $R_{max} = 72 \text{ mm h}^{-1}$ (reds) and a longer event of $R_{max} = 45 \text{ mm h}^{-1}$ (blues).

ψ_{Cz} . Whereas ψ_{Cz} approximates the shape of the universal models (fig. 2.8), no clear spectral peak is observed in ψ_{Tz} . This will complicate the execution of (3.14). Uncertainties induced in fitting a universal model to the measured ψ_{Tz} , will propagate into the computation of ψ_{CzTz} as well. Even though fig. 3.18 suggests that the conductivity variability is dominated by the anomalous salinity of the rainwater, it cannot be assumed that the rain induced temperature fluctuations are negligible. Rain from deep convective clouds can be close to freezing temperatures and will cause a significant cool anomaly on entering the seawater.

From fits of the Kraichnan universal model to the resolved parts of ψ_{Cz} the dissipation rate of scalar variance is computed with eq. 2.56 (see fig. 3.19). Temperature diffusivity κ_T is used for the computation of χ_C . Here it is shown that the patch of high scalar variance deepens over time, as can also be inferred from the last two profiles of dC/dz in fig. 3.17b. The level of elevated χ_C coincides with the bottom of the surface salinity anomaly, which deepens as a result of turbulent mixing. This mixing reduces the scalar variance above the halocline, by turbulent diffusion of the gradients.

Qualitatively the observed changes in ψ_{Cz} indicates that rain serves as a source of scalar variance to the upper ocean. Apart from the increase in variance, resulting in the upward shift of ψ_{Cz} , the spectral peak is seen to also shift to a higher wavenumber. Following the description of scalar variance spectra in sec. 2.4.4 it can therefore be concluded that the scalar variance spectra reveal the rain-induced turbulence. Although this case study is preliminary, it provides a first observation of micro-turbulence observations associated to rainfall in the open ocean, which has only been hypothesised or observed in a laboratory settings.

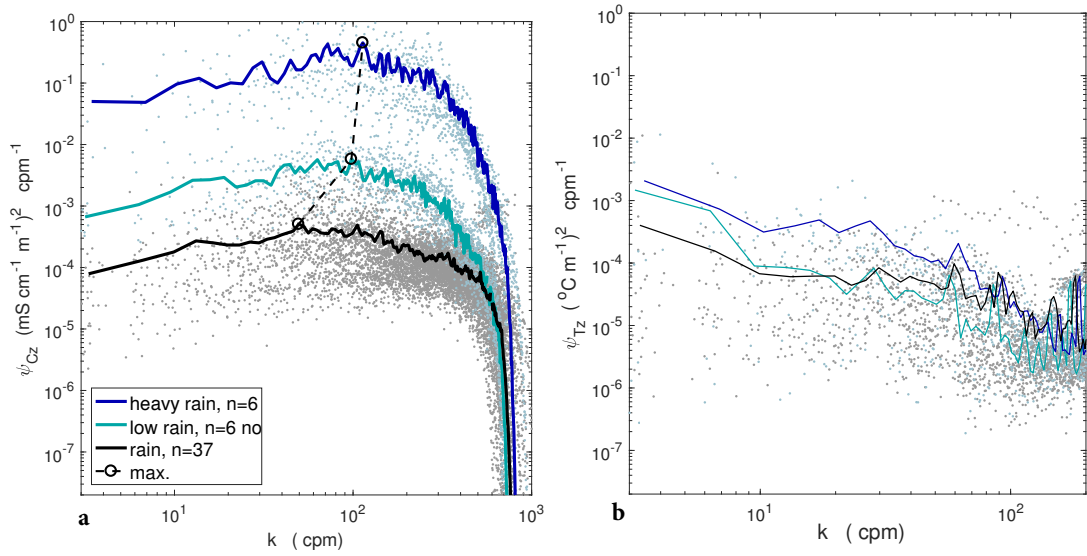


Figure 3.18: **a.** Vertical conductivity gradient spectra computed over the upper 1.5 seconds of ASIP profiles during the major (blue) and minor rain events (green-blue), and for the intermediate periods of zero rain rate. Thick lines corresponds to the mean of each ensemble of spectra. **b.** Same for vertical temperature gradient spectra. The connected circles in each mean ψ_{Cz} in **a** indicate the spectral maxima.

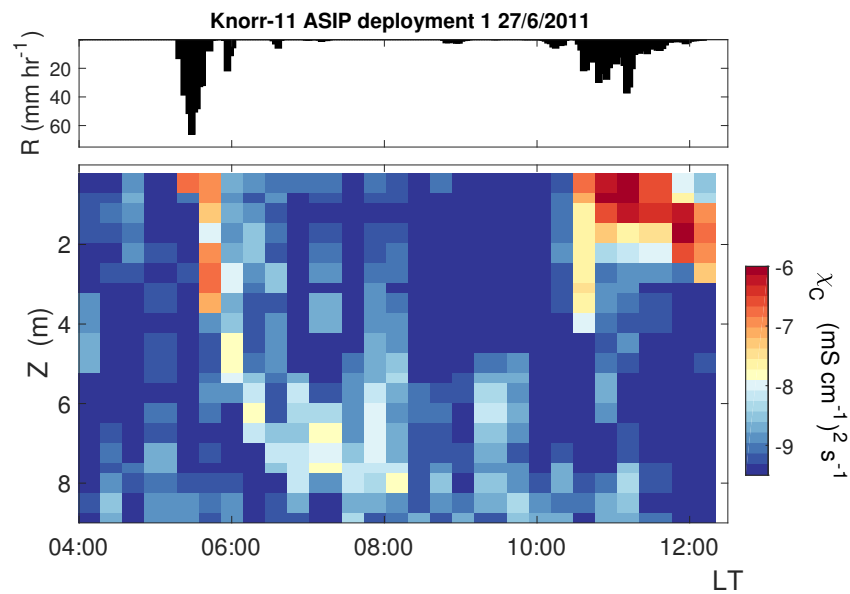


Figure 3.19: **a.** Rain rate R and **b.** Conductivity variance dissipation rate χ_C during the second half of an ASIP deployment during the Knorr-11 campaign in the North Atlantic.

4 Diurnal Warming of the Ocean Surface Boundary Layer

4.1 Introduction

Solar radiation absorbed directly below the surface and in the metres below forms the dominant heat flux during daytime. As a result, when low to moderate wind speeds prevail over the ocean, and sky conditions are clear, a warm surface layer can often be observed to form in the OSBL. This causes a diurnal variability in the sea surface temperature (SST), up to several degrees in magnitude (*Kawai and Wada, 2007*). The thermal stratification which develops in the first metres below the surface effectively shuts off the remnant mixed layer below from atmospheric forcing. Turbulence in this layer has been observed to be reduced by an order of magnitude (*Brainerd and Gregg, 1993; Caldwell et al., 1997*). Momentum from the wind and the waves are restricted to the warm layer, accelerating this layer horizontally with respect to the water below (*Woods and Strass, 1986; Price et al., 1986; Soloviev and Lukas, 2014*). Within this diurnal jet the turbulence is enhanced (*Callaghan et al., 2014; Sutherland et al., 2016; Moulin et al., 2018*), which homogenises the layer. Shear instabilities at the base of the warm layer during the second half of the day, when the solar radiation reduces in strength, followed by convection once the surface heat flux changes sign, further deepens and eventually disperses the warm layer, entraining it into the remnant mixed layer below (*Prytherch et al., 2013*) (see also fig. 2.5).

There is a major interest in the diurnal cycle of SST and thermal stratification near the ocean surface because of its influence on ocean-atmosphere fluxes of mass, energy and gasses. Increased computational capabilities now allow numerical ocean and climate models to account for diurnal variability at the air-sea interface (*Bernie et al., 2005; Large and Caron, 2015*). Global maps of SST used as boundary conditions to these models are assembled from a blend of SST measurements from remote sensing and in-situ sensors (*Karagali et al., 2017*). To match these measurements from different depths of the water column and different times of the day, it is crucial to have a good understanding of the diurnal variability of SST. Models of diverse complexity have been developed to describe the diurnal variability in SST (sec. 2.3.1). The optical properties of the water affect the absorption of solar radiation in the near-surface layer, and modulate the diurnal structure. It is therefore important that models of the diurnal warm layer include a realistic parameterisation of the absorption of light, especially in the upper 10 m of the water column, where typically $> 50\%$ of total radiation is absorbed (*Dickey and Simpson, 1983; Ohlmann et al., 2000*).

In-situ observations remain useful to validate warm layer models in as many different locations as possible, to test parameter sensitivity, and eventually improve descriptions of modelled fluxes. The vertical profiler ASIP is highly suitable to this purpose, as it measures temperature profiles of the near-surface layer up to the immediate surface. Simultaneously, the strength of turbulent mixing is determined from measurement of the turbulent velocity shear, from which the TKE dissipation rate ϵ is computed. The high-resolution measurements provide detailed information about the vertical temperature distribution of diurnal warm layers, and its variability as a result of ambient vertical mixing conditions. This chapter presents observations from the ASIP in a sub-tropical region, where on multiple days a diurnal warm layer (DWL) was observed. The observed warm layers are compared to the warm layer correction computed by the COARE bulk flux algorithm (sec. 2.2), when given an input of the local bulk meteorological and oceanographic variables.

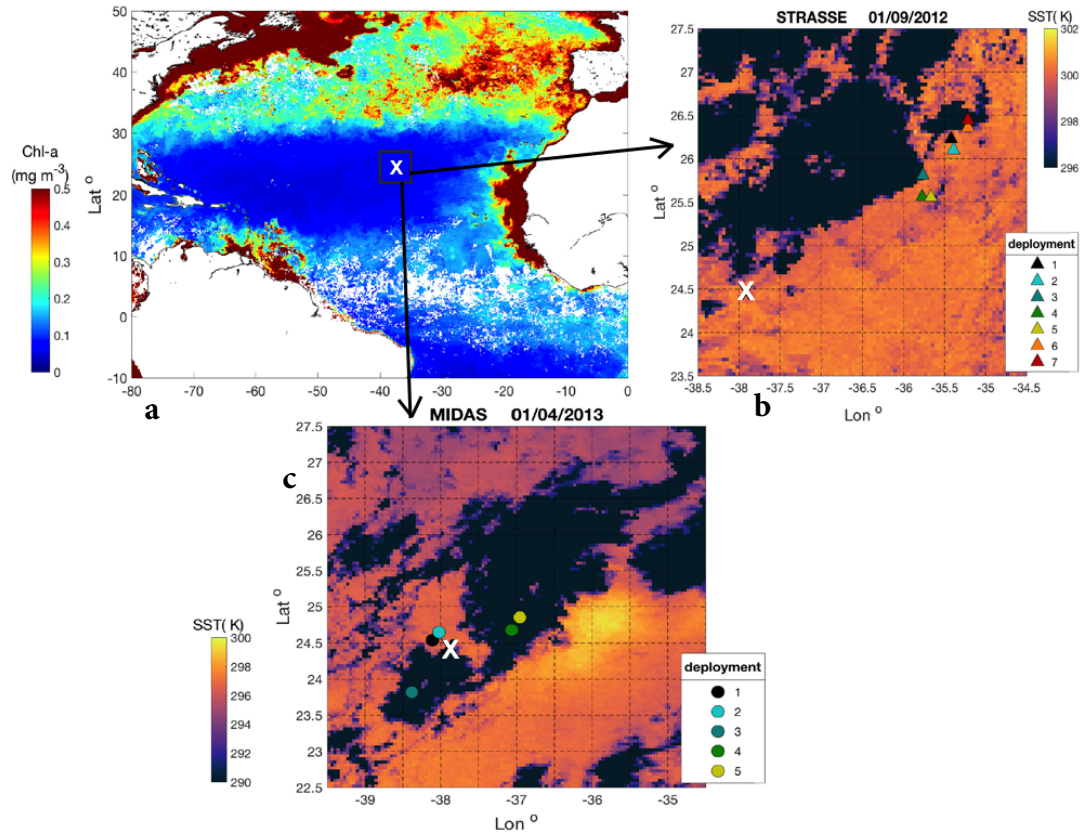
The following section presents the datasets used for the analysis in this chapter. An in-depth description of the observed evolution and vertical distribution of temperature in the near-surface layer is given, as well as of the measured turbulence in this layer. Then the observed diurnal warming is compared to the output of the COARE bulk flux algorithm. Consequently a sensitivity study is conducted to the description of solar radiation absorption in the algorithm. The same model-observations comparison and model-sensitivity study is executed for another oceanic region, the Gulf of Lions in the Mediterranean sea. Here temperature profiles were obtained with the smaller vertical profiler SkinDeEP, alongside radiometric measurements of the skin-temperature, which allow analysis of the cool skin layer.

4.2 Oceanographic Campaigns and Instrumentation

In the autumn of 2012 and the spring of 2013 two ocean research campaigns to the same region in the sub-tropical North Atlantic took place, forming the core of the European contribution to the SPURS-1 project (Salinity Processes Upper ocean Regional Study, see also <http://spurs.jpl.nasa.gov>). The study region, roughly extending from 20-29° N, 34-40° W, is characterised by warm, highly evaporative conditions, and known to contain the salinity maximum of the North Atlantic. The autonomous vertical profiler ASIP (Air-Sea Interaction Profiler) was deployed on both legs of this international field campaign:

1. The STRASSE cruise aboard the French N/O Thalassa (August/September 2012), centred around an anticyclonic current at 26° N, 35.5° W.
2. The MIDAS cruise aboard the Spanish R/V Sarmiento de Gamboa (March/April 2013), centred around 24.5° N, 38° W.

The ASIP, and the sensors with which it was equipped in both campaigns, is largely



Location of the SPURS area in the North Atlantic, and the deployment locations of the ASIP during the STRASSE and the MIDAS campaign, drawn on images of **a** chlorophyll concentration from the MODIS sensor on Nasa's Aqua satellite at 0.1 degree resolution, and **b+c** level 3C SST product at 4 km resolution from the AVHRR Pathfinder (available from <https://neo.sci.gsfc.nasa.gov> and <ftp://ftp.nodc.noaa.gov/pub/data.nodc/pathfinder/Version5.3/> respectively).

Figure 4.1: .

described in sec. 3.2. During the MIDAS campaign the profiler carried both slow C-T sensor packages for calibration of temperature and conductivity, whilst during STRASSE only the integrated NBOSI-sensor was available.

For the STRASSE cruise meteorological information is provided from the optimised combination of measurements aboard the research vessel and an autonomous platform equipped with an air-sea flux sensor package (*Bourras et al., 2014; Reverdin et al., 2015*). The R/V *Thalassa* remained in the vicinity of the ASIP during each of the profiler's deployments, so this record is assumed to well represent the meteorological conditions encountered by the ASIP.

A mooring with a meteorological sensor package, as well as a line of temperature/conductivity loggers (www.seabird.com/products/spec_sheets/39data.htm) down to 400 m depth, was deployed by the Upper Ocean Processes Group at WHOI in the centre of the study region of the MIDAS campaign. This mooring was



Figure 4.2: Photos of the instrumentation used in the SPURS-1 campaigns, from left to right: the ASIP at the surface (photo by L. Gonzalez), the Eddy-Covariance system deployed on the bow of the R/V Sarmiento de Gamboa (photo by S. Landwehr), and the mooring by the Upper Ocean Processes Group of the Woods Hole Oceanographic Institution (WHOI), centrally located in the SPURS region at 24.5° N, 38° W.

operational for a period of 380 days, starting on the 14th of September 2012, as it was deployed towards the end of the first campaign. The meteorological information provided by the mooring thus only supports the spring cruise. The yearlong record is also useful to give insight to the annual pattern in the weather and hydrography of this region. Half of the ASIP profiles during the MIDAS campaign took place within < 20 km of this mooring, and all profiles were within a distance of 85 to 100 km. During the second half of the MIDAS cruise an eddy covariance system was in operation, mounted on a mast that was pointing forward from the bow of the ship (see fig. 4.2). This system consisted of one Gill R3A sonic anemometer and a 3D inertial motion unit, to correct the wind measurements for ship motion (*Miller et al.*, 2009; *Landwehr et al.*, 2015). These high quality in situ measurements of wind speed are used when the distance between the research vessel and the ASIP is smaller than the distance between ASIP and the central mooring. The large dataset from the SPURS campaigns describes an open ocean region of typically low chlorophyll concentration (fig. 4.1).

A third dataset is used in this chapter for the purpose of extending the analysis to a different oceanic region. The dataset consists of upper ocean profiles from three

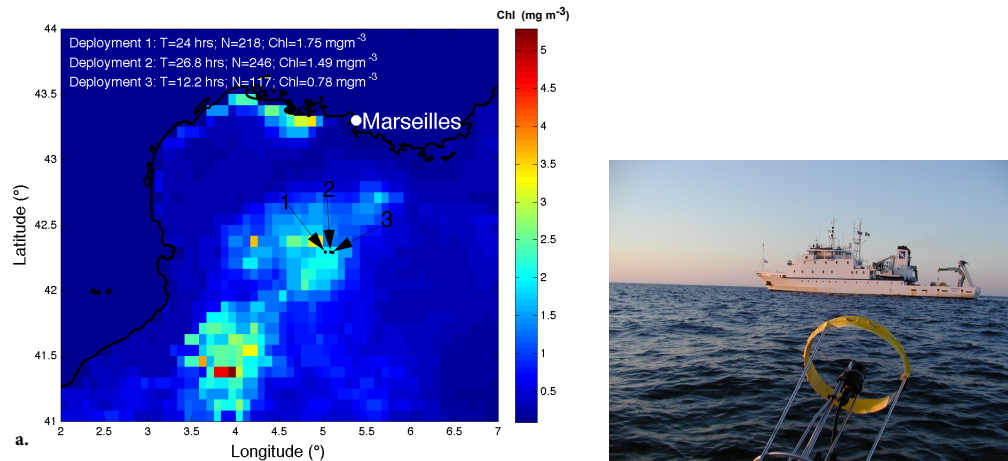


Figure 4.3: **a.** Location of the deployment of SkinDeEP during the NORBAL-5 campaign in the Mediterranean sea in April 2003. The map is overlaid with a SeaWiFS 8-day (15Apr2003 - 23Apr2003) 9-km resolution satellite image of chlorophyll (in mg m^{-3}), showing a strong biological bloom in the area of activity. **b.** Top of the SkinDeEP profiler, with R/V Urania in the background (photo by B. Ward).

deployments of the upwardly rising autonomous profiler SkinDeEP (see *Ward et al.* (2004) for details about this instrument), during a research campaign (NORBAL-5) aboard the Italian vessel R/V Urania in the Gulf of Lions in the Mediterranean sea ($\sim 42^\circ\text{N}$, 5°E , see fig. 4.3). The SkinDeEP profiler was instrumented with the following sensors: an FPO7 thermistor, a micro-conductivity sensor and a 3-channel irradiance sensor (490, 555 and 683nm), all at a sampling frequency of 200 Hz. The profiles from SkinDeEP used here are only shallow (max. depth 8 m). Due to an erroneous configuration of the instrument the upper meter during the second deployment is missing. The research vessel was equipped with a meteorological system, as well as with an instrument to measure the ocean skin temperature: the Marine-Atmosphere Emitted Radiance Interferometer, M-AERI, see *Minnett et al.* (2001). As the ship remained 100 m behind SkinDeEP throughout each deployment, both the M-AERI measurements as well as the meteorological forcing parameters from onboard measurements provide highly localised information to the subsurface record.

The Mediterranean water is expected to have different optical properties, as the region was subject to spring blooms of phytoplankton during the sampling time. In-situ chlorophyll concentration measured simultaneous to deployments of SkinDeEP range from 0.8 to 2.1 mg m^{-3} in the upper 10 m.

4.3 Observations

4.3.1 Oceanographic and Atmospheric Conditions

North Atlantic

The two SPURS campaigns are characterised by warm conditions, as the near-surface seawater temperature in this region is above 20 °C year round. To illustrate the variability in the average conditions, Figure 4.4 shows the yearlong record of daily peak insolation ($Q_{SW\ max}$), wind speed (U), air temperature (T_a) relative humidity (RH) and rain rate (R), as well as the temperature T , salinity S and potential density σ in the top 250 m recorded by the central WHOI mooring. The temporal resolution of all variables is reduced by computing 1-day bin-averages. The meteorological variables are then further smoothed using a 1-month moving average window. This results in an overview of the annual variability at the study site. This sub-tropical location is not subject to large differences between seasons. The daily peak in insolation is seldom below 600 W m⁻², and peaks to nearly 1000 W m⁻² during boreal summer. Rain rates in the area are generally low, though precipitation occurs during the winter months. Monthly mean wind speeds are moderate, during this year the highest wind speeds were measured in November and December.

The salinity record (and consequently the computed σ) of 4 sensors in the upper 10 m, as well as at 45, 80 and 200 m, is incomplete. In the time-depth overview in fig. 4.4 these data gaps have been filled using linear interpolation. The colourmap is scaled such as to emphasise the mixed layer variability, and the depth of the seasonal mixed layer (MLD_s) is indicated by a dashed line. It is computed as the level where σ has increased by 0.05 kg m⁻³ compared to the density at a reference depth of 10 m, following *de Boyer Montegut et al.* (2003). The seasonal mixed layer is shoaling from early spring onwards, to reach its minimal level during the summer months, remaining shallow until deepening starts in September/October. The onset of MLD deepening coincides with the annual maximum SST over the mixed layer. The period of time during which the observations of the spring cruise took place is indicated, showing that the campaign coincided with a period of “thermal restratifying conditions”: elevated Q_{SW} is high (up to the summer-level), and low wind speed. This is reflected in a high SST and the rapid shallowing of the mixed layer depth during the first half of the campaign, to a level which is not yet sustainable for the time of year, such that during the first week of April the mixed layer is seen to deepen again.

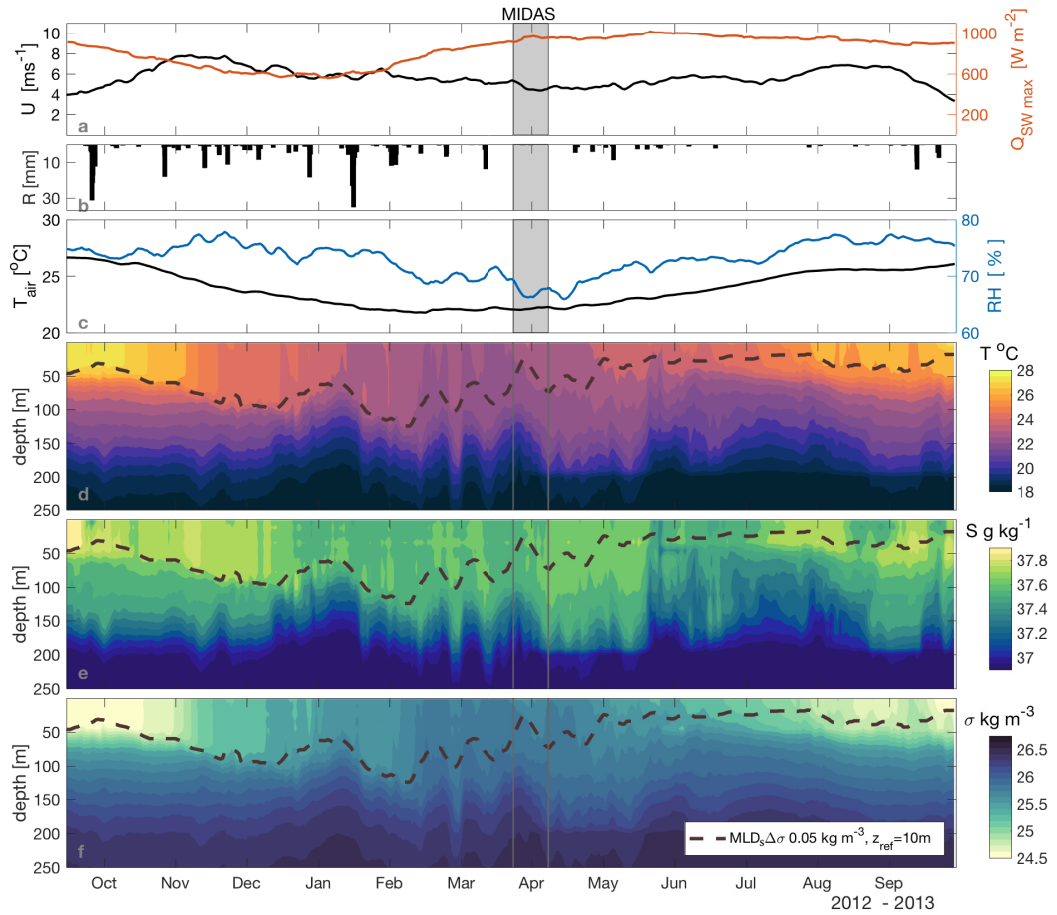


Figure 4.4: Yearlong record of the central WHOI mooring in the SPURS area (24.5°N, 38°E). **a.** Daily mean wind speed U and peak solar radiation Q_{SWmax} , **b.** hourly rain rate R and **c.** air temperature T_a and relative humidity RH . **d-f.** Contour plots of temperature T , salinity S and potential density σ in the upper 250 m of the ocean respectively, with the black dashed line showing the depth of the seasonal mixed layer.

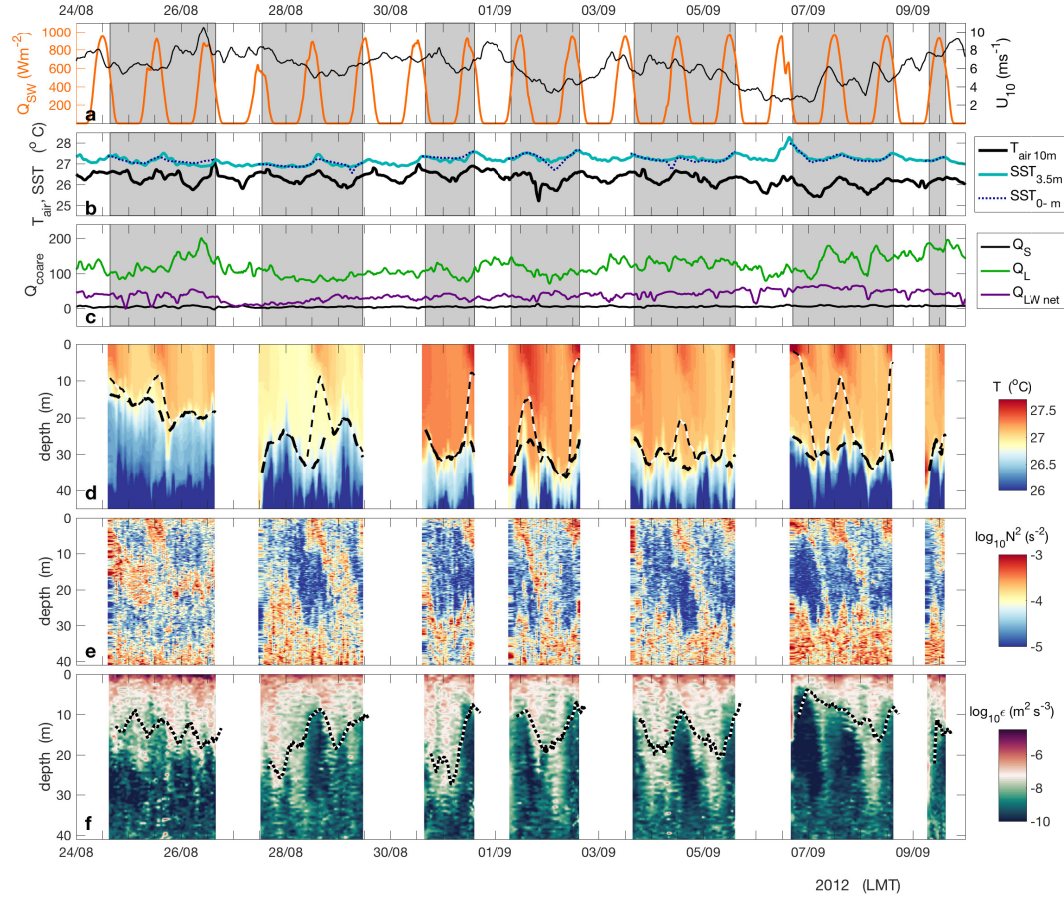


Figure 4.5: Conditions during the STRASSE cruise in August/September 2012. **a.** Downwelling shortwave radiation (orange) and 10m- wind speed (black). **b.** Air temperature from the shipboard meteorological sensors (at 10 m above the sea surface) and seawater temperature measured at the ship intake at ± 3.5 m depth and just below the surface by ASIP. **c.** Surface fluxes of sensible heat (black), latent heat (green) and net longwave radiation (purple), positive when out of the ocean. **d.** Contours of temperature T in the upper 45 m derived from ASIP profiles, black-and-white dashed line indicating the surface mixed layer depth, defined as the level where T is 0.2 °C less than at a depth of 0.5 m. The black dashed line corresponds to the seasonal mixed layer depth. **e.** Buoyancy frequency N^2 . **f.** Turbulent kinetic energy dissipation rate ϵ , with dotted line corresponding to the depth below the surface at which $\epsilon \leq 3 \times 10^{-9} \text{ W kg}^{-1}$. Shaded areas in panels a - c coincide with the deployment periods of the ASIP.

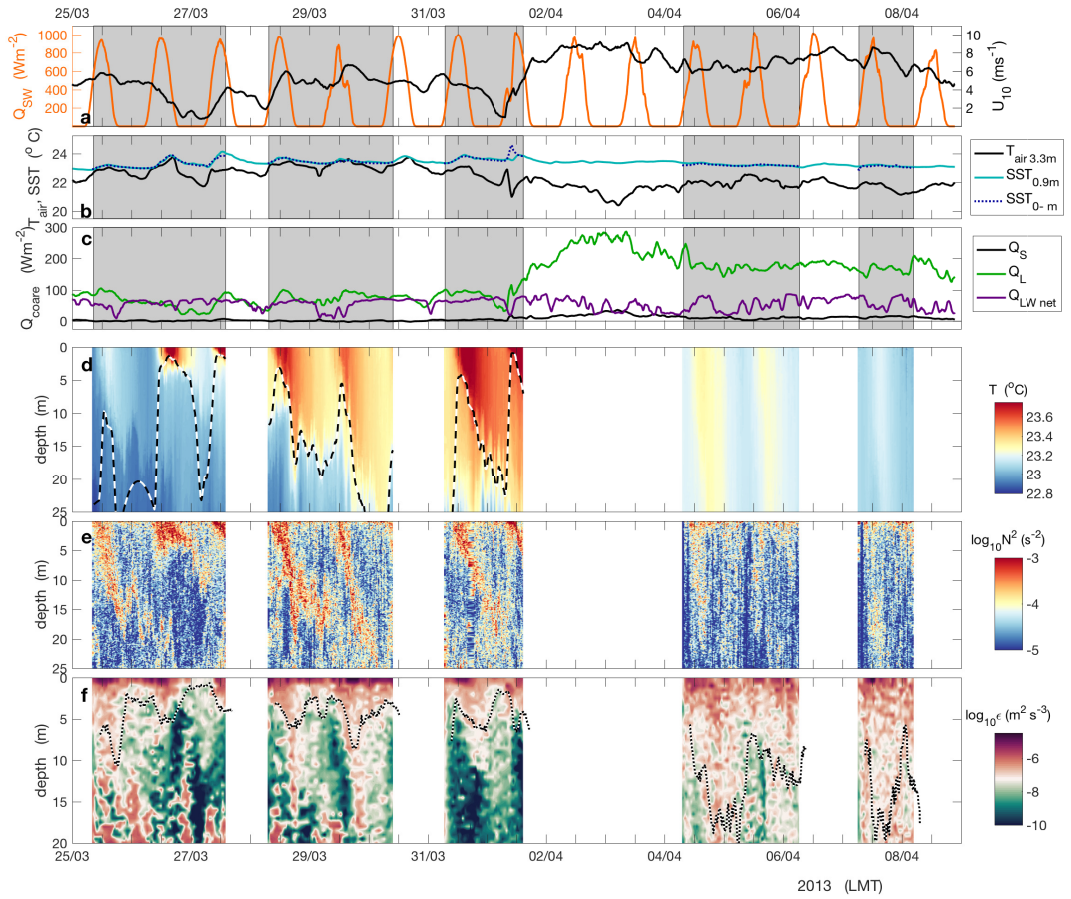


Figure 4.6: Conditions during the MIDAS - cruise in March/April 2013. **a.** Downwelling shortwave radiation (orange) and 10m- wind speed (black). **b.** Air and seawater temperature measured at the central mooring and just below the surface by ASIP (respectively at 3.3 m above the sea surface, 0.9 m and 5 cm depth). **c.** Surface fluxes of sensible heat (black), latent heat (green) and net longwave radiation (purple), positive when out of the ocean. **d.** Contours of temperature T in the upper 25 m derived from ASIP profiles, dashed line indicating the depth where T is reduced by $0.2\ ^\circ C$ compared to $T_{0.5m}$. **e.** Buoyancy frequency N^2 . **f.** Turbulent kinetic energy dissipation rate ϵ , with dotted line corresponding to the depth below the surface at which $\epsilon \leq 10^{-8} W kg^{-1}$. Shaded areas in panels a-c coincide with the deployment periods of the ASIP.

In fig. 4.5 and 4.6, time series of meteorological data, as well as observations of the near-surface layer obtained with the ASIP, during each of the campaigns in the SPURS region are shown. This provides a means to study the day-to-day variability in the meteorological forcing and the consequent response of the upper ocean. The time series of meteorological data at 5 min time resolution have been smoothed with an approximately 60 min moving average window.

The wind regimes of the autumn and spring campaign differ somewhat: during STRASSE the 10-m wind speed was gradually varying about an average of $6.2 \pm 1.7 \text{ m s}^{-1}$ for the duration of the campaign, whilst the MIDAS campaign saw a distinctive period of low wind ($U_{10} = 0.5 - 4.5 \text{ m s}^{-1}$) during the first week, followed by a week of moderate to high winds ($\overline{U}_{10} \sim 7 \text{ m s}^{-1}$). During the first half of the MIDAS campaign the air-sea temperature difference is close to zero during daytime, whilst the sea is generally 1-2°C warmer than the air during the second half of the campaign, as well as during STRASSE.

The 5 min records of atmospheric variables and bulk-*SST* from a depth of 3 m are used to compute the surface heat fluxes using the COARE 3.0 algorithm. These are plotted in panel c. of fig. 4.5 and 4.6. From (2.17) it follows that the magnitude and sign of the surface heat fluxes is determined by the air-sea difference in temperature and humidity respectively, whilst the fluxes will be enhanced by the wind speed. The relatively constant $\Delta T_{sea-air}$ and wind speed during STRASSE result in a Q_S of $5 \pm 2 \text{ W m}^{-2}$ and a little more variable Q_L of $120 \pm 25 \text{ W m}^{-2}$. The average net longwave cooling is $38 \pm 15 \text{ W m}^{-2}$. During the first half of the MIDAS campaign Q_S is close to zero, increasing up to 30 W m^{-2} when the wind regime changes on April 2nd. The latent heat flux at first is also lower than during STRASSE ($70 \pm 20 \text{ W m}^{-2}$), however this heat flux increases up to 270 W m^{-2} . During the first half of the campaign Q_{LWnet} is of the same order of magnitude as Q_L , and shows clear minima at nighttime. Its variability increases during the second half of the campaign. Even though the SST in MIDAS is a few °C lower than during STRASSE, the net longwave cooling during MIDAS is stronger. A possible explanation for this can be found in the presence of cloud during STRASSE, which would re-emit some longwave radiation down to the ocean surface. Clear evidence of cloud is found in the reduction of both Q_{SW} and Q_{LWnet} on 27/08 in Fig. 4.5 a and b.

During the autumn campaign the ASIP was deployed on 8 occasions, resulting in a total of 569 of profiles, of which 7 deployments are presented in this study. Deployments lasted between 24 and 48 hours. However, since they were rarely started in the morning, only 5 complete diurnal cycles are sampled. The profiler sampled down to 60 m at a frequency of 3 times per hour. The mean mixed layer depth in autumn was located between 25 – 40 m, so the ASIP profiles captured both the mixed layer and part of the thermocline below it (fig. 4.7 a). The seasonal mixed layer depth MLD_s is included on the contour plot of temperature in the upper 40m in fig. 4.5d following the same criterion as on fig. 4.4. On the same panel another line indicates the depth of the surface mixed layer (MLD_0 , here defined from the temperature profiles only), to be the depth where the temperature is reduced by 0.2 °C compared to the temperature 0.5 m below the surface. This

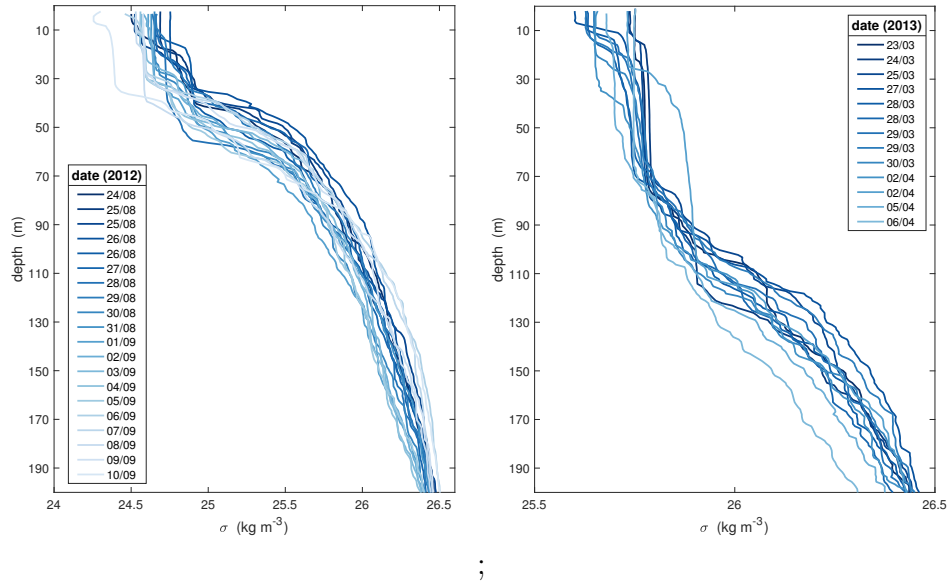


Figure 4.7: Potential density σ in the upper 200 m. as observed from daily (nighttime) CTD-casts during **a.** the STRASSE campaign and **b.** the MIDAS campaign. The MIDAS casts are from the R/V Endeavor, data available via <ftp://podaac-ftp.jpl.nasa.gov/allData/insitu/L2/spurs1>.

method was used in *Sutherland et al.* (2016) to characterise the MLD, and roughly corresponds to the depth over which diurnal warming can be observed. Another measure to characterise the depth of the surface layer is to determine the depth of active mixing, XLD from the measurement of the dissipation of turbulent kinetic energy ϵ . In fig. 4.5 and 4.6f the XLD is drawn on the contour plot of measured ϵ . During the spring campaign the seasonal mixed layer depth was expected to be a lot deeper (although, as shown in fig. 4.4 and 4.7b it experienced a phase of strong shallowing at the time of the experiment). Since the ASIP's depth limit restricts profiling beyond 100 m, during the MIDAS campaign it was chosen to profile to a depth of 30 or 40 m only. This allowed deployments of a longer consecutive period of time and with a higher frequency of profiles per hour. Panel d in fig. 4.6 therefore only shows the depth of MLD_0 . The ASIP was deployed on 5 occasions, acquiring a total of 676 profiles. An improved deployment strategy ensured that the deployments lasted 36 to 50 hours, and that 8 complete diurnal cycles were sampled.

Mediterranean

The meteorological conditions and heat fluxes during the Mediterranean campaign are shown in fig. 4.8. During the 4-day experiment in this region there was considerable insolation, with peak values of Q_{SW} reaching over 800 W m^{-2} each day. After an initial decrease in wind speed for the first two days from 6 to 2 m s^{-1} on average and to a minimum of 0.5 m s^{-1} around noon on the 22nd of April, the wind speeds increased gradually up to 8 m s^{-1} on the third day that SkinDeEP was deployed. There is a significant discrepancy between T_a from the

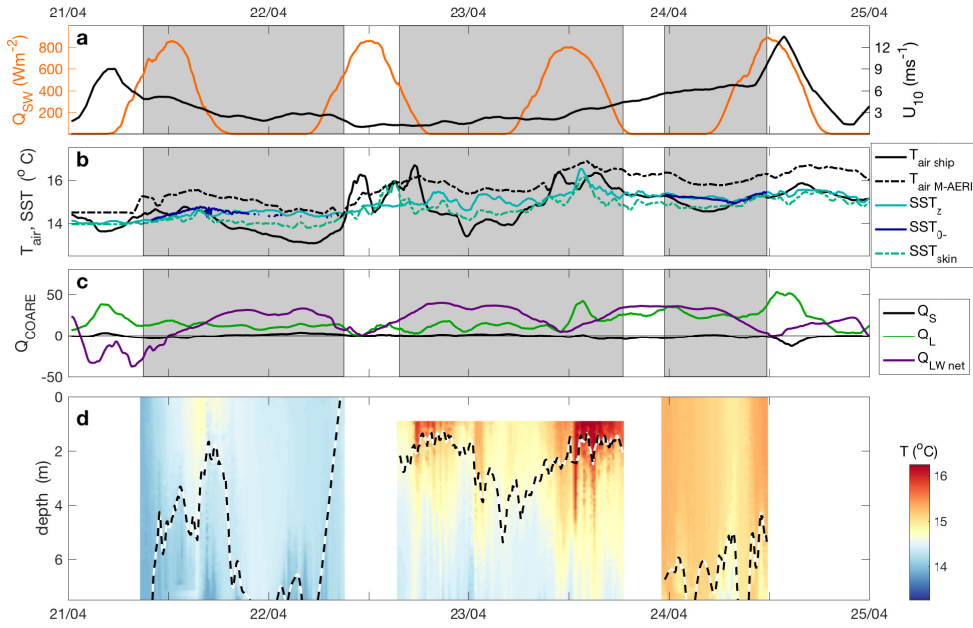


Figure 4.8: Conditions during the NORBAL-5 cruise in April 2003. **a.** Downwelling shortwave radiation (orange) and 10 m-wind speed (black). **b.** Air temperature from the shipboard meteorological sensors (at ~ 10 m above the sea surface) and the infrared radiometer M-AERI, SST measured in ship intake water, as well as just below the surface by SkinDeEP where available, and the T_{skin} by the M-AERI. **c.** Surface fluxes of sensible heat (black), latent heat (green) and net longwave radiation (purple), defined positive when *out* of the ocean. **d.** Contour plot of the temperature T in the upper 8 m. of the water, derived from SkinDeEP profiles during three deployments. The dashed line indicates the surface mixed layer depth, defined as the level where T is 0.2 $^{\circ}C$ less than at a depth of 0.5 m. Shaded areas in panels a - c. coincide with the deployment periods of the SkinDeEP profiler.

ship's meteorological system and the infrared radiometer M-AERI. This is further discussed in section 4.6.3. The SST increased about 1 $^{\circ}C$ during the experiment, and the highest temperatures at all depths are recorded during the calm days. The heat fluxes computed with the COARE model result an input of T_a from the ship and the T_{skin} from the M-AERI. Due to the small air-sea temperature difference they are very small; the net longwave cooling during nighttime is at most 75 $W m^{-2}$.

4.3.2 Observed Near-Surface Warming

Figures 4.5d and 4.6d indicate the regular development of a DWL in the SPURS area. Also during three days of the NORBAL-5 campaign a DWL can be observed, with remarkably high warming in the upper 4 m during two days.

To describe the observed warm layers the temperature just below the sea surface T_{0-} , and at several depth levels is evaluated, as well as the maximum depth extent and the phase of the diurnal temperature signal. The magnitude of the diurnal warming has a significant variability between the campaigns, and between days of each campaign individually. The temperature evolution at subsurface level, as well as at 1, 2, 3, 5, 10, 15 and 20 m can be more precisely studied from fig. 4.9c, 4.10e, and 4.10f. During the STRASSE campaign the forcing conditions were variable, wind speeds during this cruise ranged from 2-10 m s^{-1} , though moderate wind speeds of $\overline{U}_{10} = 6 \text{ m s}^{-1}$ prevailed during most days on which a complete diurnal cycle was observed. The change in regime from low to moderate/high winds occurring during the MIDAS campaign, requires the use of a different temperature range on the vertical axis of 4.10 for deployment 1-3 (e) and 4-5 (f) respectively. The variability in the forcing is reflected by differences in the magnitude of the warming, as well as in the vertical structure of the warm layer. At the surface the daily range of SST varies from 0.15 to 1 °C. On most days when a DWL is formed, there is a lag in the SST evolution at increasing depth, resulting in the gradual deepening of the diurnal thermocline.

Three different regimes in diurnal warming as a function of wind forcing can be identified from the observations:

1. Low winds, resulting in a strong shallow thermal stratification.

Warming of the surface starts once the surface buoyancy flux B_0 becomes positive. The highest amplitude of warming is observed in the top 2.5 m, and deeper levels only show a weak temperature fluctuation. This is observed on 26/3 (ASIP deployment 1), when wind speeds are less than 1 m s^{-1} . The maximum ΔT_{0-} of nearly 1 °C occurs nearly 5 hours after local noon. The continuing calm conditions result in stratification that remains overnight; the following day the DWL develops within this remnant warm layer. This can clearly be inferred from the temperature profile evolution in fig. 4.14. The observed warming on the calmest day of the STRASSE cruise (6/9) is similar with $\Delta T_{0-} \sim 0.8 \text{ °C}$ and a DWL still present at midnight, although wind speeds on this day are around 2 m s^{-1} .

2. Moderate winds, forming a diurnal mixed layer.

When wind speeds range from 1.5 - 6 m s^{-1} , the solar heating is trapped in a surface mixed layer, approximately 5 m deep, and a thermocline which deepens further once B_0 changes sign. As shown in fig. 4.9 a, as well as fig. 4.10a and 4.10b, this occurs before sunset (before Q_{SW} becomes zero). The amplitude of the diurnal signal in T_{0-} is 0.3-0.5°C, and the peak temperature at the surface occurs 2-3 hours after local noon. This pattern was observed on the 25/08, 28/08, 04/09, 06/09, 07/09 and 08/09 during STRASSE, as well as on 25/03, 28/03, 29/03 and 31/03 during MIDAS.

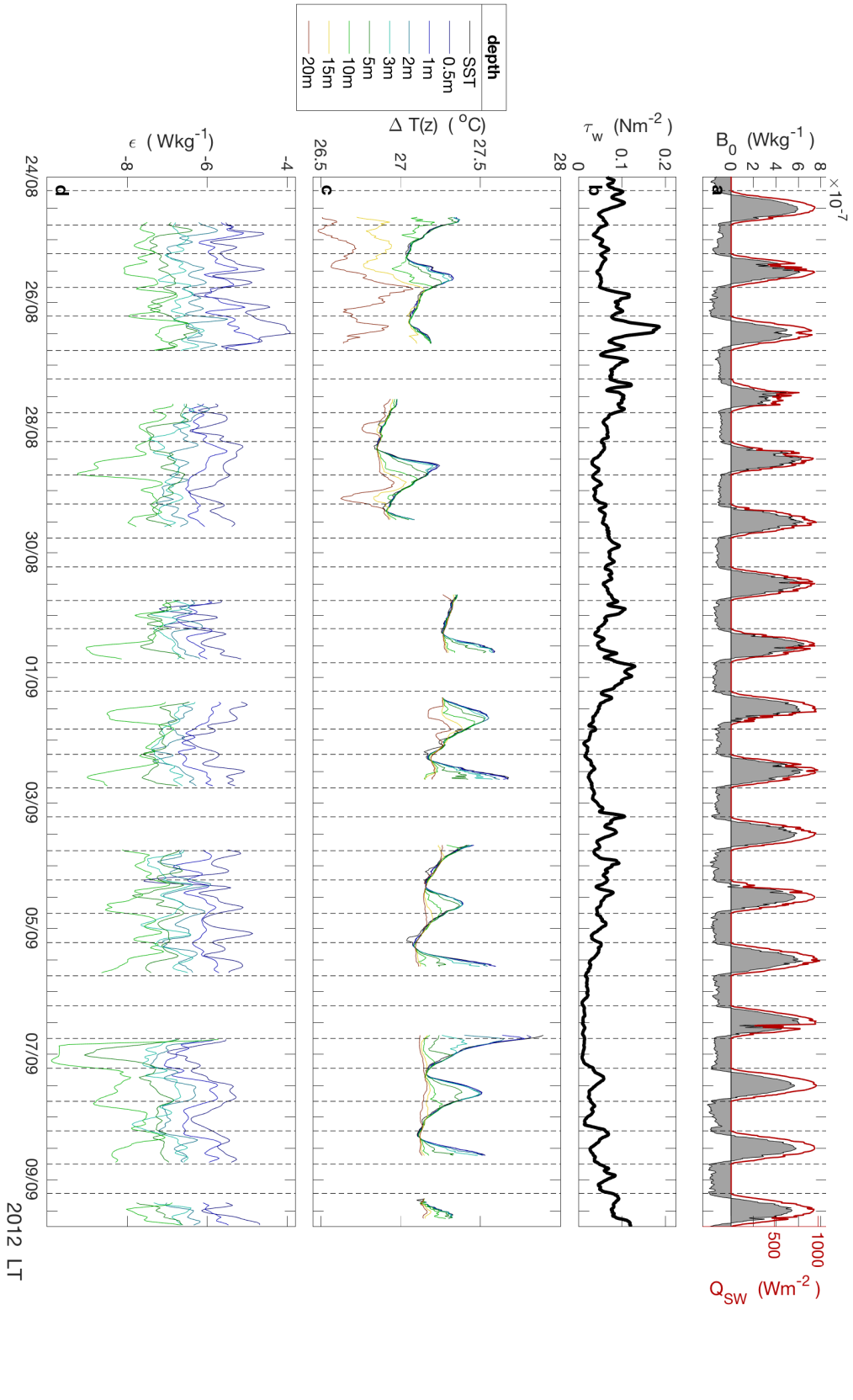


Figure 4.9: Time series from the STRASSE campaign of: **a.** Downwelling shortwave radiative flux Q_{sw} and surface buoyancy flux B_0 ; **b.** Surface wind stress τ ; **c.** SST observations from ASIP just below the surface (T_{0-} and 8 depth levels below it); **d.** TKE dissipation rate ϵ observed with ASIP at 6 depth levels below the surface. Vertical dashed lines in each panel indicate the time when Q_{sw} becomes positive in the morning / negative at the end of the day.

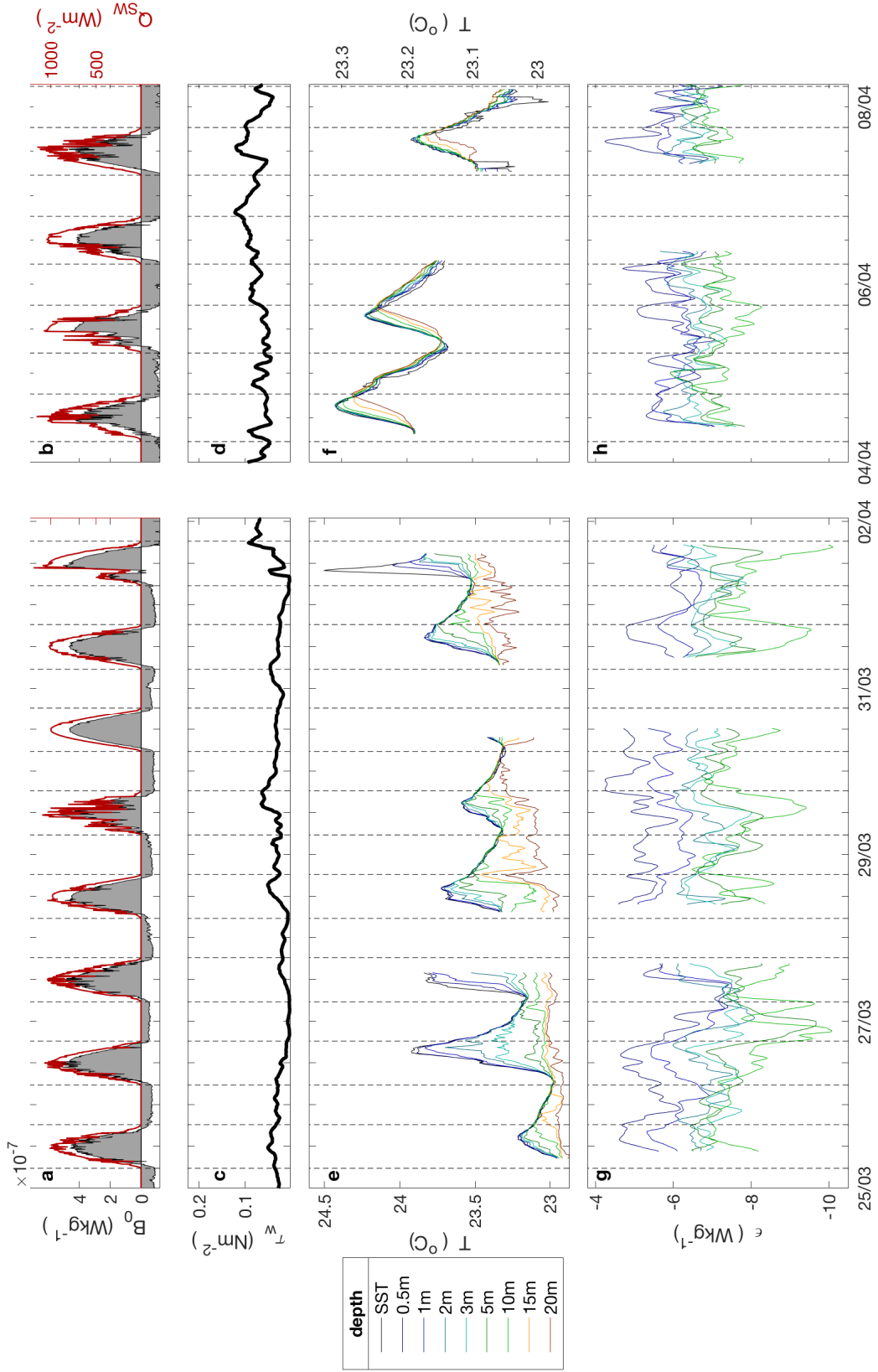


Figure 4.10: Time series from the MIDAS campaign of: **a.** Downwelling shortwave radiative flux Q_{SW} and surface buoyancy flux B_0 ; **b.** Surface wind stress τ ; **c.** SST observations from ASIP just below the surface (T_{0-} and 8 depth levels below it); **d.** TKE dissipation rate ϵ observed with ASIP at 6 depth levels below the surface. Vertical dashed lines in each panel indicate the time when Q_{SW} becomes positive in the morning / negative at the end of the day.

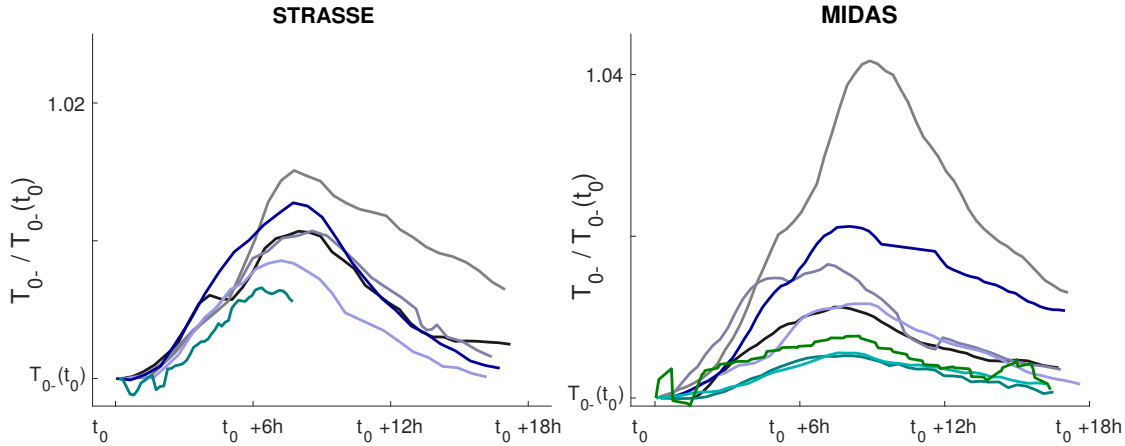


Figure 4.11: T_{0-} normalised to its value at $t = t_0$, the time when the surface buoyancy flux becomes positive in the morning, as observed by the ASIP on 6 and 8 days during the two SPURS campaigns respectively.

3. Higher wind speed ($> 6 \text{ m s}^{-1}$), resulting in a quasi-homogeneous mixed layer. During the higher wind speed conditions the diurnal warming signals observed at the surface are of small magnitude $O(0.1^\circ\text{C})$. The warming occurs throughout the full depth of the mixed layer, with only a small time shift between the surface and 20 m. This occurs on the 26, 27, 30/8 and 9/9 during STRASSE, as well as in the second half of the MIDAS campaign (observations on the 4th, 5th and 7th of April 2013).

There is an interesting transition from regime 1 to regime 3 during the third deployment of ASIP (fig. 4.10). A surface warming of similar high magnitude as on 26/03 is observed in the morning of 01/04, however the maximum ΔT_{0-} occurs before the peak in B_0 . A passing weather system causes a brief reduction in the solar radiation around 10 AM, as well as a burst of wind. This results in a sudden break-down of the stratification in the upper 5 m. The buoyancy flux returns back to its clear-sky level at noon, however a gradual increase in U_{10} leads to the hypothesis that T_{0-} is not restored to its earlier level, since the enhanced mixing persists. Unfortunately, the ASIP deployment ended at 14:50 h local time, so this has not been verified.

To illustrate the phasing of the warming at the surface, fig. 4.11 focuses on the subsurface temperature. For several days of both Atlantic campaigns the evolution of T_{0-} normalised by its value at $t = t_0$, the time that the buoyancy flux becomes positive, is plotted from t_0 until the hour corresponding to midnight. It clearly shows that there is a positive correlation between the time of peak warming, and the amplitude of the warming at the surface.

4.3.3 Remnant Warm Layers and Irregular Warming

The schematic view of the diurnal cycle of the temperature of the upper ocean describes the daily disappearance of the warm anomaly, due to vertical mixing by nighttime convection and the surface momentum flux from wind and waves (see fig.

2.5). The concept of a foundation- T assumes that at a certain depth below the surface T is free from diurnal variability, and that this temperature corresponds to the temperature of the nighttime, well mixed layer (*Donlon, 2003; Kawai and Wada, 2007*). However, the observations show that the upper ocean does not totally behave according to the model schematics. During the first half of the MIDAS campaign, when wind speeds are low to moderate (regime 1 and 2), there is not enough energy available to fully mix the upper 20 m during nighttime. The consecutive warm layer develops on top of a remnant stratification. Temperature profiles in fig. 4.14 for the 26 - 29th of March, as well as the 31st of March to the 1st of April, illustrate such a remnant diurnal thermocline, between approximately 15 and 20 m depth. The diurnal stratification of the following day develops on this remnant warm layer. As a result the foundation- T depth becomes ambiguous on these days.

Although on many days the warming is contained in a well mixed layer, the temperature profiles at times deviate from any of the shapes described in fig. 2.6. Examples of profiles containing a staircase-like fine structure are shown in fig. 4.15. These occur after the development of a new warm layer on top of the previous day's remnant thermocline, or can be the result of overturning events, which gradually deepen the DWL during the second half of the day (*Soloviev and Lukas, 2014*). The continuously changing conditions throughout the day can also contribute to the formation of these staircase-like structures within the warm layer. Staircase-like profiles are often an indication of double diffusive mixing (*Walesby et al., 2015*).

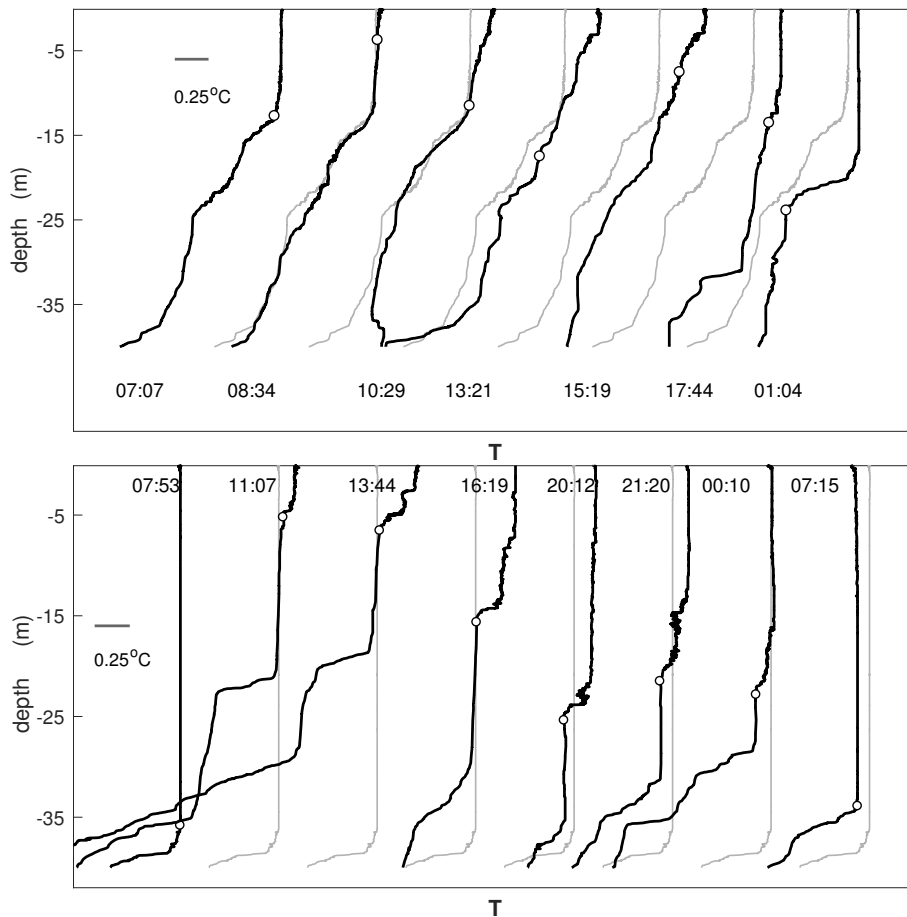


Figure 4.12: Sequence of individual temperature profiles from ASIP on selected days during the STRASSE campaign when a DWL was observed. White dot indicates the depth of the warm layer D_{w0} in each profile. To illustrate the change, the first profile in each series is re-plotted in grey next to each consecutive profile.

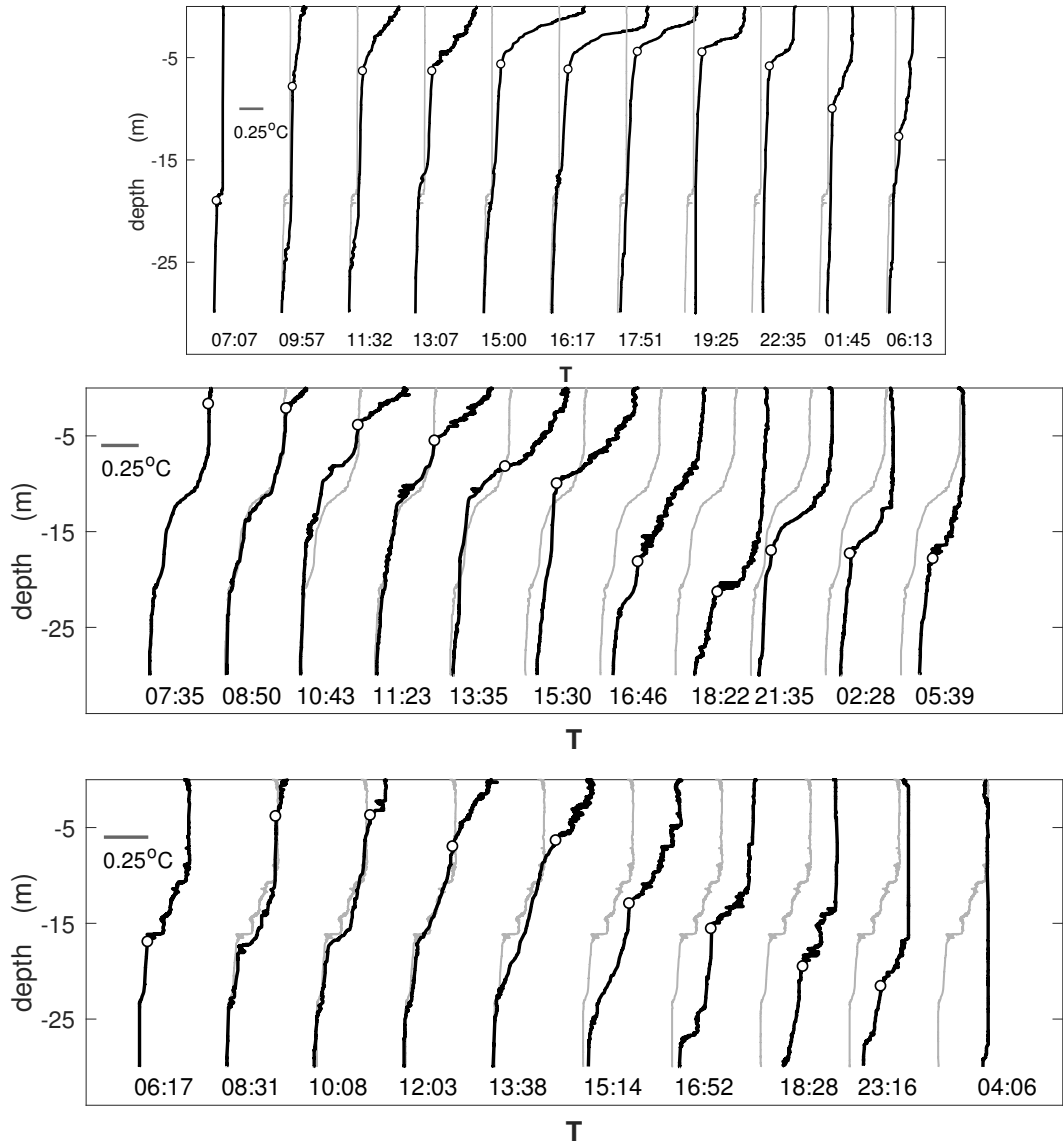


Figure 4.13: Sequence of individual temperature profiles from ASIP on selected times and days of the MIDAS campaign when a DWL was observed. A remnant diurnal thermocline is present overnight after both 26/3 and 28/3. White dot indicates the depth of the warm layer D_{w0} in each profile. To illustrate the change, the first profile in each series is re-plotted in grey next to each consecutive profile.

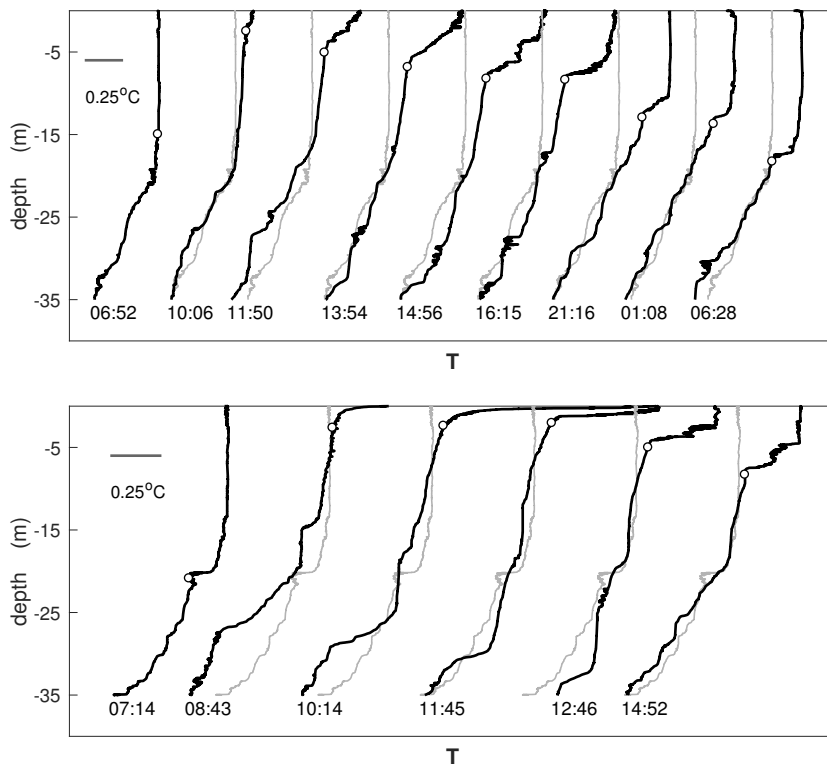


Figure 4.14: Sequence of individual temperature profiles from ASIP on two consecutive days of the MIDAS campaign between which a remnant diurnal thermocline was observed. White dot indicates the depth of the warm layer D_{w0} in each profile. To illustrate the change, the first profile in each series is re-plotted in grey next to each consecutive profile.

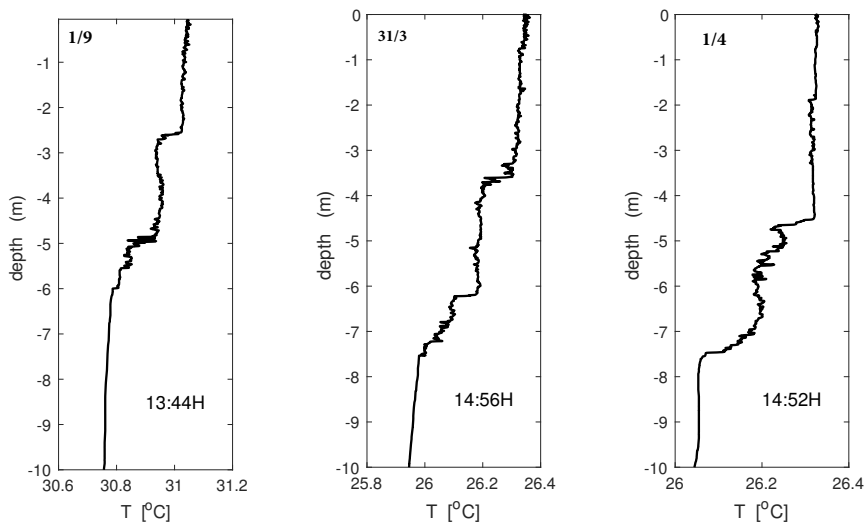


Figure 4.15: Close-up on the upper 10 m of profiles with staircase features.

4.4 Warm Layer Depth Definition

In sec. 4.6 and 4.7 the observed DWLs will be compared to the warm layer correction from the COARE model. One of the two warm layer descriptors from the model output is the depth of the warm layer, D_w . It is therefore desirable to find a robust estimator for this depth in the observations. However, the variation in profile shapes, and the presence of remnant warm layers makes the determination of the warm layer depth from measured temperature profiles somewhat subjective. As a starting point the microstructure variability is filtered out of the measured temperature profiles by reducing their vertical resolution to 10 cm using bin-averaging. To further smooth the profile a 5-point moving average is used. Consequently several systematical methods to determine the depth of the warm layer, D_w from the smoothed temperature profiles have been tested:

1. D_w is the depth where the temperature difference, compared to the temperature at 0.5 m below the surface, exceeds a specific threshold. This method is regularly used for the determination of MLD_0 , the surface mixed layer depth (Weller *et al.*, 2002; Kara *et al.*, 2000; de Boyer Montegut *et al.*, 2003), and also specifically for the STRASSE dataset in Sutherland *et al.* (2016). This is the MLD drawn on the temperature contours in Figures 4.5, 4.6 and 4.8.
2. Another threshold criterion searches for the depth where the vertical temperature gradient $\partial T/\partial z$ is larger than a certain threshold value (Thomson and Fine, 2003).
3. The depth extent of the surface warming is largely dependent on the present turbulent mixing. Therefore D_w could be equal to the depth of active mixing, XLD .
4. D_w is computed as the depth where the temperature anomaly T'' , with respect to a pre-heating near-surface foundation-T for each individual day, $\overline{T_{ref}}$ (average over upper 0.5 m), drops below a certain percentage of the maximum T''_{max} of each profile. This method is inspired on the determination of the depth of rain-induced freshwater lenses in Drushka *et al.* (2014).

To accurately describe the temperature difference over the warm layer, D_w needs to correspond to the bottom of the diurnal thermocline. For a subset of the North Atlantic data (418 profiles), each individual temperature profile has been visually examined to determine the warm layer depth. This depth is indicated on the individual profiles in fig. 4.12, 4.14. This depth, D_{w0} , has then been compared to the warm layer depth determined via the four systematic methods 1, 2, 3 and 4, using different values of temperature thresholds ΔT , $\Delta T/\Delta Z$, ϵ thresholds to define XLD , and percentages of T''_{max} respectively. In fig. 4.16 the result of these methods is drawn on the temperature contours of three days with clear warm layers.

Method 1 with a threshold criterion of $\Delta T = 0.1 - 0.2$ °C seems an accurate descriptor during strong warming/ low wind speed conditions, which prevailed during the first three deployments of MIDAS. The depth of the warmest layer was captured by this threshold, however the morning DWL was not that well captured in the moderate wind speed conditions which prevailed during the STRASSE

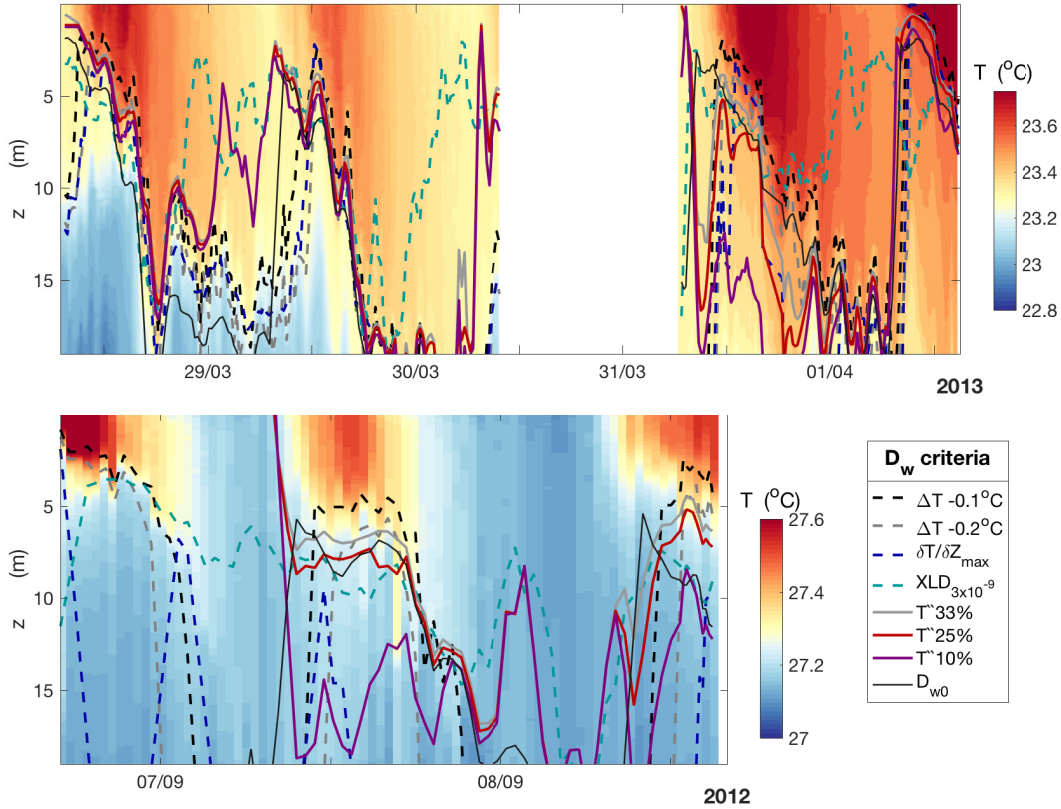


Figure 4.16: Observed temperature during the 2nd and 3rd deployments of the MIDAS campaign (a) and the 6th deployment of ASIP during STRASSE (b), with a selection of all tested criteria for D_w

campaign (fig. 4.16b). To find a robust threshold value of $\partial T/\partial Z$ in Method 2 has proven difficult. Instead it was found that the local maximum in the vertical temperature gradient is a good estimator for D_w for the MIDAS dataset. However when temperature profiles contain both a warm surface mixed layer, and the seasonal thermocline, this method often finds the latter, as can be seen in panel b of fig. 4.16. The depth of active mixing (Method 3) is a good indicator of D_w also, using an ϵ threshold of $10^{-8} - 10^{-9} \text{ W kg}^{-1}$. Method 4 is the most accurate in describing the shallow warm layer in the morning. A threshold anomaly percentage of 33% or lower is considered suitable in estimating D_w , and the 25% seems to perform best, since it most often coincides with the bottom of the newly formed diurnal thermocline in the morning and early afternoon, when the gradient over this thermocline is the largest.

The spread between the methods increases significantly for the nighttime hours. One could argue that the DWL is not defined during this part of the cycle, although a warm layer formed during daytime hours sometimes persists. To evaluate the methods further, a linear regression between each of the above systematic methods and D_{w0} is made of all data between 9 : 00 h and 18 : 00 h, for each of the two North Atlantic campaigns. An RMS error between each “systematically” determined

method	$RMS_{STRASSE}$ (m)	RMS_{MIDAS} (m)	\overline{RMS} (m)
1a. $D_{\Delta T 0.1^\circ C}$	10.66	6.89	8.75
1b. $D_{\Delta T 0.2^\circ C}$	13.50	8.01	10.72
2. $D_{\Delta T/\Delta Z_{max}}$	14.85	8.71	11.74
3a. $XLD_{3 \times 10^{-9}}$	4.65	3.93	4.29
3b. $XLD_{10 \times 10^{-8}}$	4.75	5.52	5.14
4a. $D_{T''33\%}$	5.34	4.23	4.78
4b. $D_{T''25\%}$	5.72	4.48	5.10
4c. $D_{T''10\%}$	8.90	6.21	7.54

Table 4.1: RMS-error between the systematically determined warm layer depth and the visually determined depth D_{w0} in n temperature profiles from the two SPURS datasets ($n_S = 225$, $n_M = 231$).

warm layer depth D_{wX} and the visually determined D_{w0} is computed as:

$$RMSe = \sqrt{(D_{wX} - D_{w0})^2} \quad (4.1)$$

From the linear regression in fig. 4.17 and 4.18 it appears that using a threshold temperature ΔT is not a very robust estimator for D_w , since in the majority of cases the used thresholds of 0.1 and 0.2 °C both underestimate the depth of the warm layer. The same can be said about the maximum temperature gradient ($\partial T/\partial Z_{max}$) in the MIDAS dataset; for the temperature profiles in STRASSE this method is not suitable, as discussed earlier.

Methods 3. and 4. result in the smallest RMS errors (see also Table 4.1). Both the mixing layer XLD (here tested for two ϵ -thresholds), as well as the depth of $T''33\%$ and $T''25\%$ have the least spread in fig. 4.18, especially for the MIDAS campaign. The last one consistently underestimates D_{w0} by 1-2 m, apart from some larger differences during the period of higher winds.

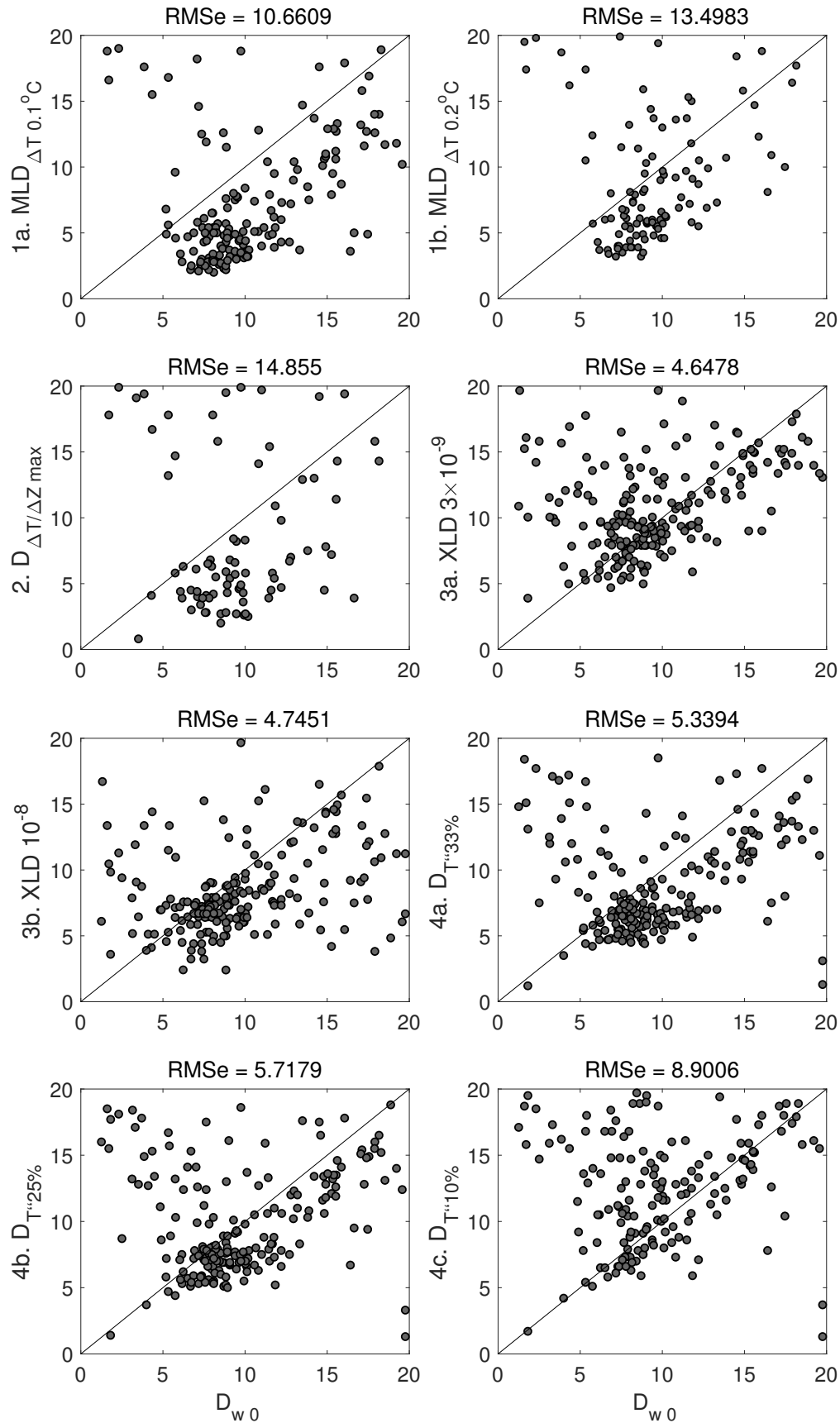


Figure 4.17: Comparison of visually determined warm layer depth D_{w0} [m] versus various systematical methods for 225 profiles from the STRASSE campaign.

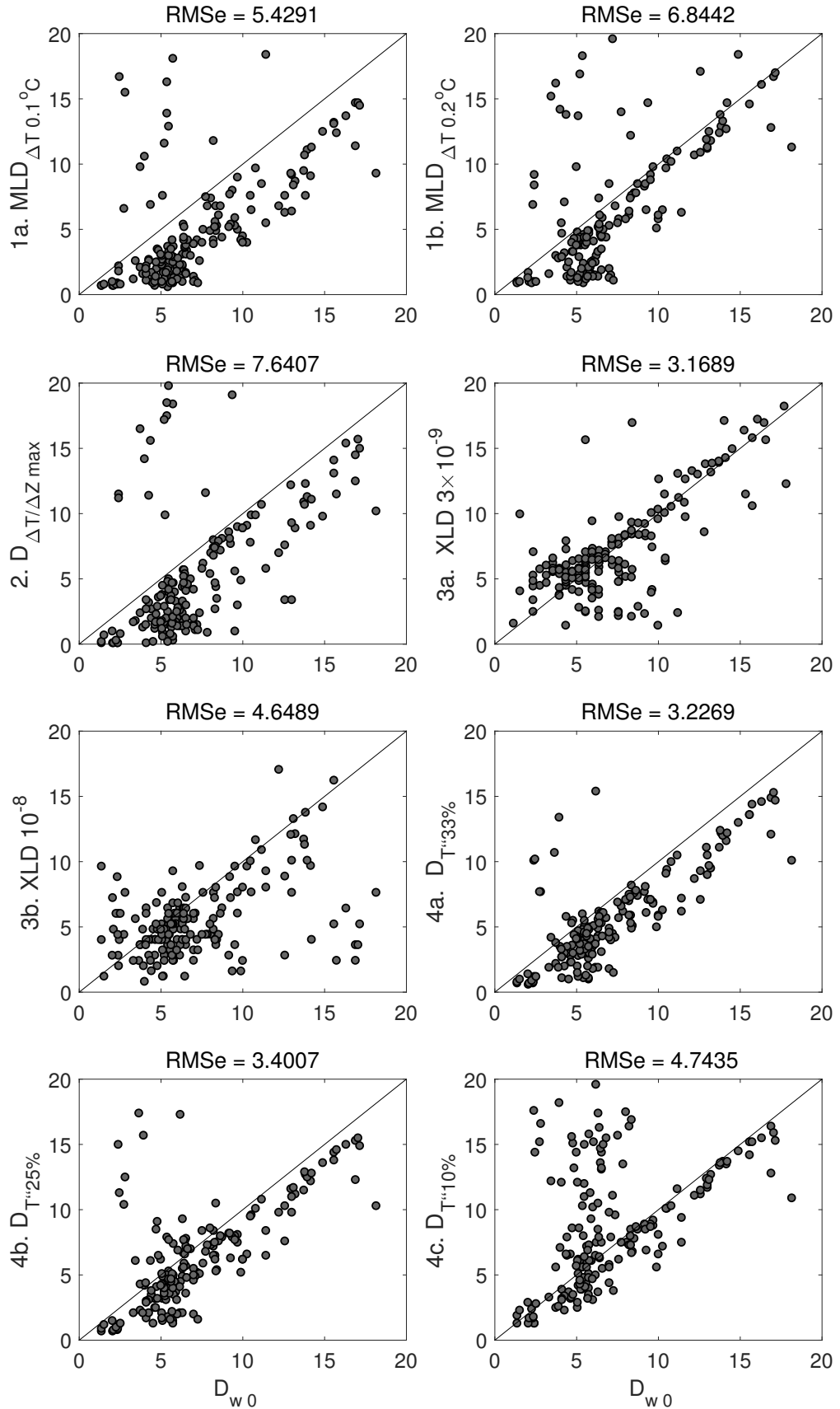


Figure 4.18: Comparison of visually determined warm layer depth D_{w0} [m] versus various systematical methods for 231 profiles from the MIDAS campaign.

4.5 Turbulent Mixing

Diurnal warming has been observed to coincide with a diurnal variability in upper ocean turbulence by e.g. *Brainerd and Gregg (1993)*. Intermittency with a diurnal pattern in the measured TKE dissipation rate ϵ in the upper 5-10 m can be inferred from fig. 4.5 and 4.6e. On most days the depth of active mixing (XLD) is seen to shoal after sunrise and reach a maximum around midnight. The stabilising buoyancy forces in the DWL are expected to contain the turbulent mixing. This relationship between the depth of active mixing is verified in fig. 4.19, where it shows that on the days of the strongest warming the depth of active mixing shoals the most.

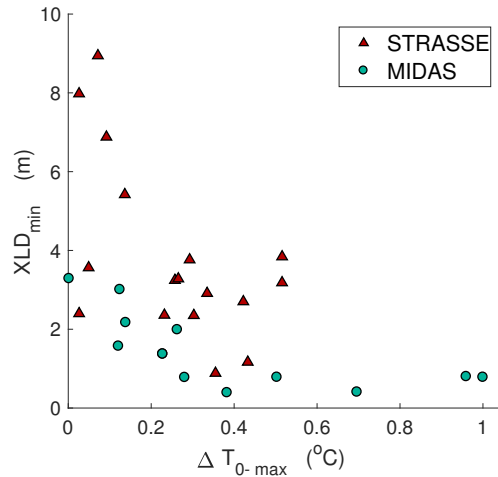


Figure 4.19: Daily minimum depth of the layer of active mixing versus the peak diurnal amplitude in T_{0-} for both SPURS cruises.

The datasets from the two cruises separate out, illustrating that the diurnal warming characteristics during part of the MIDAS campaign differ significantly from those during STRASSE. It has been shown by several authors that the amplitude of diurnal warming is sensitive to wind speed, which is also a dominant driver of upper ocean turbulence (*Price et al., 1986; Donlon et al., 2002; Ward, 2006; Merchant et al.; Gentemann and Minnett*). In figures 4.5 and 4.6 it was shown that the prevailing wind during the STRASSE campaign is of moderate strength, whereas during the first half of the MIDAS campaign it was significantly lower. This regime difference is reflected in the generally deeper XLD during STRASSE.

To verify that wind-induced turbulent mixing is the primary mechanism controlling the depth of the DWL in the observational time series, a scale analysis with the Monin-Obukhov length L is performed. This depth scale is computed as:

$$L = \frac{u_*^3}{\kappa B_0}, \quad (4.2)$$

where $\kappa \equiv 0.4$ is the von Kármán constant (*Lombardo and Gregg, 1989; Large et al., 1994*). Following (2.10) and (2.11) B_0 is positive during re-stratification, as well as L . The length scale L indicates the depth level in the OSBL beyond where turbulent

mixing is predominantly controlled by buoyancy forces, as opposed to wind induced turbulence. The ratio h/L is a commonly used parameter to estimate which process dominantly controls turbulence over a surface layer of depth h (Sutherland *et al.*, 2014a). This is determined for the depth of the warm layer, $h = D_{T''25}$ for all times during the three campaigns that ASIP or SkinDeEP was deployed, see fig. 4.20. Using the above formulation implies that when $1 < |h/L| < 0$ wind induced

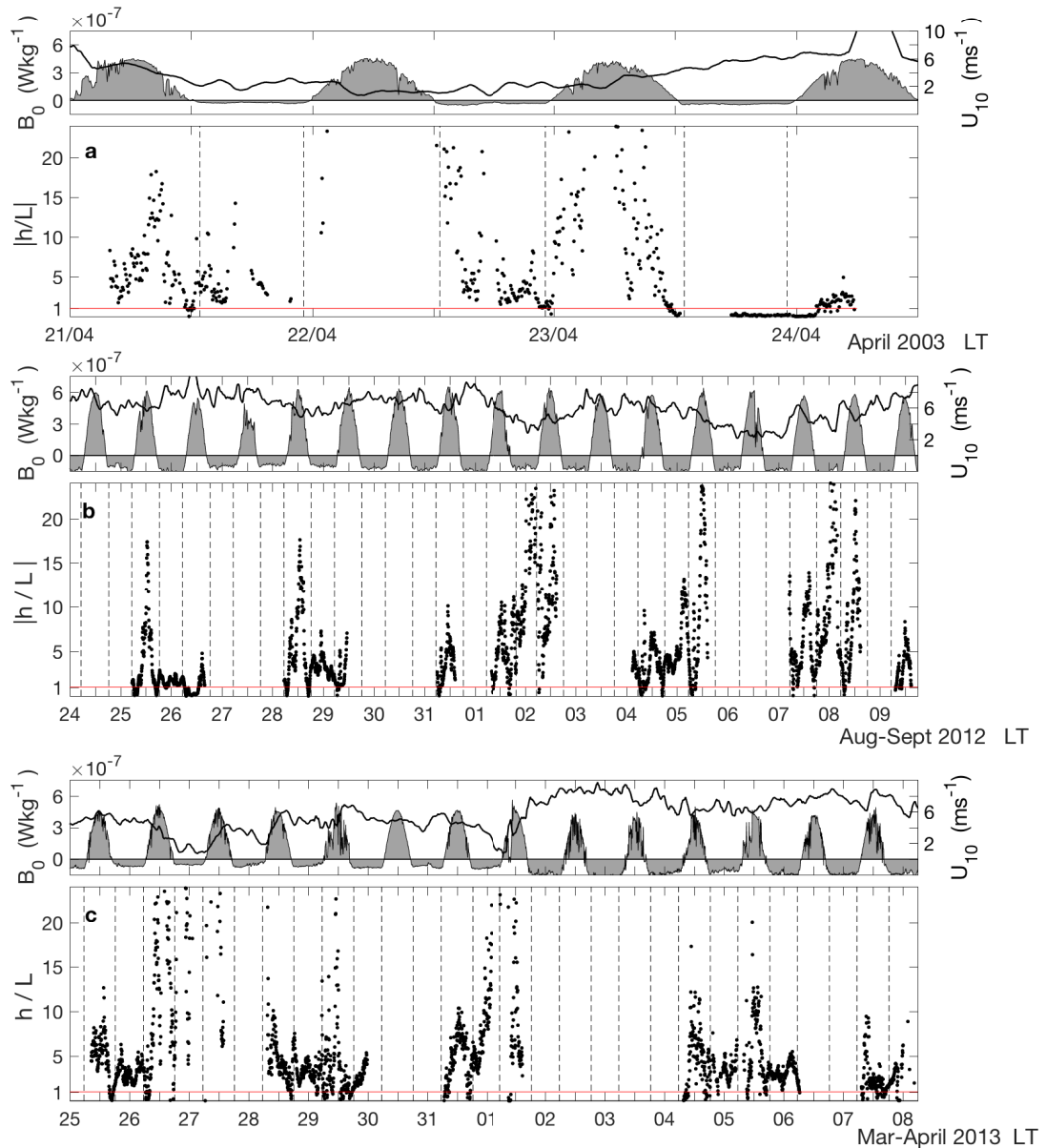


Figure 4.20: The ratio of the depth of the warm layer over the Monin-Obukhov length h/L , for all periods with profiler measurements during the NORBAL-5 (a), STRASSE (b) and the MIDAS campaign (c). Vertical dashed lines correspond to the times when B_0 changes sign on each day. Top panels again show B_0 and the 10 m-windspeed U_{10} .

turbulence dominates, whilst when $|h/L| \gg 1$ buoyancy controls the warm layer. To illustrate the meaning of this parameter on a small dataset, it is computed for the NORBAL-5 campaign as well, see fig. 4.20a. During the first three days of the time series h/L indicates a buoyancy dominated situation during both daytime stratification and nighttime convection. The increase in wind speed from the end of the 23/04 in fig. 4.20a) onwards causes a regime change towards wind dominance. The nighttime B_0 is small ($O(10^{-8} \text{ W kg}^{-1})$), explaining why during the nights that $h/L \gg 1$ the warm layer remains confined to the upper 4 m (fig. 4.8).

The moderate wind speeds during the STRASSE campaign (fig. 4.20b) illustrate the daytime near-surface layer's sensitivity to wind. The Monin-Obukhov length shoals around midday on most days as a result of diurnal warming, but $|h/L| < 1$ before B_0 changes sign again, explaining the observed afternoon deepening of the warm mixed layer. During nighttime h/L is mostly large as well, meaning that convective cooling dominantly controls the warm layer deepening (with exception of the night starting 26/09 in fig. 4.20b, when wind speeds are increasing up to 11 m s^{-1}).

On the day of lowest wind speed encountered in the MIDAS campaign (26/3), L remains shallow overnight. Similar to NORBAL-5 the absolute B_0 is quite low during the night, so although convection is dominant there is not much energy available and a remnant warm layer can persist overnight. Similarity scaling during this campaign indicates that wind and buoyancy forces compete during daytime and collaborate during nighttime in the deepening of the diurnal thermocline. During daytime the ratio h/L is close to 1 no significant diurnal restratification occurs (e.g. 7/4).

The measurements of ϵ in the North Atlantic campaigns provide an opportunity to further analyse the effect of diurnal warming on turbulence. In fig. 4.9d, 4.10g, and 4.10h the evolution of ϵ at 6 depths in the upper 10 m is plotted. An increase of ϵ can be observed in the upper 2 meter after sunrise on 26/03, 28/03, 29/03 and 31/03 (MIDAS, fig. 4.10). As opposed to *Moulin et al.* (2018), who observed a similar increase in ϵ in this layer, our observations do not show an initial decrease in surface- ϵ , neither a plateau in the dissipation rate during the afternoon and evening. Instead a rapid decay of ϵ at the shallowest depth is observed as soon as Q_{SW} turns negative. Below 2 or 3 m ϵ initially decreases, indicating that this layer is located below the DWL, and temporarily shut off from surface forcing. Later increase of ϵ in this layer reflects the deepening of the diurnal thermocline. The signal is also present, though less clear, during 28/08, 02/09, 05/09, 07/09 and 08/09 of the STRASSE campaign (fig. 4.9).

4.6 Diurnal Warming Simulation with COARE

4.6.1 Set-up of the COARE 3.0 Algorithm

The warm layer model in the COARE bulk flux algorithm, version 3.0 (*Fairall et al.*, 2003), was tested. This is the most widely used model for the computation of air-sea fluxes, developed for the TOGA-COARE program in the early 90's *Fairall et al.* (1996a). The COARE algorithm requires an input of the following (bulk) meteorological and oceanographic variables: SST, SSS, 10-m windspeed U_{10} , air temperature T_a , humidity q_{air} , barometric pressure and downward shortwave and longwave radiative fluxes Q_{SW} , Q_{LW} . For the SPURS campaigns 5 min averages of the meteorological observations are used as an input to the model, along with the sea water temperature at a depth of 3.5 / 3 m from the profilers, padded with the *SST* from the TSG-system of the research vessels or the SPURS-mooring to get a continuous time series. The agreement between ASIP-SST and the ship/mooring is generally good, except for some slightly higher values of T_{3m} during daytime from the mooring; *Prytherch et al.* (2013) describe this to be a known issue due to flow distortion around the mooring.

For the Mediterranean experiment the ship's meteorological data together with the skin-temperature from the infrared radiometer M-AERI is used.

The COARE algorithm predicts a diurnal warming correction for T_z to get to T_{int} by computing the depth of the warm layer, D_w , and the temperature difference over it, ΔT_w , assuming a temperature profile with a linear gradient. At each time step also the depth and temperature difference over the surface microlayer (D_c , ΔT_c) are computed. Implementing both corrections $T_{int} = T_z + \Delta T_w - \Delta T_c$, which is used in the computation of the heat fluxes.

In the standard configuration of the algorithm it is assumed that a warm layer that develops during the day is wiped out at local midnight. From the observations in both the subtropical Northern Atlantic and the Mediterranean we see that this does not necessarily represent reality; under calm conditions the diurnal thermocline can persist well into the night (see fig. 4.14). Therefore a small adaptation to the COARE 3.0 was made, such that the reset of the warm layer model occurs at 6 AM local time, instead of at midnight (local sunrise is after 6 AM in all three regions).

4.6.2 Model Results: North Atlantic

The modelled warm layer properties are compared to the observations from the upper ocean profilers, during all times available. Due to the ambiguity in the observed D_w , it is decided that the most practical evaluation of the model is a comparison of the predicted and observed temperature difference over the upper 5 m. This ΔT_{0-5m} gives an estimator of the COARE model's performance to derive $T_{subskin}$ from a bulk-*SST* measurement. The T_{0-} itself is also derived from the COARE model output for comparison to the observations.

Figure 4.21 shows ΔT_{0-5m} and D_{w0} observed during the STRASSE and MIDAS campaign, overlain with the output from the default COARE 3.0 algorithm. The

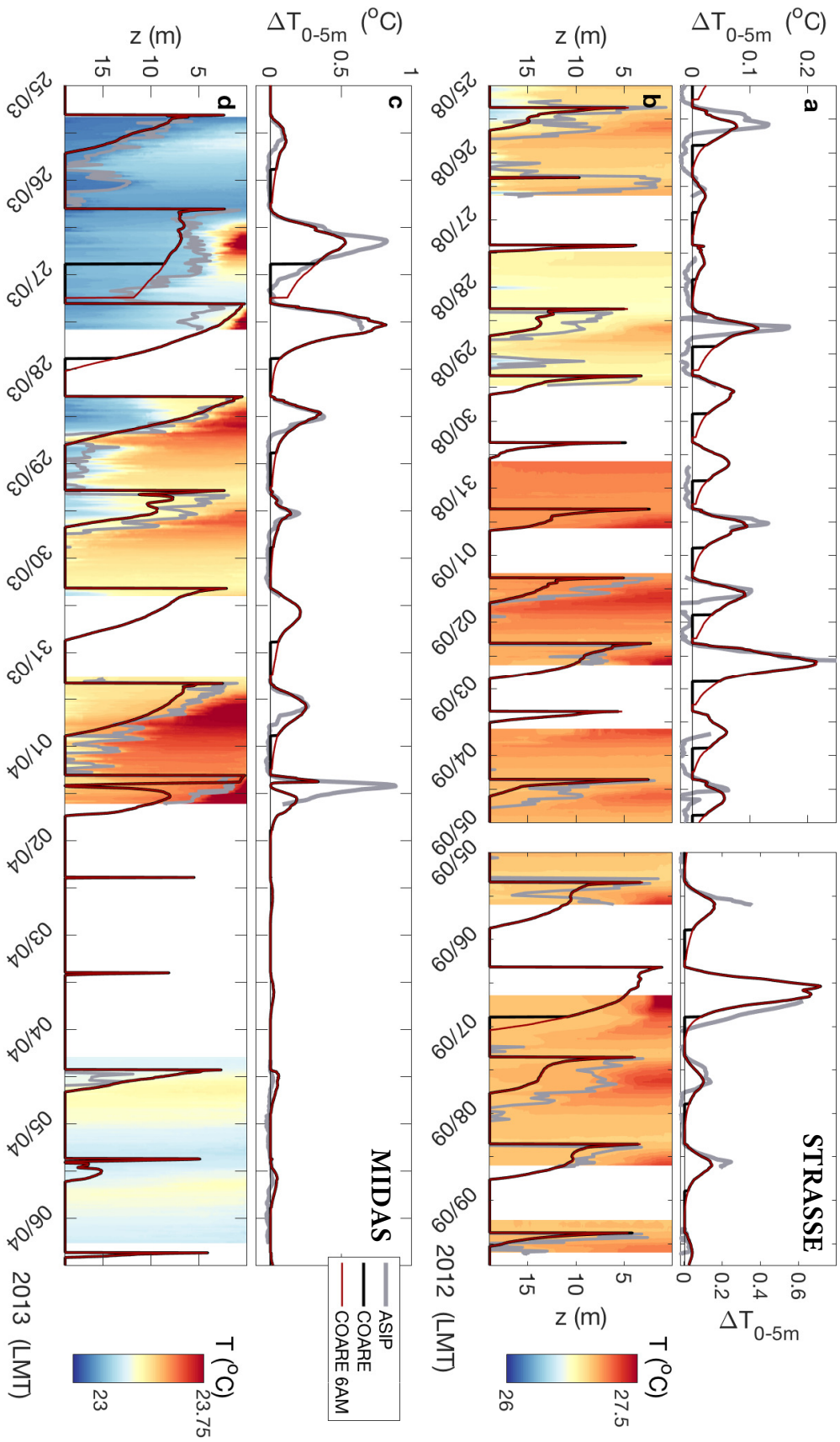


Figure 4.21: Temperature difference over the upper 5 m (a, c) as well as warm layer depth D_w (b, d) simulated by the COARE model for the STRASSE and MIDAS datasets. Black line the default COARE 3.0 model, red line the outcome from the model with the 6 AM warm layer module reset. Where available the observed ΔT_{0-5m} , D_{w0} are shown in grey.

effect of the change to the warm layer component of the algorithm, to reset at 6 AM instead of at midnight, is shown as well.

Warm-Layer Amplitude and Shape

The amplitude of ΔT_{0-5m} for the STRASSE campaign is underestimated by the COARE algorithm by at least 0.05 °C on the days that a significant warm layer is present. The timing of the peak warming is well represented by the model, but the slope in ΔT_{0-5m} is observed to be steeper than predicted, especially after the peak. Using the 6AM reset in this campaign does not improve the model during the days of moderate wind speeds, since the DWL has disappeared by midnight on these days; the 6AM-model underestimates the breakdown of the warm layer. Only on the day of the maximum warming in STRASSE, September 6th (see fig. 4.5), the default COARE algorithm overestimates the breakdown of the DWL and the 6 AM reset is required.

The modelled warming amplitude matches the observations better during MIDAS on the days of moderate wind speeds, but is underestimated on the calmer days; the observed ΔT_{0-5m} is higher by 0.3 °C on 26/3 and even 0.55 °C on 1/4. This last significant mismatch is the result of the sensitivity of the model to the passing reduction in Q_{SW} and increase in wind speed occurring at 8:30 AM on this day (see fig. 4.6). The T-profiles do not show such a response. The ASIP was on average 80 km away from the meteorological station on the WHOI mooring during its third deployment, so it is well possible that there is some delay in the passage of this weather system between the two locations. Also for this campaign, the observed reduction in ΔT_{0-5m} after the afternoon peak is more rapid than modelled. On the calmest day (26/3), although the slope is steeper, the temperature gradient near the surface persists after midnight, so the 6 AM reset of the warm layer computation is relevant on this day.

The shallowest measurement from ASIP is expected to correspond to T_{0-} (see chapter 3). It is compared to the $T_{int} + \Delta T_c$ from the COARE output in fig. 4.22. The agreement is generally good. The highest discrepancies occur in the MIDAS campaign, where on 27/3 T_{0-} is seemingly overestimated by 0.4 °C and by 0.2 °C on 31/3, and underestimated in the morning of 1/4 for reasons mentioned above. In the lower panel of this figure the sensitivity of the algorithm to the depth of the bulk-SST input is tested by using the temperature record of three different depths from the WHOI mooring. Using the deepest SST (at 8 m) results in a lower T_{0-} of maximum 0.25 °C compared to output using T_{3m} , which itself is close to the output from the 0.9 m-input most of the time.

Warm-Layer Depth

The depth of the warm layer is overestimated on days of moderate wind speed conditions during the STRASSE campaign, especially in the morning hours before the SST peak. On the 02/09 and 08/09 in fig. 4.21, which are days of calmer conditions, the simulated D_w matches the observed better. The performance of the model is also better here for MIDAS. Within the uncertainty of the D_w definition,

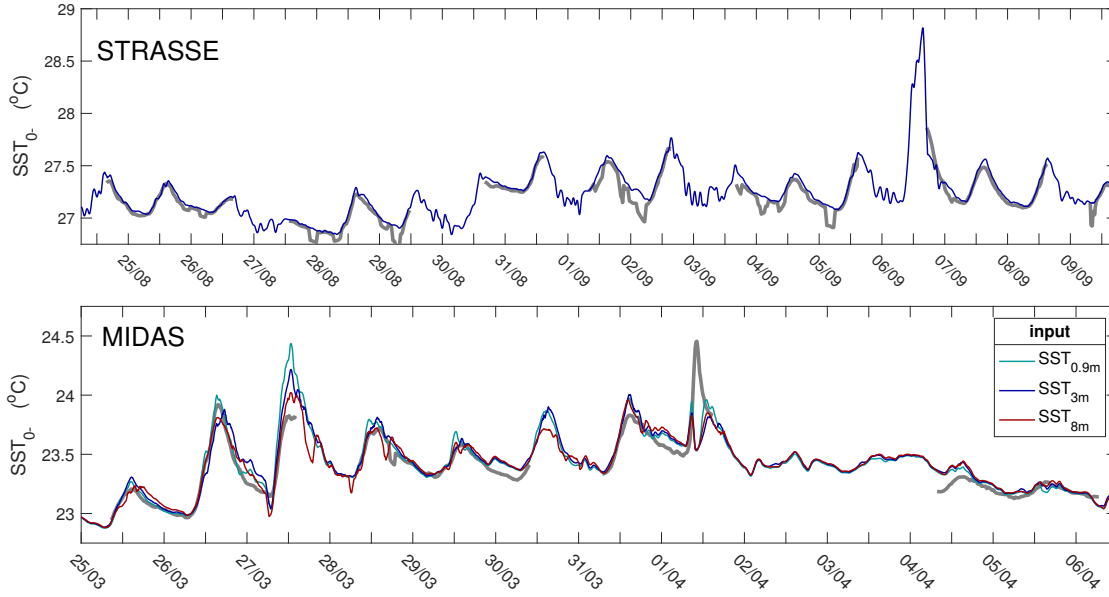


Figure 4.22: Comparison of simulated temperature directly below the surface (T_{0-}) versus the observed where available from the ASIP profiles (grey line) for both North Atlantic research cruises.

the modelled D_w can be considered equal to the observed depth on 25/03 and 28/03, a little overestimated on 26/03, 29/03, and 31/03, and remarkably shallower than observed on the first half of 27/03. The D_w simulation also benefits from the 6 AM reset on 26/03, but on any of the other days there is little or no difference with the default midnight.

Cool-Skin

Although no radiometer measurements are available for the North Atlantic datasets, to which the cool-skin correction by the COARE algorithm could be compared, a brief mention of the cool-skin temperature difference ΔT_c is made here. Figure 4.23 shows the time series of ΔT_c (absolute value) together with ΔT_w for both campaigns. It ranges from 0.11 - 0.42 °C during both campaigns, and as expected there is no obvious diurnal variability. This means that on many days ΔT_c is of the same magnitude as ΔT_w , and the two corrections to a bulk-SST measurement will thus basically cancel each other.

The cool-skin temperature difference is known to be dependent on both the wind speed and the surface heat flux (e.g. *Saunders, 1967; Wick et al., 1996*). Wind speed increases turbulent mixing, thereby enhancing the outgoing heat flux. Following equations (2.20), (2.21), and (2.22), the first effect reduces ΔT_c , whilst the second enhances it. In fig. 4.23c scatter plots of U_{10} and ΔT_c show that for STRASSE there is a good correlation between the two, whilst during MIDAS the wind speed seems of less important to the modelled ΔT_c . This is explained by the more significant correlation between U_{10} and the net outgoing heat flux Q_{out} (computed during nighttime only) during the MIDAS campaign, see fig. 4.23d. The increase in Q_{out} during MIDAS opposes the reduction of ΔT_c due to the wind.

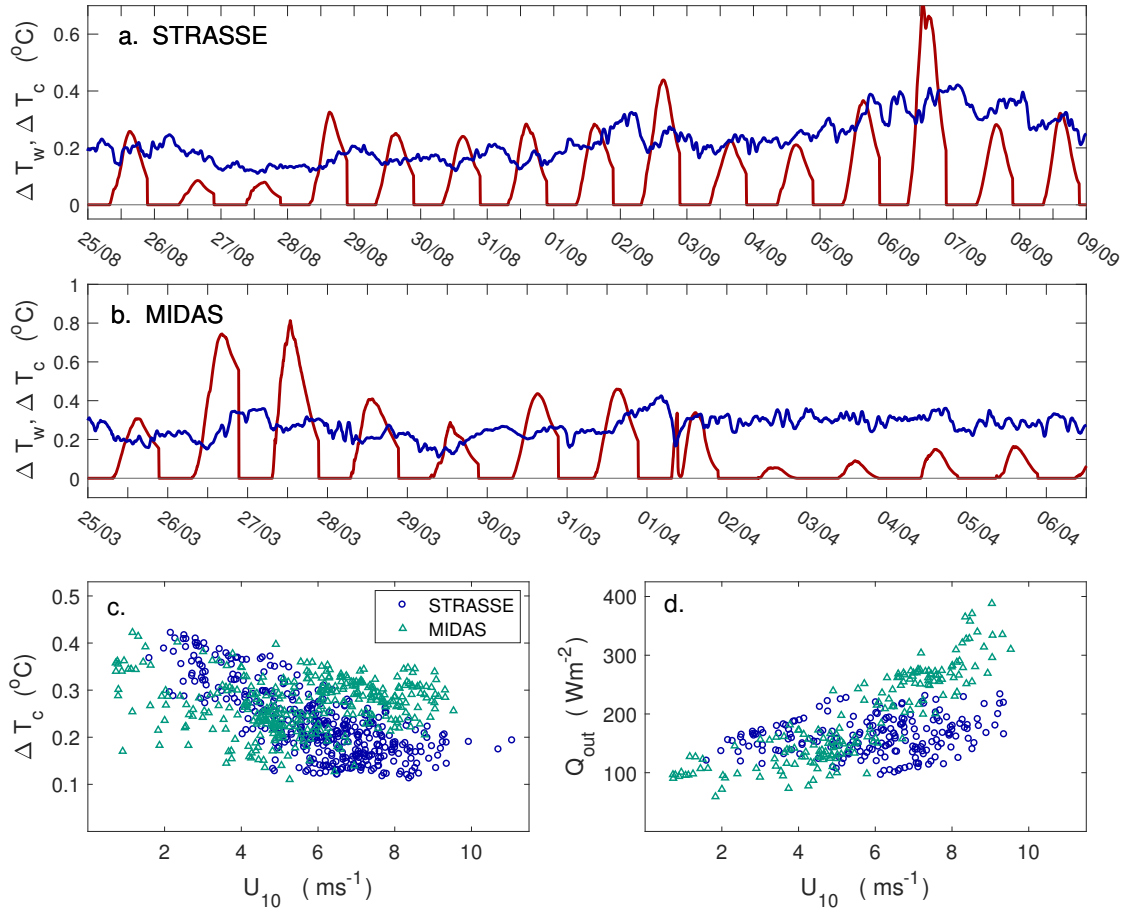


Figure 4.23: **a.+b.** Cool-skin and warm-layer correction following the COARE algorithm for the two North-Atlantic datasets. **c.** Cool-skin correction ΔT_c versus wind speed U_{10} following the COARE model runs for the STRASSE (blue circles) and MIDAS (green triangles). **d.** Idem for the ocean leaving heat flux Q_{out} and U_{10} .

4.6.3 Model results: Mediterranean

Input sensitivity study

To determine the optimal input time series to the COARE algorithm for the NORBAL-5 campaign, a short sensitivity study was performed. The air temperature measurement from the ship and the meteorological sensor package from the University of Miami (Wpak), and on the other hand the M-AERI, is based on different methods. Unfortunately, they differ by approximately $1\text{ }^\circ\text{C}$, (see fig. 4.24). Thanks to the M-AERI a time series of the skin temperature, T_{skin} , is available. Entering this into COARE would omit the need of a warm-layer and cool-skin correction to compute the heat fluxes. The algorithm then directly uses T_{skin} in the flux computations.

Four different inputs can thus be used:

1. T_a from shipborn sensors and SST from the ship's seawater intake at approx. 3.5 m below the surface.

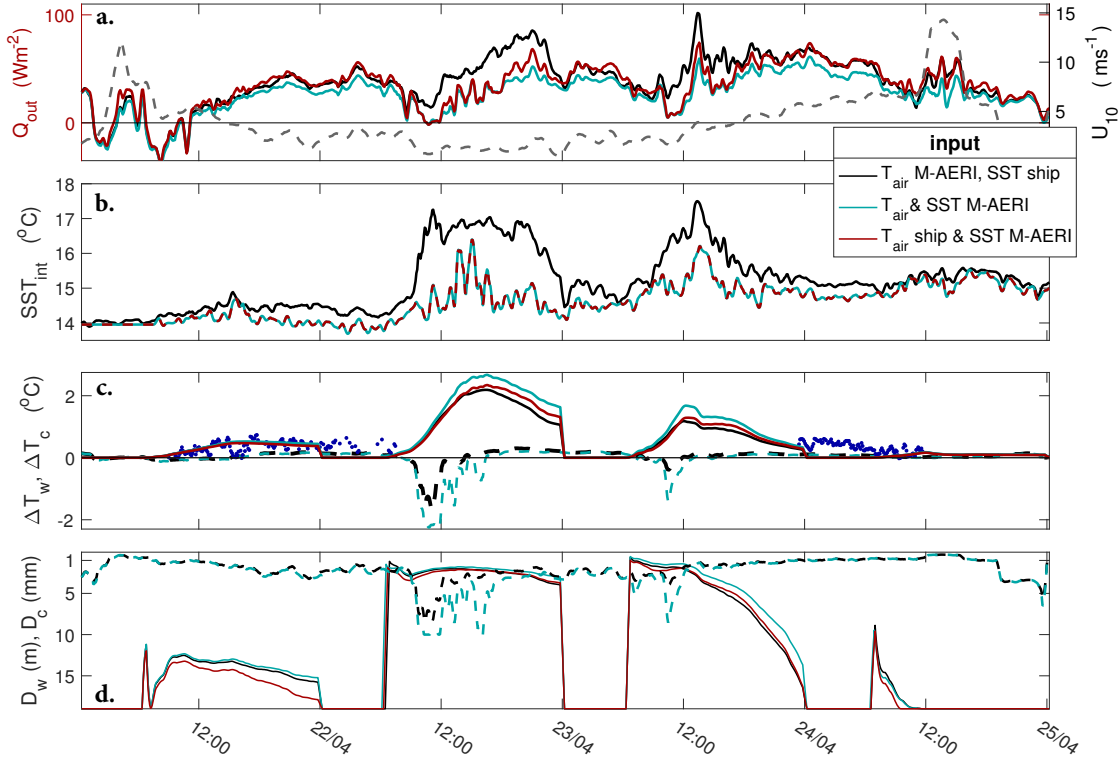


Figure 4.24: Output of COARE for 3 different combinations of input air temperature T_a and SST; **a.** Net ocean leaving heat flux Q_{out} ; **b.** T_{int} ; **c.** warm layer temperature difference ΔT_w and cool skin temperature difference ΔT_c (dashed lines). Blue dashed line is the observed ΔT_c ; **d.** Warm-layer and cool-skin depth D_w and D_c (dashed lines).

2. T from the ship intake and T_a from the infrared radiometer M-AERI.
3. T and T_a from M-AERI; since this T should correspond to T_{skin} , neither cool skin or warm layer correction are applied by the algorithm.
4. T_a from the ship's sensors and the T_{skin} from M-AERI.

The fluxes computed with T_{skin} as an input should form the best estimate, since no correction for the ‘true’ interfacial temperature has to be performed. To test the sensitivity of the COARE model to the different T_a -measurements, and to the use of T_{skin} instead of bulk- T , the result of input 2, 3 and 4 is shown in fig. 4.24. The choice of T has the largest impact on the heat fluxes; compared to the result of input 2, the net surface cooling during daytime is $5 - 10 \text{ W m}^{-2}$ less when the algorithm is forced with the measured T_{skin} (fig. 4.24 a). This is the consequence of the much higher T_{int} predicted from the bulk- T input, as shown in panel b. If both the radiometer T_{skin} , and ship intake $T_{3.5m}$ are correct, this implies that the combined cool skin/warm layer correction predicts the diurnal evolution of T_{int} with a significant uncertainty. The large deviation in T_{int} on 22 and 23/04 in fig. 4.24c is predominantly the result of the warm layer correction, but from 6 to 12 AM on these days there is also an unusually high, negative cool skin correction ΔT_c . According to Fairall *et al.* (1996b) ΔT_c is set to zero in the COARE algorithm, when the absorbed solar flux over the skin layer is larger than the total cooling;

the default algorithm obviously does not do this. Consequently a warm-skin of $D_c > 5$ mm (fig. 4.24d) is modelled, and a correction of a magnitude similar to ΔT_w is applied. Although indeed on the 22/4 the time series of T_{skin} in fig. 4.8 suggest a warm-skin, this is of a somewhat smaller magnitude and occurring a few hours later. For the remainder of the analysis presented in this chapter, the MATLAB code of the COARE algorithm was modified to prevent the presence of a warm skin. This is only of relevance to the NORBAL-5 dataset; in both North-Atlantic datasets the COARE model predicts a cool-skin of 0.2-0.3 °C at each timestep (fig. 4.23). The NORBAL-5 dataset can in principle be used to verify the cool skin correction by COARE, when assuming that the shallowest available SST measurement from the SkinDeEP profiles corresponds to T_{0-} . However, gaps in the SkinDeEP record just below the surface complicate this evaluation. The blue dots in fig. 4.24 c. show the measured ΔT_c wherever an T_{0-} measurement is available. Although somewhat noisy, it is generally higher than the modelled one, indifferent of which input is used in the COARE algorithm.

The choice of input T_a in NORBAL-5 also affects the net surface cooling. When using the ship's T_a measurement (input 4), the modelled Q_{out} is up to 10 W m⁻² higher, compared to input 3. Although the warm-layer and cool-skin correction are not necessary when using either of these inputs, the algorithm can be set-up to compute the warm layer properties nevertheless. It is remarkable to see that the warm-layer predicted from input 3 is up to 0.5 °C warmer, and up to 2 m less deep compared to input 2. T_a results in a difference of up to 0.3°C and 1 m. respectively. There is clearly a mismatch between the bulk-*SST* from the ship and the T_{skin} measurement from M-AERI. Since the last is quality controlled, whilst the exact depth of the ship's intake is unknown, the M-AERI T_{int} is considered the best input here. The uncertainty in T_a remains; to facilitate comparison with the other campaigns, it was decided to use the measurement from the meteorological systems. Input 4 is thus used in this chapter for the heat fluxes (fig. 4.8 c) and warm layer prediction (fig. 4.25 e. and f.) from COARE for the NORBAL-5 campaign.

Warm-Layer

For the days of strongest near-surface warming (22 and 23/4 in fig. 4.25) no temperature observations directly below the surface are available. Here the temperature difference over a depth of 1-5m is compared to the modelled ΔT_{1-5m} . During the first and third SkinDeEP deployment the small ΔT_{1-5m} is underestimated as a result of the deep D_w . The modelled D_w compares better with the observations during the afternoon of the 22/4 and on 23/4 (second deployment). The observed ΔT_{1-5m} however is overestimated on the first day, and underestimated on the second day. Due to the very low wind speed and small heat fluxes (see fig. 4.8), the warm layer persists overnight, so the 6AM-reset of the warm layer module is an improvement here. No reset would have been better, to allow the algorithm to develop a near-surface temperature gradient on 23/4 on the remaining gradient of the night before; omitting this results in an underestimated ΔT_{1-5m} on this day.

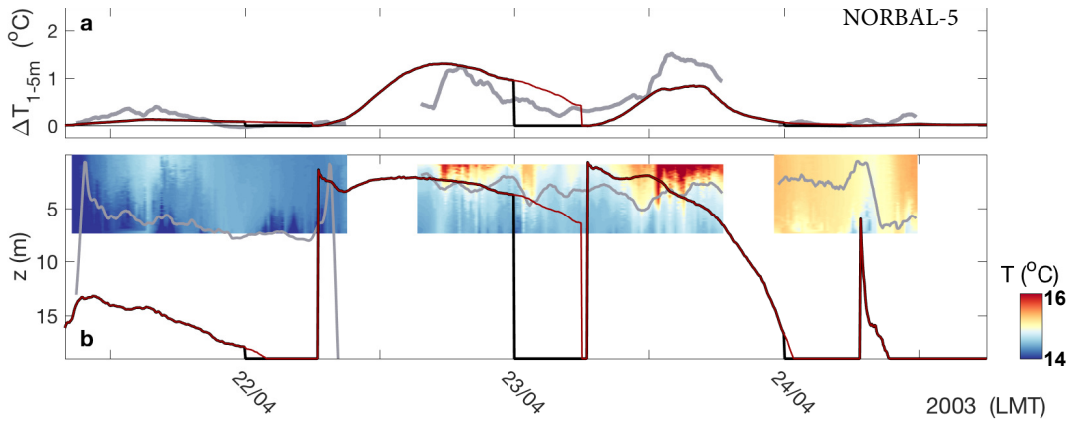


Figure 4.25: Temperature difference over the upper 5 m (a) as well as warm-layer depth D_w (b) simulated by the COARE model for the NORBAL-5 dataset. Black line the default COARE 3.0 model, red line the outcome from the model with the 6 AM warm layer module reset. Where available the observed ΔT_{0-5m} , $D_{T''25\%}$ are shown in grey.

4.7 Sensitivity Tests to the COARE Algorithm

The absorption of shortwave solar radiation is the dominant heat flux term during daytime, driving the development of the diurnal warm layer. The amount of ‘solar irradiance’ (corresponding to the radiative flux Q_{SW} in W m^{-2}) transmitted to a specific depth is dependent on the optical properties water, as well as the incident light itself. In natural waters particles and solubles add to the variability of the vertical transmission profile. Absorption of light in the ocean is also wavelength dependent; from the full solar spectrum that reaches the Earth (200 -3000 nm) a large part is attenuated within the upper two metres, due to strong absorption in the infrared and near-infrared (*Paulson and Simpson, 1977; Sweeney et al., 2005*). Below this depth chlorophyll and chlorophyll-like pigments contribute to the absorption in the visible wavelengths of the spectrum (*Morel and Antoine, 1994*). In the following the symbol $I_d z$ is used, representing the spectrally integrated total downward irradiance. The transmission profile of $I_d(z)$, for use in ocean models, is commonly parameterised with a sum of exponential decay functions:

$$\frac{I_d(z)}{I_d(0)} = \sum_{i=1}^n F_i e^{-z/L_i}, \quad (4.3)$$

In most cases $I_d(0)$ corresponds to $I_d(0^-)$, the downward irradiance directly below the air-sea interface. This is related to the above-surface irradiance $I_d(0^+)$ via the sea surface albedo a , the fraction of irradiance reflected at the sea surface.

The COARE model represents the absorption of solar irradiance over a layer of depth D_w as a fraction of the total incident shortwave radiative flux Q_{SW} directly below the surface (using a fixed value for the surface albedo). This fraction, f_x , is the vertical integral of $I_d(0^-) - I_d(z)$, using $n = 3$ in equation (4.3) to compute

$I_d(z)$:

$$f_x(z) = \frac{1}{D_w} \int_0^{D_w} (I_d(0^-) - I_d(z)) dz = 1 - \left(\sum_{i=1}^n F_i L_i [1 - e^{-z/L_i}] \right) / z, \quad (4.4)$$

with fraction $F_i = 0.45, 0.27$ and 0.28 , and attenuation length $L_i = 12.8, 0.357$ and 0.014 m.

Here, the sensitivity of the warm-layer prediction of the COARE algorithm to other formulas for f_x will be investigated, based on shortwave absorption parameterisations of varying complexity found in literature.

4.7.1 Alternative Solar Absorption Parameterisations

The algorithm for the absorption of solar radiation in the warm layer component of the COARE algorithm, has been modified to test alternative parameterisations, by adapting equation (4.4) as follows, introducing acronyms to refer to the model runs in the remainder of this chapter:

- **Jer76**

Jerlov (1968) introduced an optical classification of oceanic water, based on observed transparency. This was extended to five water types for the open ocean, and nine classes for coastal water (*Jerlov*, 1976). An exponential decay model distinguishing two components of light (red and blue) for the oceanic *Jerlov* water types of increasing turbidity was determined by *Paulson and Simpson* (1977):

$$\frac{I_d(z)}{I_d(0^-)} = [F_R e^{z/L_R} + (1 - F_R) e^{z/L_B}] \quad (4.5)$$

where F_R is the fraction of red light, L_R is the penetration depth scale of red light, and L_B is the penetration depth scale of blue light. Table 4.2 lists F_R , L_R and L_B for the different oceanic water types, and fig. 4.26 illustrates the corresponding absorption curves. Water in the subtropical west and central Atlantic is generally clear, of type I or IA (*Jerlov*, 1976). Mediterranean water can be more turbid, as a result of phytoplankton blooms and coastal effluents. The coefficients for watertype I, IB and III have been used in equation (4.4) ($n = 2$), to compute $f_x(z)$. Solar radiation absorption in the PWP mixed layer model is represented by this two-component exponential depth dependence, by default using the coefficients corresponding to watertype IA.

- **Mor94**

In *Morel and Antoine* (1994) the transmission of solar irradiance is parameterised by first dividing the total solar spectrum in two parts: The infrared (IR) and the visible/UV domain. A single exponential decay function is used to describe the spectral range of wavelength $\lambda > 750$ nm (IR and near-IR), which is largely absorbed in the upper 2m. For the visible-and UV part of the spectrum a double exponential fit is proposed, based on spectral attenua-

Type	F_R	$L_R[m]$	$L_B[m]$
I	0.58	0.35	23
IA	0.62	0.6	20
IB	0.67	1.0	17
II	0.77	1.5	14
III	0.78	1.4	7.9

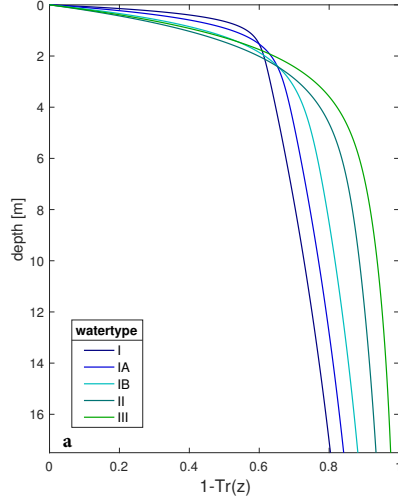


Table 4.2: Red light fraction and attenuation lengths for the oceanic water types of the optical classification by *Jerlov* (1976), from *Paulson and Simpson* (1977). Figure 4.26: Irradiance absorption curves following 4.2.

	p_0	p_1	p_2	p_3	p_4	p_5
v_1	0.353	-0.047	0.083	0.047	-0.011	-0.009
v_2	0.647	0.047	-0.083	-0.047	0.011	0.009
L_1	1.662	-0.605	0.128	-0.033	-0.051	-0.004
L_2	8.541	-8.924	4.020	-0.077	-0.536	0.055

Table 4.3: Coefficients for the polynomial function to compute v_i or L_i in equation (4.6) and (4.7) of the chlorophyll concentration [*Chl*] (*Morel and Antoine*, 1994).

tion coefficients determined in combined measurements of spectral irradiance profiles and chlorophyll concentration (*Morel*, 1998):

$$\frac{I_d(z)}{I_d(0-)} = F_{IR} e^{-z/0.267 \cos \theta_w} + F_{vis} [v_1 e^{-z/L_1} + v_2 e^{-z/L_2}]. \quad (4.6)$$

This parameterisation includes a dependency on the solar zenith angle θ for absorption of the IR part of the spectrum as well as a dependency on local chlorophyll concentration for absorption of the shorter wavelengths. The coefficients v_i and attenuation lengths L_i are each computed by evaluating a 5th order polynomial function of the concentration of chlorophyll pigment, [*Chl*], with coefficients listed in Table 4.3:

$$Y = p_0 + p_1 X + p_2 X^2 + p_3 X^3 + p_4 X^4 + p_5 X^5, \quad (4.7)$$

where $X = {}^{10} \log(\text{Chl})$.

i	$\lambda(\mu\text{m})$	F_i	$L_i(\text{m})$		
1	0.2 - 0.6	0.237	34.8		
2	0.6-0.9	0.360	2.27		
3	0.9-1.2	0.179	$3.15 * 10^{-2}$		
4	1.2-1.5	0.087	$5.48 * 10^{-3}$		$\frac{1}{L_1}(\text{m}^{-1})$
5	1.5-1.8	0.080	$8.32 * 10^{-4}$	I	0.066
6	1.8-2.1	0.0246	$1.26 * 10^{-4}$	IA	0.076
7	2.1 - 2.4	0.025	$3.13 * 10^{-4}$	IB	0.088
8	2.4-2.7	0.007	$7.82 * 10^{-5}$	II	0.132
9	2.7-3.0	0.0004	$1.44 * 10^{-5}$	III	0.382

Table 4.4: Exponential coefficients for the nine wavelength solar absorption model from *Paulson and Simpson* (1981). In the last two columns the alternative values of $1/L_1$ for the different Jerlov water types are listed, following *Soloviev and Schlüssel* (1996).

The absorbed fraction over a layer of depth z , $f_x(z)$, is then computed as:

$$f_x(z) = 1 - \left(0.267 \cos \theta F_{IR} e^{-z/0.267 \cos \theta} + F_{vis} v_1 e^{-z/L_1} + F_{vis} v_2 e^{-z/L_2} \right) / z. \quad (4.8)$$

The solar zenith angle θ is computed at each time step using an implementation of the solar position algorithm in *Reda and Andreas* (2008). The COARE algorithm is run for $[Chl] = 0.05, 2$ and 5 mg m^{-3} to represent low, moderate and bloom concentrations (fig. 4.27b).

- **PS81**

With the aim to model the radiation absorption over the cool skin, a more complex parameterisation was proposed by *Paulson and Simpson* (1981), describing the pure water absorption over nine separate wavelength bands:

$$\frac{I_d(z)}{I_d(0^-)} = \sum_{i=1}^9 F_i \exp(z/L_i) \quad (4.9)$$

F_i : spectral fraction L_i : attenuation length of wavelength band i . Table 4.4 lists the model coefficients, which are based on measurements in pure water. For use in a variety of natural water types according to Jerlov's classification, *Soloviev and Schlüssel* (1996) have adapted the value of the attenuation length in the first wavelength band (200-600nm) for different optical water types. This results in the absorption curves in fig. 4.27a. The coefficients F_i and L_i from Table 4.4 for watertype I, IB and III have been implemented in the COARE algorithm.

- **Ohl00**

A more recently published solar irradiance transmission parameterisation, with a dependency on local water properties, was proposed in *Ohlmann et al.* (2000) and *Ohlmann and Siegel* (2000). Using the HYDROLIGHT radiative transfer model (*Mobley, 1994*) the effects of chlorophyll, cloud index, and incident solar zenith angle on the transmission of the solar spectrum between

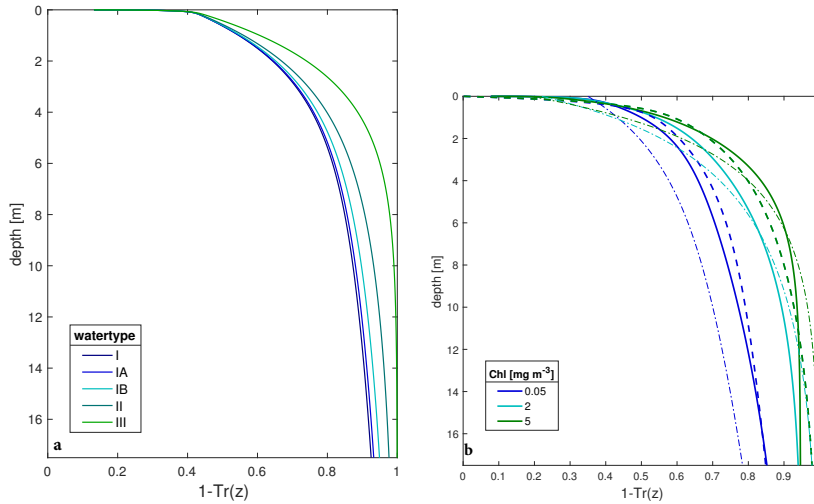


Figure 4.27: Modelled irradiance curves following parameterisations of the oceanic watertypes of the optical classification by *Jerlov* (1976), as described *Paulson and Simpson* (1981) (a), as well as for chlorophyll-dependent parameterisations by *Morel and Antoine* (1994) (dashed lines), *Ohlmann and Siegel* (2000) (solid lines) and *Ohlmann* (2003) (dash-dotted lines) for three different *Chl*-concentrations (b).

250 and 2000 nm were quantified. It is concluded that chlorophyll influences the absorption in the visible part of the spectrum, thus reducing transmission clearly between 1 and 10 m depth. However, it does not significantly influence radiant heating in the upper metre. Albedo changes due to increased scattering by phytoplankton are small and limited to the visible wavelength bands only. Clouds reduce the total irradiance and shift the distribution of energy from the near-IR to visible and shorter wavelengths, which reduces radiant heating even further. The change of solar zenith angle θ under clear skies affects the path length of the radiation. Early, and towards the end of the day, the geometry of the radiance distribution is slightly shifted towards longer wavelengths. The effect on albedo is dual: diffuse light by clouds increases the albedo when θ is low, but when the sun is low in the sky the albedo is reduced. Based on these findings a solar transmission parameterisation for use in the COARE algorithm or other models is formulated:

$$\frac{I_d(z)}{I_d(0+)} \cong \sum_{i=1}^4 A_i e^{-K_i z}, \quad (4.10)$$

in which parameters A_i and K_i are a function of the chlorophyll concentration, $[Chl]$, and either solar zenith angle θ (for clear skies) or cloud index CI . Since we do not avail of any information on cloud cover, here the clear sky parameters given in *Ohlmann and Siegel* (2000) are used. Each A_i and K_i is computed from three fit parameters:

$$A_i = X_{1i}Chl + X_{2i}/\cos(\theta) + X_{3i},$$

$$K_i = Y_{1i}Chl + Y_{3i}/\cos(\theta) + Y_{4i},$$

with X_j and Y_j , which are listed in Table 4.5.

	$X1$	$X2$	$X3$		$Y1$	$Y2$	$Y3$
A_1	0.033	-0.025	0.419	K_1	0.066	0.006	0.066
A_2	-0.010	-0.007	0.231	K_2	0.396	-0.027	0.886
A_3	-0.019	-0.003	0.195	K_3	7.68	-2.49	17.81
A_4	-0.006	-0.004	0.154	K_4	51.27	13.14	665.19

Table 4.5: Coefficients determined in the linear regression in *Ohlmann and Siegel* (2000), used to compute A_i and K_i in equation (4.10) for clear sky conditions.

For this model the COARE algorithm is also programmed to compute θ at each time step, and evaluated for the same three $[Chl]$ as in Mor94 (see fig. 4.27b). In contrast to the above models, the effect of $[Chl]$ and θ on the ocean surface albedo is incorporated into the parameterisation, such that $1 - \sum A_i = a$. This makes equation (4.4):

$$f_x(z) = \sum_{i=1}^4 A_i - \left(\sum_{i=1}^4 A_i K_i^{-1} [1 - \exp(-K_i z)] \right) / z, \quad (4.11)$$

From this parameterisation it follows that the sea surface albedo a varies from 0.04 to 0.13, and is not very different between the study locations and seasons (see fig. 4.28).

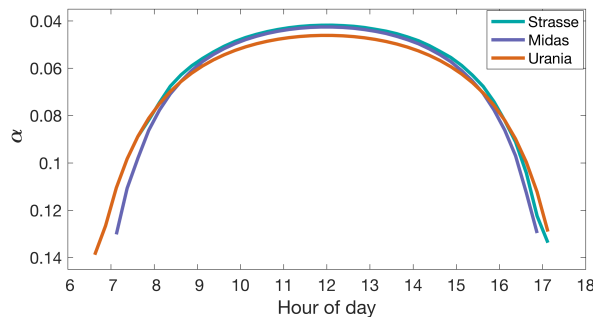


Figure 4.28: Mean evolution of the sea surface albedo a during the day at the three study sites, following the parameterisation in *Ohlmann and Siegel* (2000).

- **Ohl03**

A solar transmission parameterisation for use in climate models that do not provide the vertical resolution to dedicate more than two grid points to the surface mixed layer is given in *Ohlmann* (2003). This is an empirical fit to transmission curves simulated with HYDROLIGHT for a limited range of the solar spectrum (250-900 nm.) and a range of $[Chl]$:

$$Tr(z, Chl) = A_1 e^{-B_1 z} + A_2 e^{-B_2 z}, \quad (4.12)$$

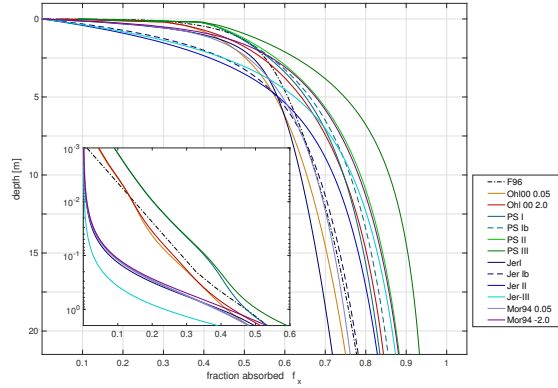


Figure 4.29: The fraction of absorbed radiation f_x as a function of depth below the surface, following the different parameterizations tested in section 4.7.2. Acronyms are explained in section 4.7.1.

$$\begin{aligned}
 A1 &= 0.571 + 0.025 \ln(0.149 \times Chl) \\
 A2 &= 0.223 + 0.010 \ln(2.329 \times Chl) \\
 B1 &= 0.015 + 0.176 \sqrt{(0.462 \times Chl)} \\
 B2 &= 0.688 + 0.060 \ln(0.125 \times Chl)
 \end{aligned} \tag{4.13}$$

The COARE model is thus adapted to use equation (4.4) for $n=2$, with partition factors A_1 and A_2 (instead of F_i), and attenuation lengths $L_1 = B_1^{-1}$ and $L_2 = B_2^{-1}$. Simulations are done for the same three chlorophyll concentrations as for Mor94 and Ohl00.

Figure 4.29 shows how the curves of f_x for the specific parameterisations used in the sensitivity study relate to each other, over a depth of 20 m as well as in the upper meter.

4.7.2 Warm-Layer Simulation

The fraction of absorbed downward solar radiation, f_x , relates to the depth of the warm layer D_w and the temperature difference over it ΔT_w via Q_{net} in equations (2.27) and (2.28). To compare the observations to the output of the COARE 3.0 algorithm for different absorption parameterisations, again the temperature difference over the upper 5 m is used. In fig. 4.30 is illustrated how each of the f_x -formulations changes ΔT_{0-5m} , with respect to the default (F96).

The absorption parameterisations that use an increasing number of exponents, increase f_x in the upper meter, whilst for an increasing watertype or chlorophyll concentration the absorption below 1 m is stronger. The sequence in the predicted ΔT_{0-5m} resulting in the f_x -formulation by PS81 for increasing watertype describes this well; applying PS81 in COARE results in a higher warm layer correction than the original absorption described in F96, on average 25% more for watertype I, increasing up to 72% for turbid waters.

The two-exponential parameterisation in Jer76 often results in a cooler warm layer. It is remarkable that for part of the dataset the underestimation is less for watertype I than for type II and III. On examination of the time-series of the individual cruises (e.g. in fig. 4.33), it is found that on the days of strongest warming and lowest wind forcing, the Jer76-absorption curve for watertype II and III coefficients can result in a *lower* warming prediction than for watertype I. This can be understood from the radiation absorption-curves in fig. 4.29, which show that above 3 or 5 m f_x for watertype I is higher than for watertype III and II respectively.

The chlorophyll-dependent two-exponential parameterisation Ohl03 results in less warming in the NORBAL-5 campaign compared to F96, however for an input of higher $[Chl]$ the result is mixed for both North Atlantic campaigns. The warming in the Ohl-00 and Mor-94 parameterizations, relative to the default, is similar, and consistent for all three datasets. In water of low $[Chl]$ the COARE model predicts a slightly cooler warm layer, whilst for moderate and high $[Chl]$ the absorption of solar radiation is higher; > 45% when $[Chl] = 2.0 \text{ mg m}^{-3}$ and up to 75% when $[Chl] = 5.0 \text{ mg m}^{-3}$ is used in the coefficients of (4.8) and (4.11).

The effect of the different shortwave absorption parameterisations on the simulation of the DWL by the COARE 3.0 algorithm is most easily visualised in the time series in figs. 4.31, 4.32 and 4.33. Here ΔT_{0-5m} and D_w have been drawn for a selection of the tested f_x -models, in comparison to the observed values from the ASIP and SkinDeEP profiles. To facilitate analysis the models have been grouped, panel a and b showing the results for the low-Chl models (Jer76 I and Ib, PS81 I and Ib, Ohl00 and Mor94 for $Chl = 0.05 \text{ mg m}^{-3}$), and panel c and d the high-Chl models (Jer76 II and III, PS81 II and III, Ohl00 and Mor94 for $Chl = 2.0 \text{ mg m}^{-3}$). The different solar absorption formulations result in a significant difference in the warm layer correction of the COARE algorithm. For the same watertype, the near surface temperature gradient ΔT_{0-5m} is significantly lower when using the Jer76-parameterisation, compared to the 9-exponent PS81 formulation. Correspondingly the simulated D_w is deepest with Jer76. In the North-Atlantic campaigns the shallowest D_w results from the Ohl00 parameterisation, for either of the $[Chl]$ concentrations tested, and the PS81. The largest improvement in the D_w prediction compared to F96 is seen on 26/3 in fig.4.32.

On days when the default COARE-run underestimates ΔT_{0-5m} , e.g. on 25 and 28/08 in fig. 4.21 (STRASSE), and 26/03 during MIDAS, the models of higher complexity ($n > 3$ and/or $f([Chl])$) increase the warm layer temperature difference towards the observed peak values in these campaigns, when using the coefficients for water type I and IB, or the low chlorophyll-concentration. The slope after the peak also matches better to the observations. Using coefficients for water type II and III in PS81, representative of higher turbidity, overestimates the warming, according to expectations, since the water of the SPURS region is relatively oligotrophic. However, applying Mor94 or Ohl00 with $[Chl] = 2.0 \text{ mg m}^{-3}$ does not overestimate ΔT_{0-5m} during STRASSE.

It is difficult to judge the performance of the different shortwave absorption parameterisations, because of the more fundamental disagreements between the COARE output and the observed warm layer depth for the NORBAL-5, discussed in

	STRASSE		MIDAS		NORBAL-5	
	$ \mu $	RMS _e	$ \mu $	RMS _e	$ \mu $	RMS _e
F96	0.032	0.045	0.038	0.056	0.19	0.32
Jer76-I	0.032	0.048	0.035	0.057	0.19	0.32
Jer76-IB	0.033	0.048	0.042	0.063	0.20	0.34
Jer76-II	0.034	0.049	0.045	0.067	0.21	0.34
Jer76-III	0.035	0.047	0.048	0.067	0.19	0.33
PS81-I	0.032	0.042	0.045	0.061	0.19	0.32
PS81-IB	0.033	0.042	0.047	0.065	0.19	0.32
PS81-II	0.035	0.044	0.053	0.072	0.19	0.32
PS81-III	0.045	0.055	0.073	0.105	0.21	0.33
Ohl00 _{0.05}	0.042	0.043	0.049	0.067	0.19	0.32
Ohl00 _{2.0}	0.035	0.044	0.075	0.105	0.19	0.32
Ohl00 _{5.0}	0.044	0.053	0.098	0.14	0.20	0.32
Ohl03 _{0.05}	0.035	0.056	0.037	0.064	0.20	0.33
Ohl03 _{2.0}	0.035	0.048	0.044	0.06	0.31	0.48
Ohl03 _{5.0}	0.040	0.050	0.053	0.072	0.18	0.31
Mor94 _{0.05}	0.032	0.046	0.036	0.053	0.19	0.32
Mor94 _{2.0}	0.035	0.044	0.051	0.069	0.20	0.32
Mor94 _{5.0}	0.041	0.050	0.067	0.092	0.21	0.32

Table 4.6: Mean Absolute error $|\mu|$ and Root Mean Square Error (RMS_e) between the observed near-surface temperature difference ΔT_{0-5m} (ΔT_{1-5m} for NORBAL-5) and the output of the COARE 3.0 algorithm for the varied shortwave absorption parameterisations.

the previous section. The period corresponding to the second SkinDeEP deployment is the most suitable part of the timeseries for comparison. The highest observed ΔT_{1-5m} on 22/4 matches the simulated when using PS81-III, confirming the in-situ observation of higher $[Chl]$ in the Mediterranean at the time of the NORBAL-5 campaign. If one would shift the ΔT_{1-5m} curve for PS81-III on the next day up such that it starts at the level of the observed remnant temperature gradient, its peak would approximately correspond to the observed. The Ohl00 and Mor94 with an input of $[Chl] = 2.0 \text{ mg m}^{-3}$ result in $0.2 \text{ }^\circ\text{C}$ lower warming. Increasing $[Chl]$ to 5.0 mg m^{-3} reduces this difference to less than $0.1 \text{ }^\circ\text{C}$ (not shown).

The scatter plots in Figure 4.34 show that the observed and modelled ΔT_{0-5m} for both North-Atlantic datasets generally follow the one-to-one line, however with a significant spread for increased warming. This comparison again shows that the choice of f_x -model significantly changes the outcome of the warm layer model.

Table 4.6 listing the mean absolute bias and RMS-error between the modelled and observed ΔT_{0-5m} , indicates that statistically there is very little difference between the different f_x models. The RMS-error in ΔT_{0-5m} varies from 0.042-0.11 $^\circ\text{C}$ for the North Atlantic datasets, and is a magnitude higher for the Mediterranean, 0.32-0.48 $^\circ\text{C}$.

The difference caused by varying the absorption parameterisations is thus smaller than the default bias between the original F96-and the observations, especially in the Mediterranean dataset. For STRASSE the PS81-I, PS81-IB, Ohl00 with $[Chl] = 0.05$ and 2.0 mg m^{-3} result in a lower RMS-error than F96; for MIDAS it is only the Mor94 for $[Chl] = 0.05 \text{ mg m}^{-3}$ that forms an improvement.

	STRASSE		MIDAS		NORBAL-5	
	$ \mu $	RMSe	$ \mu $	RMSe	$ \mu $	RMSe
F96	0.028	0.041	0.066	0.089	0.55	0.70
Jer76-I	0.025	0.037	0.060	0.079	0.53	0.68
Jer76-IB	0.028	0.039	0.061	0.078	0.51	0.65
Jer76-II	0.030	0.042	0.064	0.081	0.50	0.64
Jer76-III	0.034	0.042	0.067	0.086	0.51	0.63
PS81-I	0.032	0.042	0.071	0.096	0.55	0.71
PS81-IB	0.033	0.044	0.073	0.099	0.55	0.71
PS81-II	0.035	0.047	0.076	0.104	0.56	0.72
PS81-III	0.044	0.059	0.089	0.125	0.51	0.67
Ohl00 _{0.05}	0.028	0.039	0.073	0.103	0.54	0.70
Ohl00 _{2.0}	0.036	0.047	0.089	0.126	0.50	0.65
Ohl00 _{5.0}	0.043	0.058	0.103	0.145	0.57	0.74
Ohl03 _{0.05}	0.025	0.039	0.058	0.076	0.51	0.70
Ohl03 _{2.0}	0.033	0.045	0.064	0.083	0.52	0.66
Ohl03 _{5.0}	0.039	0.051	0.070	0.093	0.53	0.68
Mor94 _{0.05}	0.027	0.038	0.062	0.081	0.53	0.68
Mor94 _{2.0}	0.035	0.047	0.074	0.099	0.46	0.60
Mor94 _{5.0}	0.041	0.055	0.083	0.115	0.57	0.75

Table 4.7: Mean Absolute error $|\mu|$ and Root Mean Square Error (RMSe) between the observed subsurface temperature T_{0-} and the output of the COARE 3.0 algorithm for the varied shortwave absorption parameterisations. For the NORBAL-5 campaign the temperature at 1 m depth is compared.

The temperature directly below the ocean skin layer, T_{0-} , observed by the vertical profilers, is also compared to the model output. Here is used $T_{0-} = T_z + \Delta T_w$ for the COARE output of the North-Atlantic. For the NORBAL-5 campaign, since T_{skin} was used as an input to COARE, and we do not avail of a complete record of in-situ observations directly below the surface, instead the observed and predicted temperature at a depth of 1 m are compared, using $T_{1m} = T_{skin} + \Delta T_c - \frac{\Delta T_w}{D_w}$. The observed and the modelled T_{0-} / T_{1m} for the different f_x -models are plotted against each other in fig. 4.35. Tab. 4.7 lists the mean bias and RMS-error from this comparison for the three research campaigns. The mean bias and RMS-error vary little between the absorption models, ranging from RMS = 0.076-0.126 °C in MIDAS and only 0.038 - 0.59 °C in STRASSE. For NORBAL-5 again the bias and RMS-error are an order of magnitude larger, although there is little difference between the absorption parameterisations. The parameterisation resulting in the the best fit to T_{0-} remarkably is not the same as the best estimator of ΔT_{0-5m} ; in both North Atlantic campaigns the less complex parameterisations Jer76 and Ohl03 give the best result.

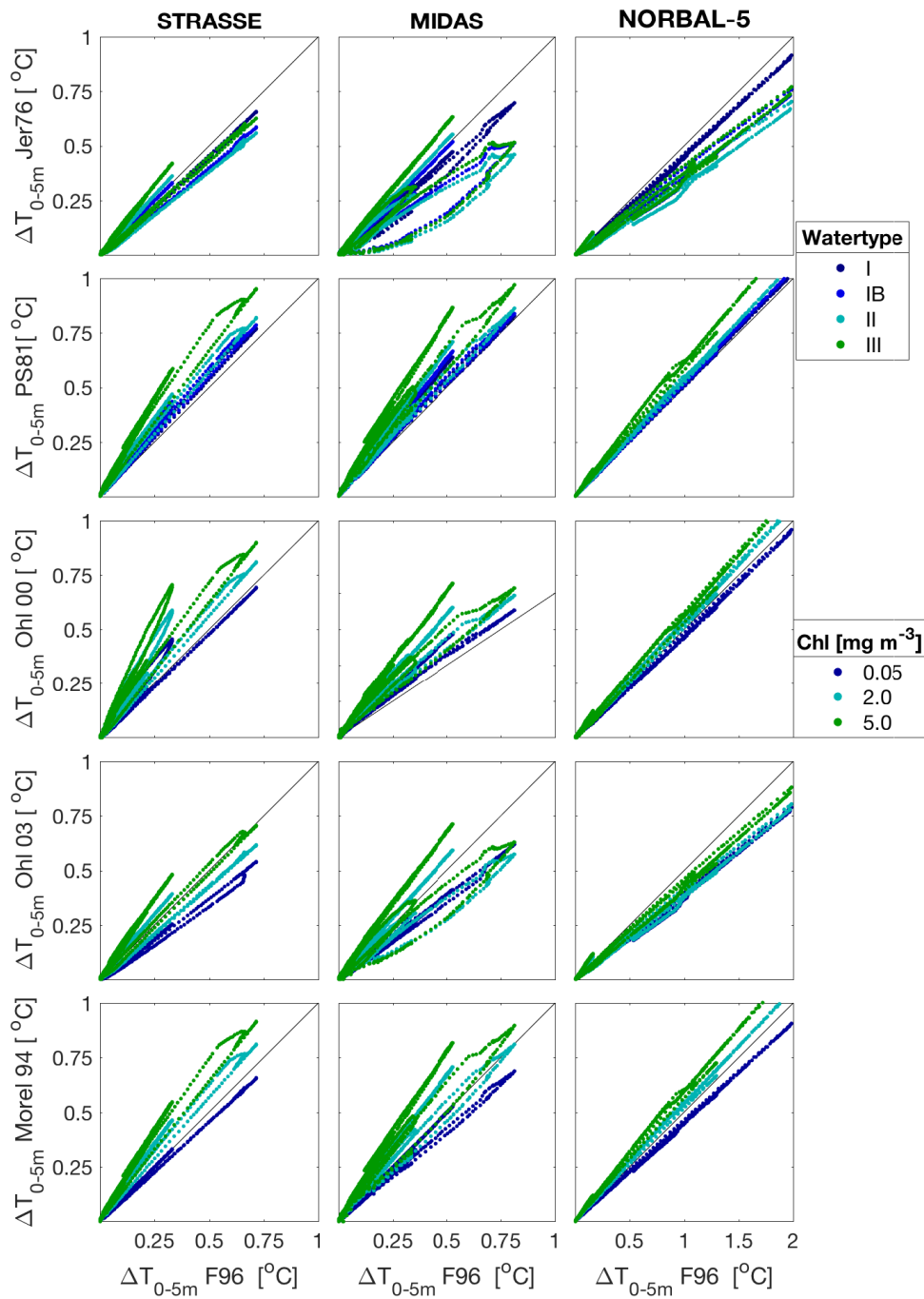


Figure 4.30: Scatter plots the change in warm layer correction ΔT_{0-5m} for different shortwave absorption parameterisations, *Jerlov* (1976) (Jer76) *Paulson and Simpson* (1981) (PS81), *Ohlmann and Siegel* (2000) (Ohl 00), *Ohlmann* (2003) (Ohl 03), *Morel and Antoine* (1994) (Morel 94), in comparison to the default ("F96"). Colors in Jer76 and PS81-plots indicate the result for different watertypes (see Tables 4.3 and 4.4), and different *Chl*-concentrations in the other panels.

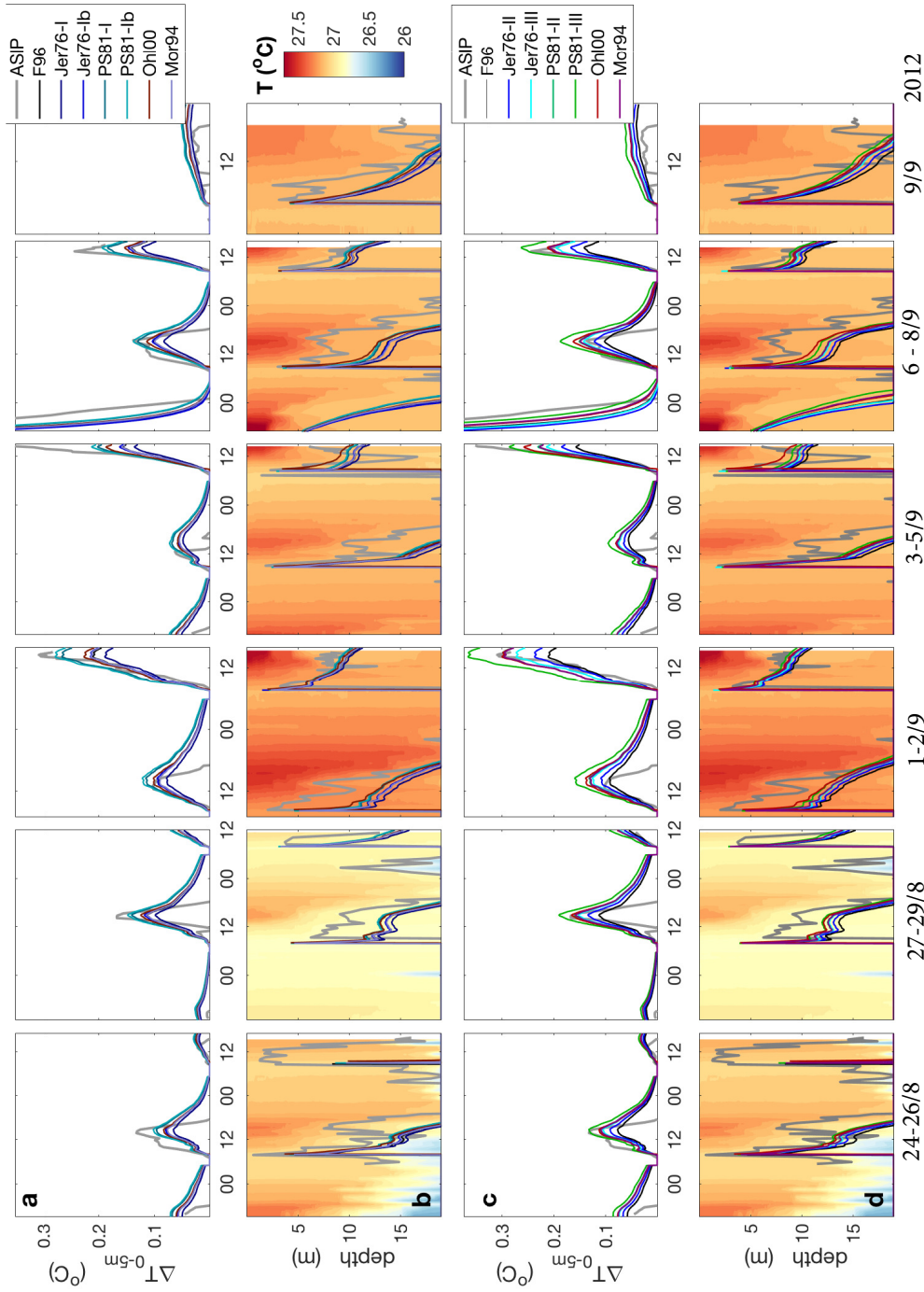


Figure 4.31: Predicted temperature difference over the upper 5 m as well as warm layer depth D_w simulated by the COARE model using different shortwave absorption parameterisations, for the STRASSE dataset. **a** and **c** show the result for the f_x -models representing optical water type I and Ib or low chlorophyll-concentration ($[Chl] = 0.5 \text{ mg L}^{-1}$), whilst in **b** and **d** the same models are shown for coefficients representing water type II and III or higher chlorophyll-concentration ($[Chl] = 2 \text{ mg L}^{-1}$).

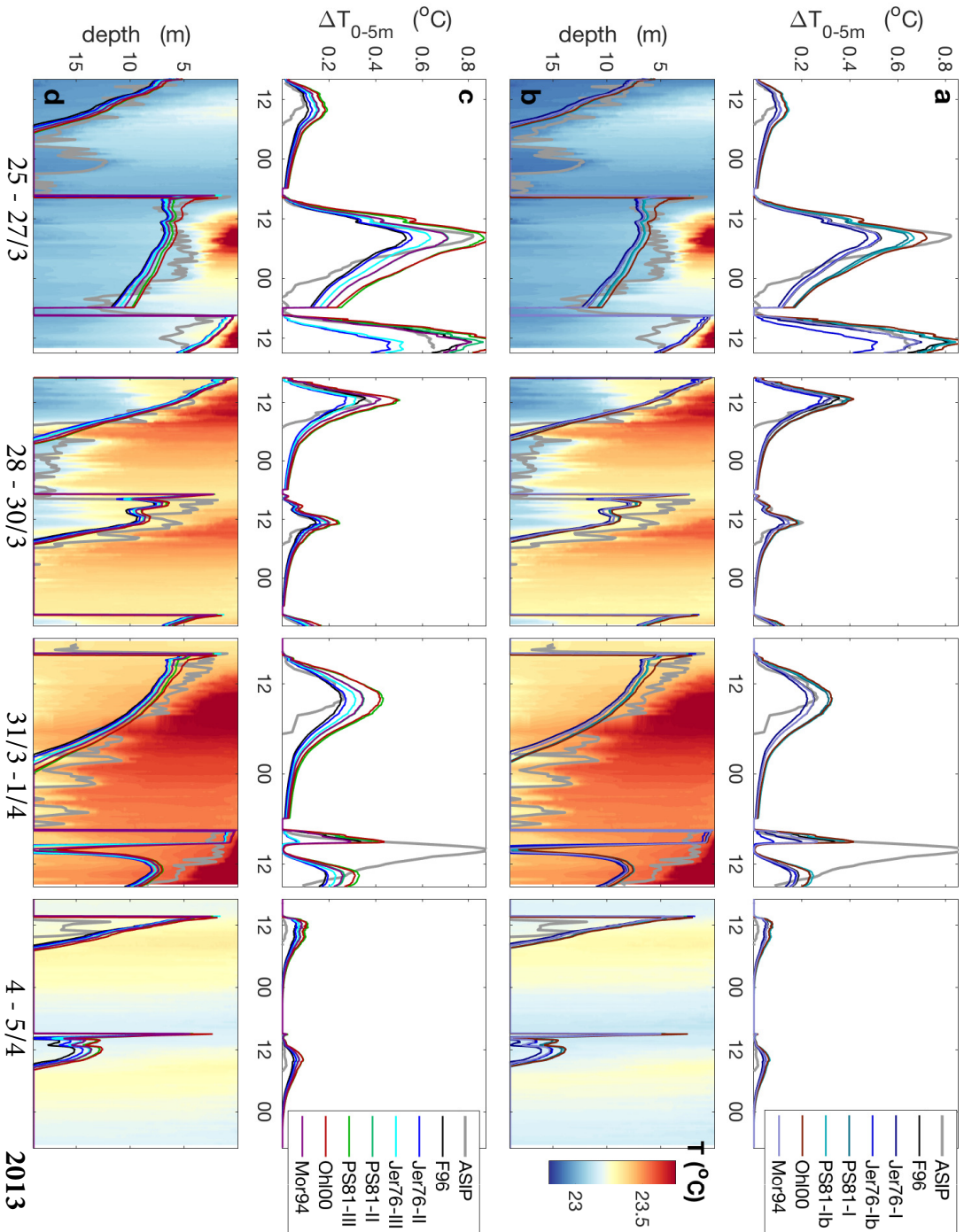


Figure 4.32: Predicted temperature difference over the upper 5 m as well as warm layer depth D_w simulated by the COARE model using different shortwave absorption parameterisations, for the MIDAS dataset. **a** and **c** show the result for the f_x -models representing optical water type I and Ib or low chlorophyll-concentration ($[Chl] = 0.5 \text{ mg L}^{-1}$), whilst in **b** and **d** the same models are shown for coefficients representing water type II and III or higher chlorophyll-concentration ($[Chl] = 2 \text{ mg L}^{-1}$).

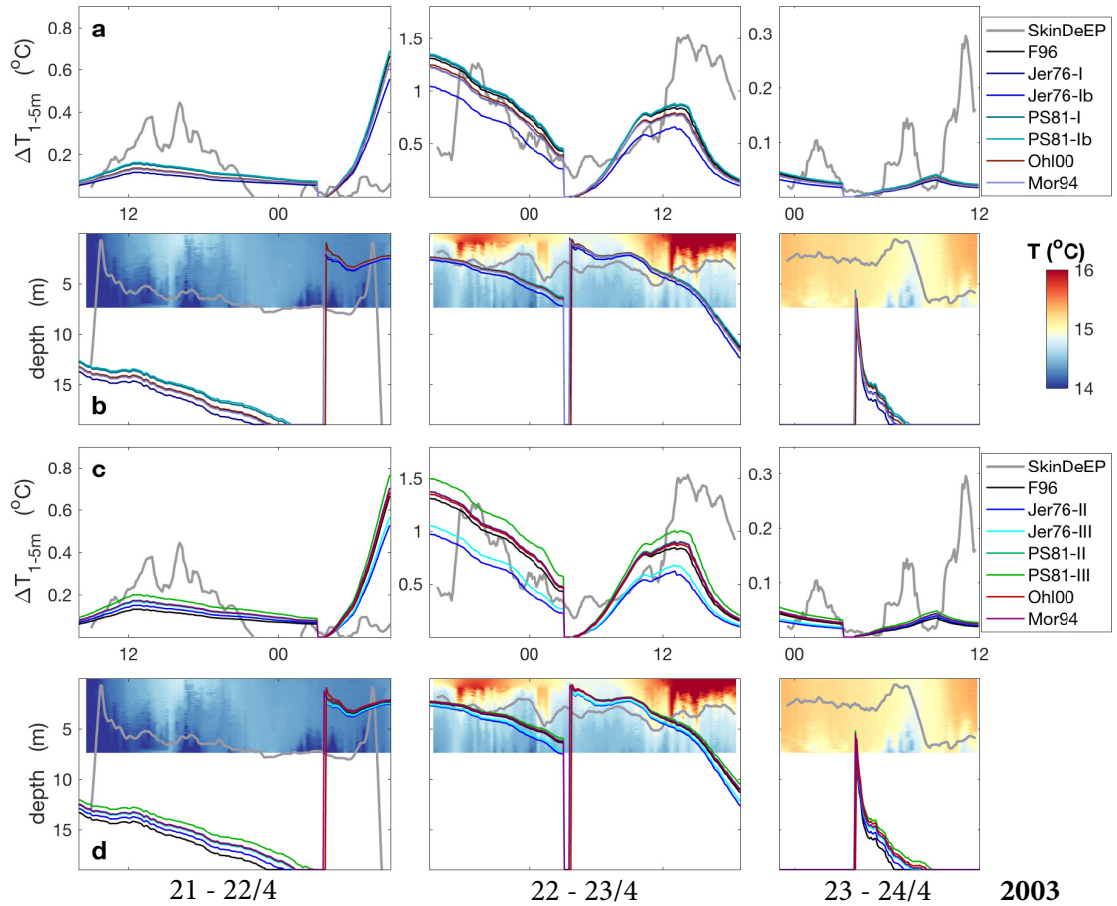


Figure 4.33: Predicted temperature difference over the upper 1-5 m as well as warm layer depth D_w simulated by the COARE model using different shortwave absorption parameterisations, for the NORBAL datasets. **a** and **c** show the result for the f_x -models representing optical water rtype I and Ib or low chlorophyll-concentration ($[Chl] = 0.5 \text{ mg L}^{-1}$), whilst in **b** and **d** the same models are shown for coefficients representing water type II and III or higher chlorophyll-concentration ($[Chl] = 2 \text{ mg L}^{-1}$).

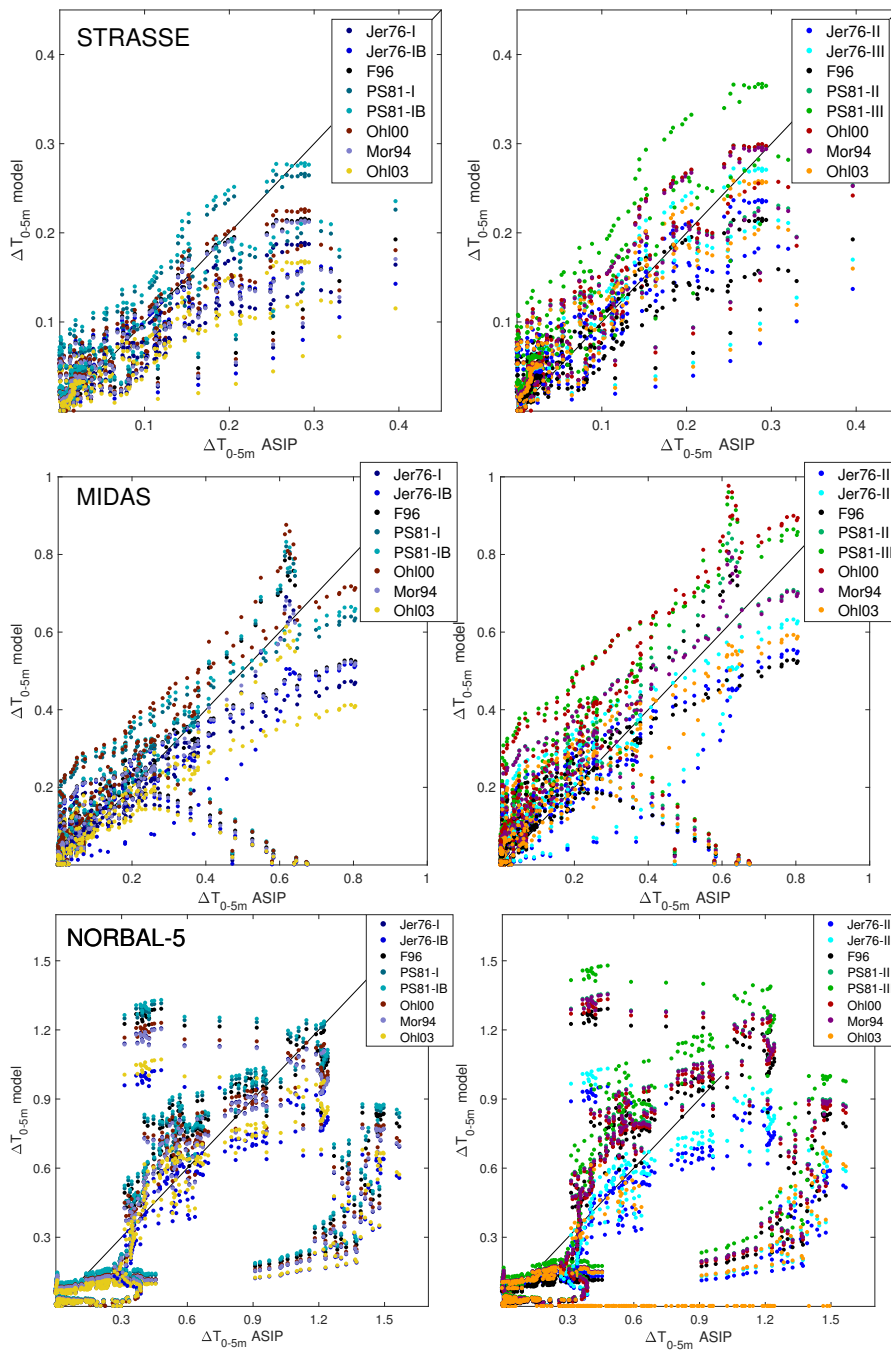


Figure 4.34: Modelled ΔT_{0-5m} versus observed from ASIP / SkinDeEP profiles, for 12 different shortwave absorption parameterisations for low turbidity/[Chl] water (left) and higher turbidity/[Chl] water (right).

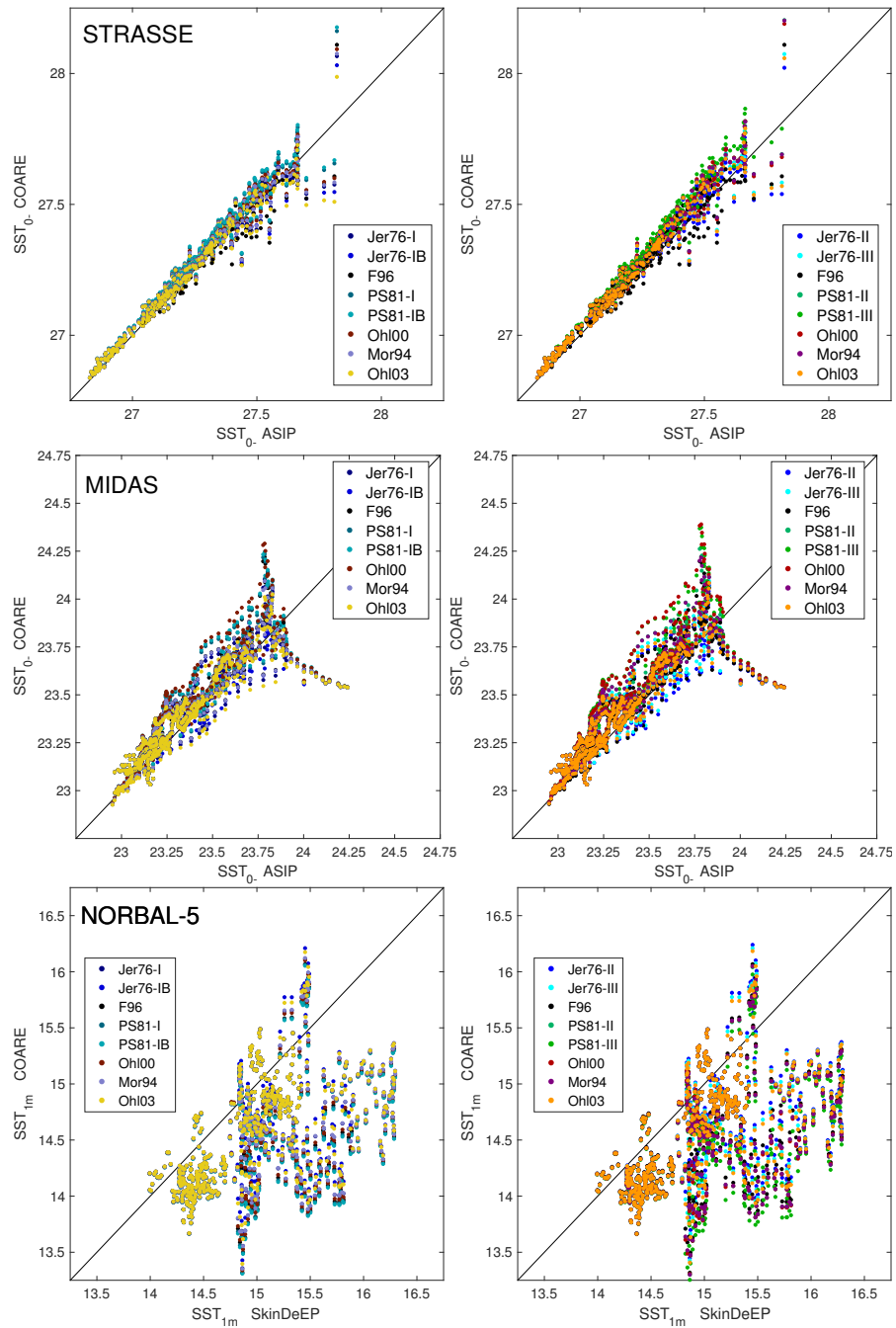


Figure 4.35: Modelled T_{0-} / T_{1m} versus observed from ASIP / SkinDeEP profiles, for 12 different shortwave absorption parameterisations for low turbidity/[Chl] water (left column) and higher turbidity/[Chl] water (right column).

4.8 Discussion and Conclusions

Diurnal warming near the ocean surface is an extensively studied phenomena, due to its implications on upper ocean mixing, satellite retrievals of sea surface temperature, and air-sea coupling in models used in weather prediction and climate simulations. In this study the vertical evolution of the temperature of the near-surface layer is investigated from both observations and a bulk flux algorithm with a 1D warm layer component. Horizontal processes, such as advection by large scale eddies and inertial oscillations, are neither taken into account in the data analysis or the model. Large scale advection in the North Atlantic dataset due to mesoscale eddies (*Farrar et al.*, 2015), acts at a slower time scale. The diurnal variability in the Mediterranean is more likely to be subject to lateral processes, although no evidence of it is seen in the temperature record presented here.

From a review of observations in several oceans *Dickey and Simpson* (1983) reported that diurnal variability of the sea-water temperature has an amplitude ranging from < 0.1 to 2 °C, and is discernible down to a depth of 30 m. The highest temperature at the surface typically follows two to four hours after the peak in insolation, whilst deeper layers warm up after a certain time lag. Characteristics of the observed DWLs in the three datasets presented in this chapter correspond well to this general description. Nevertheless, the observed diurnal warming events are quite variable between the three different datasets, and between individual events during the same research campaign. Above a certain wind speed, diurnal warming is observed throughout the mixed layer, however without the presence of a shallow thermocline. For decreasing wind speed, a warm near-surface mixed layer is observed to form during daytime, which disappears during the evening and night. During the lowest wind speed conditions, a strong amplitude in the subsurface temperature occurs, and the warming is confined to the upper 2-3 m for most of the daytime. However, the relatively limited amount of observations cannot provide a robust estimate to exactly distinguish the range of wind speeds governing each of these three regimes. In the low wind speed regime a warm surface layer is seen to remain until the following morning. Repeated days with a remnant warm layer during the spring campaign result in a period of total surface mixed layer warming. Over the course of a week the temperature of the upper 20 m increased by 0.5 °C. This remarkably rapid, though short-lived, mixed layer temperature increase must be measurable from daily satellite SST images, and could serve as a proxy for diurnal warming of significant amplitude (here 2 times the amplitude of the nighttime mixed layer temperature).

The observations from the subtropical North Atlantic show that the timing of the occurrence of the maximum daily SST increases with its amplitude. This is an important finding, since simple parameterisations, which are used to simulate diurnal warming in coupled ocean atmosphere models, do not allow for a variability in the phase of warming. As an example the *Webster et al.* (1996) parameterisation (see section 2.3.1 of diurnal amplitude is tested for conditions encountered during the MIDAS campaign (formulated in Equation (2.23)). It is found that the amplitude at the surface is consistently overestimated (fig.4.36).

To bridge the gap between simple empirical models of diurnal warming and computationally more costly bulk-mixed layer models, *Stuart-Menteth et al.* (2005) used four wind speed and two insolation values per day, to include the effect of meteorological fluctuations on diurnal SST variability. The warm layer component of the COARE bulk flux algorithm is a simplified 1D-vertical model, which responds directly to variability in the meteorological forcing. Consequently the phase of the diurnal warming is not fixed. From the comparison between the output of the algorithm, and the observed temperature difference over the upper 5 m, it follows that COARE accurately simulates the timing and amplitude of the peak warming (fig. 4.21 and 4.25). Where COARE does not perform well is in the reduction of the warm layer after the peak warming. Although the deepening rate of the modelled D_w does correspond to observations, the temperature gradient over the upper 5 m is much higher than observed. This was previously concluded by *Prytherch et al.* (2013) after an analysis of 4712 days of SST observations in the upper metre from moorings in (sub-) tropical locations. One explanation for this is the under-representation of convective mixing in the COARE model, since the DWL is only determined by the balance between stratification and accumulated shear momentum over its depth. Similarity scaling shows that convection often dominates the turbulence after sunset, and in those cases the COARE model will underestimate the breakdown of the DWL. It also confirms that the buoyancy effect of the diurnal warming suppresses the turbulence during daytime, resulting in $|h/L| > 1$, although only for a short period during the days of stronger winds in both campaigns.

The algorithm's linear temperature profile between the surface and D_w deviates most from reality during the second part of the day, since after the peak warming the temperature profile of the warm layer is typically well mixed between the surface and the top of the diurnal thermocline. Although the bias between the observed and modelled sub-surface temperature is smaller than 0.1 °C (fig. 4.22). The total heat content of the DWL therefore must be accurately simulated, and can be understood by the fact that D_w is nearly always overestimated. This leads to the conclusion that the DWL correction in COARE is accurate in predicting diurnal variability of the interfacial sea surface temperature, and can be used for satellite validation and air-sea flux computations. However, the output from the warm layer model should not be taken literally to correct a given T_z towards T_{0-} , when $z < D_w$.

This shortcoming has been one of the motivations to the development of an improved bulk flux algorithm in *Gentemann et al.* (2009). The main change in this model is the replacement of the linear profile in COARE by a windspeed dependent exponential curve. The vertical structure introduced in the POSH model (Profiles of Ocean Surface Heating) corresponds to a more realistic temperature profile (fig. 2.6). To represent losses of heat and momentum by entrainment at the bottom of the mixed layer, conduction and dissipation, a reduction rate to the accumulated heat and momentum is applied at each time step. Similar to the modification to COARE used in this chapter, the POSH model resets the accumulated heat-and momentum fluxes in the mixed layer at 6 AM, instead of at midnight. After

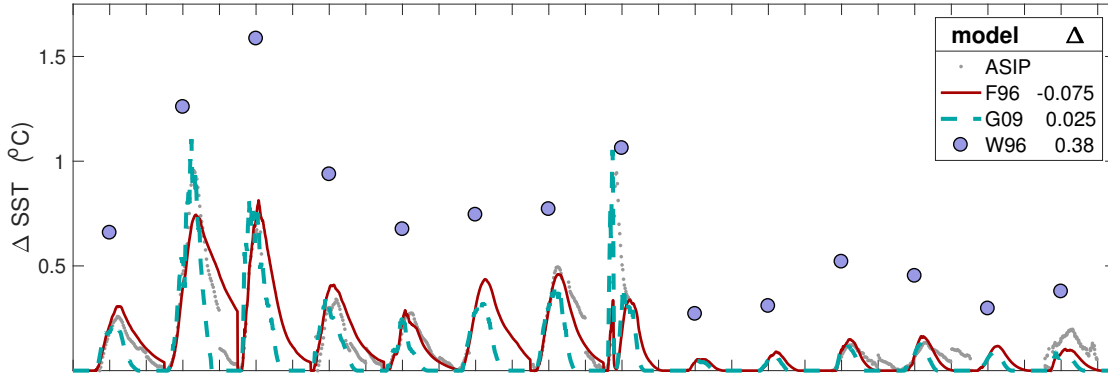


Figure 4.36: Diurnal amplitude in T_{0-} from ASIP measurements during the MIDAS campaign, and following the COARE 3.0 and POSH algorithms. Purple dots indicate the diurnal amplitude following the parameterisation of *Webster et al.* (1996). Δ is the mean bias between the modelled and observed peak ΔT .

personal communication with C. Gentemann the POSH model was run for a subset of the MIDAS campaign, the result of which is shown in fig. 4.36. The wind speed dependent profile improves the predicted peak SST during the days of low wind speed. The reduction of the DWL during the afternoon is more rapid according to POSH, but generally even more rapid than observed. POSH is still a bulk-flux algorithm, which is computationally efficient, however, like COARE, cannot be expected to fully simulate the vertical structure of the warm layer due to the simplified formulation of the mixed layer dynamics.

Whether a DWL forms, its amplitude at the surface and the evolution of the warming in the vertical, is highly sensitive to the atmospheric forcing, as is the COARE algorithm. This results in its performance, as well as that of models of higher complexity in simulating the amplitude of the diurnal SST variability, being strongly dependent on the input data set (*Karagali et al.*, 2017), as illustrated with the sensitivity test in fig. 4.24. It is crucial in predicting the amplitude and phase of diurnal warming to avail of reliable local meteorological information. Nevertheless, the autonomy of the ASIP implies that at times there can be a spatial separation between the oceanic measurements and the meteorological station used to force the model. Small differences in wind speed and insolation over this distance (e.g. due to the passage of clouds), can explain the differences in near surface warming between the model and the observed SST time series.

The sensitivity of the modelled diurnal warming to the parameterisation of the radiative flux is found to be significant, leading to differences in predicted warm layer temperature of > 0.1 °C. Increased turbidity or $[Chl]$ results in a more shallow warm layer with a higher diurnal SST amplitude. This can be either a permanent state near coasts, or reflect a seasonal variation (phytoplankton blooms). The amount of days with warm layers used in this study is relatively limited, and the individual DWL's are quite variable. It is therefore not possible to choose the optimal parameterisation for shortwave absorption to use in the COARE algorithm

with statistical confidence. No systematic difference in the warm layer prediction was found by *Wick et al.* (2005), who tested the performance of the modified COARE algorithm, using the shortwave transmission parameterisation of *Ohlmann and Siegel* (2000), to describe the cool skin and warm layer. Statistically any change of f_x -parameterisation does not lead to a major improvement in the simulated warm layer temperature difference or SST.

It is preferable to use a model which is independent of the availability of chlorophyll-pigment concentration, and in that case the F96 description of radiation absorption is reasonably accurate. For more local studies when $[Chl]$ can be obtained from in-situ samples or ocean-colour satellite data, nevertheless it is worthwhile to include the dependence of f_x on $[Chl]$, either using the Mor94 or Ohl00 formulation (equations(4.6) and (4.8) or(4.10) and (4.11) respectively). The albedo changes to the path length of the incoming radiation, which significantly changes the absorption profile, especially for the IR part of the spectrum. Both the Mor94 and Ohl00 parameterisations improve the physics, by explicitly including the change in light absorption as a function of the sea surface albedo and the spectral distribution of light on the solar zenith angle. *Gentemann et al.* (2009) also suggested a zenith angle effect into the nine-exponent *Paulson and Simpson* (1981) absorption formulation:

$$\frac{I_d(z)}{I_d(0^-)} = \sum_{i=1}^9 F_i \exp\left(\frac{-z \cos \theta}{L_i}\right) \quad (4.14)$$

DWL-simulations by other bulk-mixed layer models as well as by diffusion models, have proven to perform better with this or other more complex shortwave absorption parameterisations as well. In the POSH model the nine-wavelength band by *Paulson and Simpson* (1981) (PS81) was used. The 1D turbulence closure model GOTM was also found to perform better with this, in comparison to its default 2-exponent absorption curve (*Pimentel et al.*, 2008; *Karagali et al.*, 2017). After sensitivity tests with the turbulence closure model by *Kantha and Clayson* (1994) the parameterisation by *Morel and Antoine* (1994) (Mor94) was chosen to be sufficiently accurate. Advances in in-situ measurements of the light transmission may give insight to which of the parameterisations is the most accurate in representing reality. DWL models can then be adapted to use the most realistic model.

5 Upper Ocean Response to Rainfall

5.1 Introduction and Motivation

Rainfall forms a flux of freshwater to the OSBL. Its variability directly influences the rate of exchange of heat, momentum and mass (moisture, greenhouse gases, etc.) between the ocean and the atmosphere. The OSBL is typically well mixed and has a quasi-homogeneous density profile. However, rain falling on the surface can induce a vertical salinity gradient in the upper few meters, changing the buoyancy of the near-surface water. There is a lot of uncertainty about the magnitude and duration of these rain-induced salinity anomalies, also known as freshwater lenses. Most direct observations of rain effects in the open ocean are in tropical regions, where rainfall is frequent and intense. Rain-induced salinity anomalies here can have lateral scales of tens of kilometres (*Soloviev and Schlüssel, 1996; Wijesekera et al., 1999; Asher et al., 2014*) and last for a few hours (*Price, 1979; Brainerd and Gregg, 1997; Anderson and Riser, 2014; Drushka et al., 2014*), up to tens of hours (*Walesby et al., 2015*). *Riser et al. (2015)* observed a rainfall event within a dominantly evaporative region of the sub-tropical North Atlantic, which initially caused a significant surface salinity and temperature anomaly (1 psu and 0.7°C respectively), and consequently a decrease of the salinity of the total mixed layer. Turbulent mixing in the OSBL, resulting from wind-driven shear, breaking waves, and convection, as well as ambient currents, interact with the rain-induced stratification and eventually disperse it. The mechanical impact of the raindrops itself is thought to be a source of turbulence in the upper centimetres of the ocean. The falling raindrops break the surface and increase the surface stress, potentially enhancing surface renewal rates. However the simultaneous freshening of small, non-penetrating raindrops can also stabilise the very surface (skin) layer, which would reduce the air-sea exchange rates (*Schlüssel et al., 1997*).

The individual effects of rain on the turbulent dynamics and air-water fluxes have predominantly been studied in laboratory settings; the response of the ocean to rain has been rarely monitored in-situ, due to technological challenges of measuring close to the surface, as well as the complexity of the phenomena. Therefore the importance of the ocean's response to rain on the coupled ocean-atmosphere system still remains uncertain. Tropical rain-induced freshwater lenses could affect the mixed layer dynamics to a similar magnitude as diurnal warming (*Drushka et al., 2014*), which has been shown to cause a significant error in global heat flux estimates (e.g. *Clayson and Bogdanoff, 2013*). Uncertainties about the surface water budget can cause significant errors to latent heat flux computations (*Marullo et al., 2016*).

It requires many observations of individual rain events in different regions of the World's oceans to adequately characterise their variability, estimate their total impact, and appropriately parameterise rainfall effects for use in climate models. Another reason to further quantify the magnitude and frequency of rain-induced surface anomalies is the implications for satellite remote sensing of SSS and SST. A freshwater bias is often encountered in validation studies, which compare satellite-SSS to measurements from ARGO floats. This bias is partially ascribed to rainfall effects, especially in tropical oceans. Outside the presence of rain the OSBL is well mixed and has a quasi-homogeneous density profile. In these conditions an in-situ measurement at a few meters below the surface is expected to correspond to the surface salinity. However, a rain induced vertical salinity gradient in the upper few meters will be missed by most ARGO floats, which do not measure at depths shallower than 5 m (*Reverdin et al.*, 2012). *Boutin et al.* (2013) estimated that the difference between satellite (SMOS) and ARGO SSS at 5 m below the surface is linearly correlated to rain rates inferred from collocated satellite observations.

5.2 Oceanographic Campaign and Instrumentation

Measurements were conducted during an oceanographic campaign aboard the R/V-Knorr in the early summer of 2011 in the North Atlantic. The ship went from Woods Hole MA towards the south of Greenland (fig. 5.1). The main goal of this campaign was to acquire an observational dataset of surface ocean properties and air-sea fluxes during phytoplankton blooms through a combination of meteorological, wave, and whitecap measurements, as well as direct measurements of temperature, salinity, and turbulence in the mixed layer (sec. 3.1).

5.2.1 Microstructure Measurements

Microstructure profiles of the upper 60m of the water column were obtained with the ASIP, equipped with the sensor suite described in sec. 3.2 In open ocean conditions the ASIP is assumed to be a semi-Lagrangian instrument; the profiler will be moving along with a specific water mass and thus is expected to capture its response to changing surface forcing.

In this study measurements obtained during the first deployment of the ASIP are used. A total of 58 profiles were obtained between June 26th 18:30 h and June 27th 12:15 h (local time), at the approximate location indicated by '1' in fig. 5.1 (~ 40.25 N, 58.9 W).

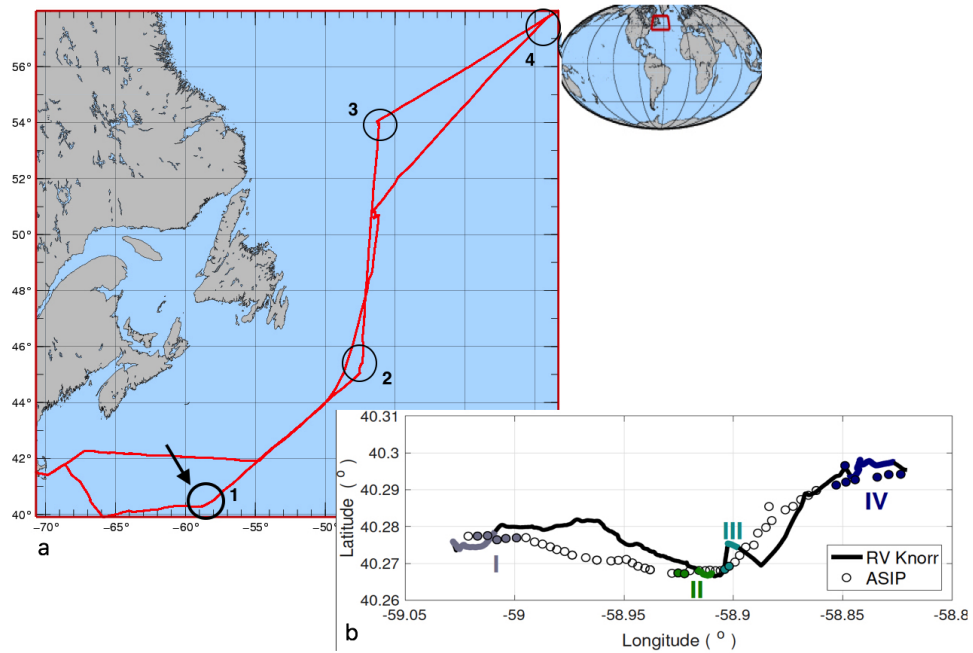


Figure 5.1: **a.** Map of the ship track of the Knorr-11 cruise, with circles indicating the approximate locations of ASIP deployments. Observations from deployment 1 are used in this chapter. **b.** The exact location of the ASIP profiles, with colors indicating the sections of both the ASIP and the ship track corresponding to the rainy periods.

5.2.2 Meteorology and Air-Sea Fluxes

An eddy covariance system was installed on the bow mast of the research vessel, consisting of two CSat3 sonic anemometers and a 3D inertial motion unit, to correct the wind measurements for ship motion (*Miller et al.*, 2009; *Landwehr et al.*, 2015). The setup resulted in direct estimates of momentum, heat, and gas fluxes (*Bell et al.*, 2013, 2017). General meteorological observations were made with two Vaisala WXT520 weather system on the research vessel, also mounted on the bow mast. These systems contain a piezoelectrical sensor to measure rain intensity from the impact of individual raindrops recorded over 10 s-intervals. The data was made available as 1-minute averages, and to compute rain rate the mean of both weather systems is computed. Other meteorological observations were wind speed, wind direction, downwelling short- and longwave radiation, air temperature, barometric pressure, and relative humidity. These data were used to compute heat and momentum fluxes using the COARE 3.0 bulk-flux algorithm (*Fairall et al.*, 1996a, 2003). The algorithm was run for an input time series at 2-minute resolution, to ensure that the rain rates and the rapid variability in other parameters associated to the passing of a rain event is retained. Instead of bulk-temperature and salinity from the ship intake, a time series from the interpolated record of the average T and S in the top 5 cm observed with the vertical profiler ASIP is used. This was conducted to improve the flux computations (avoiding the need for a warm layer correction) and because of a mismatch between the ship's thermosalinograph

record and the ASIP observations.

As can be seen in fig. 5.1 the vessel remained in the vicinity of the profiler for the duration of this ASIP deployment, so the atmospheric conditions of the profiler's location are expected to be well represented by the meteorological measurements from the ship. Rain of various intensity occurred during the measurement period. Four rain events are considered, each of an intensity larger than 10 mm h^{-1} and a duration long enough for a minimum of two ASIP profiles to take place. Characteristics of the rain events are listed in Table 5.1.

#	R_{max} [mm h^{-1}]	R_{tot} [mm]	duration [min]	\overline{U}_{10}	U_{10max} [m s^{-1}]
I	20	4.4	96	7.1	10.2
II	15	2.6	45	9	10.7
III	72	14.6	45	7.8	9.6
IV	45	18.4	135	6	8.6

Table 5.1: Characteristics of the four observed rain events: peak rain rate R_{max} , cumulative rain R_{tot} , duration, mean and maximum 10-m windspeed U_{10} during the rain event.

5.2.3 Wave Observations

One-dimensional spectra of surface gravity waves, from which the significant wave height H_{sig} and the wave spectral energy $E(f)$ are derived, are measured using an ultrasonic altimeter in combination with a motion correction device. These were mounted at the end of a steel pole, pointing down from a hole on the bow of the research vessel (see *Christensen et al. (2013)* for a detailed description). The waves measured were limited to the frequency band $f = 0.05 - 0.4 \text{ Hz}$; the high-frequency tail of the wave spectrum, to which the rain is thought to have a dampening effect, is not within the resolution of the sensor.

5.3 Air-Sea Fluxes during Rain

The initial formation and evolution of a freshwater lens depend on the balance between the stabilizing buoyancy forces and de-stabilizing processes of shear-driven and wave-induced turbulent mixing during and after a rainfall event. To understand the observed changes near the ocean surface following rainfall, the measured air-sea fluxes and relations between them are analyzed.

The stability of the OSBL is determined by the density profile, and changes therein due to the fluxes of heat and moisture at the surface. This is described by the density flux Q_ρ and the surface buoyancy flux B_0 , defined in eq. 2.11 and 2.10 respectively. Under the assumption that the rain is at the wet-bulb temperature, the intrusion of rainwater at the sea surface can be interpreted as a heat flux contributing to additional ocean cooling when the air-sea temperature difference is negative. For use in a bulk-flux algorithm this additional sensible heat flux Q_{Sr}

can be computed as:

$$Q_{Sr} = R c_{pw} \alpha_w \left(\Delta T + \frac{\Delta q L_e}{c_{pa}} \right) \quad (5.1)$$

where R is the rain rate (in units of m s^{-1}), c_{pw} and c_{pa} are the specific heat of water and air respectively, ΔT and Δq are the sea-air temperature and specific humidity differences respectively, L_e is the latent heat of evaporation, and α_w is the Clausius-Clapeyron wet-bulb factor (*Gosnell et al.*, 1995; *Fairall et al.*, 1996a). Precipitation often occurs together with changes in the wind conditions. Whether the average surface wind speed increases together with gusts before and during the rain, or the opposite occurs, and rainfall coincides with a calmer atmosphere, is largely dependent on the type of cloud associated with the rain event (*Webster et al.*, 1996). Modification of the momentum flux into the ocean has a direct effect on the available energy for vertical mixing and waves. Rain carried by the wind will have acquired both vertical and horizontal momentum when hitting the surface, producing an additional momentum flux. The horizontal momentum of the falling raindrops in windy conditions is represented as a tangential surface stress τ_r , linearly related to the rain rate and the 10 m-wind speed U_{10} (*Caldwell and Elliott*, 1971):

$$\tau_r = 0.85 U_{10} \rho_r R, \quad (5.2)$$

where ρ_r is the density of the raindrops. Raindrops that break through the surface create splashes, jets, bubbles and high-frequency waves, which increases the turbulent mixing directly below the surface (*Tsimplis*, 1992; *Schlüssel et al.*, 1997; *Liu et al.*, 2017). This can be described with a kinetic energy flux (E_k in W m^{-2}), computed as a function of the terminal velocity of raindrops, w_t (*Green and Houk*, 1979):

$$E_k = \frac{1}{2} \rho_r R w_t^2. \quad (5.3)$$

Considering R a volume flux, the total volume of rain is the integral of the volume of the individual rain drops. Assuming drops of a spherical shape with radius r :

$$V = V_u \int_0^\infty \frac{4}{3} \pi r^3 n(r) dr. \quad (5.4)$$

V_u is the unit volume, and $n(r)$ is the drop-size distribution. A simple but commonly used drop-size distribution, $n(r)$, for natural rain is the Marshall-Palmer distribution (*Marshall and Palmer*, 1948):

$$n(r) = n_0 \exp(-2\Lambda r). \quad (5.5)$$

$\Lambda = 4.1 R^{-0.21} \text{ mm}^{-1}$, $n_0 = 8 \times 10^{-3} \text{ m}^{-3} \text{ mm}^{-1}$, so $n(r)$ is only dependent on the rain rate R (see fig. 2.4). In reality $n(r)$ and R will also be dependent on the type of rain, position relative to the centre of the raincloud, relative humidity and cloud

height (*Best*, 1950).

Also the terminal velocity of rain at the ocean surface level is dependent on the size of the rain drops. An empirical formula by *Best* (1950) describes an exponential dependance:

$$w_t = w_v [1 - \exp(-(r_0/r_v)^v)]. \quad (5.6)$$

This is approximated for radii $r \leq 6$ mm as (*Schlüssel et al.*, 1997):

$$w_t = w_v [b_1 - b_2(\exp(-r/r_v))]. \quad (5.7)$$

Various values for the coefficients in (5.7) can be found in literature, e.g. *Lhermitte* (1988); *Schlüssel et al.* (1997); *Craeye and Schlüssel* (1998); *Soloviev and Lukas* (2014). Here the values from *Soloviev and Lukas* (2014) are used, since they agree best with *Best* (1950):

$w_v = 9.43 \text{ m s}^{-1}$, $b_1 = 1.0528$, $b_2 = 1.07733$ and $r_v = 1.77$ m.

The smallest raindrops will not submerge into the ocean, but form a surface-freshwater flux. An often assumed critical radius (r_c) for drop penetration is 0.4 mm (*Oguz and Prosperetti*, 1991). The fraction of the total volume of rain that penetrates the water surface, f_0 , then is

$$f_0 = \frac{V(r_c \rightarrow \infty)}{V(0 \rightarrow r_c)} = \frac{1}{6} \Gamma(4, 2\Lambda r_c), \quad (5.8)$$

where $\Gamma(j, x)$ is an upper incomplete gamma function, which can be expanded to (*Schlüssel et al.*, 1997):

$$f_0 = (1 + 2\Lambda r_c + 2\Lambda^2 r_c^2 + \frac{4}{3}\Lambda^3 r_c^3) \exp(-2\Lambda r_c). \quad (5.9)$$

Using to eq.5.3, for natural, non-homogenous rain, computation of E_k thus requires solving an integral over the range of dropsizes $r > r_c$:

$$E_k = \int_{r_c}^{\infty} \frac{2}{3} \rho_r \pi r^3 n(r) w_t(r)^3 dr, \quad (5.10)$$

and when using equations (5.5) and (5.7) this becomes

$$\begin{aligned} E_k &= \frac{2}{3} \pi \rho_r \int_{r_c}^{\infty} r^3 n_0 \exp(-2\Lambda r) [w_v (b_1 - b_2 \exp(-r/r_v))]^3 dr, \\ &= \frac{2}{3} \pi \rho_r n_0 w_v^3 \int_{r_c}^{\infty} r^3 [b_1^3 \exp(2\Lambda r) - 3b_1^2 b_2 \exp(-r(2\Lambda + r_v^{-1})) \\ &\quad + 3b_1 b_2^2 \exp(-r(2\Lambda + 2r_v^{-1})) - b_2^3 \exp(-r(2\Lambda + 3r_v^{-1}))] dr. \end{aligned} \quad (5.11)$$

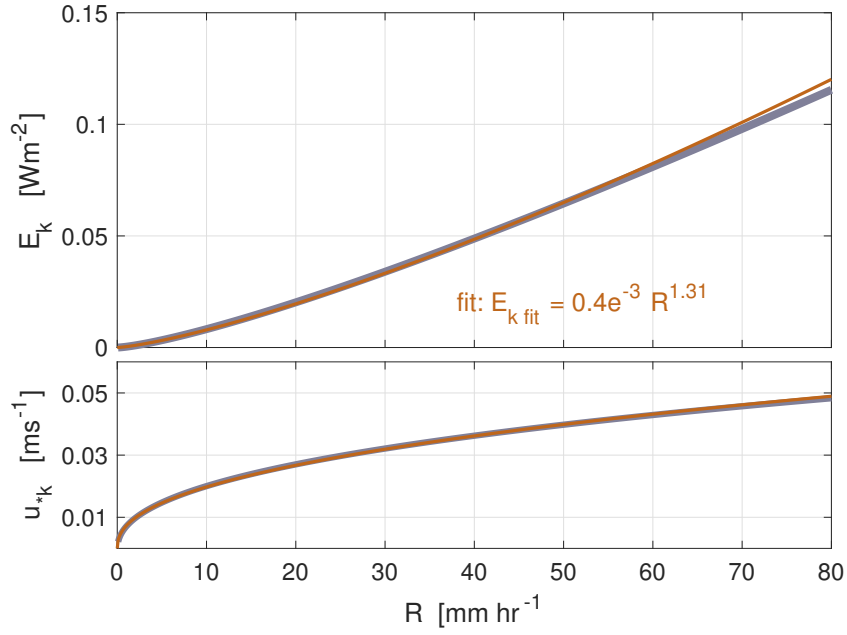


Figure 5.2: Power law fit (red) to the exact solution (blue) of E_k in *Schlüssel et al.* (1997) and *Soloviev and Lukas* (2014)

As in eq. 5.8 this integral can be solved with an incomplete gamma function:

$$\begin{aligned}
 E_k = & \frac{2}{3} \rho_r \pi n_0 w_v^3 \left[\frac{b_1^3}{(2\Lambda)^4} \Gamma(4, 2\Lambda r_c) - \frac{3b_1^2 b_2}{(2\Lambda + r_v^{-1})^4} \Gamma(4, 2\Lambda r_c + \frac{r_c}{r_v}) \right. \\
 & \left. + \frac{3b_1 b_2^2}{(2\Lambda + 2r_v^{-1})^4} \Gamma(4, 2\Lambda r_c + \frac{2r_c}{r_v}) - \frac{b_2^3}{(2\Lambda + 3r_v^{-1})^4} \Gamma(4, 2\Lambda r_c + \frac{3r_c}{r_v}) \right]. \quad (5.12)
 \end{aligned}$$

Instead of the exact solution described in (5.12), *Bellenger et al.* (2017) suggested to use a power law fit of E_k to rainrate R (fig. 5.2). To accomplish this, (5.12) is computed for a series of $R = 0 : 0.1 : 80 \text{ mm h}^{-1}$, using a critical rain drop size $r_c = 0.4 \times 10^{-3} \text{ m}$, and the following constants:

$$\begin{aligned}
 \rho_r &= 998 \text{ kg m}^{-3}, \\
 w_v &= 9.43 \text{ m s}^{-1}, \quad b_1 = 1.0528, \quad b_2 = 1.07733 \quad \text{and} \quad r_v = 1.77 \times 10^{-3} \text{ m}. \\
 n_0 &= 8 \times 10^6 \text{ m}^{-3} \text{ m}^{-1} \quad \text{and} \quad \Lambda = 4.1 \times 10^3 R^{-0.21} \text{ m}^{-1},
 \end{aligned}$$

The exact solution is then approximated as:

$$E_k(R) = mR^n, \quad (5.13)$$

with $m = 0.4 \times 10^{-3}$ and $n = 1.3$, as shown in fig. 5.2.

The rain-induced momentum and kinetic energy fluxes in equations (5.2) and (5.13) can both be translated into a water-side friction velocity (u_{*r} , u_{*k}), which are additional to the water side friction velocity by wind alone (u_{*w}):

$$u_{*w} = \sqrt{\tau_w / \rho_w} \quad (5.14)$$

$$u_{*r} = \sqrt{\tau_r / \rho_w} \quad (5.15)$$

$$u_{*k} = (E_k / \rho_w)^{1/3}. \quad (5.16)$$

5.4 Results

5.4.1 Overview of Oceanographic Conditions

The meteorological forcing and the evolution of salinity, temperature, buoyancy frequency N^2 , turbulent kinetic energy (TKE) dissipation rate ϵ in the upper 25 m observed with the ASIP are presented in fig. 5.3 (all time stamps reflect mean local time using the approximate location of the target deployment - 40.3°N, 58.9°W). Figure 5.3d and 5.3e show that ASIP profiled through a density-compensated layer of variable temperature and salinity. During each of the four rain events a shallow negative anomaly is observed in the profiles of salinity. The base of this anomaly, determined from visual inspection of individual profiles, is drawn by a black line on panels d-g.

The first two rain events took place during the night, event III shortly after sunrise, and event IV occurred during daytime. There is a strong reduction in the solar radiation Q_{SW} during both events. Wind speeds were variable within a range of 3 to 10 m s⁻¹ from a south to southwesterly direction (fig. 5.3b). The first three rain events coincided with peaks in U_{10} , whilst wind was reduced during rain event IV. Figure 5.3b also shows a time series of the significant wave height H_{sig} , which gradually increases during the study period, peaking during rain event II. The wave energy during event III and IV is fairly similar, $H_{sig} \sim 1.9$ m.

Under the assumption of steady and isotropic turbulence, ϵ is equal to the production of turbulence from buoyancy and shear forces (*Osborn and Cox, 1972*). The depth of active mixing, also known as the mixing layer depth (XLD) can be determined from the ϵ profiles by finding the depth below the surface in each profile where ϵ reduces to a background value (*Sutherland et al., 2014a*). For this observational period $\epsilon = 1 \times 10^{-8} \text{ m}^2 \text{ s}^{-3}$ best represents the threshold value below which turbulence drops back to the background state. The mixed layer depth (MLD) is determined as the depth at which the potential density is 0.05 kg m^{-3} higher than its reference value σ_{ref} taken at 10 m depth. Both the MLD and XLD are indicated on the profiles of dissipation (fig. 5.3 f, g). They are unequal except for a short period around 00:00 h, when a ‘plume’ of increased turbulence reaches down to the MLD. This coincides with a steady increase in the wave energy during the night, as well as a change in the mixed layer current velocity measured by an ADCP (not shown). Consequently the MLD deepens. The XLD closely follows the base of the rain-induced halocline ($Z_{\Delta S}$) for all four rain events.

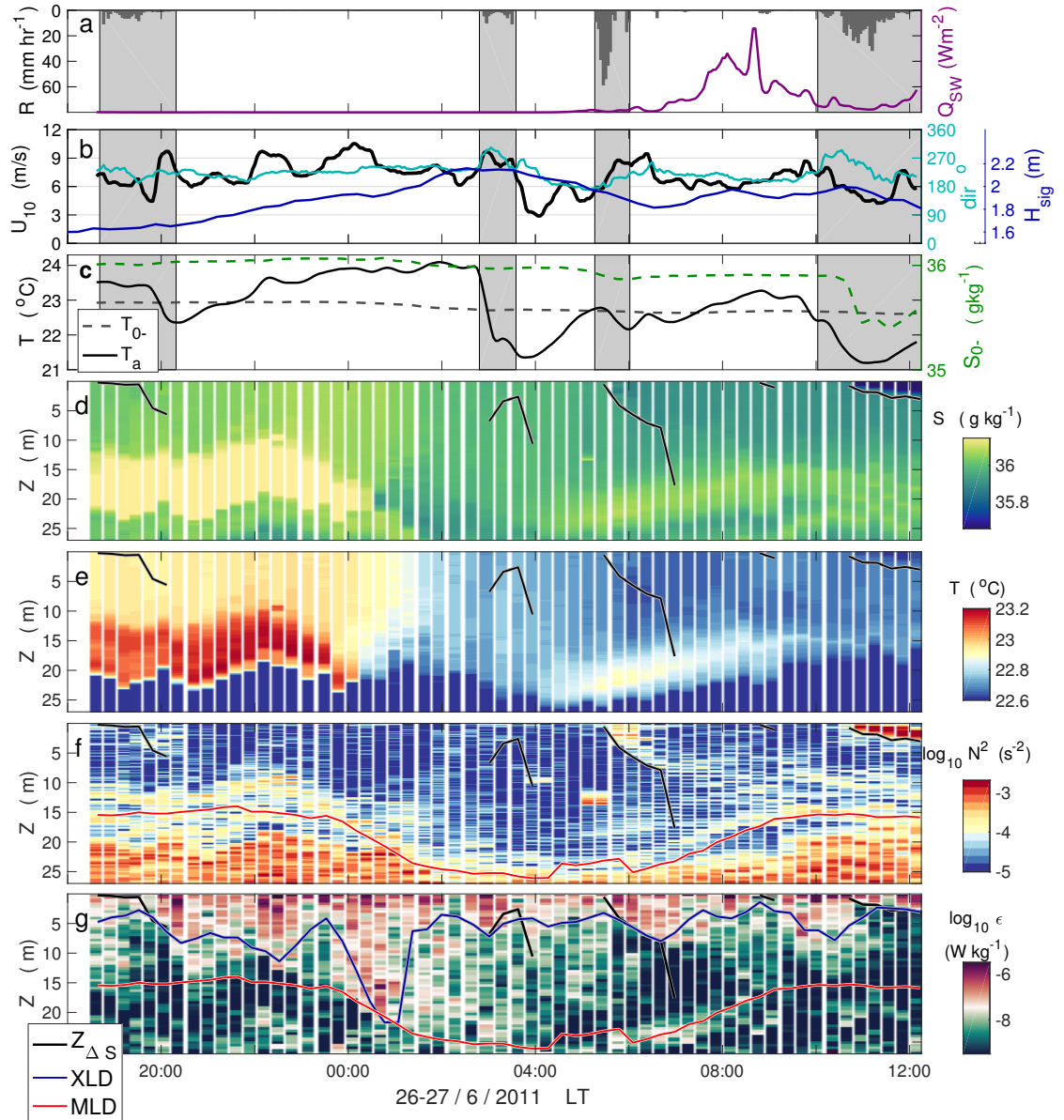


Figure 5.3: Overview of the observations made during the first deployment of the ASIP in the Knorr-11 campaign. **a.** Rain rate R and downwelling solar radiation Q_{SW} . **b.** 10 m-windspeed U_{10} , wind direction, and significant wave height H_{sig} . **c.** Temperature and salinity of the seawater at sub-skin level (T_{0-} , S_{0-} , and the air temperature T_a). **d-g.** 58 profiles from ASIP, showing respectively the salinity S , temperature T , the buoyancy frequency N^2 , and the TKE dissipation rate ϵ in the top 25 m. Black lines on all four panels indicates the depth of the salinity anomaly $Z_{\Delta S}$. The mixing layer depth XLD (blue) and the mixed layer depth MLD (red), both determined by threshold criteria, are indicated in panel f and g.

5.4.2 Salinity, Temperature and Density Anomalies

Rain induces temperature and salinity anomalies which affect the upper 10 m of the ocean. Figure 5.3e shows that although only the third and fourth rain events

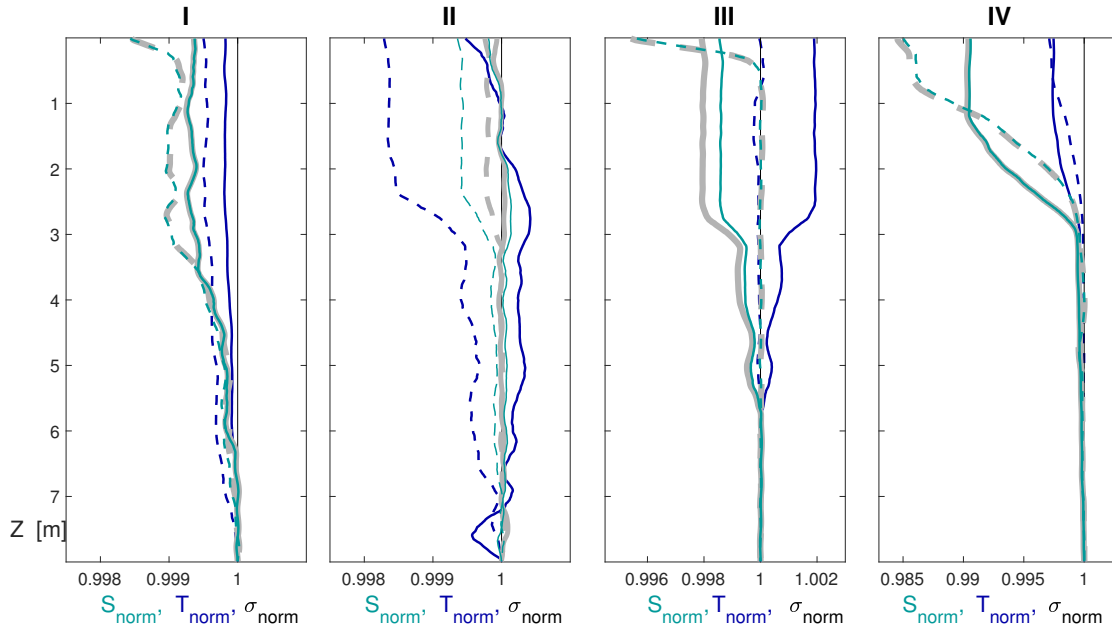


Figure 5.4: Near-surface profiles of salinity (S), temperature (T) and potential density (σ) normalised to their value at 8 m, during each of the four rain events. Dashed line: profile corresponding to the occurrence of the maximum salinity difference between the surface and a reference depth for the specific rain event. Solid line: consecutive profile.

significantly change the near-surface stratification, there are differences between the two. Rain event IV results in a salinity and temperature reduction, which is confined to the upper 3 m, above a strong halocline. For rain event III our measurements capture a small reduction in salinity, which extends over a depth of 10 m, and only weakly stratifies the near-surface water. During rain event III there is an ongoing decrease of the mixed layer temperature due to nighttime cooling, to which the rain did not further contribute.

Profiles of temperature, salinity and the potential density σ in fig. 5.4 are normalised by their value at 8 m, to further illustrate the magnitude and shape of the rain-induced anomalies. This reference depth for normalisation is chosen after visual inspection of the time series of T , S , and seawater density ρ_w , because it is the deepest level above which the surface water is well mixed before any of the four rain events. For each of the four rain events the profiles corresponding to the maximum salinity anomaly between the surface and the reference depth, ΔS_{max} , as well as one of the consecutive profiles are plotted. The highest anomaly typically occurs early in the rain event, before the freshwater is further mixed down to form a shallow rain-induced mixed layer as described in *Price (1979)*. Such a fresh mixed layer is clearly formed in rain event III and IV, and to a lesser extent in event I and II.

The associated temperature anomalies are most often a fraction of the salinity anomaly, e.g. during rain event IV the surface value of S_{norm} is nearly 1.5% lower than at the reference depth, whilst the temperature anomaly is only 0.3%. Similarity in the shape of the σ_{norm} and S_{norm} profiles, further indicates that the

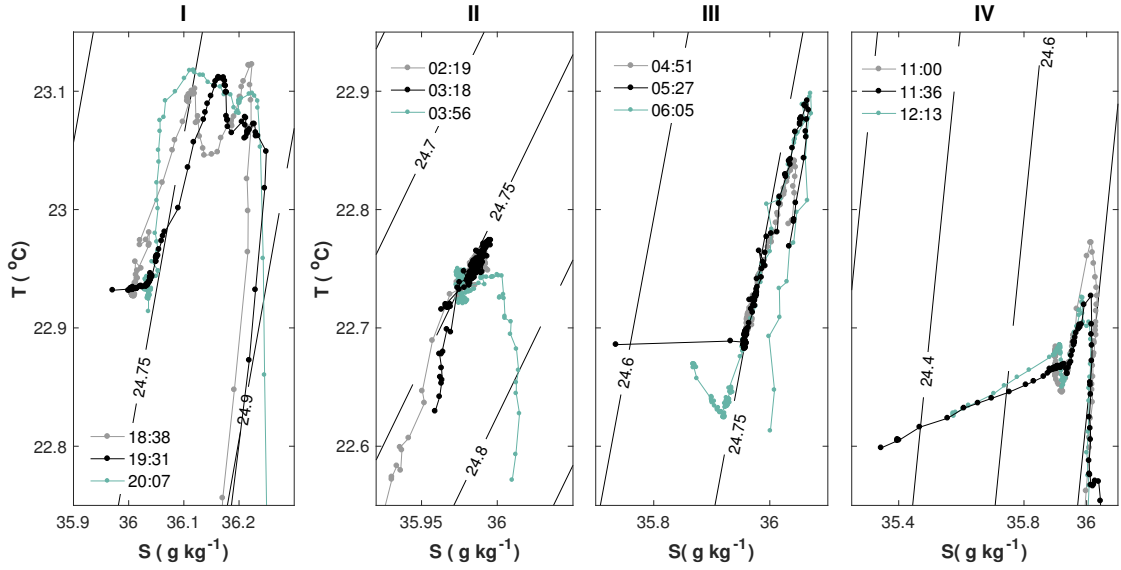


Figure 5.5: T-S curves of the upper 25 m, during each of the four rain events. In each panel a profile before (gray), at the peak of the rain rate (black) and after the rain (green) is plotted. The T-S relationship is evaluated at each 20 cm interval. To enhance detail the salinity scale is varied between the plots, and the temperature scale on the vertical axis in panel I differs from the other three.

density profile near the surface is dominantly controlled by the freshwater flux, except for rain event II. The relative change in surface temperature is larger than the change in salinity, consequently the density changes are compensated. The warm SST-anomaly measured during rain event III is remarkable, as rain is assumed to be at the wet-bulb temperature of the air, which is usually cooler than the SST. The rain is associated with a different air temperature T_a , and indeed the air-water temperature difference is near zero during rain event III (see fig. 5.3c).

In fig. 5.5 the T-S relationships during each of the rain events is evaluated for the upper 25 m, before, during, and after the actual rainfall. All profiles show a temperature maximum corresponding to the warmer, saltier layer between 10 and 20 m visible in fig. 5.3 d and e. Above this lies a well-mixed layer in which the T-S relation is aligned with the 24.75 kg m^{-3} isopycnal. During rain events I, III, and IV the T-S curve corresponding to the upper 0.5 – 2 m of the profile deviates from the isopycnal, instead lying along a nearly horizontal line in the direction of lower salinity. Such a T-S relation near the surface was hypothesised by *Wijesekera et al.* (1999), and clearly shows the dilution by the rainwater.

5.4.3 Air-Sea Fluxes

From the meteorological time-series it is deduced that the weather conditions during this experiment were highly variable, in likely association with the passing of a frontal system. This causes fluctuations in the air temperature T_a and consequently the sea-air temperature difference ΔT_{s-a} is observed (fig. 5.3c) to change sign several times. A negative difference is quite unusual, and related to advection of

warm air. Rainfall during rain events II and IV is seen to rapidly cool T_a by $1 - 2^\circ\text{C}$. This means that the rain itself is significantly cooler, and forms an explanation for the relatively large sea surface temperature anomaly observed during this event (see fig. 5.4). On the other hand, air temperatures are rapidly rising afterwards, such that ΔT_{s-a} is near zero at the start of event III, thus forming a possible validation of the measured warm SST-anomaly.

The air temperature (fig. 5.3c) is observed to have strong variability associated with the rain events, as it reduces by up to 2°C during rain. This makes the sea-air temperature difference ΔT_{s-a} reverse to positive values for rain events II and IV. Rain event II is associated with cooler air, explaining the relatively large sea surface temperature anomaly observed during this event.

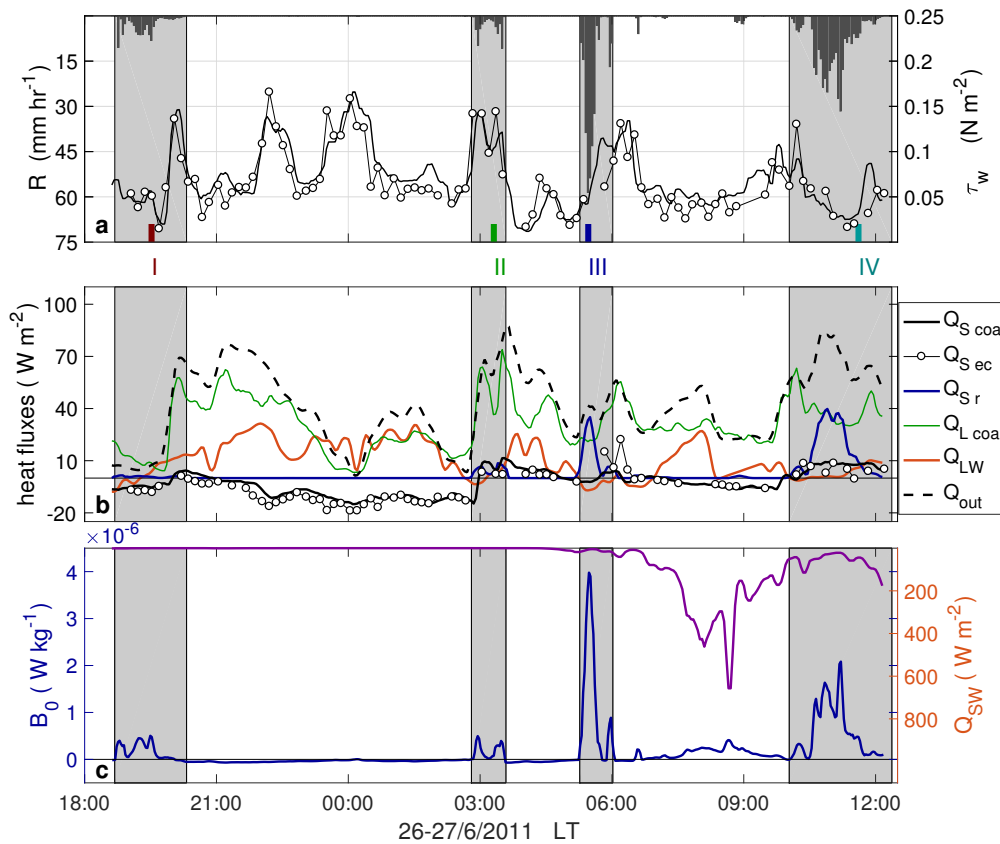


Figure 5.6: Air-sea fluxes during the deployment of ASIP: **a.** rain rate R and wind stress τ_w computed using COARE (solid black line), as well as from the eddy-covariance measurements (dotted line). Colored markings on the lower horizontal axis indicate the time of the ASIP profile in which the maximum salinity anomaly ΔS_{max} for each rain event was observed. **b.** Heat fluxes (ocean heat loss defined positive): sensible heat flux (Q_S), latent heat flux (Q_L) and net longwave radiation (Q_{LW}) computed using the COARE 3.0 algorithm. Also shown are the measured sensible heat flux from the eddy covariance system (Q_{SEC}) and the rain-induced heat flux following equation 5.1 (Q_{Sr}). Q_{out} is the sum of the outgoing heat fluxes. **c.** Downwelling shortwave radiation Q_{SW} and surface buoyancy flux B_0 (defined positive into the ocean).

The variability of ΔT_{s-a} and wind speed associated with the rain events directly modulate the heat fluxes. Figure 5.6b shows a time series of the outgoing latent heat flux, sensible heat flux, and long wave radiative flux (each flux component is defined positive from sea to air). The measured and computed sensible heat flux Q_{SEC} and Q_{SCOA} agree very well, apart from during rain events III and IV, when the measured flux shows more variability. This may be due to the additional heat flux from the cooling by rain, Q_{Sr} , which when computed following equation 5.1, forms a significant component to the heat balance. The modelled latent heat flux Q_L is dominantly controlled by the wind speed variability. The net long wave radiation Q_{LW} is highest during clear sky conditions, and thus reduces to zero or negative values during rain. Nevertheless, during most rain events the total surface cooling is doubled, compared to the non-rain average net outgoing sea-to-air heat flux (Q_{out}) of 42 W m^{-2} . This enhanced cooling has little effect on the surface buoyancy flux B_0 , which during rainfall is dominated by the surface freshening. The time series of B_0 , computed using equation (2.10), is illustrated in fig. 5.6c. Under no-rain conditions, the buoyancy of the surface water is controlled by the diurnal cycle of the heat flux; during rain the haline component in B_0 is dominant, positively enhancing the total buoyancy input by an order of magnitude. The friction velocity from wind stress u_{*w} , the rain-induced surface stress u_{*r} , and the kinetic energy of falling raindrops u_{*k} , as defined in equations (5.14), (5.15), and (5.16), are computed for the period of the ASIP deployment, and shown in fig. 5.7a. The conceptual surface roughness due to the kinetic energy of surface penetrating raindrops corresponds to a friction velocity at least twice as high as the conventional u_{*w} from wind stress. However, this component has been shown to only be effective in mixing the water in the upper ten centimetres (*Harrison and Veron, 2017; Bellenger et al., 2017*). The momentum represented by u_{*w} and u_{*r} is thought to influence the total rain-induced mixed layer and the evolution of the fresh lens. The sum of these two scaling velocities is 45% larger in event II and III than for rain event I and IV.

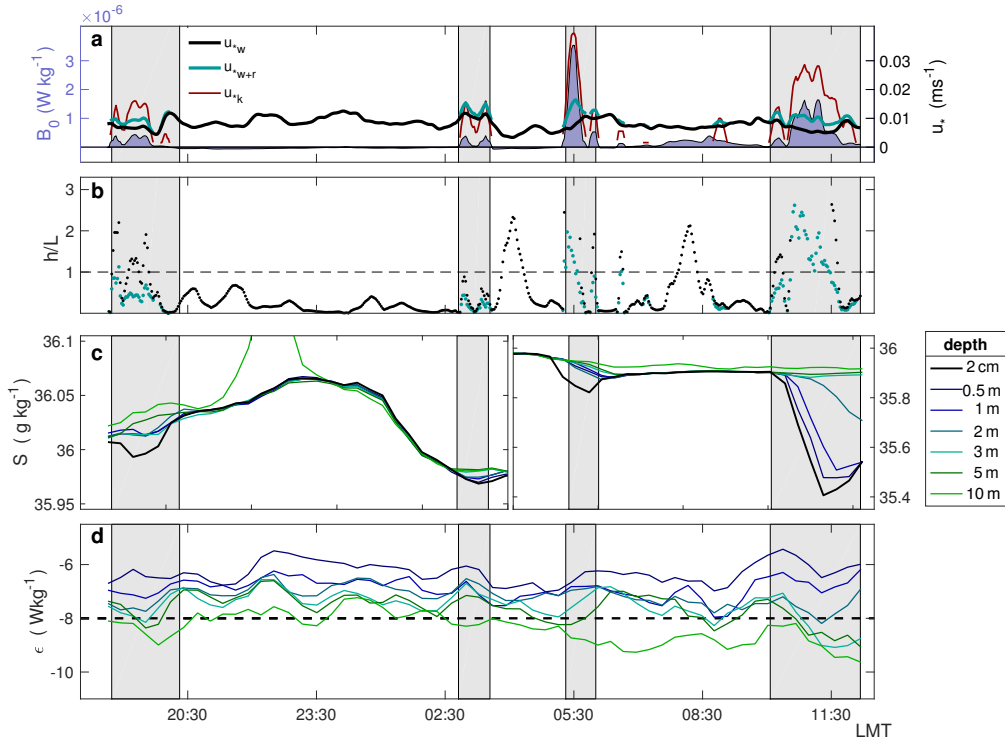


Figure 5.7: **a.** Time-series of the surface buoyancy flux B_0 (blue shaded area, defined positive into the ocean), the water-side friction velocity of the horizontal momentum of the wind (u_{*w}), wind + rain (u_{*w+r}), as well as due to the kinetic energy of the raindrops (u_{*k}). **b.** The ratio of the depth of the layer of active turbulent mixing and the Monin-Obukhov length, $|h/L|$ with $h = XLD$, in which L is computed with either u_{*w} (black dots) or u_{*w+r} (blue-green dots). **c.** Salinity S at selected depths below the surface. **d.** TKE dissipation rate ϵ at approximately the same depths as in panel c. The limits of the y-axis in panel c are reduced in the first half of the time series to improve the resolution for the small salinity anomalies. Dashed line in panel d is the threshold level used to define the XLD. Gray shading in each plot indicates the periods of the four rain events.

5.4.4 Turbulence during Rain

Profiles of ϵ provide a means to observe the evolution of upper ocean turbulence in the rain-affected region. The turbulence in the upper 5 m is intermittent during this deployment of ASIP, as several periods of enhanced vertical mixing below the ocean surface occur at approximately 20:30 h, 22:45 h, 00:00 h, 03:00 h, 6:00 h, 08:30 h and 10:00 h local time (see fig. 5.3g). Most of these periods coincide with peaks in the wind speed, thus we expect the turbulence to be dominantly driven by wind-induced shear, and possibly wave effects. During nighttime, convectively driven turbulence will likely play a role too, due to a net buoyancy flux out of the ocean. The depth of the layer of active turbulent mixing, XLD varies between 2.5 and 20 m, the deeper limit coinciding with the seasonal MLD (fig. 5.3g). Additionally the enhanced levels of ϵ at deeper levels after 00:00 h occur during a period of increase in the wave energy (fig. 5.3b) and mixed layer deepening.

Using similarity scaling (*Lombardo and Gregg, 1989; Large et al., 1994*), the Monin-Obukhov length L represents the depth below the surface where the buoyancy and momentum fluxes are equally effective at controlling turbulence. The scaling parameter L was defined in (4.2). The ratio h/L can be used to verify whether the turbulent mixing over the layer h is dominantly wind or convectively-driven (*Weller et al., 2002*). Figure 5.7b illustrates the absolute value of this ratio, where L is computed using either u_{*w} or $(u_{*w} + u_{*r})$ and $h = XLD$, the depth of active mixing, is used. In analogy to the analysis in sec. 4.5, the absolute value of the ratio is computed. The ratio $|h/L| < 1$ during nighttime, and close to zero at all times listed above, which indicates that the turbulence near the surface is dominantly wind-driven. Only for a short period after rain event II is convection dominant, following a reduction in u_{*w} . When B_0 changes sign in the morning $|h/L| > 1$, and the same happens during rain events I, III, and IV. At these times the active mixing layer is temporarily controlled by buoyancy suppression. Using $u_{*w} + u_{*r}$ in (4.2) enhances L , which somewhat changes the balance for event I to a more wind-dominated regime.

The presence of a shallow stratified layer can inhibit downward transport of turbulence in the upper ocean. A second possible consequence of the stratification is that the surface momentum flux from the wind and waves will be focussed into a shallow layer. To study the evolution of ϵ along with S during rainfall in more detail, time series of both variables are shown for different levels in the upper 10 m in fig. 5.7c and d. Focussing on the fresh water lens formation during rain event IV, an initial increase in ϵ before and at the start of the rain is followed by a decrease at all levels. The reduction in ϵ coincides with the period in which $|h/L| > 1$, which further illustrates that the turbulence near the surface is suppressed by the stratification. It is observed that after the peak in the rain rate, and the corresponding maximum in B_0 in fig. 5.7a, ϵ increases in the upper 3 m. Enhanced ϵ within a shallow stratified layer was shown to indicate the presence of a surface jet during conditions of diurnal warming by *Sutherland et al. (2016)*. It is expected that the observed increase in ϵ reflects enhanced momentum within the fresh lens, which will lead to shear-instabilities at the pycnocline (*Price et al., 1986*). As soon as $0 < |h/L| < 1$ the momentum input by the wind is large enough to break down some of the stratification. At the end of the time series the upper meter is well mixed and a salinity gradient remains between 1 m and 3 m. Below this level the turbulence continues to decrease until the end of the observational period. At the 5 m and 10 m levels ϵ is reduced by approximately 2 orders of magnitude compared to the pre-rain situation, whilst the shallow surface layer responds rapidly to wind forcing.

The observed salinity anomaly caused by rain event III is 70% smaller than in rain event IV at all depths, causing a weak stratification to form between 2 m and 10 m (see also fig. 5.3f). Nevertheless, a small reduction in ϵ is observed at 10 m. Turbulence increases at all depths above this level, in response to the increased wind forcing. Although $|h/L|$ indicates that buoyancy controls the turbulence during the first half of rain event III, this is not reflected in a reduction of ϵ in the fresher layer. The rain induced freshening by rain event I and II is even smaller,

and the evolution of ϵ is similar at all depths, reflecting the changes in the wind speed.

The impact of the raindrops may contribute to enhanced turbulence in the fresh lens as well. *Zappa et al.* (2009) observed that the velocity fluctuations caused by falling raindrops can induce turbulence with a dissipation rate of $3 \times 10^{-4} - 1 \times 10^{-3} \text{ W kg}^{-1}$ in the upper 20 cm of the water column. Using a particle image velocimetry (PIV) technique *Harrison and Veron* (2017) measured TKE dissipation rates of $10^{-5} \text{ W kg}^{-1}$ in the upper 10 cm. Since both are only 0.1-0.3% of the supplied E_k , substantial dissipation occurs closer to the interface. Our most shallow spectral estimate of ϵ is determined over a bin of approximately 50 cm depth; the observed increase in ϵ reflects the average increase in turbulent mixing over this layer.

5.5 Modelling Rain Induced Salinity Anomalies

The magnitude of sea surface salinity changes following precipitation have been parameterised based on several remote sensing validation studies (*Boutin*, 2016) as well as in modelling efforts (*Drushka et al.*, 2014, 2016; *Bellenger et al.*, 2017)

5.5.1 Numerical Models

The one-dimensional General Ocean Turbulence Model (GOTM), which is designed to model vertical mixing, was used by *Drushka et al.* (2016) to test its representation of rain-induced salinity anomalies. Comparison between two different observational data sets showed that GOTM can accurately describe the evolution of the upper ocean under rainfall in the absence of horizontal processes. Numerical experiments were performed to study the response to different forcing factors (wind speed, peak rain rate, and total rain amount). Sensitivity runs with the GOTM model resulted in a relation between ΔS_{max} (the maximum salinity difference between a reference depth of 5 m) and the sub-surface, and peak rain rate R_{max} as a function of mean wind speed \bar{U} :

$$\Delta S_{max} = a R_{max} \bar{U}^{-b}. \quad (5.17)$$

Forcing the model with a constant wind speed and a 1-hour Gaussian pulse of rain with a peak corresponding to R_{max} produced $a = 0.11 \pm 0.03 \text{ psu mm}^{-1} \text{ h}^{-1}$ and $b = 1.1 \pm 0.03$.

The four observed rain events are compared to the relationship in (5.17). Instead of using the high-resolution rain rate, the time series are slightly smoothed with a 5 min moving average, and \bar{U}_{10} for windspeed (listed in table 5.1).

Figure 5.8a compares the ΔS_{max} prediction from the parameterisation in *Drushka et al.* (2016) (D'16) to the observed maximum salinity anomaly over the top 5m (circles). The modelled ΔS_{max} is in agreement with the observation for rain event I and IV, and overestimates the observed ΔS_{max} for events II and III. For event III the parameterisation predicts a much stronger salinity anomaly (+0.6 psu) than

was observed. Possibly the model is underestimating the strength of the vertical mixing at a mean wind speed of 7.7 m s^{-1} . The relation in (5.17) was determined from sensitivity tests of R_{max} versus ΔS_{max} and U , using a constant U . However, wind speed is seldom constant during a rain event — the meteorological time series presented here (fig. 5.6 and 5.7), show that event II and III are typical of squalls (*Smyth et al.*, 1997), as the rain coincides with strong gradients in the wind. Figure 5.8 therefore also shows ΔS_{max} when instead of \bar{U} the maximum U during the rain event is used in (5.17). This reduces the bias in ΔS_{max} , especially for rain event IV.

A short, bursty rain event like II and III is spatially inhomogeneous (*Wijesekera et al.*, 1999). Although the ship was generally following the ASIP, fig. 5.1 shows that during the third rain event they were over 1 km apart. This could imply that the rain rate measured at the ship was not quite as intense at the location of the ASIP. Also, as the profiler was measuring only 3 times per hour, the actual maximum ΔS_{max} could have occurred in between two profiles.

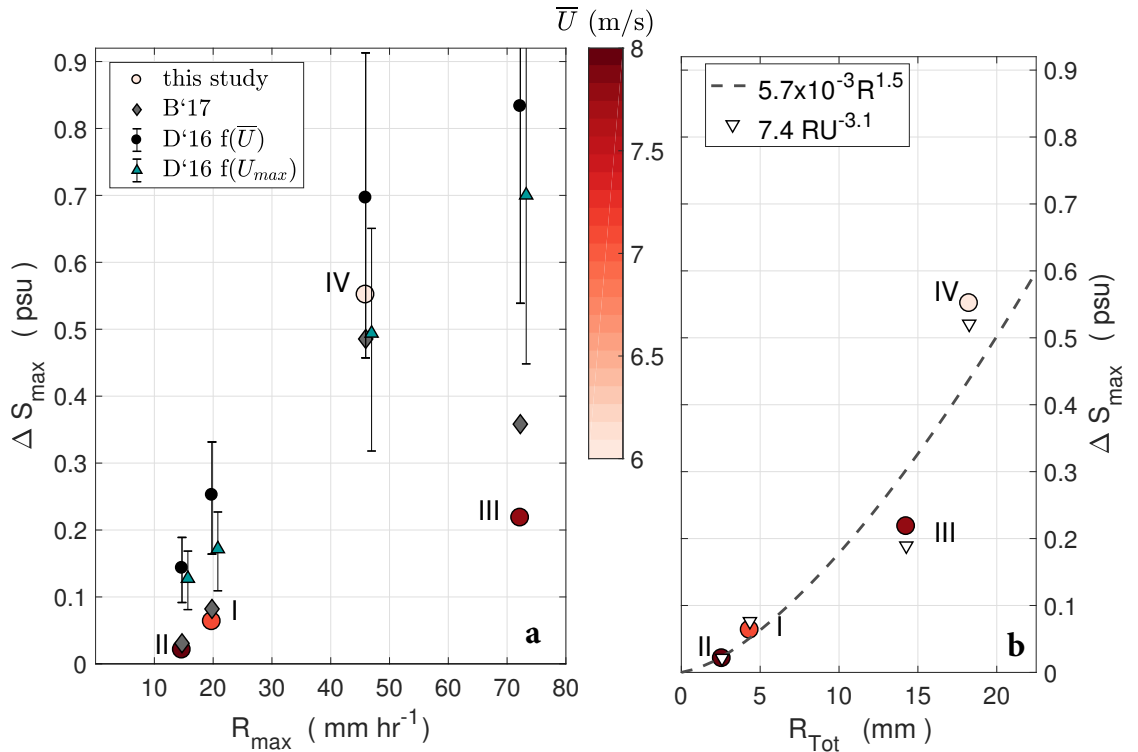


Figure 5.8: **a.** Observed ΔS_{max} between 5 m and 2 cm of ASIP profiles versus peak rain rate R_{max} (coloured circles), compared to ΔS_{max} resulting the model by *Drushka et al.* (2016) (D'16, black circles when using (5.17) with \bar{U} , green triangles when using U_{max}), and resulting the prognostic model by *Bellenger et al.* (2017) (B'17, diamonds). **b.** ΔS_{max} versus the total amount of rainfall R_{tot} for the observed rain events. A power law is fit to R_{tot} only (black dashed line) and to R_{tot} and the mean windspeed \bar{U} (white triangles).

On the other hand, the peak value of the rain rate R_{max} , may not be the right

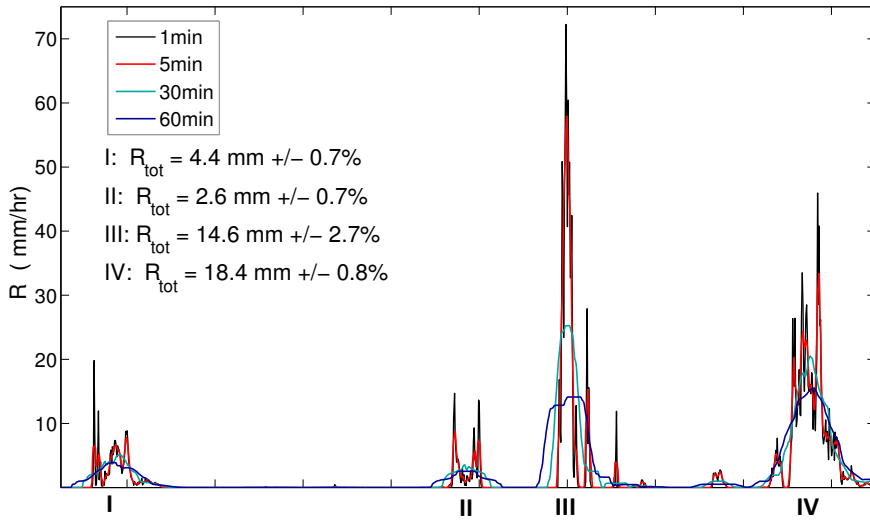


Figure 5.9: Illustration of the effect of applying a moving average to the time series of rain rate R ; for increasing averaging period from 1 up to 60 min the peak rain rate reduces strongly, whilst the total rain rate for each rain event only changes by a small percentage.

metric to describe rain events, as it is highly dependent on the resolution of the meteorological data. Peak rates observed here hardly last longer than two minutes; only after time-averaging the rain rate approximates a Gaussian distribution like the rain forcing used in *Drushka et al. (2016)*. Averaging the time series of R over different windows strongly reduces R_{max} but hardly affects the total amount of rain per event, R_{tot} , as shown in fig. 5.9. After forcing GOTM with a fixed R_{tot} for variable R_{max} *Drushka et al. (2016)* concluded that the first metric is positively correlated to the duration of a fresh lens, whilst the second controls ΔS_{max} . However, a test to the effect of a fixed peak but increasing the duration of the rain forcing, thereby deviating from the Gaussian curve, was not reported.

Total (R_{tot}) and peak rain rate (R_{max}), and rain duration (t_{rain}) relate to each other as $R_{tot} = m t_{rain} R_{max}$. When the rain time series is described with a Gaussian curve of which the full width at one-tenth of the peak corresponds to the rain duration t_{rain} , then $m \approx 0.584 t_{rain}$. The natural variability in rainfall events is large, and therefore the relationship between R_{tot} and R_{max} , for the observed rain events m varies from 3 to 6.5.

This leads to the hypothesis that R_{tot} may be a more robust parameter from which to estimate ΔS_{max} . Panel b of fig. 5.8 illustrates that the observed rain events support this hypothesis. The sparsity of observations doesn't allow for a robust statistical analysis here. However, a simple fit shows that a power law could describe the relationship well:

$$\Delta S_{max} = 5.7 \times 10^{-3} R_{tot}^{1.5}. \quad (5.18)$$

Incorporating the wind speed as in 5.17 suggests:

$$\Delta S_{max} = 7.4 R_{tot} U^{-3.1}. \quad (5.19)$$

The prognostic model for diurnal warming by *Zeng and Beljaars* (2005) was adapted by *Bellenger et al.* (2017) to represent rainfall effects. How rain changes the stratification in the microlayer depends on the net effect of the freshening (stabilising) and the cooling (destabilising). Under non-rainy conditions the ocean surface microlayer with a thickness of $O(1 \text{ mm})$ is typically more salty and cooler than the water below it (e.g. *Saunders*, 1967). However, during rain this cool and haline skin disappears, as only the fraction of the raindrops with a large enough drop radius will break through the surface, and the other fraction contributes to freshening of the skin-layer (*Schlüssel et al.*, 1997).

Turbulent mixing due to the kinetic energy of the raindrops E_k is included in the microlayer component of the *Bellenger et al.* (2017) model, as well as the sum of u_{*w} and u_{*r} , which both contribute to the parameterisation of turbulent mixing below the skin layer.

Given an input of bulk seawater temperature and salinity from ASIP (at 5 m depth), surface heat fluxes, solar radiation, surface wind stress and rain rate, the model will compute the temperature and salinity differences between the bulk water and the sub-skin level (ΔT and ΔS , respectively), as well as the difference across the microlayer. The maximum salinity difference computed with the *Bellenger et al.* (2017)-model, using S_{5m} from ASIP and the modelled sub-skin salinity S_{0-} , are shown in fig. 5.8 (B'17). The agreement is reasonably good, although there remains a 0.15 psu overestimation of the salinity anomaly induced by rain event III.

The complete time series of the modelled S_{0-} , T_{0-} , S_{int} and T_{int} is shown in fig. 5.10. The prognostic scheme predicts S_{0-} with a total RMS-error of 0.05 psu, and up to 0.09 psu during rain only. The RMS error of T_{0-} is 0.02 °C, up to 0.03 °C during rain. Mainly for rain event II and IV, the rain-induced cooling is slightly underestimated, but the model is known to underestimate surface cooling in moderate and high wind speed conditions (personal communication H. Bellenger). Figure 5.10 also illustrates the significant skin-freshening effect of the precipitation. The output from the scheme suggests that the rain-induced salinity anomaly of the surface microlayer is 0.5-1 psu.

5.5.2 Satellite Validation

Simple linear relationships between rain rate and SSS-anomaly have been inferred from validation studies of remote sensing of SSS and rain (*Boutin et al.*, 2014; *Drucker and Riser*, 2014):

$$\Delta S = cR. \quad (5.20)$$

The rain freshening constant c resulting from various studies using data from both the SMOS and Aquarius satellites, ranges from 0.07 to 0.36 (*Boutin*, 2016). To

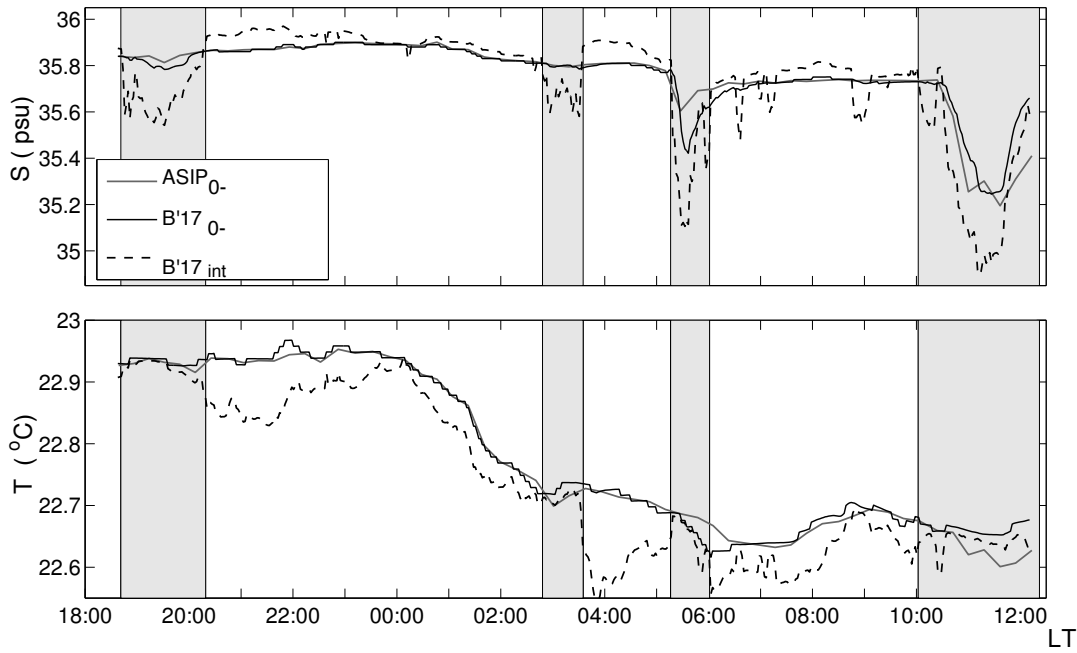


Figure 5.10: Skin and sub-skin salinity S (top) and temperature T (bottom) output from the prognostic scheme in *Bellenger et al. (2017)*. Thin grey line is the subskin value from the ASIP for comparison.

compare observations to this relationship requires interpolating the high resolution time series of rain rate to a scale comparable to the resolution of the various satellite microwave radiometers ($\geq 20\text{km}$).

To approximate this the hourly averaged rainfall rates R_{60} are computed. This R_{60} is thought to compare better to rainfall rates from remote sensing, for example the rainfall product from the SSM/I and SSMIS (Special Sensor Microwave Imager, see www.remss.com). This data has a spatial resolution of 0.25° , approximately 25×25 km in mid-latitudes, which corresponds well to the estimated average lateral extent of a rain event of one hour's duration. Figure 5.11 shows the observed ΔS_{max} over the upper 5 m versus the mean R_{60} for each rain event, as well as the calculated value from $\Delta S_{max} = cR$ for the range of c -values listed in *Boutin (2016)*.

Only one of the observed rain events (IV) falls into the area of the satellite-derived relationships, for the other three ΔS is overestimated by any of the satellite relationships. However, when comparing satellite to in-situ salinity, the skin-effect becomes of importance. It was shown in fig. 5.10 that there is a strong gradient in salinity over the surface microlayer. As the surface measurement of the ASIP is an average over the top 2 - 5 cm, whilst the optical depth of the satellites is shallower, this gradient could explain the lower ASIP ΔS_{0-5m} . After adding ΔS over the skin layer to the ASIP observations, using the outcome of the prognostic scheme by *Bellenger et al. (2017)*, the salinity anomaly is enhanced such that all rain events fall within the predicted range.

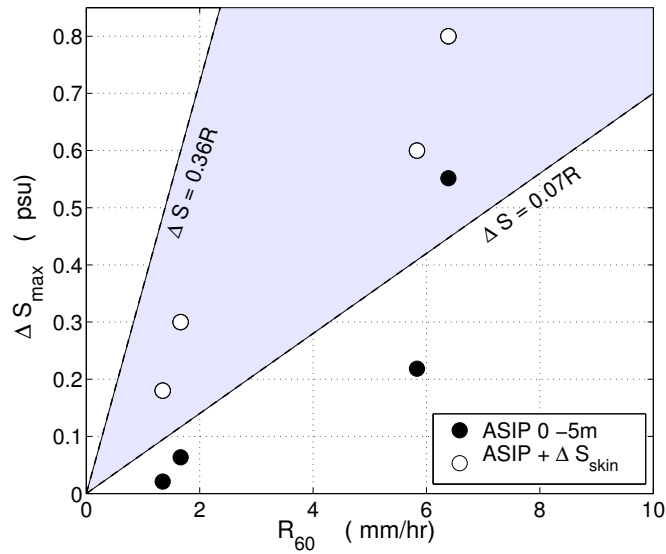


Figure 5.11: Comparison of the observed 60 min averaged rain rate R_{60} versus maximum salinity difference observed in the Knorr-11 campaign to linear relationships derived from satellite-data, as described in *Boutin (2016)*. Observed ΔS_{max} from ASIP (black dots) is generally lower than any of the predictions (blue shaded area), however when adding the modelled skin-layer ΔS (white dots) all points fall within the predicted range

5.6 Discussion and Conclusion

Rain over the ocean predominantly has an impact if it causes the formation of a layer at the ocean surface with a lower density than the original surface water. This fresh lens formation is a phenomenon best observed in tropical regions, where rainfall amounts are generally large. However, this opportunistic data set from an experiment not specifically targeting rain shows that it can also occur in mid-latitude regions.

To study rain effects on the upper ocean in open ocean conditions is challenging, as many of the boundary conditions, which can be fixed in a laboratory environment, cannot be controlled and are often unknown. Naturally occurring rain is typically quite variable. The rain events considered in this study are each different in intensity, duration and total rain amount. At the same time the ambient wind conditions and the air-sea temperature gradient differ significantly, although the four events occur in the same area and within the same 24 hours. The large variability makes it difficult to draw firm conclusions on the effect of rain on stratifying the upper ocean from such a small experiment.

Observations during four rain events in a midlatitude region of the Northern Atlantic show that small differences in the surface forcing lead to a significantly different response of the upper ocean. Although peak rain rates of event III are largest, the total freshwater input between rain event III and IV does not differ much. However, the observed salinity anomaly during rain event III extends down to 10 m, whilst for rain event IV the freshwater is confined to the upper 3 m,

resulting in a stronger surface salinity anomaly, and the formation of a more typical fresh lens. The weather conditions are observed to be variable, and to somewhat co-vary with the rain events, as the rain often coincides with bursts in the wind as well as the advection of air masses with different temperatures. This modulates the local air-sea fluxes of momentum and heat, the balance of which affects the formation and lifetime of a salinity anomaly. Similarity scaling indicates that the turbulent mixing is dominantly wind driven, and the rapidly changing wind causes major differences in the response of the upper ocean to a freshwater input. The third rain event, of the highest peak rain rate, is squall-like, which results both in a stabilising buoyancy flux by the rain, and an increase in the momentum flux and energy available to vertically mix the salinity anomaly. The two earlier rain events carry a smaller quantity of freshwater, and similar reasoning explains that during the squall-like second rain event hardly any freshwater anomaly is observed. The small salinity anomaly observed in two ASIP profiles during the first rain event disappears due to the wind burst following the tail of the rain. The wind and wave forcing during the final rain event is reduced and less variable during the course of the rain. This event is also of slightly longer duration, the sum of all factors resulting in an environment in which a stable freshwater lens can develop.

The presence of this fresh lens modulates both the turbulent mixing within it as well as below. Like *Soloviev et al.* (1999), an initial increase in ϵ over the depth of the freshwater lens formed by rain event IV was observed, as well as a 2 order of magnitude reduction in turbulence in the mixed layer below the lens. The limited amount of observations of well developed fresh water lenses prevents a solid conclusion about the turbulence within these features. The initial increase in ϵ could either indicate that the rain-induced halocline concentrates the surface momentum flux over the shallow layer, or that our observations include a signal from the enhanced turbulence due to the rain drop impact. However, the vertical resolution of the ϵ measurement by ASIP is deemed unsuitable to resolve rain-induced turbulence. In this case the rapid reduction of ϵ over the upper meter during rain event IV coincides with a reduction in wind speed at this time, and a suppression of turbulence by buoyancy forces. To address the very interfacial layer, where rainfall affects gas exchange, as well as the calibration and interpretation of the remote sensing signals, a profiler like ASIP requires more precise instrumentation to accurately measure the salinity-and temperature gradients, and the turbulence caused by the rain.

Unfortunately the deployment of the ASIP was stopped before the freshwater lens associated with rain event IV had dissipated, so it is impossible to make any conclusions about its duration. *Drushka et al.* (2016) simulated this specific freshwater lens with the GOTM model, finding that a sea surface salinity anomaly could have persisted for at least 6 hours. The air-sea exchange of the surface mixed layer would thus have been limited to the depth of the fresh lens for a significant part of the day. The profiler is Lagrangian, so it is likely that repeated profiles will approximately measure the same volume of water, allowing for the observation of the vertical evolution of a rain-induced freshwater lens, as well as the ambient vertical mixing. This is at the same time the largest limitation of this study, as

we have no information about the horizontal extent of the freshwater anomalies. Along its path the ASIP encountered some variability in the T-S properties of the layer below the surface mixed layer, and ADCP measurements in the mixed layer show that horizontal currents are present and variable. It is thus quite likely that horizontal processes play a role in the evolution of surface anomalies in this specific study region, which is located just north of the mean path of the Gulf Stream. *Soloviev et al.* (2015) showed the edge effects in the presence of horizontal advection can be of major influence on a fresh water lens. Linear relationships between salinity-anomaly, rain rate and windspeed, like those determined in *Boutin et al.* (2013) and *Drushka et al.* (2016), are unlikely to make accurate predictions of ΔS in the presence of advection.

Spatial and temporal averaging lowers the resolution of time series of rain rate, wind speed and sea surface properties, which has direct implications to the predictive capability of the models. Wind squalls and changes in air temperature in association with rain can be large and of direct importance to the mixing conditions (*Wijesekera et al.*, 2005). Averaging rain rates over a certain period or area also causes a reduction of the peak rate. This may explain why the simulated surface salinity anomaly as a function of the peak rain rate, following the relation by *Drushka et al.* (2016) over-predicts the salinity anomaly caused by rain event III. The correlation with the observed near-surface salinity anomaly is improved when R_{tot} is used instead of R_{max} . With a more extensive observational record a parameterisation based on integrated rain rate and momentum flux should be determined, to facilitate comparison of datasets of different temporal resolution.

In-situ measures of R_{max} and R_{tot} both are ‘bucket-measures’ of the rainfall. They do not give information about the size distribution and impact velocity of the rain, and measured rain rates may be affected by the motion of the ship (*Klepp*, 2015). The terminal velocity and penetration depth of rain drops is dependent on the dropsize distribution. Small drops add fresh water to the surface skin layer, whereas larger droplets can penetrate to tens of centimetres depth, forming a volume source instead (*Schlüssel et al.*, 1997; *Peirson et al.*, 2013). Models like the prognostic scheme from *Bellenger et al.* (2017), use parameterisations to account for these effects, however the natural variability of them has seldom been measured in oceanic field studies

6 Conclusions and Future Work

Solar radiation is the main source of energy to the OSBL, and its daily cycle invokes a diurnal cycle of heating the upper ocean. The density effect of this heating results in the development of a positively buoyant, warmer near-surface layer during daytime. Surface cooling when the solar influx reduces to zero during nighttime produces convective instability, driving turbulent overturns which result in a homogenised mixed layer. Both the daytime heating and nighttime cooling are reduced when clouds are present, which can either be formed locally or advected over a region by synoptic weather systems. Clouds will partially block the downwelling solar radiation, and also prevent the loss of longwave radiation out of the atmosphere, re-emitting it back towards the ocean. Rain is a source of fresh water at a different temperature than the ocean surface. It reduces the salinity, and thereby the density of the near-surface ocean, and can thereby also lead to a stable shallow stratification. How much the air-sea fluxes are influenced by either rainfall or diurnal warming is dependent on the magnitude, and the lifetime of the surface density anomalies. The near-surface layer and the density anomalies therein are largely dependent on the competing forces of buoyancy and turbulent kinetic energy, which works to disperse the temperature and/or salinity gradients laterally and in the vertical.

In this thesis the developments of density stratification in the OSBL as a result of diurnal warming and precipitation, and associated changes to the turbulent mixing of the OSBL have been investigated, using novel in-situ observations from different oceanic regions. These observations comprise of profiles of temperature, salinity and turbulence velocity shear made with the Air-Sea Interaction Profiler (ASIP), a state-of-the art autonomous ocean profiler. ASIP is developed to measure fine structure profiles throughout the OSBL. The profiler is one of few instruments which provide high-resolution measurements in the 10 metres up to the ocean surface, and is therefore specifically suitable for the observation of shallow stratification and upper ocean turbulence.

The observational record presented is new and required specialised data-processing techniques. Revision of the turbulence data processing for a number of profiles from different campaigns has indicated that there can be order of magnitude differences in the computation of ϵ , depending on the method used. For this work it was chosen to update the ASIP turbulence data processing towards the methods used by the main producers of shear probes, as presented in (*Lueck, 2016a*). The turbulence measurements used originate from relatively calm environments, which may affect the choice of optimal method. In rougher conditions the shear spectra will be shifted towards higher wave numbers, which may be too high to resolve, but on

the other hand the signal-to-noise ratio can be expected to improve. Future work will see a further evaluation of these methods for a wider range of sea states.

Observations from two sea-going research campaigns in the subtropical North Atlantic are used to study diurnal warming. Rain-induced stratification mainly occurs in tropical oceans, where precipitation is high. However, here the changes brought to the near-surface layer by four rain events opportunistically encountered during a campaign in a mid-latitude region of the North Atlantic are presented. The ASIP measurements are used to analyse the upper ocean's response to both phenomena, from the perspective of changes in the vertical distribution of physical variables. The evolution of the oceanic variables is analysed in conjunction with simultaneous measurements of meteorological variables, to establish the relationship between the observed ocean response and atmospheric forcing.

Diurnal warming was observed to create a temperature difference of up to 1 °C between the surface and 10 m depth; various authors have reported higher values of up to 6 degrees (*Fairall et al.*, 1996b; *Ward*, 2006; *Gentemann and Minnett*). The regular occurrence of such strong vertical gradients emphasises the need to accurately report the measurement depth of sea surface temperature data assembled into global products of SST, used as boundary conditions to ocean and weather prediction models. The diurnal cycle in the sea surface temperature (SST) is shown to modify air-sea heat and moisture fluxes. The ambient wind conditions during warming are a critical factor in this. Under low-wind conditions the amplitude of the diurnal SST cycle is high, whilst the surface mixed layer shoals. In this situation surface renewal is limited on both sides of the air-sea interface. Under moderate winds a warm mixed layer of 5-10 m depth is observed to develop which reduces the SST amplitude at the surface, whilst positively influencing the heat fluxes.

The high resolution datasets provide a means to evaluate the computation of warm-layer models. The diurnal warm layer (DWL) can be modelled in various ways, using methods of increasing complexity which resolve the diurnal cycle of the near-surface layer with increasing precision. The COARE bulk-flux algorithm, which is widely used to derive air-sea fluxes of heat, momentum and gases from routinely measured bulk-variables, represents diurnal warming by means of a correction to the SST used in the flux computations. The warm-layer in COARE is described by a depth D_w and a linear temperature gradient resulting in the temperature difference between this depth and the ocean interface ΔT_w . The COARE algorithm has been used to compute air-sea fluxes for the period and location corresponding to the two research campaigns in the subtropical Northern Atlantic, as well as for an additional data set from the Mediterranean sea. During this last campaign upper ocean measurements of temperature are available from the profiler SkinDeEP.

The observed temperature gradient over the upper 5 m, as well as the sea surface temperature at sub-skin level T_{0-} are compared to the diurnal warming simulated with COARE. It is found that the amplitude and phase of the diurnal warming are well represented by the algorithm. The time of day at which the maximum in

T_{0-} occurs is shown to be later with increasing warming amplitude. The COARE model generally overestimates the near-surface temperature gradient after the peak warming, and also T_{0-} is then somewhat higher than observed. The first is explained by the linear temperature gradient used by the model, which does not well represent the warm mixed layer during the second part of the day. The under-representation of convective mixing by COARE contributes to an overestimation of the heat content of the afternoon warm layer too. Varying the absorption of solar irradiance described in COARE affects the amount of heat absorbed over the layer, thereby changing ΔT_w and D_w .

A shallow thermal stratification can put significant constraints on the distribution of matter in the OSBL. Further use of the ASIP could be made by combining the T, S and ϵ measurements with the distribution of bio-chemical components in the OSBL, or with profiles of light. The COARE model has proven quite sensitive to the formulation of the absorption of the solar radiative flux; it could be of interest to perform a similar sensitivity study to shortwave absorption parameterisations on warm layer prediction with a model that describes the physics of warm layer evolution better (e.g. *Price et al.*, 1986; *Gentemann et al.*, 2009).

The future should also see a renewed focus on the temperature gradient over the skin-layer during warming, both from an observational as well as a modelling perspective. ASIP's autonomy and upward profiling strategy make it a very suitable vehicle for measuring this layer, provided that faster C/T-sensors are used, and that the profiler's rise velocity is lowered. This will improve the resolution of both the microstructure temperature and salinity features, which is essential for the observation of small scale variability directly below the surface.

Compared to solar heating, rain is only an episodic event, although it can be of significant impact to the near-surface layer in tropical regions of the world's oceans. The rain-induced salinity anomalies observed in a mid-latitude region, do not create a shallow stratification as strong and persistent as the observed stratification from diurnal warming. However, the dilution of the surface salinity by the rain water leaves a clear signature in the T-S curves of the surface water, proving that the formation of stable fresh lenses at the ocean surface is not a feature of tropical regions only. The rainfall here observed created a difference of at most 0.4 g kg^{-1} between the surface and 10 m depth. Although small, these rainfall signatures in the sea surface salinity may still lead to a misrepresentation of the near-surface salinity by satellite mounted sensors.

The buoyancy effects of rain are highly dependent on the ambient ocean and atmospheric forcing conditions. In calm conditions a rain event can result in the formation of a stable freshwater lens at the surface, the extent and duration of which is variable. They work as a shallow layer, confining and speeding up the air-sea interaction process within them, whilst temporarily shutting off the mixed layer below from interaction with the atmosphere. The single freshwater lens observed in this study, indeed has this effect; between the surface and the rain-induced halocline ϵ is two orders of magnitude higher compared to the remnant mixed layer below. Rain drop impact is thought to cause small scale turbulence, and to

positively enhance the gas-exchange of e.g. CO_2 between the ocean and atmosphere. A re-analysis of gas flux measurements during the Knorr-11 campaign may provide further evidence for this. Shear probe measurements on a moving platform are not the most suitable to quantify the rain induced turbulence, due to the relatively large spatial averaging required in deriving ϵ from the shear spectrum. In ch. 3 the signature of rain in microstructure signals was investigated. A significant increase of the spectra of vertical conductivity gradient directly below the surface was observed. From the T-S relation it can be inferred that this conductivity variance dominantly reflects the turbulent salinity fluctuations. The extent to which this is also reflective of the dynamic impact of turbulence has still to be verified. The scattered and variable nature of precipitation puts challenges to both its observation and the implication of rain effects in ocean models. In relating rainfall rate to salinity anomalies, this strongly variable nature of rain is often ignored. Episodes of rainfall typically coincide with local changes in the wind field. The observations suggest that for short bursts of rain, typical of cold fronts in mid-latitudes, the peak rain rate is not the most appropriate metric to predict the surface salinity anomaly, as this is dependent on the resolution of the time series used. It is found that there is a more significant causal relation between the total rain amount and the salinity anomaly at the surface, than between the peak rain rate and the salinity response. Understanding the magnitude and lifetime of fresh lenses is important to quantify their role in variability of mesoscale air-sea exchange processes and the water cycle, as well as their impact on remote sensing of sea surface salinity. A research campaign specifically targeting the upper ocean response to rainfall should focus on the upper ten metres of the ocean. Such an experiment has to put high demands on the accuracy of measurement techniques of both the the physical oceanographic parameters as well as the atmospheric forcing parameters (rain rates, wind speed near the surface, heat fluxes). To quantify the turbulent mixing induced by the rain, high resolution measurements of T , S and ϵ close to the surface are essential. At the same time both the vertical and horizontal extent of rain-induced salinity anomalies have to be monitored. The SPURS-2 project, comprising research campaigns to the tropical Pacific in 2016/2017, seems to have successfully targeted many of the unknowns remaining about the upper ocean response to rainfall.

Scaling of the turbulent kinetic energy equation indicates that there is a balance between production of TKE, its dissipation and the loss to buoyancy. The negative density flux resulting from near-surface heating and rainfall increases the buoyancy of the surface mixed layer, thereby suppressing turbulent mixing, quantified with TKE dissipation. Similarity scaling can provide insight into the evolution of the dominant turbulence generating mechanism controlling the surface density anomaly. When the Monin-Obukhov length L is positive, there is a positive buoyancy flux into the ocean. It then depends on the available surface momentum flux whether the density anomaly is contained near the surface, suppressing dissipation below it, or that wind induced turbulence will control the mixed layer. During nighttime both wind and buoyancy induced turbulence (convection) collaborate in the dispersion of vertical gradients of temperature and salinity. The observations from the

subtropical ocean, as well as the Mediterranean show that on calm nights it can occur that the atmospheric conditions limit surface cooling. Under these conditions it is observed that convective mixing is not strong enough to fully homogenise the OSBL, such that the following day a new thermal stratification develops within the remnant warm-layer. It is likely that these episodes of warming are critical for the spring restratification process. Specifically they can be important to the development of the high surface salinity maximum characteristic of the region in the North Atlantic where observations took place.

The analysis of L in the rainfall study illustrates the effect that rain can have on the surface buoyancy flux, changing its sign during nighttime. The fact that during the first three rain events h/L still indicates that wind induced momentum is dominant, explains why only during the fourth event a fresh water lens is formed. No observation of rainfall on a thermally stratified near-surface layer was observed. One can imagine that the two effects combined can be of significant impact to the near-surface layer, leading to a shallow stratification below the ocean surface for periods beyond the diurnal cycle. It has been hypothesised that the splashing of raindrops enhances turbulence below the surface, partially counteracting the reduction of TKE dissipation by the buoyancy increase. However, turbulence close to the ocean interface is rarely quantified. Further research to the enhanced dissipation levels observed both within warm and fresh layers, and around the level of the associated pycnocline is required, to determine the governing balance between sources and sinks of TKE.

This thesis is based on local ‘snapshots’ of the thermodynamic state of the OSBL. Observations of changes to this state are related to local air-sea fluxes. However, the ASIP measurements are limited in their temporal and spatial extent. Alongside the deployment of different types of instruments it has provided a valuable contribution to integrated meso-scale experiments. The measurements contribute to the fundamental study of small-scale processes. If more repeat experiments under a wider variety of conditions were made, ultimately the observations could also form an input to parameterisation of sub-grid processes in numerical weather prediction and climate models. The future will hopefully see re-deployment of the profiler, equipped with updated sensor technology and/or different types of sensors to enhance ASIP’s application in multidisciplinary ocean experiments.

Bibliography

- Anderson, J. E., and S. C. Riser (2014), Near-surface variability of temperature and salinity in the near-tropical ocean: Observations from profiling floats, *J. Geophys. Res.*, *119*(11), 7433–7448, doi:10.1002/2014JC010112.
- Asher, W., A. Jessup, R. Branch, and D. Clark (2014), Observations of rain-induced near-surface salinity anomalies, *J. Geophys. Res.*, *119*, 5483–5500, doi:10.1002/2014JC009954.
- Bao, S., S. Raman, and L. Xie (2003), Numerical simulation of the response of the ocean surface layer to precipitation, *Pure and Applied Geophysics*, *160*.
- Batchelor, G., I. Howells, and A.A.Townsend (1959), Small-scale variation of convected quantities like temperature in turbulent fluid. part 1: General discussion and the case of small conductivity, *J. Fluid Mechanics*, *5*, 134–139, doi:10.1017/S002211205900009X.
- Batchelor, G. K. (1952), The effect of homogeneous turbulence on material lines and surfaces, *Proceedings of the Royal Society of London A: Mathematical, Physical and Engineering Sciences*, *213*(1114), 349–366, doi:10.1098/rspa.1952.0130.
- Bell, T., W. D. Bruyn, S. Miller, B. Ward, K. Christensen, and E. Saltzman (2013), Air-sea dimethylsulfide (DMS) gas transfer in the North Atlantic: evidence for limited interfacial gas exchange at high wind speed, *Atm. Chem. Phys.*, *13*, 11,073–11,087, doi:10.5194/acp-13-11073-2013.
- Bell, T. G., S. Landwehr, S. D. Miller, W. J. de Bruyn, A. H. Callaghan, B. Scanlon, B. Ward, M. Yang, and E. S. Saltzman (2017), Estimation of bubbled-mediated air-sea gas exchange from concurrent DMS and CO₂ transfer velocities at intermediate-high wind speeds, *Atmos. Chem. Phys.*, doi:10.5194/acp-17-9019-2017.
- Bellenger, H., K. Drushka, W. Asher, G. Reverdin, M. Katsumata, and M. Watanebe (2017), Extension of the prognostic model of sea surface temperature to rain-induced cool and fresh lenses, *J. Geophys. Res.*, *122*, 484–507.
- Bengtsson, L. (2010), The global atmospheric water cycle, *Env. Res. Lett.*, *5*.
- Bernie, D. J., S. J. Woolnough, J. M. Slingo, and E. Guilyardi (2005), Modeling diurnal and intraseasonal variability of the ocean mixed layer, *J. Climate*, *18*(8), 1190–1202, doi:10.1175/JCLI3319.1.

- Best, A. (1950), The size distribution of rain, *Quarterly Journal of the Royal Meteorological Soc.*, *76*, 16–36.
- Bogucki, D., H. Luo, and J. Domaradzi (2012), Experimental evidence of the Kraichan scalar spectrum at high Reynolds numbers, *J. Phys. Oceanogr.*, *42*, 1717–1728, doi:10.1175/JPO-D-11-0214.1.
- Bourras, D., H. Branger, G. Reverdin, L. Mari, R. Cambra, L. Baggio, C. Caudoux, G. Caudal, S. Morisset, N. Geyskens, A. Weill, and D. Hauser (2014), A new platform for the determination of airsea fluxes (ocarina): Overview and first results, *J. Atmos. Oceanic Technol.*, *31*(5), 1043–1062, doi:10.1175/JTECH-D-13-00055.1.
- Boutin, J. (2016), Satellite and in situ salinity: Understanding near-surface stratification and sub-footprint variability, *Bull. Am. Meteorol. Soc.*, *5*.
- Boutin, J., N. Martin, G. Reverdin, X. Yin, and F. Gaillard (2013), Sea surface freshening inferred from SMOS and ARGO salinity: impact of rain, *Ocean Science*, *9*, 183–192, doi:10.5194/os-9-183-2013.
- Boutin, J., N. Martin, G. Reverdin, S. Morisset, X. Yin, L. Centurioni, and N. Reul (2014), Sea surface salinity under rain cells: SMOS satellite and in situ drifters observations, *J. Geophys. Res.*, *119*(8), 5533–5545, doi:10.1002/2014JC010070.
- Brainerd, K., and M. Gregg (1993), Diurnal restratification and turbulence in the oceanic surface mixed layer 1. observations, *J. Geophys. Res.*, *98*, 22,645–22,656.
- Brainerd, K., and M. Gregg (1995), Surface mixed and mixing layer depths, *Deep Sea Res. I*, *42*(9), 1521–1543.
- Brainerd, K. E., and M. C. Gregg (1997), Turbulence and stratification on the tropical ocean-global atmosphere-coupled ocean-atmosphere response experiment microstructure pilot cruise, *J. Geophys. Res.*, *102*(C5), 10,437–10,455, doi:10.1029/96JC03864.
- Burchard, H., K. Bolding, and M. Ruiz-Villarreal (1999), GOTM, a general ocean turbulence model. theory, implementation and test cases, *Tech. rep.*, European Commission, rep. EUR 18745.
- Busecke, J., A. L. Gordon, Z. Li, F. M. Bingham, and J. Font (2014), Subtropical surface layer salinity budget and the role of mesoscale turbulence, *J. Geophys. Res.*, *119*(7), 4124–4140, doi:10.1002/2013JC009715.
- Caldwell, D., and W. P. Elliott (1971), Surface stresses produced by rainfall, *J. Phys. Oceanogr.*, pp. 145–148.
- Caldwell, D. R., R.-C. Lien, J. N. Moum, and M. C. Gregg (1997), Turbulence decay and restratification in the equatorial ocean surface layer following nighttime convection, *J. Phys. Oceanogr.*, *27*(6), 1120–1132, doi:10.1175/1520-0485(1997)027<1120:TDARIT>2.0.CO;2.

- Callaghan, A. H., B. Ward, and J. Vialard (2014), Influence of surface forcing on near-surface and mixing layer turbulence in the tropical Indian Ocean, *Deep-Sea Res.*, *4*, doi:10.1016/j.dsr.2014.08.009.
- Cavaleri, L., L. Bertotti, and J.-R. Bidlot (2015), Waving in the rain, *J. Geophys. Res.*, pp. 3248–3260, doi:10.1002/2014JC010348.
- Charnock, H. (1955), Wind stress on a water surface, *Quarterly Journal of the Royal Meteorological Society*.
- Chen, S. S., and R. A. Houze (), Diurnal variation and life-cycle of deep convective systems over the tropical pacific warm pool, *Quarterly Journal of the Royal Meteorological Society*, *123*(538), 357–388, doi:10.1002/qj.49712353806.
- Christensen, K., J. Rohrs, B. Ward, I. Fer, G. Brostrom, O. Saetra, and O. Breivik (2013), Surface wave measurements using a ship-mounted ultrasonic altimeter, *Methods in Oceanography*, *6*(Supplement C), 1 – 15, doi:https://doi.org/10.1016/j.mio.2013.07.002.
- Clayson, C., and A. Bogdanoff (2013), The effect of diurnal sea surface temperature warming on climatological air-sea fluxes, *J. Climate*, *26*, 2546–2556.
- Clayson, C. A., and A. Chen (2002), Sensitivity of a coupled single-column model in the tropics to treatment of the interfacial parameterizations, *J. Climate*, *15*(14), 1805–1831, doi:10.1175/1520-0442(2002)015<1805:SOACSC>2.0.CO;2.
- Craeye, C., and P. Schlüssel (1998), Rainfall on the sea: surface renewals and wave damping - research note, *Boundary layer meteorology*, *89*, 349–355.
- Cronin, M. F., and W. S. Kessler (2002), Seasonal and interannual modulation of mixed layer variability at 0, 110w, *Deep Sea Res. I*, *49*(1), 1 –17, doi:10.1016/S0967-0637(01)00043-7.
- de Boyer Montegut, C., G. Madec, A. Fischer, A. Lazar, and D. Iudicone (2003), Mixed layer depth over the global ocean: and examination of profile data and a profile-based climatology, *J. Geophys. Res.*, *109*, doi:10.1029/2004JC002378.
- Dickey, T. D., and J. J. Simpson (1983), The influence of optical water type on the diurnal response of the upper ocean, *Tellus B*, *35B*(2), 142–154, doi:10.1111/j.1600-0889.1983.tb00018.x.
- Dillon, T., and D. Caldwell (1980), The batchelor spectrum and dissipation in the upper ocean, *J. Geophys. Res.*, *85*(C4), 1910–1916.
- Donlon, C. (2003), A new generation of global coverage sea surface temperature data, *Eos, Transactions American Geophysical Union*, *84*(14), 127–133, doi:10.1029/2003EO140005.
- Donlon, C. (2005), The recommended ghrsst-pp data processing specification gds, *Tech. rep.*, Met Office, Exeter, U.K.

- Donlon, C., P. Minnett, C. Gentemann, T. Nightingale, I. Barton, B. Ward, and M. Murray (2002), Toward improved validation of satellite sea surface skin temperature measurements for climate research, *J. Climate*, *15*.
- Drennan, W. M., K. K. Kahma, and M. A. Donelan (1999), On momentum flux and velocity spectra over waves, *Boundary-Layer Meteorology*, *92*(3), 489–515, doi:10.1023/A:1002054820455.
- Drucker, R., and S. C. Riser (2014), Validation of Aquarius sea surface salinity with ARGO: Analysis of error due to depth of measurement and vertical salinity stratification, *J. Geophys. Res.*, *119*(7), 4626–4637, doi:10.1002/2014JC010045.
- Drushka, K., S. T. Gille, and J. Sprintall (2014), The diurnal salinity cycle in the tropics, *J. Geophys. Res.*, *119*(9), 5874–5890, doi:10.1002/2014JC009924.
- Drushka, K., W. E. Asher, B. Ward, and K. Walesby (2016), Understanding the formation and evolution of rain-formed fresh lenses at the ocean surface, *J. Geophys. Res.*, *121*.
- Edson, J. B., V. Jampana, R. A. Weller, S. P. Bigorre, A. J. Plueddemann, C. W. Fairall, S. D. Miller, L. Mahrt, D. Vickers, and H. Hersbach (2013), On the exchange of momentum over the open ocean, *J. Phys. Oceanogr.*, *43*(8), 1589–1610, doi:10.1175/JPO-D-12-0173.1.
- Emery, W., and R. Thomson (1998), *Data analysis methods in physical oceanography*, Pergamon.
- Esters, L., O. Breivik, S. Landwehr, A. ten Doeschate, G. Sutherland, K. H. Christensen, J. Bidlot, and B. Ward (), Turbulence scaling comparisons in the ocean surface boundary layer, *J. Geophys. Res.*, *123*(3), 2172–2191, doi:10.1002/2017JC013525.
- Fairall, C., E. Bradley, D. Rogers, J. Edson, and G. Young (1996a), Bulk-parameterization of air-sea fluxes for tropical ocean global atmosphere coupled-ocean atmosphere response experiment, *J. Geophys. Res.*, *101*, 3747–3764.
- Fairall, C., E. Bradley, J. Godfrey, G. Wick, J. Edson, and G. Young (1996b), Cool-skin and warm-layer effects on sea surface temperature, *J. Geophys. Res.*, *101*, 1295–1308.
- Fairall, C., E. Bradley, J. Hare, A. Grachev, and J. Edson (2003), Bulk parameterization of air-sea fluxes: Updates and verification for the coare algorithm, *J. Climate*, *16*, 571–591.
- Fairall, C. W., M. Yang, L. Bariteau, J. B. Edson, D. Helmig, W. McGillis, S. Pezoa, J. E. Hare, B. Huebert, and B. Blomquist (2011), Implementation of the coupled ocean-atmosphere response experiment flux algorithm with co₂, dimethyl sulfide, and o₃, *J. Geophys. Res.*, *116*(C4), doi:10.1029/2010JC006884.

- Farrar, J. T., L. Rainville, A. J. Plueddemann, W. S. Kessler, C. Lee, B. A. Hodges, R. W. Schmitt, J. B. Edson, S. C. Riser, C. C. Eriksen, and D. M. Frantantoni (2015), Salinity and temperature balances at the spurs central mooring during fall and winter, *Oceanography*, *28*, doi:10.5670/oceanog.2015.06.
- Gargett, A. E. (1989), Ocean turbulence, *Annual Review of Fluid Mechanics*, *21*(1), 419–451, doi:10.1146/annurev.fl.21.010189.002223.
- Gentemann, C., and P. J. Minnett (), Radiometric measurements of ocean surface thermal variability, *J. Geophys. Res.*, *113*(C8), doi:10.1029/2007JC004540.
- Gentemann, C., P. J. Minnett, and B. Ward (2009), Profiles of ocean surface heating (posh): A new model of upper ocean diurnal warming, *J. Geophys. Res.*, *114*.
- Gentemann, C. L., C. J. Donlon, A. Stuart-Menteth, and F. J. Wentz (2003), Diurnal signals in satellite sea surface temperature measurements, *Geophysical Res. Lett.*, *30*(3), doi:10.1029/2002GL016291.
- Gentemann, C. L., P. J. Minnett, P. Le Borgne, and C. J. Merchant (2008), Multi-satellite measurements of large diurnal warming events, *Geophysical Res. Lett.*, *35*(22), doi:10.1029/2008GL035730.
- Gill, A. E. (1982), *Atmosphere-Ocean Dynamics*, vol. 30, Academic Press.
- Goodman, L., E. Levine, and R. Lueck (2006), On measuring the terms of the turbulent kinetic energy budget from an auv, *J. Atmos. Oceanic Technol.*, *23*, 977–990.
- Gordon, A. L., C. F. Giulivi, J. Busecke, and F. M. Bingham (2015), Differences among subtropical surface salinity patterns, *Oceanography*, *28*, doi:10.5670/oceanog.2015.02.
- Gosnell, R., C. Fairall, and P. Webster (1995), The sensible heat flux of rainfall in the tropical ocean, *J. Geophys. Res.*, *100*, 18,437–18,442, doi:10.1029/95JC01833.
- Grant, H., B. Hughes, W. Vogel, and A. Moilliet (1968), The spectrum of temperature fluctuations in turbulent flow, *J. Fluid Mechanics*, *34*, 423–442.
- Green, T., and D. F. Houk (1979), The removal of organic surface films by rain, *Limnology and Oceanography*, *24*(5), 966–970, doi:10.4319/lo.1979.24.5.0966.
- Gregg, M. (1999), Uncertainties and limitations in measuring ϵ and χ_t , *J. Atmos. Oceanic Technol.*, *16*, 1483–1490.
- Gregg, M. C., and T. B. Meagher (1980), The dynamic response of glass rod thermistors, *J. Geophys. Res.*, *85*(C5), 2779–2786, doi:10.1029/JC085iC05p02779.
- Hahn-Woernle, L., H. Dijkstra, and H. van der Woerd (2014), Sensitivity of phytoplankton distributions to vertical mixing along a north atlantic transect, *Ocean Science*, *10*, 993–1011.

- Harrison, E. L., and F. Veron (2017), Near-surface turbulence and buoyancy induced by heavy rainfall, *J. Fluid Mechanics*, *830*, 602–630, doi:10.1017/jfm.2017.602.
- Harrison, E. L., F. Veron, D. T. Ho, M. C. Reid, P. Orton, and W. R. McGillis (2012), Nonlinear interaction between rain- and wind-induced air-water gas exchange, *J. Geophys. Res.*, *117*(C3), doi:10.1029/2011JC007693.
- Hill, K. (1987), Observations on the velocity scaling of thermistor dynamic response functions, *Review of Scientific Instruments*, *58*, doi:10.1063/1.1139444.
- Ho, D. T., C. J. Zappa, W. R. McGillis, L. F. Bliven, B. Ward, J. W. H. Dacey, P. Schlosser, and M. B. Hendricks (2004), Influence of rain on air-sea gas exchange: Lessons from a model ocean, *J. Geophys. Res.*, *109*(C8), doi:10.1029/2003JC001806.
- Houk, D., and T. Green (1976), A note on surface waves due to rain, *J. Geophys. Res.*, *81*(24), 4482–4484, doi:10.1029/JC081i024p04482.
- IOC, SCOR, and IAPSO (2010), *The international thermodynamic equation of seawater - 2010: Calculation and use of thermodynamic properties*.
- Jerlov, N. (1968), *Optical Oceanography*, Elsevier Oceanography Series.
- Jerlov, N. (1976), *Marine Optics*, Elsevier Oceanography Series.
- Kantha, L. H., and C. A. Clayson (1994), An improved mixed layer model for geophysical applications, *J. Geophys. Res.*, *99*(C12), 25,235–25,266, doi:10.1029/94JC02257.
- Kara, A., P. Rochford, and H. Hurlburt (2000), An optimal definition for the ocean mixed layer depth, *J. Geophys. Res.*, *105*(C7), 16,803–16,821, doi:10.1029/2000JC900072.
- Karagali, I., J. L. Høyer, and C. J. Donlon (2017), Using a 1-D model to reproduce the diurnal variability of sst, *J. Geophys. Res.*, *122*(4), 2945–2959, doi:10.1002/2016JC012542.
- Katsaros, K., and K. Buettner (1969), Influence of rainfall on temperature and salinity of the ocean surface, *J. Applied Meteorology*, *8*, 15–18.
- Kawai, Y., and A. Wada (2007), Diurnal sea surface temperature variation and its impact on the atmosphere and ocean: a review, *J. Oceanogr.*, *63*, 721–744.
- Klepp, C. (2015), The oceanic shipboard precipitation measurement network for surface validation – OceanRAIN, *Atmospheric Research*, *163*(Supplement C), 74 – 90, doi:https://doi.org/10.1016/j.atmosres.2014.12.014, 6th Workshop of the International Precipitation Working Group.
- Kolmogorov, A. (1941), The local structure of turbulence in incompressible viscous fluid for very large reynolds' numbers, *Akademiia Nauk SSSR Doklady*, *30*, 301–305.

- Kraichnan, R. H. (1968), Smallscale structure of a scalar field convected by turbulence, *The Physics of Fluids*, *11*(5), 945–953, doi:10.1063/1.1692063.
- Kundu, P., and I. M. Cohen (2008), *Fluid Mechanics*, 4th ed., Elsevier.
- Lagerloef, G. (2012), Satellite mission monitors ocean surface salinity, *Eos. Transactions American Geophysical Union*, *93*(25), 233–234, doi:10.1029/2012EO250001.
- Landwehr, S., N. O’ Sullivan, and B. Ward (2015), Direct flux measurements from mobile platforms at sea: Motion and airflow distortion corrections revisited, *J. Atmos. Oceanic Technol.*, *32*(6), 1163–1178, doi:10.1175/JTECH-D-14-00137.1.
- Large, W. G., and J. M. Caron (2015), Diurnal cycling of sea surface temperature, salinity, and current in the cesm coupled climate model, *J. Geophys. Res.*, *120*(5), 3711–3729, doi:10.1002/2014JC010691.
- Large, W. G., and S. Pond (1981), Open ocean momentum flux measurements in moderate to strong winds, *J. Phys. Oceanogr.*, *11*(3), 324–336, doi:10.1175/1520-0485(1981)011<0324:OOMFMI>2.0.CO;2.
- Large, W. G., J. C. McWilliams, and S. C. Doney (1994), Oceanic vertical mixing: A review and a model with a nonlocal boundary layer parameterization, *Reviews of Geophysics*, *32*(4), 363–403, doi:10.1029/94RG01872.
- Levine, E. R., and R. G. Lueck (1999), Turbulence measurement from an autonomous underwater vehicle, *J. Atmos. Oceanic Technol.*, *16*(11), 1533–1544, doi:10.1175/1520-0426(1999)016<1533:TMFAAU>2.0.CO;2.
- Lhermitte, R. M. (1988), Observation of rain at vertical incidence with a 94 ghz doppler radar: An insight on mie scattering, *Geophysical Res. Lett.*, *15*(10), 1125–1128, doi:10.1029/GL015i010p01125.
- Lindstrom, E., F. Bryan, and R. Schmitt (2015), SPURS: Salinity processes in the upper-ocean regional study -the North Atlantic experiment, *Oceanography*, *28*.
- Liss, P. S., and R. A. Duce (2010), *The sea surface and global change*, Cambridge University Press.
- Liu, W., K. Katsaros, and J. Businger (1979), Bulk parametrization of air-sea exchanges of heat and water vapor including the molecular constraints at the interface, *J. Atmos. Sci.*, *36*, 17221,735.
- Liu, X., Q. Zheng, R. Liu, M. A. Sletten, and J. H. Duncan (2017), A model of radar backscatter of rain-generated stalks on the ocean surface, *IEEE Transactions on Geoscience and Remote Sensing*, *55*(2), 767–776, doi:10.1109/TGRS.2016.2614897.
- Lombardo, C., and M. Gregg (1989), Similary scaling of viscous and thermal dissipation in a convective surface boundary layer, *J. Geophys. Res.*, *94*, 6273–6284.

- Lueck, R. (2016a), RSI TN 028: Calculating the rate of dissipation of turbulent kinetic energy, *Tech. rep.*, Rockland Scientific International Inc.
- Lueck, R., and J.J.Picklo (1990), Thermal inertia of conductivity cells: Observations with a sea-bird cell, *J. Atmos. Oceanic Technol.*, *7*, 756–768.
- Lueck, R., F. Wolk, and H. Yamazaki (2002), Oceanic velocity microstructure measurements in the 20th century, *J. Oceanogr.*, *58*, 153–174.
- Lueck, R. G. (2016b), Ocean turbulence, a 5-day introduction with data collection.
- Luketina, D. A., and J. Imberger (2001), Determining turbulent kinetic energy dissipation from batchelor curve fitting, *J. Atmos. Oceanic Technol.*, *18*(1), 100–113, doi:10.1175/1520-0426(2001)018<0100:DTKEDF>2.0.CO;2.
- Macoun, P., and R. Lueck (2004), Modeling the spatial response of the airfoil shear probe using different sized probes, *J. Atmos. Oceanic Technol.*, *21*, 284–297.
- Manton, M. J. (1973), On the attenuation of sea waves by rain, *Geophysical Fluid Dynamics*, *5*(1), 249–260, doi:10.1080/03091927308236119.
- Marshall, J., and W. M. Palmer (1948), The distribution of raindrops with size, *J. Meteorology*, *5*, 165–166.
- Marullo, S., P. J. Minnett, R. Santoleri, and M. Tonani (2016), The diurnal cycle of sea-surface temperature and estimation of the heat budget of the Mediterranean Sea, *J. Geophys. Res.*, *121*(11), 8351–8367, doi:10.1002/2016JC012192.
- McMillan, J. M., A. E. Hay, R. G. Lueck, and F. Wolk (2016), Rates of dissipation of turbulent kinetic energy in a high reynolds number tidal channel, *J. Atmos. Oceanic Technol.*, *33*(4), 817–837, doi:10.1175/JTECH-D-15-0167.1.
- Mecklenburg, S., M. Drusch, Y. Kerr, J. Font, M. Martin-Neira, S. Delwart, G. Buenadicha, N. Reul, E. Daganzo-Eusebio, R. Oliva, and R. Crapolicchio (2012), ESA’s soil moisture and ocean salinity mission: Mission performance and operations, *IEEE Transactions Geoscientific Remote Sensing*, *50*, 1354–1366, doi:10.1109/TGRS.2012.2187666.
- Mellor, G. L., and T. Yamada (1982), Development of a turbulence closure model for geophysical fluid problems, *Reviews of Geophysics*, *20*(4), 851–875, doi:10.1029/RG020i004p00851.
- Mensah, V., M. L. Menn, and Y. Morel (2009), Thermal mass correction for the evaluation of salinity, *J. Atmos. Oceanic Technol.*, *26*(3), doi:10.1175/2008JTECH0612.1.
- Merchant, C., M. Filipiak, P. L. Borgne, H. Roquet, E. Autret, J. Piollé, and S. Lavender (), Diurnal warm-layer events in the western Mediterranean and European shelf seas, *Geophysical Res. Lett.*, *35*(4), doi:10.1029/2007GL033071.

- Merchant, C. J., O. Embury, J. Roberts-Jones, E. Fiedler, C. E. Bulgin, G. K. Corlett, S. Good, A. McLaren, N. Rayner, S. Morak-Bozzo, and C. Donlon (2014), Sea surface temperature datasets for climate applications from phase 1 of the european space agency climate change initiative (sst cci), *Geoscience Data Journal*, 1(2), 179–191, doi:10.1002/gdj3.20.
- Miller, S., C. Marandino, W. de Bruyn, and E. S. Saltzman (2009), Air-sea gas exchange of CO₂ and DMS in the North Atlantic by eddy covariance, *Geophysical Res. Lett.*, 36(15), doi:10.1029/2009GL038907.
- Millero, F., R. Feistel, D. Wright, and T. McDougall (2008), The composition of standard seawater and the definition of the reference-composition salinity scale, *Deep Sea Res. I*, 55.
- Minnett, P., R. Knuteson, F. Best, B. Osborne, J. Hanafin, and O. Brown (2001), The marine-atmospheric emitted radiance interferometer: a high-accuracy seagoing infrared spectroradiometer, *J. Atmos. Oceanic Technol.*, 18, 994–1013.
- Mobley, C. D. (1994), *Light and Water: Radiative Transfer in Natural Waters*, Academic Pres.
- Monin, A. S., and A. M. Obukhov (1954), Basic laws of turbulent mixing in the surface layer of the atmosphere, *Tr. Akad. Nauk SSSR Geophys. Inst*, 24, 163–187, adapted by Keith McNaughton (2008) from a translation by John Miller (1959).
- Morel, A. (1998), Optical modeling of the upper ocean in relation to its biogeous matter content (case i waters), *J. Geophys. Res.*, 93, 10,749–10,768.
- Morel, A., and D. Antoine (1994), Heating rate within the upper ocean in relation to its bio-optical state, *J. Phys. Oceanogr.*, 24(7), 1652–1665, doi:10.1175/1520-0485(1994)024<1652:HRWTUO>2.0.CO;2.
- Morison, J., R. Andersen, N. Larson, E. D’Asaro, and T. Boyd (1994), The correction for thermal-lag effects in sea-bird ctd data, *J. Atmos. Oceanic Technol.*, 11, 1151–1164.
- Moulin, A., J. Moum, and E. Shroyer (2018), Evolution of turbulence in the diurnal warm layer, *J. Phys. Oceanogr.*, in press, doi:10.1175/JPO-D-17-0170.1.
- Moum, J., and W. Smyth (2001), Upper ocean mixing processes, *Encyclopedia of Ocean Sciences*, 6, 3093–3100, doi:10.1006/rwos.2001.0156.
- Moum, J. N., M. C. Gregg, R. C. Lien, and M. E. Carr (1995), Comparison of turbulence kinetic energy dissipation rate estimates from two ocean microstructure profilers, *J. Atmos. Oceanic Technol.*, 12(2), 346–366, doi:10.1175/1520-0426(1995)012<0346:COTKED>2.0.CO;2.
- Mudge, T., and R. Lueck (1991), Digital signal processing to enhance oceanographic observations, *J. Atmos. Oceanic Technol.*, 11, 825–836.

- Nash, J., and J. Moum (1999), Estimating salinity variance dissipation rate from conductivity microstructure measurements, *J. Atmos. Oceanic Technol.*, *16*, 263–274.
- Nash, J., and J. Moum (2002), Microstructure estimates of turbulent salinity flux and the dissipation spectrum of salinity, *J. Phys. Oceanogr.*, *32*, 2312–2333.
- Nash, J., D. Caldwell, M. Zelman, and J. Moum (1999), A thermocouple probe for high-speed temperature measurement in the ocean, *J. Atmos. Oceanic Technol.*, *16*, 1474–.
- Oakey, N. (1982), Determination of the rate of dissipation of turbulent kinetic energy from simultaneous temperature and velocity shear microstructure measurements, *J. Phys. Oceanogr.*, *12*, 256–271.
- Oguz, H., and A. Prosperetti (1991), Numerical calculation of the underwater noise of rain, *J. Fluid Mechanics*, *228*, 417–442.
- Ohlmann, J. C. (2003), Ocean radiant heating in climate models, *J. Climate*, *16*, 1337–1351.
- Ohlmann, J. C., and D. A. Siegel (2000), Ocean radiant heating. part II: Parameterizing solar radiation transmission through the upper ocean, *J. Phys. Oceanogr.*, *30*, 1849–1865.
- Ohlmann, J. C., D. A. Siegel, and C. Mobley (2000), Ocean radiant heating. part I: Optical influences, *J. Phys. Oceanogr.*, *30*, 1833–1848.
- Osborn, T. (1974), Vertical profiling of velocity microstructure, *J. Phys. Oceanogr.*, *4*, 109–115.
- Osborn, T., and C. Cox (1972), Oceanic fine structure, *Geophysical Fluid Dynamics*, *3*(1), 321–345, doi:10.1080/03091927208236085.
- Osborn, T. R. (1980), Estimates of the local rate of vertical diffusion from dissipation measurements, *J. Phys. Oceanogr.*, *10*(1), 83–89, doi:10.1175/1520-0485(1980)010<0083:EOTLRO>2.0.CO;2.
- Paulson, C., and J. Simpson (1977), Irradiance measurements in the upper ocean, *J. Phys. Oceanogr.*, *7*, 952–956.
- Paulson, C., and J. Simpson (1981), The temperature difference across the cool skin of the ocean, *J. Geophys. Res.*, *86*(C11), 11,044–11,504, doi:10.1029/JC086iC11p11044.
- Peirson, W., J. Beyá, M. Banner, J. Peral, and S. Azarmsa (2013), Rain-induced attenuation of deep-water waves, *J. Fluid Mechanics*, *724*, 5–35, doi:10.1017/jfm.2013.87.

- Perlin, A., and J. N. Moum (2012), Comparison of thermal variance dissipation rates from moored and profiling instruments at the equator, *J. Atmos. Oceanic Technol.*, *29*(9), 1347–1362, doi:10.1175/JTECH-D-12-00019.1.
- Pimentel, S., K. Haines, and N. K. Nichols (2008), Modeling the diurnal variability of sea surface temperatures, *J. Geophys. Res.*, *113*(C11), doi:10.1029/2007JC004607.
- Price, J. (1979), Observations of a rain-formed mixed layer, *J. Phys. Oceanogr.*, *9*(3), 643–649, doi:10.1175/1520-0485(1979)009<0643:OOARFM>2.0.CO;2.
- Price, J., R. Weller, and R. Pinkel (1986), Diurnal cycling: Observations and models of the upper ocean response to diurnal heating, cooling and wind mixing, *J. Geophys. Res.*, *91*(C7), 8411–8427, doi:10.1029/JC091iC07p08411.
- Prytherch, J., J. Farrar, and R. Weller (2013), Moored surface buoy observations of the diurnal warm layer, *J. Geophys. Res.*, *118*(9), 1–17, doi:10.1002/jgrc.20360.
- Reda, I., and A. Andreas (2008), Solar position algorithm for solar radiation applications, *Tech. rep.*, National Renewable Energy Laboratory, Golden, Colorado.
- Reverdin, G., S. Morisset, J. Boutin, and N. Martin (2012), Rain-induced variability of near sea-surface T and S from drifter data, *J. Geophys. Res.*, *117*, doi:10.1029/2011JC007549.
- Reverdin, G., S. Morisset, L. Marié, D. Bourras, G. Sutherland, B. Ward, J. Salvador, J. Font, Y. Cuypers, L. Centurioni, V. Hormann, N. Koldziejczyk, J. Boutin, F. D’Ovidio, F. Nencioli, N. Martin, D. Diverres, G. Alory, and R. Lumpkin (2015), Surface salinity in the North Atlantic subtropical gyre during the STRASSE/SPURS summer 2012 cruise, *Oceanography*, *28*, 114–123, doi:10.5670/oceanog.2015.09.
- Riser, S., L. Ren, and A. Wong (2008), Salinity in Argo, *Oceanography*, *21*, 56–67, doi:10.5670/oceanog.2008.67.
- Riser, S., J. Anderson, A. Shcherbina, and E. D’Asaro (2015), Variability in near-surface salinity from hours to decades in the eastern North Atlantic: The SPURS region, *Oceanography*, *28*, 66–77, doi:10.5670/oceanog.2015.11.
- Roemmich, D., G. C. Johnson, S. Riser, R. Davis, J. Gilson, W. Brechner, S. L. G. andd C. Schmid, and M. Ignaszewski (2009), The argo program: Observing the global ocean with profiling floats, *Oceanography*, *22*.
- Ruddick, B., A. Anis, and K. Thompson (2000), Maximum likelihood spectral fitting: The batchelor spectrum, *J. Atmos. Oceanic Technol.*, *17*(11), 1541–1555, doi:10.1175/1520-0426(2000)017<1541:MLSFTB>2.0.CO;2.
- Sanchez, X., E. Roget, J. Planella, and F. Forcat (2011), Small-scale spectrum of a scalar field in water: The batchelor and kraichnan models, *J. Phys. Oceanogr.*, *41*(11), 2155–2167, doi:10.1175/JPO-D-11-025.1.

- Saunders, P. (1967), The temperature at the ocean-air interface, *J. Atmos. Sci.*, *24*, 269–273.
- Scanlon, B., and B. Ward (2016), The influence of environmental parameters on active and maturing oceanic whitecaps, *J. Geophys. Res.*, *121*, 3325–3336, doi:10.1002/2015JC011230.
- Scanlon, B., Ø. Breivik, J. R. Bidlot, P. A. E. M. Janssen, A. H. Callaghan, and B. Ward (2016), Modelling whitecap fraction with a wave model, *J. Phys. Oceanogr.*, *46*, 887–894, doi:10.1175/JPO-D-15-0158.1.
- Schuessel, P., W. Emery, H. Grassl, and T. Mammen (1990), On the bulk-skin temperature difference and its impact on satellite remote sensing of sea surface temperature, *J. Geophys. Res.*, *95*(C8), 13,341–13,356, doi:10.1029/JC095iC08p13341.
- Schlüssel, P. (1996), Satellite remote sensing of evaporation over sea, in *Radiation and Water in the Climate System*, vol. 45, edited by E. Raschke, Springer Berlin Heidelberg, doi:10.1007/978-3-662-03289-3_16, nato ASI Series I: Global Environmental Change.
- Schlüssel, P., A. Soloviev, and W. Emery (1997), Cool and freshwater skin of the ocean during rainfall, *Boundary Layer Meteorology*, *82*, 437–472.
- Schmitt, R. (1995), The ocean component of the global water cycle, *Reviews of geophysics, suppl.*, *33*, 1395–1409.
- Schmitt, R., P. S. Bogden, and C. E. Dorman (1989), Evaporation minus precipitation and density fluxes for the north atlantic, *J. Phys. Oceanogr.*, *10*, 1210–1221.
- Smith, S. (1988), Coefficients for sea surface wind stress, heat flux and wind profiles as a function of wind speed and temperature, *J. Geophys. Res.*, *93*, 467–472.
- Smyth, W. D. (1999), Dissipation-range geometry and scalar spectra in sheared stratified turbulence, *J. Fluid Mechanics*, *401*, 209–242, doi:10.1017/S0022112099006734.
- Smyth, W. D., P. O. Zavialov, and J. N. Moum (1997), Decay of turbulence in the upper ocean following sudden isolation from surface forcing, *J. Phys. Oceanogr.*, *27*(5), 810–822, doi:10.1175/1520-0485(1997)027<0810:DOTITU>2.0.CO;2.
- Soloviev, A., and R. Lukas (1997), Observation of large diurnal warming events in the near-surface layer of the western equatorial Pacific warm pool, *Deep Sea Res. I*, *44*(6), 1055–1076, doi:10.1016/S0967-0637(96)00124-0.
- Soloviev, A., and R. Lukas (2014), *The Near-Surface Layer of the Ocean, structure, dynamics and applications*, 2 ed., Springer.
- Soloviev, A., and P. Schlüssel (1996), Evolution of cool skin and direct air-sea gas transfer coefficients during daytime, *Boundary-Layer Meteorology*, *77*, 45–68.

- Soloviev, A., R. Lukas, P. Hacker, H. Schoeberlein, M. Baker, and A. Arjannikov (1999), A near-surface microstructure sensor system used during TOGA COARE. part II: Turbulence measurements, *J. Atmos. Oceanic Technol.*, *16*(11), 1598–1618, doi:10.1175/1520-0426(1999)016<1598:ANSMSS>2.0.CO;2.
- Soloviev, A. V., S. Matt, and A. Fujimura (2015), Three-dimensional dynamics of freshwater lenses in the ocean’s near-surface layer, *Oceanography*, *28*.
- Sommer, T., J. Carpenter, M. Schmid, R. Lueck, and A. Wüest (2013), Revisiting microstructure sensor responses with implications for double-diffusive fluxes, *J. Atmos. Oceanic Technol.*, *30*, 1907–1923.
- Stommel, H., K. Saunders, W. Simmons, and J. Cooper (1969), Observations of the diurnal thermocline, *Deep-Sea Research*, *16*, 269–284.
- Stuart-Menteth, A., I. Robinson, and C. Donlon (2005), Sensitivity of the diurnal warm layer to meteorological fluctuations. part 2: A new parameterisation for diurnal warming, *J. Atmos. Sci.*, *10*(3), 209–234, doi:10.1080/17417530500529539.
- Sutherland, G., K. Christensen, and B. Ward (2013), Wave-turbulence scaling in the ocean mixed layer, *Ocean Science*, *9*, 597–608, doi:10.5194/os-9-597-2013.
- Sutherland, G., G. Reverdin, L. Mari, and B. Ward (2014a), Mixed and mixing layer depths in the ocean surface boundary layer under conditions of diurnal stratification, *Geophysical Res. Lett.*, *41*, 8469–8476, doi:10.1002/2014GL061939.
- Sutherland, G., K. Christensen, and B. Ward (2014b), Evaluating langmuir turbulence parameterizations in the ocean surface boundary layer, *J. Geophys. Res.*, *119*, 1899–1910, doi:10.1002/2013JC009537.
- Sutherland, G., L. Mari, G. Reverdin, K. Christensen, G. Broström, and B. Ward (2016), Enhanced turbulence associated with the diurnal jet in the ocean surface boundary layer, *J. Phys. Oceanogr.*, *46*, 3051–3067, doi:10.1175/JPO-D-15-1072.1.
- Sweeney, C., A. Gnanadesikan, S. M. Griffies, M. J. Harrison, A. J. Rosati, and B. L. Samuels (2005), Impacts of Shortwave Penetration Depth on Large-Scale Ocean Circulation and Heat Transport, *J. Phys. Oceanogr.*, *35*, 1103.
- ten Doeschate, A., G. Sutherland, L. Esters, D. Wain, K. Walesby, and B. Ward (2017), ASIP: Profiling the upper ocean, *Oceanography*, *30*, doi:10.5670/oceanog.2017.216.
- Terray, E., M. Donelan, Y. Agrawal, W. Drennan, K. Kahma, A. Williams, P. Hwang, and S. Kitaigorodskii (1996), Estimates of kinetic energy dissipation under breaking waves, *J. Phys. Oceanogr.*, *26*(5), 792–807, doi:10.1175/1520-0485(1996)026<0792:EOKEDU>2.0.CO;2.
- Thomson, R., and I. Fine (2003), Estimating the mixed layer depth from oceanic profile data, *J. Atmos. Oceanic Technol.*, *20*, 319–329.

- Thorpe, S. (2005), *The Turbulent Ocean*, Cambridge University Press.
- Thorpe, S. (2007), *An introduction to Ocean Turbulence*, Cambridge University Press.
- Tsimplis, M. (1992), The effect of rain in calming the sea, *J. Phys. Oceanogr.*, *22*, 404–412.
- Turk, D., C. J. Zappa, C. S. Meinen, J. R. Christian, D. T. Ho, A. G. Dickson, and W. R. McGillis (2010), Rain impacts on CO₂ exchange in the western equatorial Pacific Ocean, *Geophysical Res. Lett.*, *37*(23), doi:10.1029/2010GL045520.
- Unesco (1981), Background papers and supporting data on the practical salinity scale 1978, *Unesco technical papere in marine science*, *37*.
- Veron, F., W. K. Melville, and L. Lenain (2011), The effects of small-scale turbulence on airsea heat flux, *Journal of Physical Oceanography*, *41*(1), 205–220, doi:10.1175/2010JPO4491.1.
- Walesby, K., J. Vialard, P. Minnett, A. Callaghan, and B. Ward (2015), Observations indicative of rain-induced double diffusion in the ocean surface boundary layer, *Geophysical Res. Lett.*, *42*, 3963–3972, doi:10.1002/2015GL063506.
- Ward, B. (2006), Near-surface ocean temperature, *J. Geophys. Res.*, *111*(C2), doi:10.1029/2004JC002689.
- Ward, B., and M. A. Donelan (2006), Thermometric measurements of the molecular sublayer at the air-water interface, *Geophysical Res. Lett.*, *33*(7), doi:10.1029/2005GL024769.
- Ward, B., R. Wanninkhof, P. J. Minnett, and M. Head (2004), SkinDeEP: A profiling instrument for upper decameter sea surface measurements, *J. Atmos. Oceanic Technol.*, *21*, 207–222.
- Ward, B., T. Fristedt, A. H. Callaghan, G. Sutherland, X. Sanchez, J. Vialard, and A. ten Doeschate (2014), The Air-Sea Interaction Profiler (ASIP): An autonomous upwardly-rising profiler for microstructure measurements in the upper ocean, *J. Atmos. Oceanic Technol.*, *31*, 2246–2267, doi:10.1175/JTECH-D-14-00010.1.
- Webster, P., and R. Lukas (1992), TOGA COARE: The coupled ocean-atmosphere response experiment, *Bulletin American Meteorological Society*, *73*(9), 1377–1416, doi:10.1175/1520-0477(1992)073<1377:TCTCOR>2.0.CO;2.
- Webster, P., C. Clayson, and J. Curry (1996), Clouds, radiation, and the diurnal cycle of sea surface temperature in the tropical western Pacific, *J. Climate*, *9*.
- Weller, R., A. Fisher, D. Rudnick, C. Eriksen, T. Dickey, J. Marra, C. Fox, and R. Leben (2002), Moored observations of upper-ocean response to the monsoons in the Arabian Sea during 1994-1995, *Deep Sea Res. II*, *49*, 2195–2230, doi:10.1016/S0967-0645(02)00035-8.

- Weller, R., S. Majumder, and A. Tandon (2014), Diurnal restratification events in the southeast pacific trade wind regime, *J. Phys. Oceanogr.*, *44*, 2569–2587, doi:10.1175/JPO-D-14-0026.1.
- Wick, G., W. Emery, and L. Kantha (1996), The behavior of the bulk-skin sea surface temperature difference under varying wind speed and heat flux, *J. Phys. Oceanogr.*, *26*(11).
- Wick, G., J. Ohlmann, C. Fairall, and A. Jessup (2005), Improved oceanic cool-skin corrections using a refined solar penetration model, *J. Phys. Oceanogr.*, *35*(10), 1986–1996.
- Wijesekera, H., C. Paulson, and A. Huyer (1999), The effect of rainfall on the surface layer during a westerly wind burst in the western equatorial Pacific, *J. Phys. Oceanogr.*, *29*, 612 – 632.
- Wijesekera, H., D. Rudnick, C. Paulson, S. Pierce, W. S. Pegau, J. Mickett, and M. Gregg (2005), Upper ocean heat and freshwater budgets in the eastern Pacific warm pool, *J. Geophys. Res.*, *110*(C8), doi:10.1029/2004JC002511.
- Wolk, F., H. Yamazaki, L. Seuront, and R. Lueck (2002), A new free-fall profiler for measuring biophysical microstructure, *J. Atmos. Oceanic Technol.*, *19*, 780–793, doi:10.1175/1520-0426(2002)019<0780:ANFFPF>2.0.CO;2.
- Woods, J. D., and V. Strass (1986), The response of the upper ocean to solar heating ii: The wind-driven current, *Quarterly Journal of the Royal Meteorological Society*, *112*(471), 29–42, doi:10.1002/qj.49711247103.
- Zappa, C., D. Ho, W. McGillis, M. Banner, J. Dacey, L. Bliven, B. Ma, and J. Nystuen (2009), Rain-induced turbulence and air-sea gas transfer, *J. Geophys. Res.*, *114*, doi:10.1029/2008JC005008.
- Zeng, X., and A. Beljaars (2005), A prognostic scheme of sea surface skin temperature for modeling and data assimilation, *Geophysical Res. Lett.*, *32*(14), doi:10.1029/2005GL023030.